Selective Catalytic Reduction of NO_x by NH_3 (NH_3-SCR) in small pore Cu-exchanged Chabazite (CHA) catalysts

A Dissertation

Presented to

the Faculty of the Department of Chemical and Biomolecular Engineering

University of Houston

In Partial Fulfillment

of the Requirements for the Degree

Doctor of Philosophy

in Chemical Engineering

by

Di Wang

May 2014

Selective Catalytic Reduction of NO_x by NH_3 (NH_3-SCR) in small pore Cu-exchanged Chabazite (CHA) catalysts

Di Wang

Approved:

Co-Chair of the Committee
William Epling, Associate Professor,
Chemical and Biomolecular Engineering

Co-Chair of the Committee
Michael P. Harold, Professor,
Chemical and Biomolecular Engineering

Committee Members:

Jeffrey Rimer, Assistant Professor,
Chemical and Biomolecular Engineering

Shankar Chellam, Professor,
Civil and Environmental Engineering

Krishna Kamasamudram, Technical Advisor,
Catalyst Technology, R&T, Cummins Inc

Suresh K. Khator, Associate Dean,
Cullen College of Engineering

Michael P. Harold, Professor and Chair,
Chemical and Biomolecular Engineering

Acknowledgements

I would like to thank my PhD advisor, Dr. William Epling for valuable instructions and support throughout my PhD life. During the past years, not only his insightful inputs leaded me to be a qualified researcher, more importantly, his great characters positively inspired me of developing a respectable personality. I would like to thank him for giving me freedom to study and think and always being readily available for instructive discussion. I will cherish all the fond memories of working with this great person.

I would thank my former advisors Dr. Michael P. Harold and Dr. Jeffrey Rimer who essentially opened the door for my PhD research. I could not have accomplished my PhD degree without their consistent love and support. The knowledge and experience I learned from Dr. Harold and Dr. Rimer have built up a solid background towards my future work. I deeply appreciate their help throughout my PhD life.

I would also like to express my gratitude to Dr. Krishna Kamasamudram who provided me incredible help and advice to my work. I admire his professional attitude and have thoroughly enjoyed our conversations and discussions about research and other things in life. I would like to thank Dr. Shankar Chellam for serving on my committee and for his constructive comments and recommendations on my research project. I am also truly thankful to Dr. Vincent Donnelly for his kind advice and help at the beginning of my PhD years.

I am grateful to my family: mother, father, and all the other family members for always supporting me throughout the past years. Special thanks to Yang Li, for her love, understanding, and encouragement.

Appreciation is given to my former and current fellow lab mates: Li, Tayebeh, John, Chaitanya, Victor, Yong, Melanie, Munish, Ali, Monique, Yasser, Anh, Alex, Sahar, Matt, Yang, Yi, and Greg. I would like to thank my colleagues at Cummins for many valuable technical suggestions. I would also like to acknowledge my friends Lixin, Tian, Jiejie, and Xiaoqing for making my life colorful in Houston.

Selective Catalytic Reduction of NO_x by NH_3 (NH_3-SCR) in small pore Cu-exchanged Chabazite (CHA) catalysts

An Abstract

of a

Dissertation

Presented to

the Faculty of the Department of Chemical and Biomolecular Engineering

University of Houston

In Partial Fulfillment

of the Requirements for the Degree

Doctor of Philosophy

in Chemical Engineering

by

Di Wang

May 2014

Abstract

Nitrogen oxides, NO_x ($NO+NO_2$), are considered significant air pollutants. Selective catalytic reduction of NO_x with NH_3 (NH_3-SCR) is a leading technology candidate for NO_x emissions control for diesel engine vehicles. Recently, the Cu-exchanged chabazite framework type zeolite with small pores, such as SAPO-34 and SSZ-13, has received a great deal of attention due to exceptional hydrothermal durability and enhanced SCR activity. I have carried out a systematic study over both Cu-SAPO-34 and Cu-SSZ-13 catalysts to elucidate the reaction mechanisms, acid properties, Cu structures, active centers and deactivation modes.

First, the intrinsic mechanism of the SCR reaction over a Cu-exchanged SAPO-34 catalyst at low temperature was studied by in-situ diffuse reflectance infrared Fourier transform spectroscopy (DRIFTS), coupled with a mass spectrometer to measure inlet and outlet gas concentrations. The evolution of the surface intermediates, as well as the reactivity of NH_3 with surface NO_x species and NO_x with surface NH_3 species, was evaluated.

Second, a series of SAPO-34 catalysts with various Cu loadings (ranging 0.7-3.0 wt%) was prepared by a solid state ion exchange method (SSIE). The acid properties as well as the Cu structures were characterized by XRD, NH_3-TPD, UV-vis, DRIFTS and H_2-TPR.

Third, a SSIE method was developed to synthesize Cu-SSZ-13 catalysts with excellent NH_3-SCR performance and durable hydrothermal stability. After the SSIE process, the SSZ framework structure and surface area was maintained. DRIFTS and

NH_3-TPD experiments provide evidence that Cu ions were successfully exchanged with Brønsted acid protons in the pores.

Fourth, the hydrothermal stability of Cu-SAPO-34 and Cu-SSZ-13 was studied. Their different evolutions of zeolite framework, acidity and Cu structure during the hydrothermal aging were probed by XRD, DRIFTS and NH_3-TPD. The results suggest that Cu-SAPO-34 is more resistant to hydrothermal aging in comparison to Cu-SSZ-13.

Last, the SO_2 poisoning effect over Cu-SAPO-34 catalyst was investigated by using in-situ DRIFTS combined with temperature programmed desorption (TPD) experiments. It was found that the low temperature deactivation mechanism involved the formation of ammonium sulfate species as well as the competitive adsorption SO_2 with NO_x.

Table of Contents

List of Figures

List of Tables

Nomenclature

NO_X	Nitrogen oxides ($NO + NO_2$)
PM	Particulate Matter
USEPA	United States Environmental Protection Agency
NH_3-SCR	Selective Catalytic Reduction of NO_x by NH_3
LNT	Lean NO_x Trap
NSR	NO_x Storage/Reduction
DOC	Diesel Oxidation Catalyst
AMO_X	NH_3 oxidation Catalyst
DPF	Diesel Particulate Filter
WGS	Water Gas Shift
DRIFTS	Diffuse Reflectance Infrared Fourier Transform Spectroscopy
UV-vis	Ultraviolet-Visible Spectroscopy
XANES	X-ray Absorption Near Edge Structure
EXAFS	Extended X-ray Absorption Fine Structure
XRD	X-Ray Diffraction
EPR	Electron Paramagnetic Resonance

TPD	Temperature Programmed Desorption
TPR	Temperature Programmed Reduction
WIE	Wetness Ion Exchange
IMP	Incipient Wetness Impregnation
SSIE	Solid State Ion Exchange
SEM	Secondary Electron Multiplier
SDA	Structural Directing Agent
HGB	Houston-Gaveston-Brazoria area
HGAC	Houston-Galveston Area Council
MFC	Mass Flow Controller
FTIR	Fourier Transform Infrared Spectroscopy
ID	Inner Diameter
PID	Proportional Integral Derivative
IR	Infrared Radiation
CVD	Chemical Vapor Deposition
KM	Kubelka-Munk
ICP	Inductively Coupled Plasma

T-O-T	Tetrahedral-Oxygen-Tetrahedral
GHSV	Gas Hourly Space Velocity
TOF	Turnover Frequency
BET	Brunauer Emmett Teller
XAS	X-ray Absorption Spectroscopy
TEM	Transmission Electron Microscopy
LMCT	Ligand to Metal Charge Transfer

Chapter 1 Introduction and Background

1.1 Introduction

Over the last two decades, the lean burn diesel engine has attracted significant interest due to better fuel economy and greater power density compared to conventional gasoline engines. However, to meet regulations, their use depends on the effective reduction of two primary diesel exhaust components: nitrogen oxides (NO_x) and particulate matter (PM). NO_x, which is a mixture of NO and NO_2, is one of the main air pollutants causing acid rain and ground ozone formation as well as affecting human health by irritating the lungs. According to the United States Environmental Protection Agency (US-EPA), about 15.5 million tons of NO_x have been emitted into the atmosphere in the United States in 2011 and about 57 % of this is attributed to automobile exhaust (Figure 1.1) [1]. Fuel combustion in stationary sources, industrial emissions and other processes contributed to the rest.

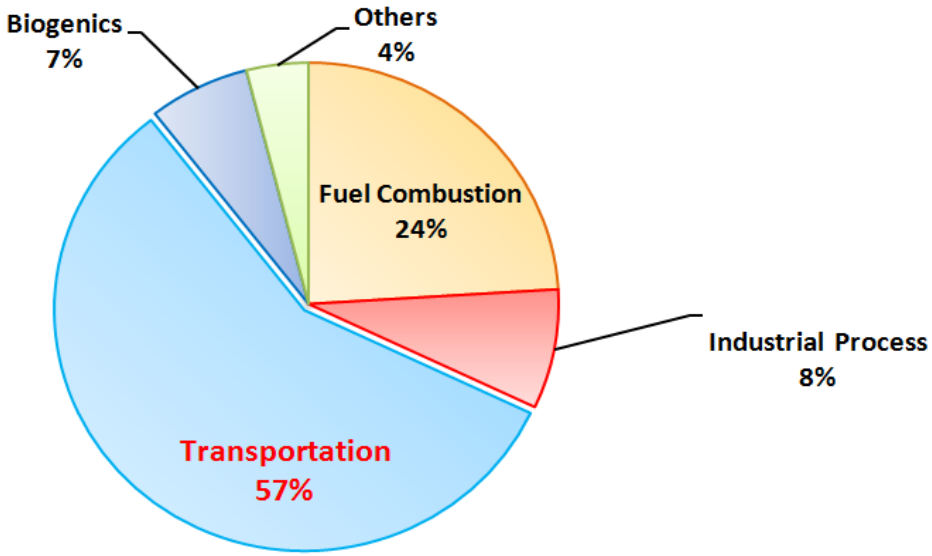

Figure 1.1 2011 NO_x emission by sources in United States (Source: USEPA)

Among the transportation sources, a significant amount of NO_x emissions came from heavy duty diesel engine exhaust. For example, NO_x emissions from on-road mobile sources in the Houston-Galveston-Brazoria area reached 56,000 tons in 2009 and accounted for 38% of the total annual NO_x emissions. As shown in Figure 1.2, among these on-road mobile NO_x emission sources, heavy-duty diesel contributed 48% [2].

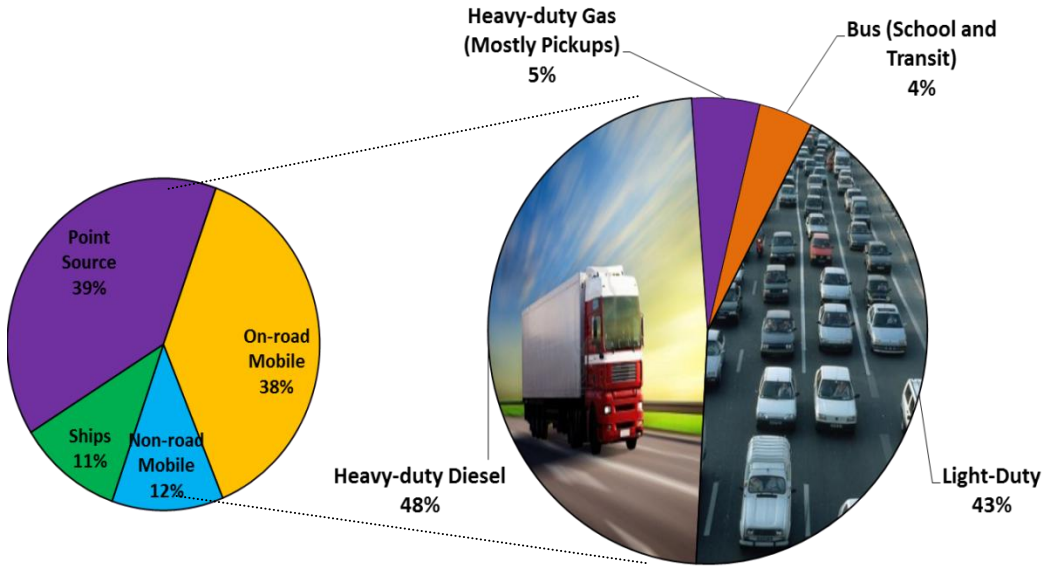

Figure 1.2 2009 NO_x emission by sources in Houston-Gaveston-Brazoria area (HGB) provided by Houston-Galveston Area Council (HGAC)

In order to efficiently treat NO_x emissions from heavy duty diesel engines, the United States Environmental Protection Agency (USEPA) has been legislating very strict emission standards. Figure 1.3 lists the EPA regulations for NO_x and PM emissions during the past two decades [3]. From 1988 to 2010, the EPA has mandated a 98% reduction in NO_x emissions from heavy duty diesel engines. In 2010, the NO_x emission standard was set to 0.2 g/bhp-hr; and in Europe, the ongoing emission standard Euro 6 (effective January 1, 2014) regulates the NO_x emission limit to be 0.4 g/kWh (0.58 g/bhp-hr), which is an 80% reduction in comparison to the Euro 5 standard that was effective from 2010 [4].

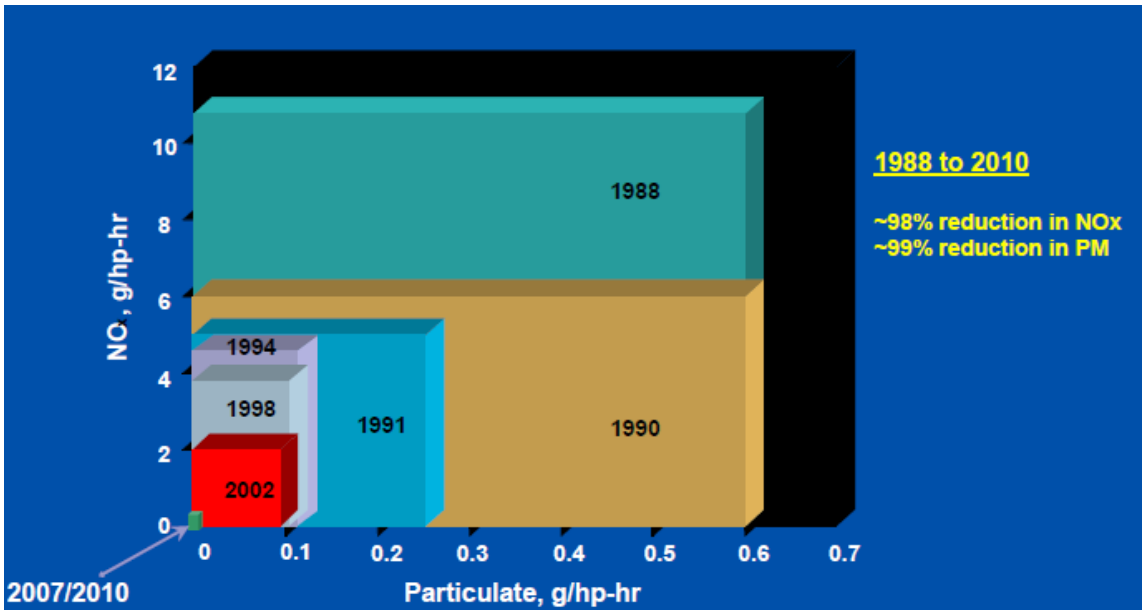

Figure 1.3 US heavy duty emission requirements by USEPA [3]

As the legislated targets become more and more stringent, new catalyst-based after-treatment technologies have been developed. Here, the "traditional" three-way catalytic converter technology used in today's gasoline-powered vehicles does not result in the needed reductions to meet most legislated standards and therefore is not applicable to diesel engines. The main reason is that three-way catalysts are designed for emissions control in exhaust conditions that are net stoichiometric while the diesel engine is lean-burn. As a result, the fundamental challenge for NO_x control in lean-burn engine exhaust is the reduction of NO_x in an O_2-containing environment. Until now, the most promising NO_x abatement technologies are the selective catalytic reduction (SCR) catalyst and lean-NO_x trap (LNT). Besides NO_x, the other key pollutants that need to be reduced are hydrocarbons, CO, and particulate matter (PM). In terms of CO and hydrocarbons, the excess oxygen released from combustion promotes the oxidation reaction. The challenge is the lower temperatures associated with lean-burn engine exhaust and ensuring light-off over an oxidation catalyst can be achieved. Particulate matter is filtered, typically using

what is called a wall-flow filter, where the exhaust gas passes through a highly porous cordierite or silicon carbide wall and a cake builds up. The challenge is the controlled, intermittent regeneration of the filter to remove the built-up carbonaceous species so that the back-pressure is decreased while simultaneously ensuring that thermal runaway due to the exotherm produced does not overheat the filter or downstream catalysts. For the variety of pollutants, a series of devices needs to be used in a diesel engine after-treatment system.

1.2 Diesel engine after-treatment system

Figure 1.4 shows an example of a commercial Cummins diesel exhaust after-treatment system equipped with a SCR catalyst for NO_x reduction [5]. The upstream diesel oxidation catalyst (DOC) removes CO and hydrocarbons, and is followed by a diesel particulate filter (DPF) where soot is filtered and removed. Subsequently, NO_x is reduced by a SCR catalyst (or lean-NO_x trap in other systems). Here, NH_3 is supplied by the decomposition of urea injected from a fluid dosing system. An NH_3 oxidation catalyst (AMO_x) is used after the SCR to prevent any NH_3 slip from the SCR catalyst.

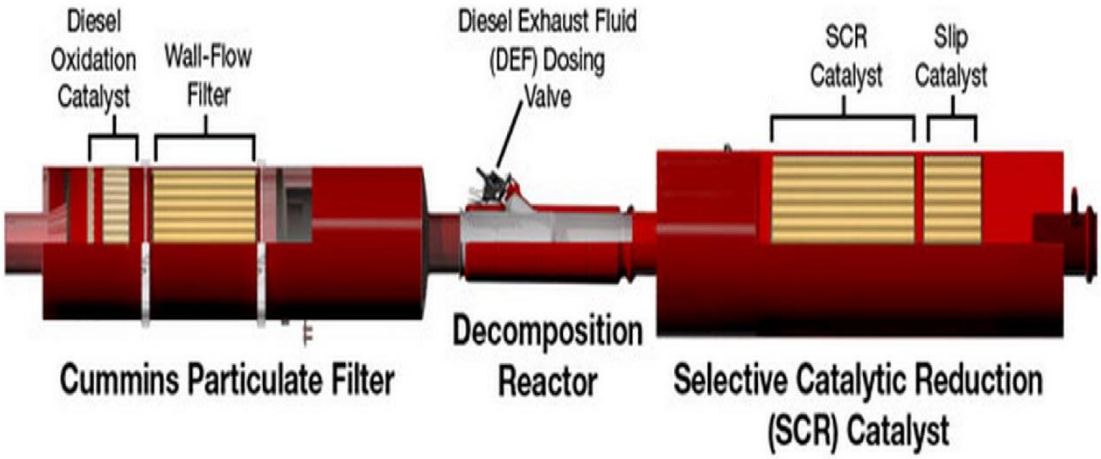

Figure 1.4 An example of Cummins diesel after-treatment system [5]

1.2.1 Diesel Oxidation Catalyst (DOC)

The DOC oxidizes the hydrocarbons, NO, and CO in the diesel exhaust. The major reactions that take place on the DOC are as follows:

$$CO + ½\ O_2 \rightarrow CO_2, \quad (1\text{-}1)$$

$$NO + ½\ O_2 \rightarrow NO_2, \quad (1\text{-}2)$$

$$HC + O_2 \rightarrow CO_2 + H_2O, \text{ and} \quad (1\text{-}3)$$

$$SO_2 + ½\ O_2 \rightarrow SO_3. \quad (1\text{-}4)$$

In many after-treatment designs, the DOC is used upstream of the SCR or LNT catalysts and the DPF. On one hand, the NO_2 produced over the DOC enhances NO_x reduction catalyst performance and over particulate filters, soot is oxidized at significantly lower temperatures with NO_2 as NO_2 is a stronger oxidant than O_2 [6-8]. On the other hand, hydrocarbons, which poison the NO_x reduction catalyst, can be removed in the DOC before entering the NO_x reduction catalyst unit [9, 10]. In addition to NO, hydrocarbon and CO oxidation, another primary role of the oxidation catalyst is to heat up the exhaust for downstream NO_x and soot control components. The rapid warm-up can be accomplished by adding hydrocarbons to the exhaust mixture, either by directly injecting fuel into the exhaust upstream of the oxidation catalyst or by decreasing the air-to-fuel ratio.

The DOC typically contains Platinum (Pt) and/or Palladium (Pd) due to their high catalytic activity. In addition, Cerium (Ce) and zeolites additives are sometimes added. It

is reported that the inclusion of Pd to Pt-based DOCs can prevent Pt particle sintering at high temperature and therefore enhance the total DOC lifetime and durability [11-13]. Furthermore, if some Pt can be replaced by Pd, this reduces the DOC cost. Pt and Pd show very different activities for hydrocarbon oxidation. The optimal ratio of Pd:Pt to achieve lower light-off temperatures varies from 4:1 to 1:3, depending on the feed composition [14, 15]. However, this dependence is non-linear, with particle sizes and oxidation states a function of the ratio [13, 16-18].

1.2.2 Diesel Particulate Filter (DPF)

Diesel particulate matter (PM) is one of the primary pollutants in diesel engine exhaust. It consists of carbon, inorganic oxides and hydrocarbons, caused by local low temperature areas in the cylinder where the fuel is not fully atomized [19]. Particulate matter can penetrate into the lung and is a potential occupational carcinogen of the human respiratory system [20]. EPA regulations, detailed in Figure 1.3, mandate at least 90% reduction of the PM from heavy duty diesel engines. The diesel particulate filter (DPF) is the current technology of choice for PM removal from diesel engine exhaust [21-23]. Figure 1.5 describes a schematic of a DPF section [24]. A typical DPF consists of thousands of square parallel channels with the opposite ends of alternative channels being blocked so the exhaust gas is forced though the porous walls, with typically more than 95% PM accumulated on the filter wall [25]. Although the DPF is efficient in treating particulates from the engine exhaust, periodic regeneration is required to eliminate any plugging and/or backpressure. O_2 can oxidize the soot particles, typically at quite high temperatures though, on the order of > 550°C. However, soot can be oxidized at much lower temperatures by NO_2 [6-8].

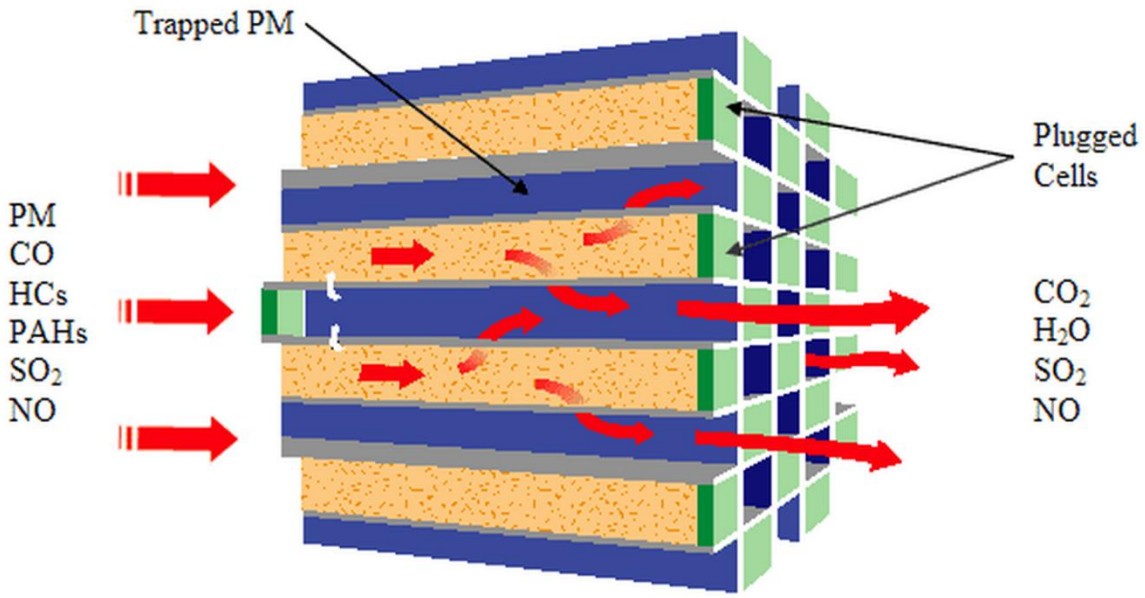

Figure 1.5 The schematic of DPF channels [24]

1.2.3 Lean NO_x Trap (or NO_x Storage/Reduction – NSR) catalysts

LNT/NSR is one of the leading technologies for lean NO_x emission control. It was first applied to vehicles in 1995 by researchers at Toyota [26]. In LNT, NO_x is alternately stored on a catalyst under the normally lean exhaust conditions and then reduced to N_2 in a rich exhaust. The lean mode usually lasts 60-90s and is followed by a much shorter 1-5s rich cycle. The most commonly studied LNT catalyst is Pt-Ba/Al_2O_3 [27-30]. A proposed mechanism of the NO_x storage and reduction is described in Figure 1.6 [26]. NO is first oxidized to NO_2 on a precious metal component during the lean-burn operation. Subsequently, NO and NO_2 spills over to BaO to form nitrites and nitrates. Under rich-burn conditions, nitrites and nitrates decompose and the released NO is reduced by H_2, CO and/or hydrocarbons into N_2 over the Pt. The significance of Pt-Ba interface for NO_x storage and reduction has been reported [31, 32]. It was concluded that the reactions were more rapid with Ba and Pt sites being close. CeO_2, well known as an effective oxygen

storage component, is typically incorporated into LNT catalysts to improve their overall activity, durability and desulfation properties [33-35]. Firstly, additional NO_x storage capacity combined with enhanced NO oxidation by CeO_2-supported Pt, result in increased NO_x adsorption [36]. Secondly, Ce-based nitrates have lower thermal stability than Ba-based nitrates, enabling more effective stored NO_x regeneration [37]. Thirdly, ceria mitigates of CO poisoning by promoting either the CO oxidation or water gas shift (WGS) reaction at low temperature [38]. For the WGS reaction, CeO_2-supported precious metal can exhibit a rate that is several orders of magnitude higher than precious metal alone, significantly promoting H_2 generation at low temperatures [33].

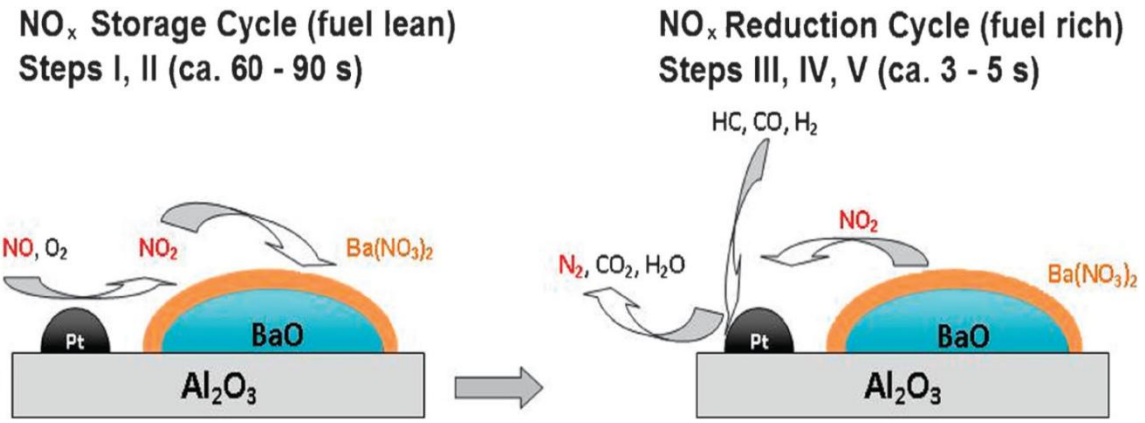

Figure 1.6 Proposed mechanism of NO_x storage and reduction on the NSR catalyst [26]

1.2.4 Selective Catalytic Reduction of NO_x by NH_3 (NH_3-SCR)

NH_3-SCR refers to the selective catalytic reduction of NO_x by NH_3, in which the NO_x exhaust is selectively reduced to N_2 in excess O_2 by using NH_3 as a reducing agent. This technology was first applied in Japan during the 1970's to control lean NO_x exhaust from stationary power plants [39]. The first generation NH_3-SCR catalyst was a vanadia-based catalyst. However, for vehicular applications, these suffer from low activity and

selectivity at high temperature. Other drawbacks are oxidation of SO_2 to SO_3, the formation of byproduct N_2O and the toxicity of vanadia if it sublimes at high temperature [40]. In the late 1980s, transition metal (Fe or Cu) exchanged zeolite frameworks with medium and large pores, such as MFI (ZSM-5), FER and BEA, were evaluated and considered as SCR catalyst candidates [41]. Although there is still some argument, the roles of the transition metals (Fe or Cu) include promoting the NO oxidation reaction as well as creating acid sites for NH_3 adsorption [42-44]. However, the hydrothermal stability of these catalysts was/is problematic [45, 46]. In the last several years, the focus has been on Cu-exchanged small pore zeolite catalysts, such as Cu-SAPO-34 and Cu-SSZ-13. Here, it is worthwhile pointing out that SAPO-34 is a zeotype material (with Si, Al and P as the tetrahedral) whose framework is very similar to zeolite, therefore, we regard it as a "zeolite" type material in this dissertation. In 2010, researchers from PNNL published the first paper reporting enhanced SCR activity using Cu-SSZ-13 in comparison to Cu-ZSM-5 and Cu-Beta [47]. Fickel et al., showed that Cu-SAPO-34, which is another Chabazite (CHA) type material, gave very similar results to SSZ-13 in terms of SCR activity and hydrothermal stability [45]. Following these initial publications, a tremendous amount of work has focused on gaining a better understanding of Cu-exchanged SAPO-34 and SSZ-13.

The CHA framework structure is constructed by stacking layers of double 6-membered ring in an AABBCCAA sequence through the tilted 4-membered rings [48]. It is generally called a small pore zeolite since it has relatively small pore openings of 3.8Å [49], however, the CHA structure also contains large cavities accessible through three-dimensional 8-membered rings. As shown in Figure 1.7, there are four different possible

cation positions in the CHA framework structure: (1) in the center of the double-6-membered rings (position I), in the cavity near the face of the 6-membered ring (position II), (3) in between two units of cavities (position III), and (4) in (or near) the 8-membered ring window (position IV) [50]. The Si/Al ratio in CHA framework can vary from 1 to infinity, however, the typical Si/Al ratio of Cu-SSZ-13 for SCR reaction is in the range of 6-18 [48].

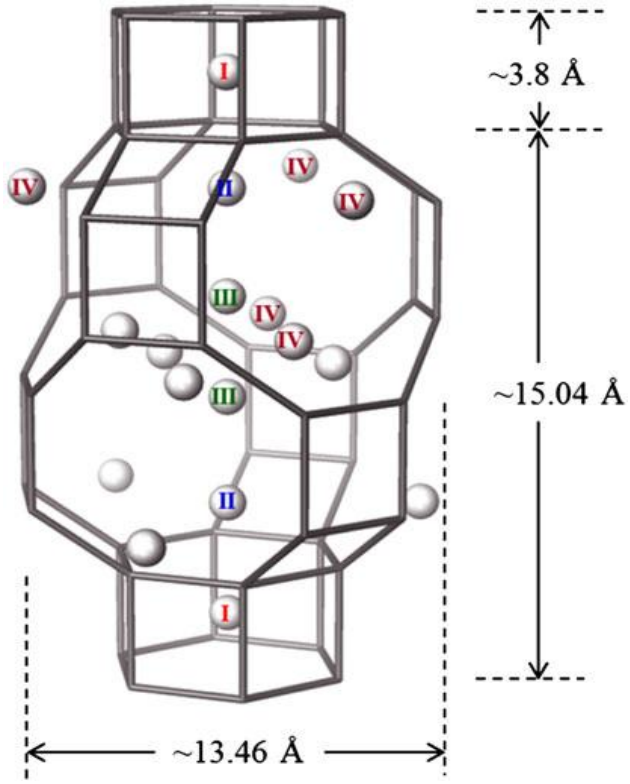

Figure 1.7 Possible cation positions in the CHA structure [50]

1.3 Review of previous NH_3-SCR studies

1.3.1 Basics of NH_3-SCR

In the commercial diesel after-treatment system, an aqueous solution of urea is injected into the exhaust upstream of the SCR catalyst and NH_3 is generated via urea

hydrolysis [51]. In some cases, an NH_3 oxidation catalyst (AMO_X) is installed downstream of the SCR catalyst to prevent any NH_3 slip. In typical lean-burn engine exhaust, NO is the primary NO_x constituent with a smaller fraction of NO_2 [52]. Thus, the more common reaction is between NO and NH_3 and is called "standard SCR" [44],

$$4NH_3 + 4NO + O_2 \rightarrow 4N_2 + 6H_2O. \quad (1\text{-}5)$$

In the upstream oxidation catalyst, some of the NO could be oxidized to NO_2 and the reaction between equimolar NO and NO_2 and NH_3 is faster than the standard SCR reaction, and is called the "fast SCR" reaction [44],

$$2NH_3 + NO + NO_2 \rightarrow 2N_2 + 3H_2O. \quad (1\text{-}6)$$

If the fraction of NO_2 is larger than NO, NO_2 can react with NH_3 and reaction is called "NO_2 SCR" [44],

$$4NH_3 + 3NO_2 \rightarrow 3.5N_2 + 6H_2O. \quad (1\text{-}7)$$

Although the mechanism of the NH_3-SCR reaction is still under debate, there is a general consensus that (1) the extra-framework Cu sites in the zeolite materials catalyze the NH_3-SCR reaction, with H form zeolites having negligible SCR activity [53] and (2) the inclusion of excess O_2 in the reactant feed is critical. It has been widely reported that NO has to be oxidized to NO_2 for the SCR reaction to proceed, at least over transition metal exchanged ZSM-5 and Beta, and therefore the NO oxidation reaction was considered to be the rate-determining step of the mechanism [43, 44, 53, 54]. A detailed reaction pathway summarized by Branderberger et al., and including NO oxidation is described in Figure 1.8 [51].

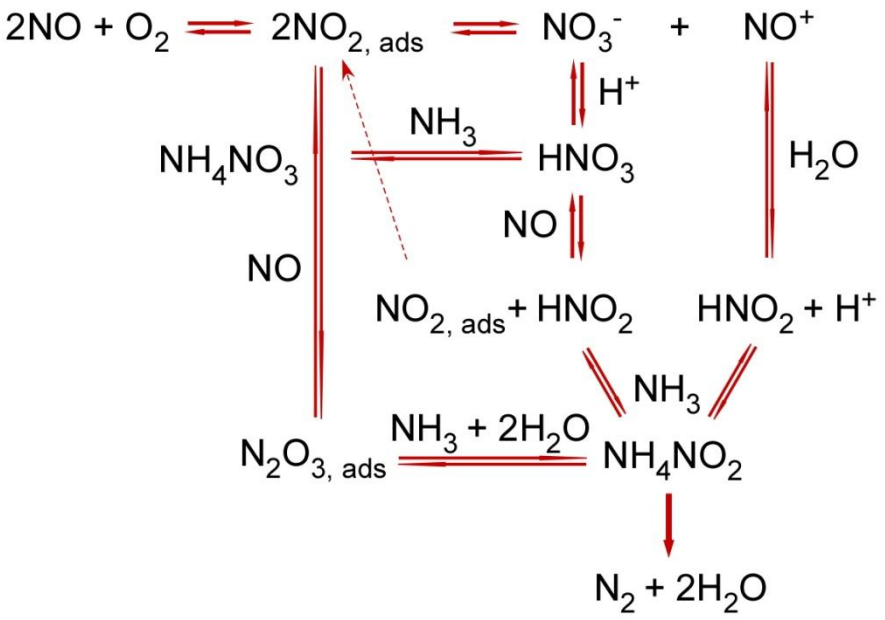

Figure 1.8 Reaction pathway for SCR over metal-exchanged zeolites [51]

In the reaction pathway proposed, the surface nitrates and nitrites formed, originating from NO oxidation, are the key intermediates for the NH_3-SCR reaction. Recently, Feng et al., proposed a different reaction pathway by demonstrating that the Cu-CHA catalysts, which showed excellent SCR activity, turned out to be very poor NO oxidation catalysts, especially in the presence of H_2O [55]. They therefore proposed the SCR activity has nothing to do with the NO oxidation reaction. In the reaction mechanism proposed by the same group (Figure 1.9), the formation of nitrosyl NO^+ species, evidenced by a strong NO^+ band in the in-situ DRIFTS spectra, is the key step in the SCR reaction, and Cu^{2+} is reduced to Cu^+ as part of the reaction, in turn followed by re-oxidation to Cu^{2+} by O_2 to complete a redox cycle [56]. However, there is lack of direct evidence on how the surface NO^+ species and SCR activity were related. Therefore, further investigation is still needed with respect to the reaction mechanism of NH_3-SCR on the small pore Cu zeolite catalyst.

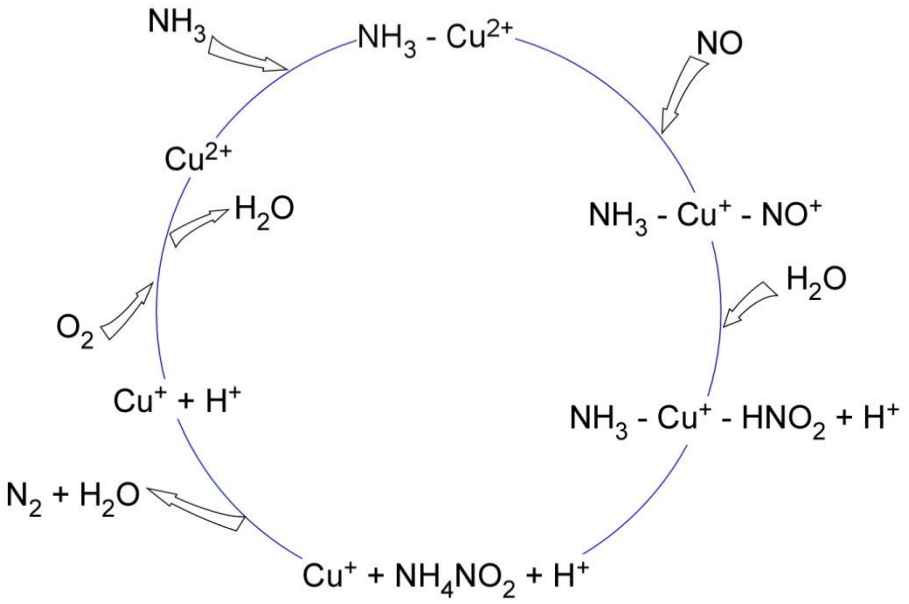

Figure 1.9 Proposed low-temperature standard NH_3-SCR reaction path-ways catalyzed by isolated Cu ion monomers [48]

With respect to the active sites for NH_3-SCR over/within Cu-exchanged small pore zeolites, there is still some debate although most agree that isolated Cu^{2+} sites are the reactive sites in the catalyst. Different types of Cu structures have been observed, such as isolated Cu^{2+}, Cu^{+}, Cu dimers $(Cu\text{-}O\text{-}Cu)^{2+}$, Cu_xO_y clusters, and CuO particles [45, 49, 57-60]. However, the characterization and quantification of these species are not straightforward. It seems to be commonly accepted that isolated Cu^{2+} are the active sites for NH_3-SCR in both SSZ-13 and SAPO-34 at low temperature [45, 57, 61]. Isolated Cu^{2+} has been observed with EPR spectroscopy [60, 62]. However, Cu dimers and Cu_xO_y clusters are EPR silent. Other groups have used H_2 temperature programmed reduction (TPR) measurements to distinguish Cu structures; however, again no agreement has been made on the assignments of the different H_2 consumption peaks [60, 62, 63]. Figure 1.10 shows the H_2-TPR results obtained on Cu-SSZ-13 with different Cu loadings. The sample with the lowest Cu loading only resulted in one single H_2 consumption peak at 340°C,

while with increasing Cu loading, an additional peak at 230°C was observed. Therefore, the authors proposed that there are two different Cu^{2+} species in Cu-SSZ-13 catalysts whose proportion also changed with changing the Cu loading and they are most likely placed in and/or close to the 6-membered rings (position I and II, Figure 1.7) and inside the large cages of the CHA structure (position III and IV), respectively [64]. The Cu loading effects were further investigated by Feng et al., using electron paramagnetic resonance (EPR) spectroscopy [62]. The measurement was conducted at 155K in order to accurately monitor the dipole-dipole interactions of Cu. Based on the fitted hyperfine features from the EPR results, the authors confirmed the existence of two Cu^{2+} ions: one is in/close to a 6-membered ring and the other is near to an 8-membered ring [62].

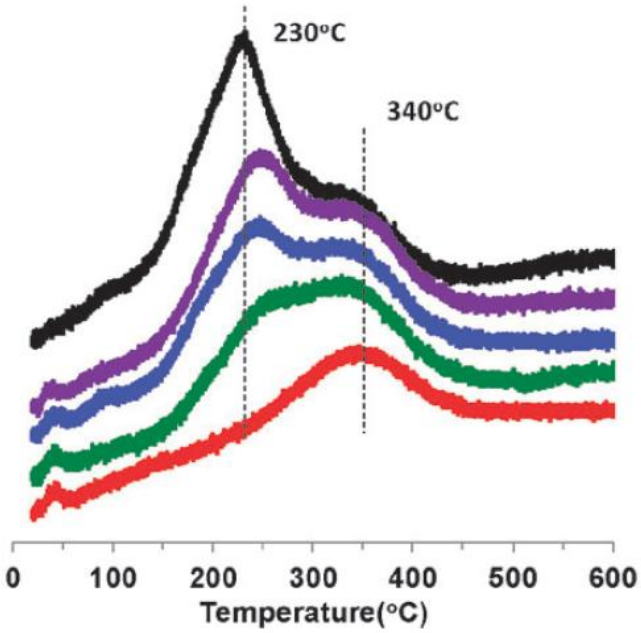

Figure 1.10 H_2 consumption profiles during H_2-TPR on 500°C calcined Cu-SSZ-13 (sample weight = 50 mg; heating rate = 10 °C/min; total flow rate = 60 ml/min, 2% H_2/Ar) [64]

1.3.2 Catalyst preparation

Both SAPO-34 and SSZ-13 have the same Chabazite (CHA) structure that contains the double-six membered prism in the large cavities of the structure. However, the hydrothermal synthesis of these two zeolites turns out to be different. In particular, the hydrothermal synthesis of SSZ-13 utilizes a relatively expensive structural directing agent (SDA), *N,N,N*-trimethyl-1-adamantammonium hydroxide (TMAdaOH). This method was invented and patented by Zones in 1985 [65]. Different from SSZ-13, whose framework is constructed by tetrahedral Si and Al, SAPO-34 material is generated by the substitution of Si in the AlPO structure, initially formed from P and Al. The SDA that can be used in the synthesis of SAPO-34 is TEA, TEAOH or MOR [45, 66, 67]. Gao et al., however, reported that these SDAs undergo different extents of irreversible hydrolysis during the synthesis process of SAPO-34 materials. Particularly, TEA turned out to be a better SDA than MOR and a TEA/MOR mixture since the latter two led to a significant loss in surface area and pore volume [66]. The as-synthesized SSZ-13 and SAPO-34 are in the Na^+ form and subsequently transformed into NH_4^+ form by ion exchange with NH_4^+ salt solutions. This ion exchange step is very crucial since the protons in the zeolites create the Brønsted acid sites for NH_3 storage. The resulting NH_4^+ form zeolite is ion exchanged into Cu-SSZ-13 as the final product. Here, different preparation methods can be applied and the wetness ion exchange (WIE) is the most common. In this approach, the NH_4^+ or H^+ form zeolite is added to the Cu^{2+} salt solution under constant stirring for several hours followed by a wash and dry process. It is widely reported that the samples prepared by WIE are highly active in the NH_3-SCR reaction [45, 47, 57, 58, 61, 62, 66]. This was explained by the fact that the Cu ions selectively exchange into the pores as

isolated Cu^{2+} sites, which are commonly accepted to be the active sites for NH_3-SCR at low temperature, however, other approaches may result from other types of Cu species [45, 57, 61, 68]. Recently, Ren et al., developed a so-called "one pot" synthesis approach in which the Cu ions were incorporated with the zeolite framework during the hydrothermal synthesis of the zeolite material. Particularly, Cu–tetraethylenepentamine (Cu–TEPA) was used as the SDA instead of the more expensive TMAdaOH, therefore the cost of the process was drastically reduced [69]. The SCR activity and hydrothermal durability of the samples that were prepared by this direct synthesis method were reported to be comparable to those obtained from WIE [68-70]. In addition, a precipitation (or impregnation) method was also reported. However, the efficiency of this approach was quite low and the formation of CuO particles appeared to be very critical problem for this method [61, 68].

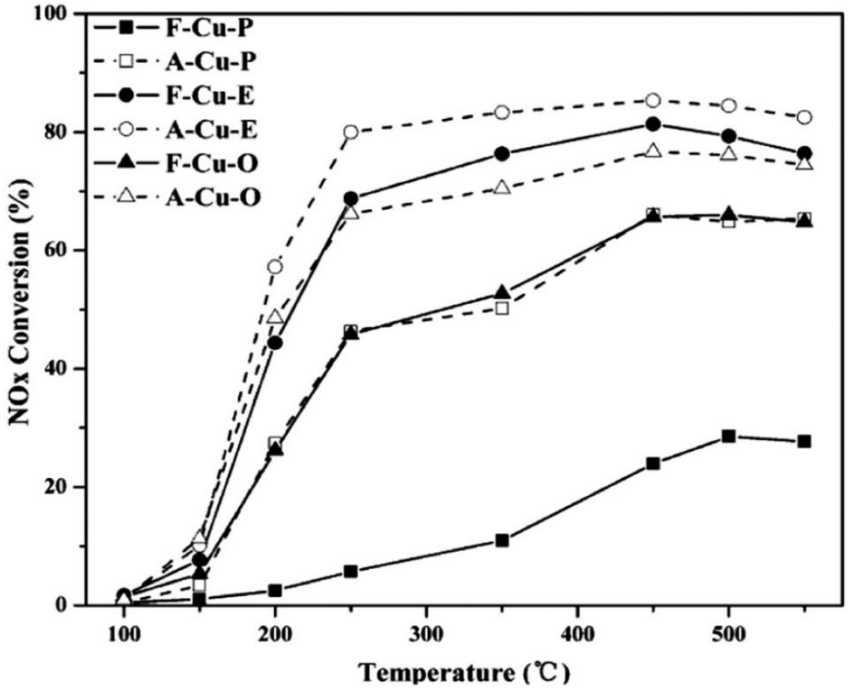

Figure 1.11 NO_x conversions as a function of reaction temperature (reaction conditions: 500 ppm NO, 500ppm NH_3, 5% O_2, 8% CO_2, 5% H_2O balanced with N_2; the flow rate: 2 L min^{-1}; WHSV: 1511 h^{-1}, catalyst weight 100mg) [68]

Figure 1.11, which was recently published by Fan et al., compares the effects of preparation methods on the SCR activity [68]. It is clear that the wetness ion-exchanged Cu-SAPO-34 sample resulted in much higher SCR activity than the precipitated Cu-SAPO-34 sample. And the one-pot method turned out to be a good alternative as it showed comparable activity and hydrothermal durability relative to the samples prepared by the ion exchange method.

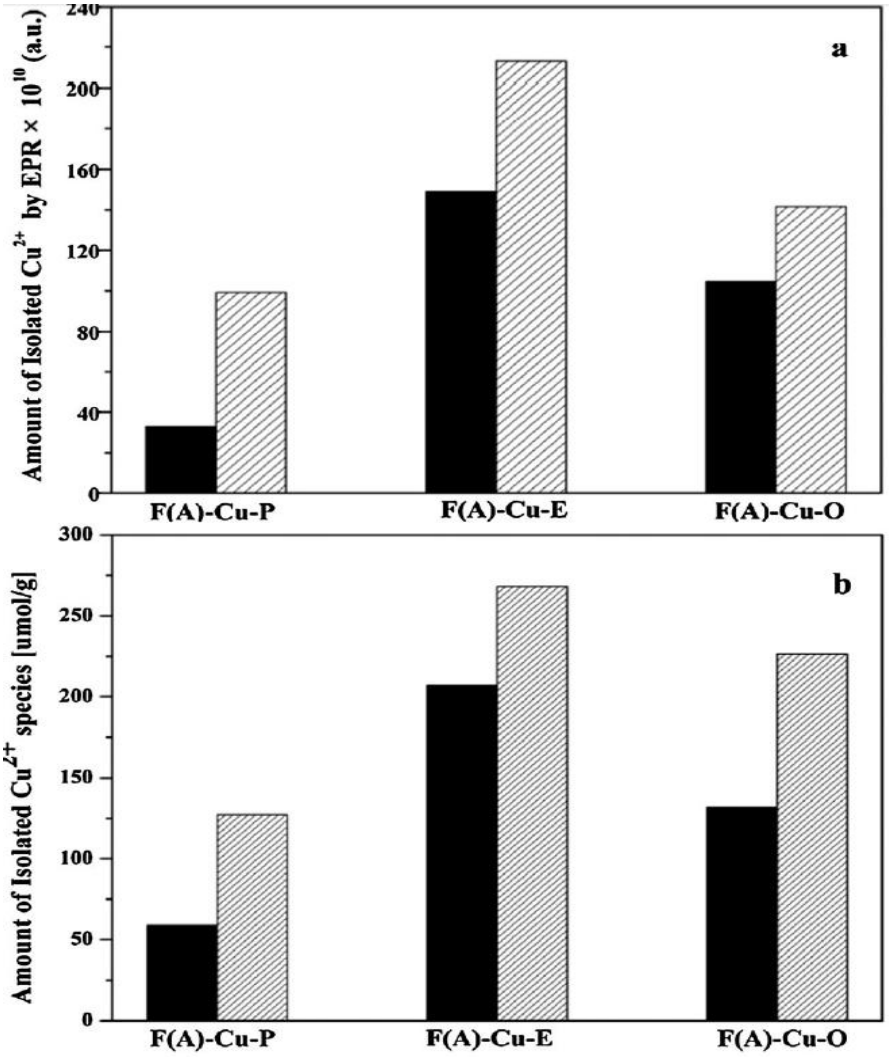

Figure 1.12 (a) Amount of isolated Cu^{2+} quantified by EPR spectroscopy. (b) Amount of isolated Cu^{2+} quantified by the H_2-TPR. The "solid pillar" represents the fresh samples; the 'grid pillar' represents the aged samples [68]

The amount of isolated Cu^{2+} was also estimated by EPR and H_2-TPR (Figure 1.12) and a straightforward relationship between the isolated Cu^{2+} and SCR activity was found. The authors therefore confirmed isolated Cu^{2+} to be the active sites of the NH_3-SCR, which had nothing to do with the preparation method. This conclusion is consistent with the results reported Deka et al., who discovered that the isolated Cu^{2+} species are dominant and highly active in Cu-SAPO-34 prepared by WIE and Cu species at other locations seem not benefit the SCR reaction [71].

1.3.3 Catalyst deactivation

The SCR catalyst needs to be resistant to different kinds of deactivation. For example, the heat released during the regeneration of the particulate filter can result in temperatures in excess of 700^{o}C on the filter and since the SCR catalyst is normally configured after the filter, the hydrothermal stability of SCR catalyst becomes very critical. In fact, the development of the small pore zeolite SCR catalysts was a big breakthrough with respect to hydrothermal durability. It has been reported that both Cu-SSZ-13 and Cu-SAPO-34 maintained their activity after hydrothermal aging at 800^{o}C for 16 hours while other types of frameworks collapsed at the same aging conditions [45, 46, 66]. It is the small pores (< 3.8Å) of these CHA zeolites that are considered hindrances to hydrothermal aging [45, 67], as under hydrothermal conditions, the zeolite materials lose their crystallinity via a dealumination process. The formed $Al(OH)_3$ species, with an estimated kinetic diameter of 5.03 Å, cannot exit the small pores of the CHA framework and may reincorporate into the framework during the cooling process through a reverse reaction [45]. Surprisingly, Cu-SAPO-34 even showed enhanced SCR activity after hydrothermal aging [66, 68, 72]. This was believed to be due to the migration of Cu

species from the external surface into the ion exchange positions, thus forming more isolated Cu^{2+} species [72].

Cu/zeolite SCR catalysts are sensitive to sulfur poisoning [73-75]. If an oxidation catalyst is located upstream of the SCR catalyst, at least a portion of the SO_2 will be oxidized to SO_3. In the presence of H_2O in the exhaust, H_2SO_4 is also likely to form. Figure1.13 shows the influence of SO_2 and SO_3 on the standard SCR performance over a commercial Cu-zeolite catalyst [75]. The NO_x conversion after exposing the catalyst to 40 ppm SO_2 at different temperatures decreased. In comparison, when 40 ppm SO_3 was present in the feed, the NO_x conversion dropped much more significantly. It seems possible that SO_2 and SO_3 therefore have different poisoning effects. In particular, SO_3 had a more significant impact than SO_2, and the authors proposed that $CuSO_4$ formed upon SO_3 exposure, resulting in deactivation [75]. Their analysis also showed that even after the sulfate formed, the Cu remained in a highly dispersed state, at its initial ion-exchange locations. As a side note, it has also been reported that hydrocarbon inhibition of the SCR reaction is also diminished with Cu-exchanged CHA catalysts due to the small pores excluding larger hydrocarbon molecules [67].

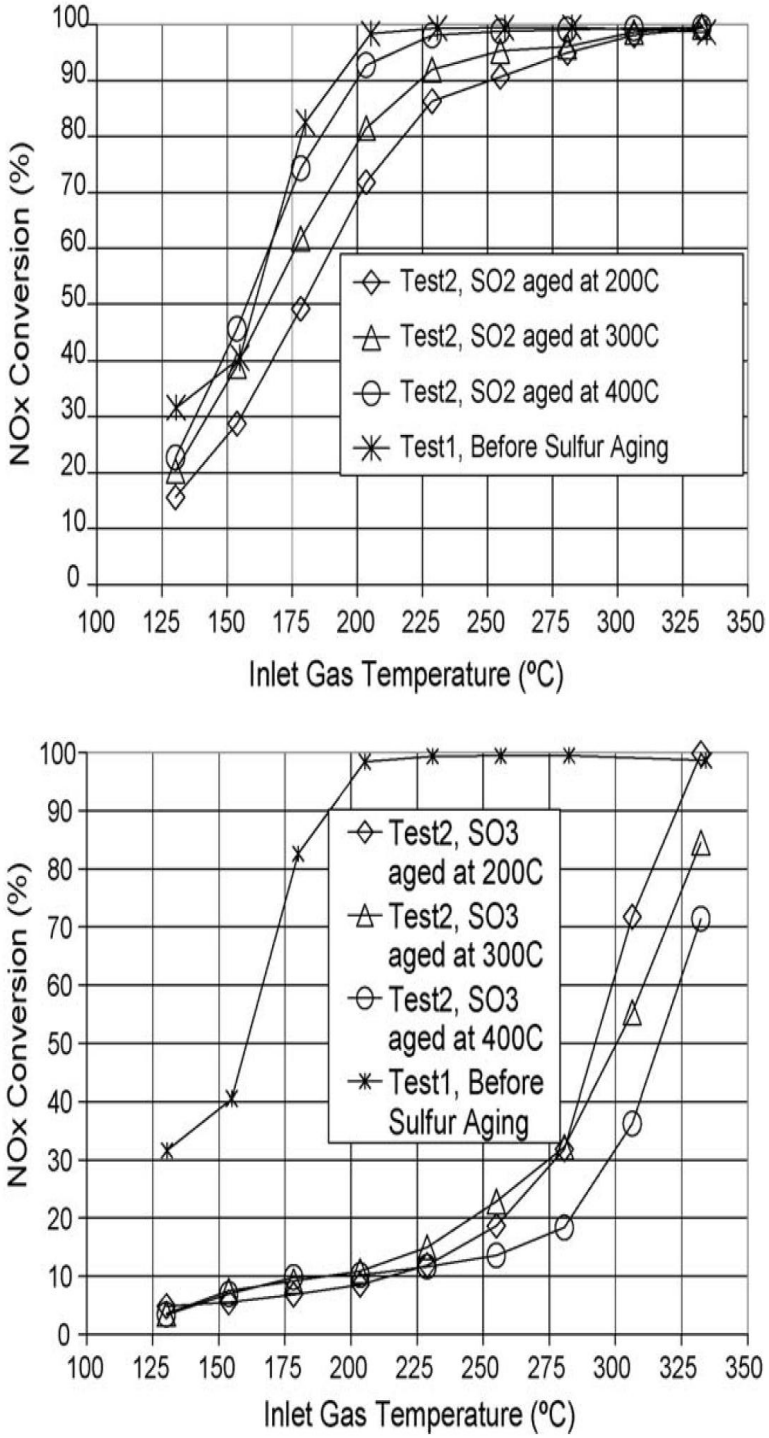

Figure 1.13 Steady state NO_x conversions for Cu/zeolite SCR catalysts before and after SO_2 and SO_3 aging at 200, 300, and 400 ^oC [75]

1.4 Research objectives and thesis outline

With excellent SCR performance and durable hydrothermal stability, both Cu-SAPO-34 and Cu-SSZ-13 catalysts have been commercialized for diesel after-treatment systems in the last several years. However, the fundamental mechanisms still require further investigation. The SCR reaction pathway, Cu structures, Cu loading effects and deactivation modes need to be carefully addressed to better understand the intrinsic properties of this novel catalyst. Furthermore, it is also important to further improve the Cu-CHA catalyst in application to satisfy more stringent emission targets in the future. Therefore, the objective of this dissertation focuses on the reaction pathway of NH_3-SCR over the small pore Cu-CHA catalyst and the active sites of the SCR reactions as well as the deactivation mechanism (e.g., hydrothermal aging and sulfur poisoning). In addition, the relationship between Cu loading, acidity properties and SCR activity have been examined. Catalyst design and preparation methodologies are also described, with emphasis on a solid state ion exchange method developed to obtain Cu-exchanged SAPO-34 and SSZ-13 catalysts with excellent SCR activity and hydrothermal stability.

This dissertation is organized as follows. The experimental setups and procedures used for catalyst characterization and testing are described in Chapter 2. In Chapter 3, results from an in-situ-DRIFTS study of SCR over a commercial Cu-exchanged SAPO-34 are presented and discussed. Chapter 4 provides an analysis of zeolite acidity and Cu structure changes as a function of Cu loading for a Cu-exchanged SAPO-34 catalyst. The solid state preparation approach as an efficient alternative to obtain Cu-CHA catalysts with excellent SCR performance is described in Chapter 5. A comparison between the as-prepared Cu-SSZ-13 and Cu-SAPO-34 upon hydrothermal aging is presented in Chapter

6. Chapter 7 describes the SO_2 poisoning impact on the NH_3-SCR reaction over a commercial Cu-SAPO-34. Chapter 8 summarizes the main conclusions of this study and recommends future research.

Chapter 2 Experimental

The experiments included in this dissertation were conducted with multiple instruments. Reactor tests were performed in three different reactor systems: a bench-scale reactor system for the monolithic catalyst tests, micro-scale reactor system for the powder catalyst tests and in-situ Diffuse Reflectance Infrared Fourier Transform Spectroscopy (DRIFTS) reactor system for surface adsorption and reaction studies. Other experimental apparatus used includes a surface area and porosity analyzer, X-ray diffraction (XRD) and Ultraviolet-visible spectroscopy (UV-vis). However, these instruments are not included in this chapter and will be introduced in the following chapters where used.

2.1 Bench-scale and micro-scale reactor systems

2.1.1 Introduction

The schematic of the bench-scale reactor system is depicted in Figure 2.1. In this system, the simulated exhaust gases were introduced from both main and "rich" manifolds. There are two pathways that the gases are either directed to the reactor inlet or through a bypass to a vent: a reactor pathway and the bypass pathway. The micro-scale reactor system configuration is similar to that of the bench-scale reactor system, except in reactor size and total flow.

The major components of both configurations can be divided into four basic systems: (1) Gas supply system, which consists of gas cylinders, mass flow controllers (MFC), switching valves, filters and pressure gauges; (2) reactor system, including the

quartz tube reactor, tube furnace with temperature control, thermocouples and bypass; (3) analytical system consisting of a FTIR spectrometer, a mass spectrometer, control valves and pressure check configurations; and (4) data acquisition system, which includes PCs and commercial data collecting software.

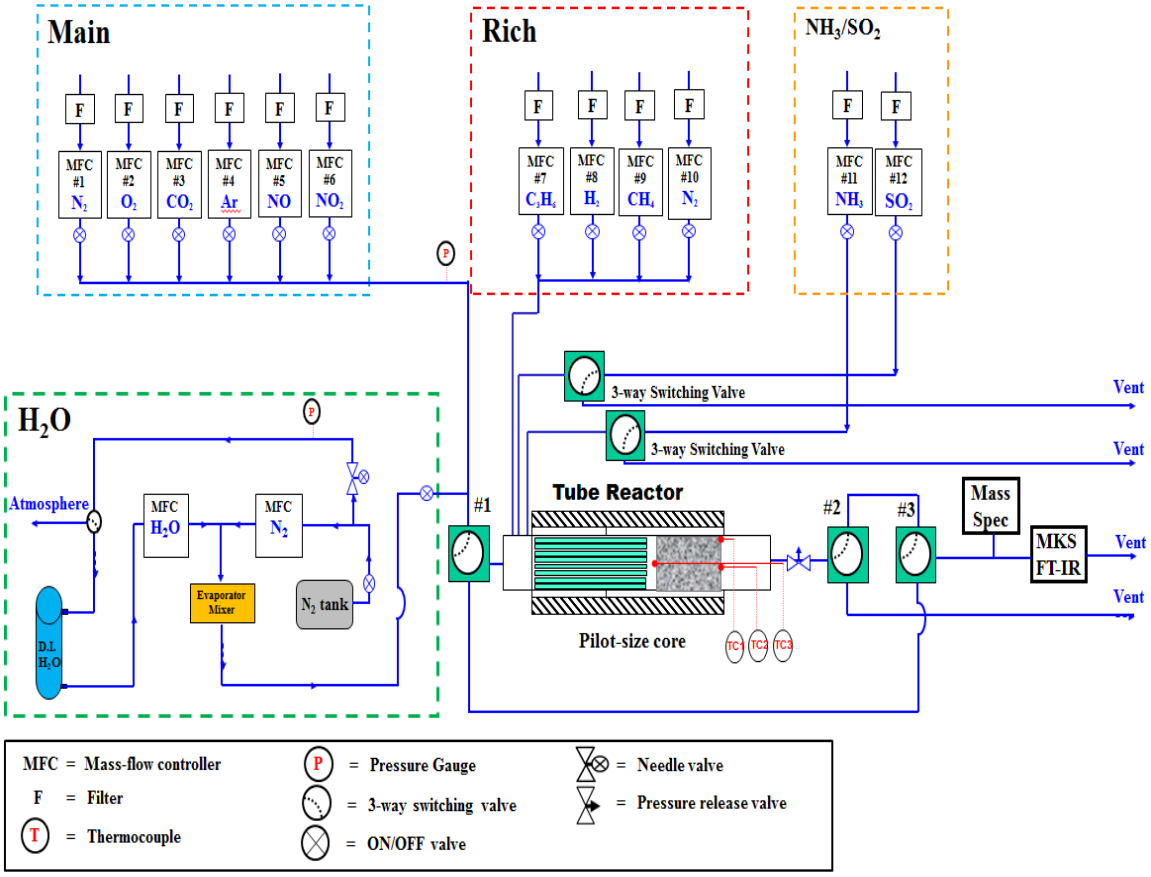

Figure 2.1 Bench-scale reactor system in the lab

2.1.2 Gas supply system

Pure N_2 was used as the carrier gas for both the micro-scale and bench-scale reactor and is supplied from a N_2 generator (ON SITE gas systems). All the other gases originated from cylinders, which were provided by Praxair. All the gases used in the

bench-scale and micro-scale reactor systems and the corresponding calibrated gas concentrations in the cylinders are listed in Table 2.1.

Table 2.1 Specifications of gases used in the bench- and micro- scale reactor systems

Gas	Description	Purity
N_2	Diluent for reactive feed gas, purge gas for reactor	99.999% Purity
O_2		99.98% Purity
H_2		99.98% Purity
NH_3	5 %, balanced with N_2	Certified standard
NO	5 %, balanced with N_2	Certified standard
NO_2	5000 ppm, with 1 % O_2 and balanced with N_2	Certified standard
SO_2	1%, balanced with N_2	Certified standard

The gas flow rates were controlled using mass flow controllers (MFC; 1179A, MKS). Each mass flow controller was calibrated using digital flow meters (Bios Definer 220-H). Water was fed by using a Bronkhorst CEM. The details of the water injector are also described in Figure 2.1. NH_3 and SO_2 were directly fed into the reactor instead of mixing with other gases in the manifolds in order to avoid possible reactions and minimize adsorption along the inlet lines thus reducing the response time.

2.1.3 Reactor systems

For the monolithic catalyst bench-scale reactor, a 470 mm long quartz tube with 22 mm inner diameter (ID) was used. A schematic of the monolithic catalyst quartz tube

reactor is shown in Figure 2.2. Small quartz tubes were positioned upstream of the catalyst to improve gas distribution and preheating. The monolith sample was 35.5 mm long with an ID of 20.3 mm, and was placed downstream of the small quartz tubes. In order to prevent gas bypass, the sample was wrapped with insulation material (Tetraglas 3000) before being installed into the quartz tube reactor. Four thermocouples were inserted to monitor the temperatures at positions upstream, front-face center, back-face center and back-face outer edge of the monolith. The temperature differences during all experiments were less than 4°C. Therefore, the averages of these four temperatures were used when analyzing the data. The reactor was placed inside a Lindberg temperature-controlled furnace whose temperature was monitored in-situ by two K-type thermocouples configured in the center of the heated zone. The parameters in the proportional integral derivative (PID) controller of the furnace were adjusted in order to prevent temperature overshooting problems. The controller P, I and D parameters were 20,120 and 30, respectively.

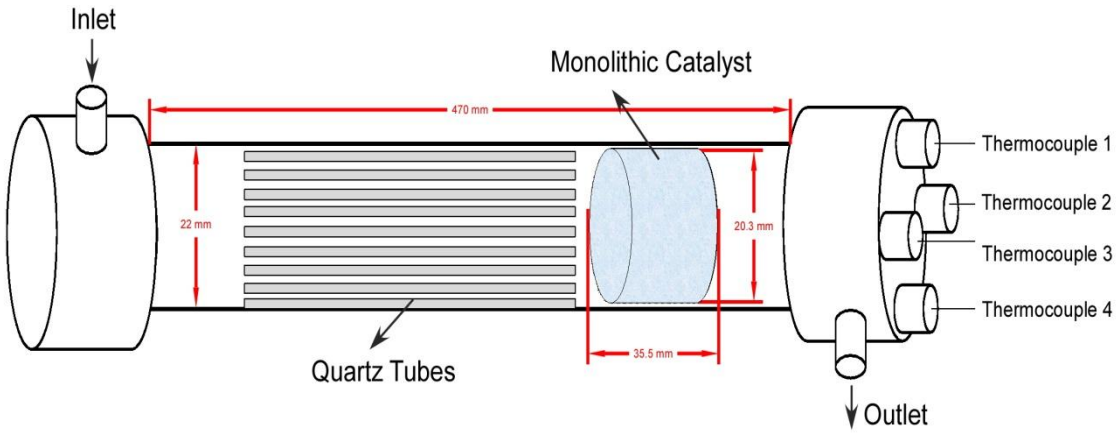

Figure 2.2 Schematic of the monolithic quartz tube reactor

The powder catalyst quartz tube reactor is 500 mm in length with a 10.5 mm inner diameter (ID). The sketch of the powder catalyst quartz tube reactor design is provided in

Figure 2.3. The powder catalysts were pressed from two sides of the tube using quartz wool to prevent the dispersion of powder. Swagelok Ultra-Torr fittings were used as the end caps of the quartz tube reactor and the reactor was sealed by Swagelok rubber ferrules. The feed temperature was measured by a K-type thermocouple, which was placed downstream of the catalyst configuration.

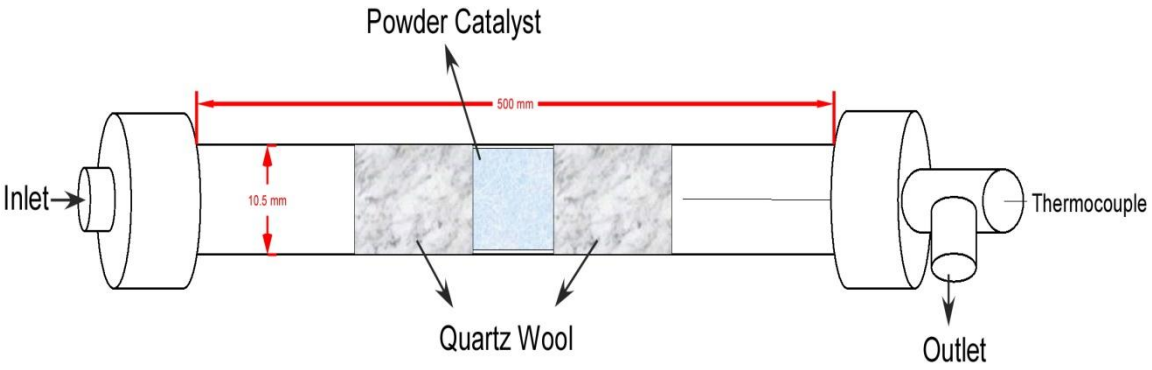

Figure 2.3 The sketch of powder catalyst quartz tube reactor

2.1.4 Analysis system and data acquisition system

A FTIR spectrometer (MKS MultiGas^{TM} 2030) equipped with a 5.11 m high-optical-throughput 200 mL gas sampling cell was positioned downstream the reactor system to analyze the effluent gas composition. The analyzer incorporates a high sensitivity liquid nitrogen cooled MCT detector. The gas cell was maintained at 191 °C by a digital temperature controller. The species concentrations measured by the FTIR included NH_3, H_2O, N_2O, NO, NO_2, SO_2 and SO_3. The calibration recipes of these species were provided with the instrument. The FTIR configuration of the sample and nitrogen line is depicted in Figure 2.4. The inlet and exhaust lines of the FTIR were

connected with ¼'' stainless steel lines with Swagelok fittings. The instrument was purged with 20 psig purified air generated from a FTIR purge gas generator (Parker Balston). A background was taken prior to each test. For the background, 16 scans were collected. When measurements were not being taken, 1 L/min pure nitrogen flow was used to protect the gas cell.

A GSD 320 Pfeiffer Vacuum mass spectrometer was also used to measure effluent concentrations for some tests. Mass spectroscopy is a well-established analytical technique to identify chemical compounds by measuring their molecular mass. It consists of a capillary inlet, a quadrupole mass spectrometer, a diaphragm vacuum pump and a turbomolecular pump. The gas was drawn down the capillary at 1 sccm. The GSD 320 mass spectrometer is equipped with two detector types: Faraday ion detector and Secondary Electron Multiplier (SEM) detector. In all of the experiments using the mass spectrometer, the SEM detector was selected.

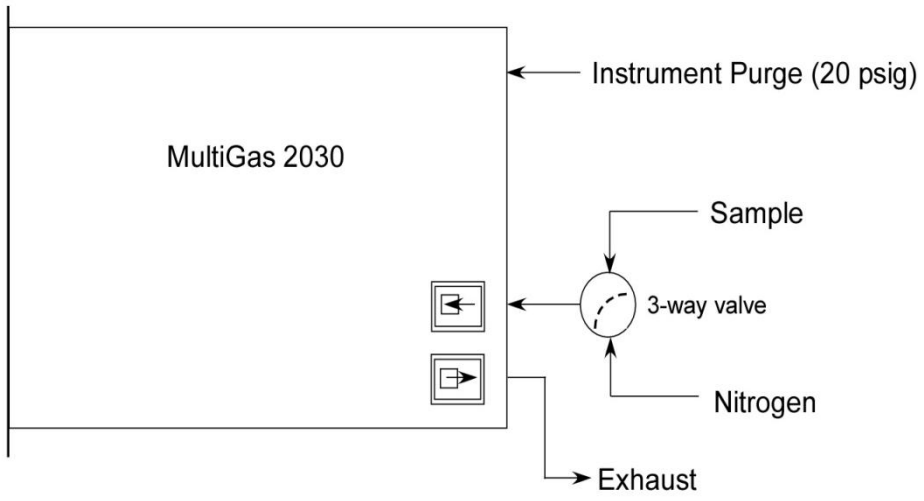

Figure 2.4 Configuration of the sample and nitrogen lines for FTIR

The data acquisition system included Nation Instruments modules (Field point controller CFP-TC120 and CFP-CB200) and two PCs. The catalyst temperatures

measured by the thermocouples inserted into the reactor were recorded with Labview® software. The FTIR data was collected with a second PC, which was equipped with MG2000® software (MKS). The mass spectrometer data was recorded by the QUADERA® software (Pfeiffer). The data collected by the software were saved into a Microsoft Excel file for subsequent analysis.

2.2 Diffuse reflectance infrared Fourier Transform spectroscopy (DRIFTS)

2.2.1 Introduction

In-situ Diffuse Reflectance Infrared Fourier Transform Spectroscopy (DRIFTS) is a sampling technique used to identify the compounds adsorbed on the catalyst surface and measure their surface concentration based on the infrared radiation (IR) absorbed. Two-parameter Kubelka-Munk (KM) expression was used to convert the spectra to the form that is comparable to the transmitted spectrum of different materials. The Kubelka-Munk (KM) equation for an infinite thickness sample is described as

$$f(R_\infty) = \frac{(1-R_\infty)^2}{2R_\infty} = \frac{k}{s}, \quad (2\text{-}1)$$

where $f(R_\infty)$ represents the KM function and R_∞ is the ratio of the intensity of the reflected light to the intensity of the incident light. The parameters k and s are the absorption coefficient and the scattering coefficient of the sample, respectively. The absorption coefficient k is defined by the Beer-Lambert equation

$$I = I_0 e^{-kx}, \quad (2\text{-}2)$$

in which I and I_0 are the transmitted radiation and the incident radiation intensities, respectively. x is the beam path length through the sample. The parameter s can also be defined by the following equation

$$J = I_0 e^{-sx}, \tag{2-3}$$

where J is the intensity of the diffuse reflection and I_0 is the intensity of the indent radiation. Usually, R_∞ is derived from the measured ratio of the absolute reflectance of a sample to that of a standard sample

$$r_\infty = \frac{r_\infty(\text{samples})}{r_\infty(\text{standard})}. \tag{2-4}$$

If a linear function between the absorption coefficient and the surface concentration is considered, the surface concentration of a species can be derived from the following equation

$$f(r_\infty) = 2.303\ a \times c/s, \tag{2-5}$$

where a is the absorptivity and c is the concentration.

2.2.2 Gas supply system

All the feed gases were acquired from Praxair. The specifications of gases used in the DRIFTS rector systems are listed in Table 2.2.

Table 2.2 Specifications of gases used in the DRIFTS reactor systems

Gas	Description	Purity
He		99.999% Purity
O_2		99.98% Purity
NH_3	5000 ppm, balanced with He	Certified standard
NO	5000 ppm, balanced with He	Certified standard
NO_2	5000 ppm, with 1% O_2 and balanced with He	Certified standard
SO_2	1%, balanced with N_2	Certified standard

The gas flow rates were controlled with a series of mass flow controllers (1179A, MKS). Helium was used as the carrier gas in the DRIFTS reactor system and all the other gases except NH_3 were mixed before entering the reaction chamber. NH_3 was injected to the DRIFTS reactor separately using a three-way switching valve close to the inlet of the reactor chamber. All the gas lines were built from stainless steel 1/8'' tubes and the inlet lines were heated to 120°C using insulated heat tapes (Cole Parmer) wrapped with insulation tape (Tetraglas 3000 Woven Tape).

2.2.3 Reactor system

In the DRIFTS setup, a Harrick Scientific Praying Mantis accessory was used as the reactor system. This system is specifically designed for examining powders by diffuse reflection spectroscopy and an interior view of this accessory is shown in Figure 2.5.

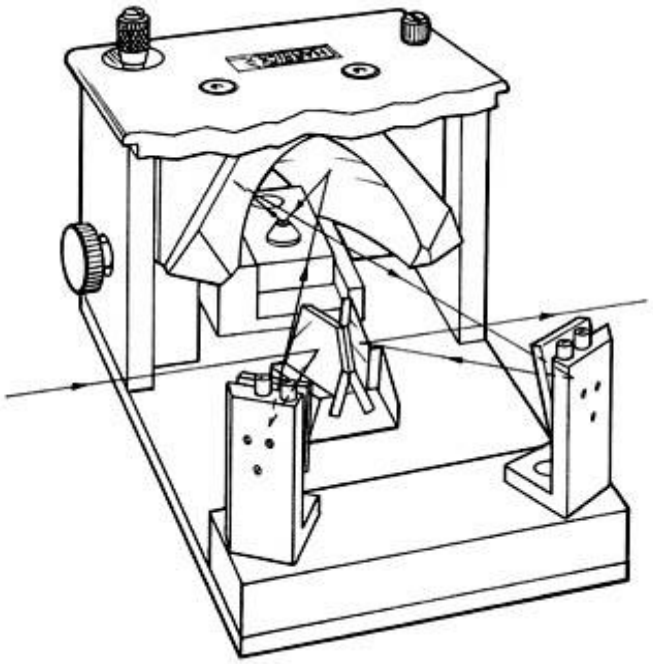

Figure 2.5 An interior view of Praying Mantis DRIFTS accessory [76]

Two 6:1 90°C off-axis ellipsoid mirrors are optically arranged so that their near focal points coincide and the sample is placed in the common focal points of the two ellipsoid mirrors. The height of the stage can also be adjusted for optimal signal. The whole Praying Mantis box was purged with 9 L/min pure N_2 to reduce the H_2O and CO_2 levels, entering from the atmosphere. This reaction chamber is constructed of stainless steel and incorporates a sample cup that is part of a sample stage whose temperature is controlled by a cartridge heater and K-type thermocouple connected to a Harrick temperature controller. The powder sample was placed in the sample cup with a porous screen at the bottom surface, allowing the gas to uniformly pass through the catalyst from top to bottom. The stage is thermally isolated from the outer chamber and a water circulating jacket is also provided to cool the temperature of the outer chamber and windows when the system is operated at high temperature. The sketch of the high temperature reaction chamber is shown in Figure 2.6.

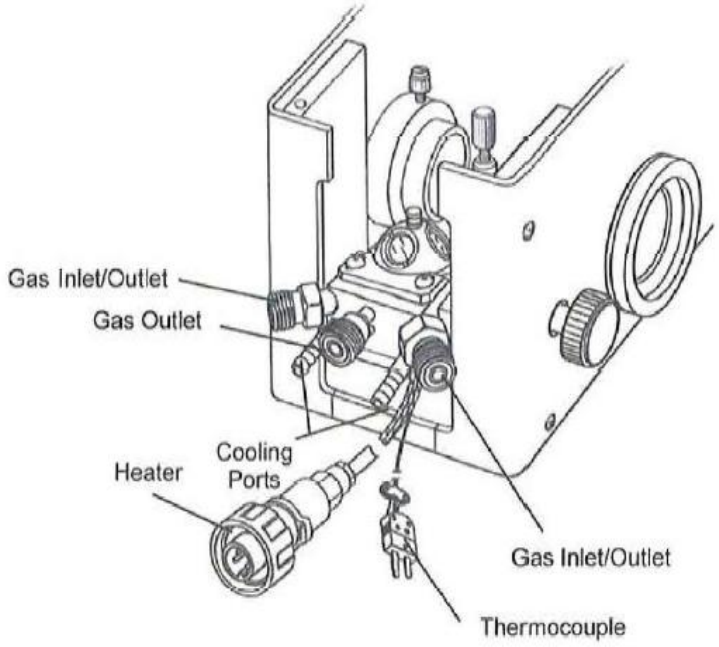

Figure 2.6 High temperature reaction chamber used in DRIFTS [76]

The reaction chamber consists of two gas ports for evacuating or flowing gas through the sample. One of the ports functions as the gas inlet that leads the gases into the sides of the chamber and the other port is the outlet for the gases from underneath the sample cup. Two optical ZnSe windows were installed on a removable stainless steel dome using o-ring seals. The windows are mounted in a certain tilt angle to make sure the radiation enters and exits the chamber with the minimum loss of the reflection and maximum light interaction with the sample. The operating temperature of the high temperature reaction chamber can achieve 910 °C in vacuum. The total flow rate during the experiments run was maintained at 50 cm^3/min (STP) with MKS mass flow controllers.

2.2.4 Analysis system and data acquisition system

All the DRIFTS analysis was performed using a Nicolet 6700 spectrometer equipped with a MCT detector. A schematic layout of ThermoNicolet IR spectrometer is described in Figure 2.7. In this setup, the above-mentioned Praying Mantis DRIFTS accessory was installed in the sample compartment. The system consists of an infrared source, an interferometer, a sample, a detector and a computer.

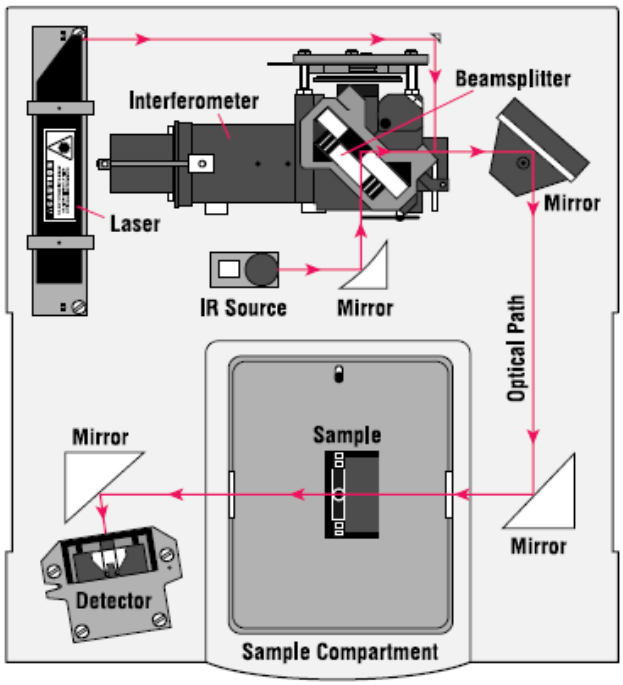

Figure 2.7 A schematic layout of ThermoNicolet IR spectroscopy [77]

2.3 Safety

Multiple detectors (Beacon 410 Gas Monitor, RKI Instruments) were placed throughout the lab in order to detect any possible toxic gas leaks including (NO_x, SO_2, H_2 and NH_3) emitted from experiments. In addition, two CO alarms (Kidde) were also placed near the CO cylinders for detection of any CO leakage.

Chapter 3 In-situ DRIFTS study of NH_3-SCR over Cu-exchanged SAPO-34

Note: the material in this chapter has been published. The introduction and experimental methods material has been summarized to avoid redundancy with Chapters 1 and 2, however. Reference and figure numbers changed for thesis consistency.

3.1 Introduction

NH_3-SCR reaction mechanism research over zeolite-based catalysts has not led to a consensus. Most agree that the Langmuir-Hinshelwood mechanism occurs, in which the reaction between adsorbed NH_3 and surface nitrites and nitrates are the key steps in NH_3-SCR of NO_x [78-81]. This reaction pathway includes (i) the formation of the surface nitrites and nitrates (ii) the reduction of nitrates by NO to form nitrites, (iii) the reaction between adsorbed NH_3 and nitrites to produce N_2 via ammonium nitrite decomposition, and (iv) the reaction between adsorbed NH_3 and nitrates to form ammonium nitrate and its subsequent reduction and/or decomposition to N_2 and N_2O. Alternatively, the Eley-Rideal mechanism has been proposed, where gas-phase NO_2 reacts with two adjacent NH_4^+ ions to form an $(NH_4)_xNO_2$ complex which can be further reduced to N_2 by NO [43, 53, 82]. Recently, Feng et al., [48] suggested NO^+ species as a reaction intermediate involved in the standard SCR reaction. However, there is lack of sufficient evidence on how NO^+ and SCR activity are connected. Since the Cu-exchanged chabazite framework type zeolite with small pores, such as SAPO-34 and SSZ-13, was discovered, lots of work has focused on material characterization and confirmation of the transition metal active sites in Cu-CHA catalysts. The present study is directed at understanding the SCR

reaction mechanism on a Cu-SAPO-34 catalyst. The surface chemistry of the SCR reaction on Cu-SAPO-34 was investigated using in-situ DRIFTS via identification and reactivity of the adsorbed surface species and surface reaction intermediates.

3.2 Experimental

The catalyst used in this study was a Cu-SAPO-34 catalyst supplied by Cummins Inc. The Cu-SAPO-34 catalyst sample had a Si/(Al+P) ratio of 0.2. The Cu loading was 0.95 wt%. For SCR activity tests, a monolithic-supported sample was used, and was 1.4" long and 0.8" in diameter. Before testing, the catalyst was degreened at 650°C for 4 hours in flowing 8% O_2, 5% H_2O and a balance of N_2. The simulated exhaust gas contained 500 ppm NO, 500 ppm NH_3, 8% O_2 and 5% H_2O with a balance of N_2. The total flow rate was 5 L/min and the corresponding gas hourly space velocity (GHSV) was 28000 h^{-1}. The NO and NH_3 conversions were calculated using the following equations:

$$X_{NO} = \frac{C_{NO_{x\,in}} - C_{NO_{x\,out}}}{C_{NO_{in}}} \times 100\% \text{ and} \tag{3.1}$$

$$X_{NH_3} = \frac{C_{NH_{3\,in}} - C_{NH_{3\,out}}}{C_{NH_{3\,in}}} \times 100\%. \tag{3.2}$$

The powder sample used in the DRIFTS experiments was scraped from the monolith sample and was pressed into a 60 mg pellet of 6.5 mm diameter and placed in the sample cup. At the same time, the effluent gas composition from the DRIFTS cell was measured using the mass spectrometer. NH_3 (m/e=17), NO (m/e=30), N_2 (m/e =28) and N_2O (m/e =44) were monitored. Prior to each test, the catalyst sample was pretreated at 600°C in a flow of 5% O_2 in He for 30 minutes and then cooled to the target temperature. Background spectra were recorded in flowing He and subtracted from the

sample spectrum for each measurement. For temperature-programmed desorption (TPD) experiments, background spectra were collected in He every 50°C from 100 to 500°C. During the temperature ramp reaction experiments, DRIFTS spectra were recorded every 50°C, and the corresponding backgrounds were then subtracted. It should be pointed out that all the DRIFTS experiments were performed in the absence of water, in this case due to its wide interference of the IR bands. However, it is noted that the inclusion of water may competitively adsorb on the catalyst surface and hinder NH_3 or NO_x adsorption. We assume that the surface intermediate and the global reaction mechanism still apply to the exhaust feed in the presence of water. Note, when this chapter was submitted for publication, ceria as a part of the formulation was not known.

3.3 Results and Discussion

3.3.1 Activity measurements

The standard SCR reaction activity was evaluated over the monolith-supported Cu-SAPO-34 catalyst from 150 to 600°C and the NO and NH_3 conversion results are shown in Figure 3.1. About 40% NO conversion was achieved at 150°C. The maximum NO conversion (95%) occurred at 200°C. With increasing temperature from 200°C, the conversion decreased due to the competitive NH_3 oxidation reaction at high temperature, as evidenced by 100% NH_3 conversion at these temperatures. In addition, very little N_2O (< 5 ppm) and NO_2 (< 20 ppm) were detected during these tests, indicating a high selectivity of NO to N_2 was achieved. In terms of NO_2, it would be expected that any formed would participate in the fast SCR reaction and thus be consumed, leading to its absence at the outlet.

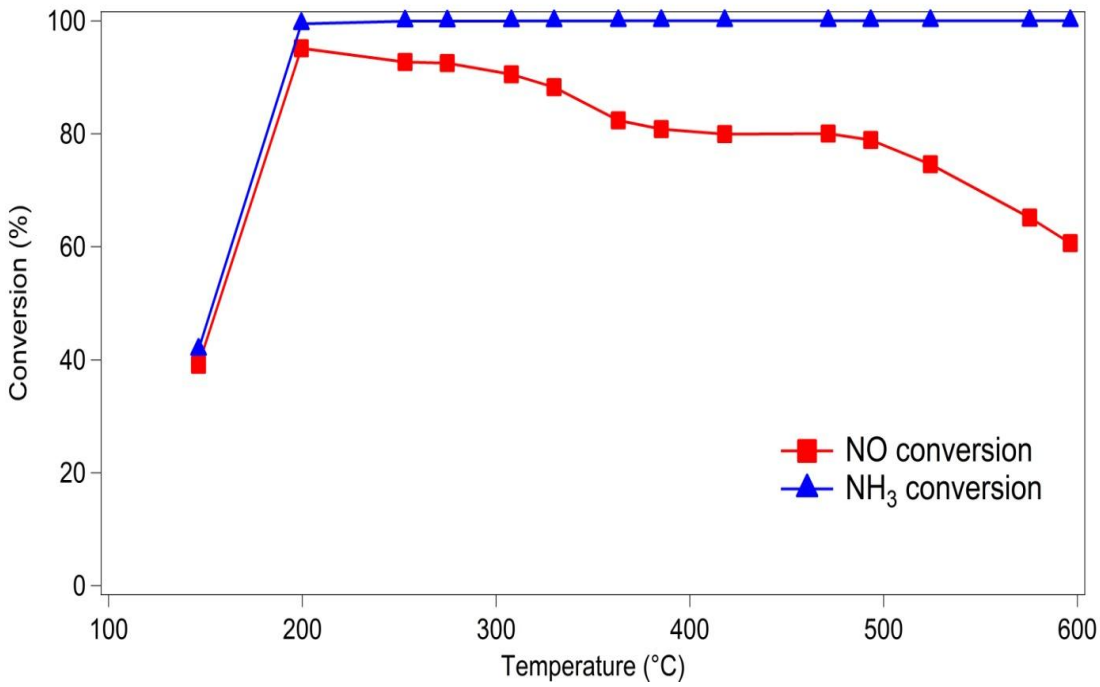

Figure 3.1 NO and NH_3 conversion under "standard SCR" conditions (500 ppm NO, 500 ppm NH_3, 8% O_2, 5% H_2O in N_2) over Cu/SAPO-34 (GHSV: 28000 hr^{-1})

3.3.2 NO_x adsorption

In order to investigate the interaction of NO_x with the Cu-SAPO-34 surface, the catalyst sample was exposed to NO, NO + O_2 and NO_2 in He for 30 min and then purged with pure He for 30 min at 100°C. The DRIFTS spectra are shown in Figure 3.2-3.4. NO, NO + O_2 and NO_2 adsorption resulted in three common bands at ~1625, 1610 and 1602 cm^{-1}. Two additional bands at 1575 and 1530 cm^{-1} were present only when NO + O_2 or NO_2 were introduced. The bands in the range of 1650 cm^{-1}-1500 cm^{-1} are widely accepted to be the surface nitrate or nitro species adsorbed primarily on the transition metal active sites of catalyst [83-85]. However, accurate identification of these bands is not straightforward due to the similar vibrations of different nitrate structures (monodentate, bridging monodentate, chelating bidentate and bridging bidentate species) [84, 85].

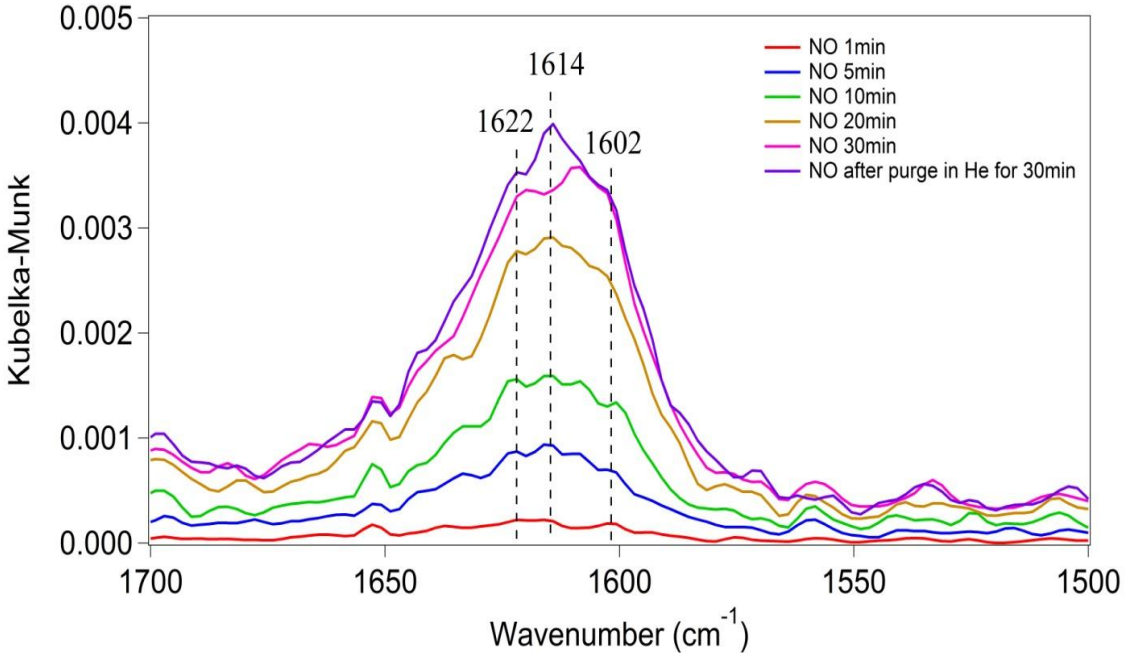

Figure 3.2 DRIFTS spectra obtained after exposing the Cu-SAPO-34 sample, for 30 min at 100°C, to 500 ppm NO followed by a 30 min exposure to He only

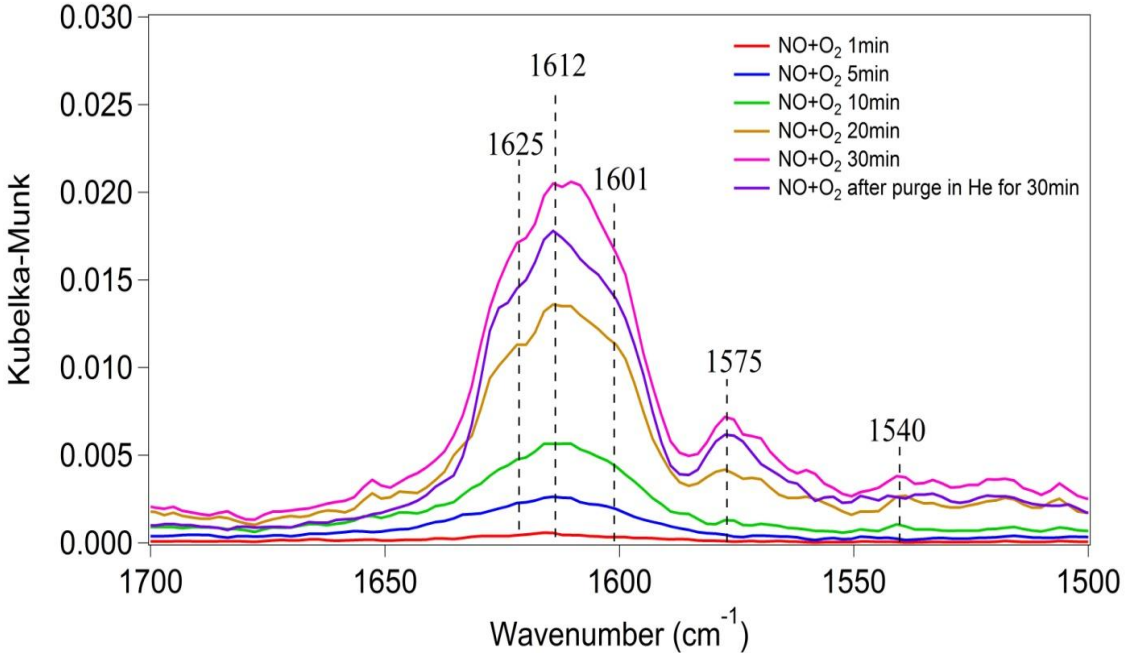

Figure 3.3 DRIFTS spectra obtained after exposing the Cu-SAPO-34 sample, for 30 min at 100°C, to 500 ppm NO and 5% O_2 followed by a 30 min exposure to He only

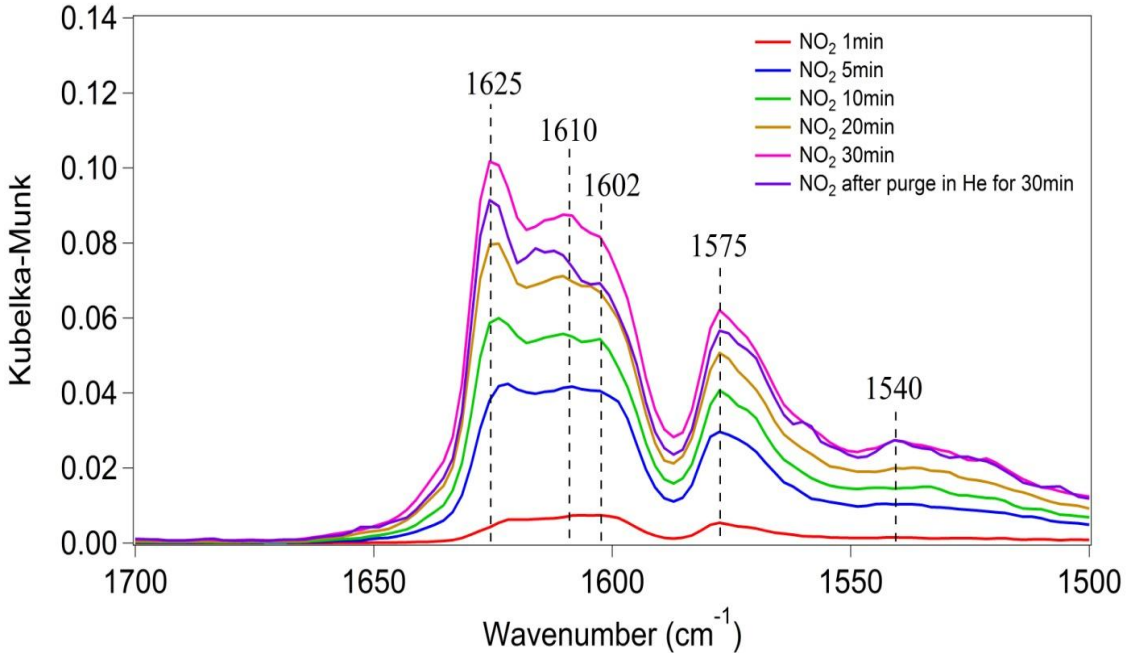

Figure 3.4 DRIFTS spectra obtained after exposing the Cu-SAPO-34 sample, for 30 min at 100°C, to 500 ppm NO_2 followed by a 30 min exposure to He only

For example, Long and Yang observed two bands, at 1622 cm^{-1} and 1568 cm^{-1}, upon NO_2 exposure to NH_3 pre-adsorbed on Fe-ZSM-5 and they assigned these bands to adsorbed NO_2 and nitrate species, respectively [43]. Ruggeri et al., observed similar bands at 1620 cm^{-1} and 1574 cm^{-1} with Fe-ZSM-5 and assigned both of them to bridging or bidentate nitrate species on Fe^{3+} ions [81]. Rivallan et al., compared the adsorbed NO_2 species on H-ZSM-5, silicalite, Fe-silicalite and Fe-ZSM-5 [86]. They concluded that the band at 1658 cm^{-1} was due to NO_3^- species that formed by NO_2 attaching to SiO*Si group, the band at 1635 cm^{-1} was due to NO_3^- species formed on FeO*Al groups, and the features between 1580 and 1620 cm^{-1} were due to nitrate-like species on FeOSi bridges, and the shift from 1620 cm^{-1} to 1610 cm^{-1} due to the formation of a $NO_3^-(N_2O_4)$ complex. Adelman et al., observed three bands in the same region when characterizing Cu-ZSM-5 and they attributed the bands at 1628, 1594 and 1572 cm^{-1} to a nitro group, a bridging

monodentate nitrate and a bidentate nitrate, respectively [87]. By analogy with the assignments of adsorbed NO_x species on other zeolites, the bands at 1625 cm^{-1}, 1610 cm^{-1} (and 1602 cm^{-1}) and 1575 cm^{-1} (and 1530 cm^{-1}) can be tentatively assigned to adsorbed NO_2 species, monodentate nitrates and bidentate nitrates, respectively. These nitrate species were relatively stable as all these bands maintained their intensities during subsequent exposure to just He. By comparing the intensities of the NO_3^- bands detected upon passing NO, NO + O_2 and NO_2 over the catalyst surface, it is obvious that the NO_3^- concentrations that formed on the surface are in the order of NO_2 > NO + O_2 > NO. This strongly indicates that NO oxidation by O_2 would promote the formation of surface nitrates, especially since CeO_2 was a part of the catalyst formulation and can adsorb NO_x and form nitrates. Indeed, NO_2 was formed in the full temperature window when 500 ppm NO and 5% O_2 were introduced over the monolithic Cu-SAPO-34 catalyst (Figure 3.5).

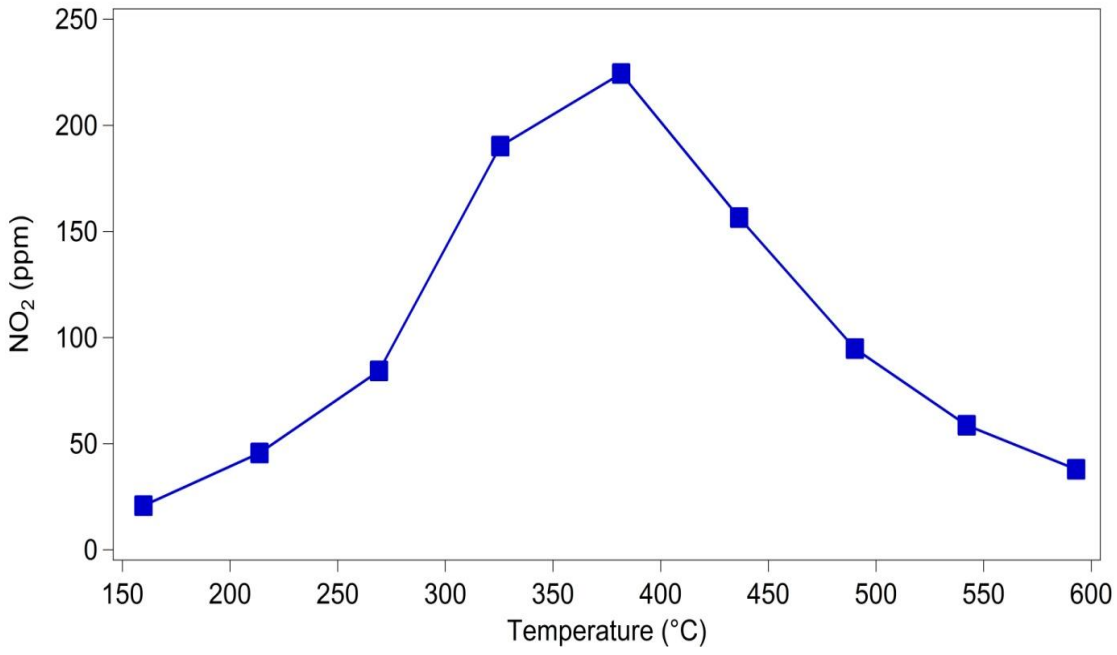

Figure 3.5 Effluent NO_2 concentration obtained during an NO oxidation experiment (500 ppm NO, 5% O_2)

However, the adsorption of NO was significantly lower. This is consistent with the NO_x adsorption properties reported on a Cu-ZSM-5 catalyst [88]. Many authors have agreed that NO oxidation to NO_2 is a key factor for surface nitrate formation under standard SCR conditions and therefore it is considered a crucial step for NH_3-SCR [88-90]. NO oxidation is inhibited by NO_2, which is found to more stably adsorbed on Cu-Chabazite than Fe-ZSM-5 [89]. This appears to explain the lower NO oxidation activity on Cu-SAPO-34. It is worth pointing out that no peaks related to nitrite species were detected. This could be due to the fact that surface nitrite bands, which are usually found in the 1440 to 1100 cm^{-1} range, were obscured by the asymmetric stretching framework modes in the same region [81, 84, 91]. In fact, a small band at around 1350 cm^{-1} was observed during NO_x adsorption, which could be assigned to nitrite groups [91]; however, this band was too weak to be assigned with certainty. In addition to surface nitrate species, a broad band between 2100 cm^{-1} and 2200 cm^{-1} was detected. This band was reversible once the NO_x flow was turned off, and therefore was attributed to NO^+ species that weakly adsorbed on acid sites. A similar assignment has been reported by many authors [83, 85, 86, 91]. Additionally, a weak band at 1903 cm^{-1} was detected upon exposure to NO and this is assigned to mononitrosyl species on Cu^{2+} sites [92]. In the OH stretching region (4000 cm^{-1} to 2400 cm^{-1}), bands at 3740, 3679, 3657 and 3560 cm^{-1} were observed and attributed to perturbed Si-OH, P-OH and OH groups associated with the extra-framework Al and Cu, respectively [61, 91, 93, 94]. The weak negative bands at 3627 and 2599 cm^{-1} originated from the depletion of Brønsted acid sites (Si-OH-Al) by NO^+. This assignment is confirmed via evolution of a similar band at 2145 cm^{-1}, which corresponds to NO^+ on acid sites. Upon exposure to NO_2, DRIFTS spectra revealed two

additional peaks at 3236 cm^{-1} and 2597 cm^{-1} (data not shown). These two peaks were assigned to the first overtone band and combination band of a NO_2 group (1625 cm^{-1}), respectively [95, 96].

3.3.3 NH_3 adsorption and NH_3-TPD

The catalyst sample was exposed to 500 ppm NH_3 in He for 30 minutes at 100°C and then purged in He for 30 min at the same temperature. The DRIFTS spectra collected during exposure to NH_3 are shown in Figure 3.6. A major band at 1460 cm^{-1} and a weak band at 1617 cm^{-1} were immediately detected after introducing NH_3 for 1 min. The former is assigned to NH_4^+ species resulting from NH_3 adsorbed on Brønsted acid sites including terminal Si-OH, P-OH groups and bridging OH sites (Al-OH-Si) on SAPO-34 [61, 97]. The band at 1617 cm^{-1} is attributed to molecularly adsorbed NH_3 on Lewis acid sites [61, 97]. It has been cited that Lewis acid sites are primarily composed of the transition metal ions in metal ion exchanged zeolites [61, 98, 99], while some extra-framework Al, mostly located at the external surface of the zeolite, may also contribute to the number of Lewis acid sites [100-102]. After a 20 min exposure, both Brønsted acid sites and Lewis acid sites were saturated with NH_3. During the following purge with He, a small amount of NH_3 adsorbed on the weak acid sites was removed, resulting in a slight decrease in the bands 1460 cm^{-1} and 1617 cm^{-1}. In the OH stretching region, negative bands at 3677, 3624, 3598 cm^{-1} were observed. The negative band at 3677 cm^{-1} is assigned to the occupation of P-OH sites by NH_3, reducing the corresponding OH stretching vibrations and the two other bands are attributed to the depletion of Si-OH-Al acid sites by NH_3 [61]. The different IR bands corresponding to Si-OH-Al sites were due

to the OH groups with equal acidity strengths located in various oxygen environments in the chabazite framework [103].

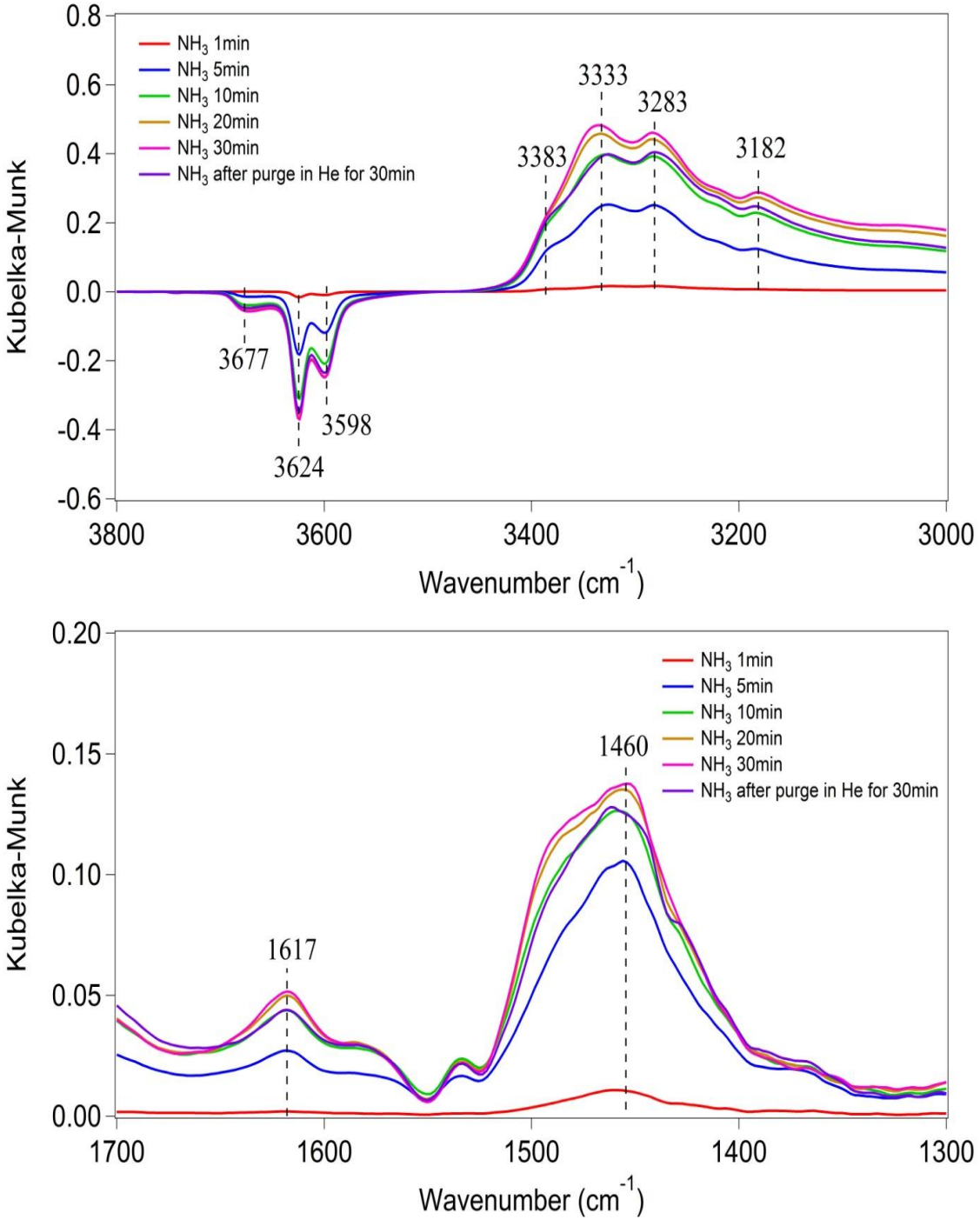

Figure 3.6 DRIFTS spectra obtained after exposing the Cu-SAPO-34 sample to 500 ppm NH_3 for 30 min followed by exposure to only He for 30 min, at 100^{o}C

A band at 3740 cm^{-1} was also detected upon exposure to NH_3 at room temperature, and can be assigned to NH_3 adsorbed onto Si-OH groups [61]. This, however, was not observed in NH_3 adsorption spectra taken at temperatures higher than 100°C, due to the weak adsorption strength of NH_3 on this site. In addition, positive bands at 3333, 3383, 3283 and 3182 cm^{-1} were detected. The bands in the 3400 to 3000 cm^{-1} range are often assigned to N-H stretching vibrations [10, 85]. Specifically, bands at 3333 cm^{-1} and 3283 cm^{-1} have been assigned to NH_4^+ groups [53]. The band at 3383 cm^{-1} has been attributed to NH_3 molecules and the band at 3182 cm^{-1} due to NH_3 adsorbed on Cu^+ sites on SAPO-34 [61, 85, 97, 104]. It is worth noting that all of these NH_3 adsorption species were relatively stable at 100°C after turning off NH_3 and purging in He.

The NH_3 adsorption process was followed by a temperature-programmed desorption (TPD) experiment in order to study the NH_3 adsorption strength and acid properties of the Cu-SAPO-34 sample. Representative DRIFTS spectra collected at different temperatures, with a 10°C/min ramp from 100 to 500°C, are shown in Figure 3.7. At the beginning of the temperature ramp, the intensity of the 1460 cm^{-1} feature decreased due to NH_3 desorption from weak Brønsted acid sites. Interestingly, the intensity of the band at 1617 cm^{-1} increased between 100 and 150°C, and then decreased with increasing temperature. This indicates that some of the NH_3 that desorbed from weak Brønsted acid sites or from P-OH like species might have re-adsorbed onto the Lewis acid sites in this low temperature region. The other possibility is that some Lewis acid sites became more accessible to NH_3 at 150°C. Indeed, a significant reduction of the 3677 cm^{-1} band, which was assigned to the weak P-OH group, was observed in the corresponding DRIFTS spectra.

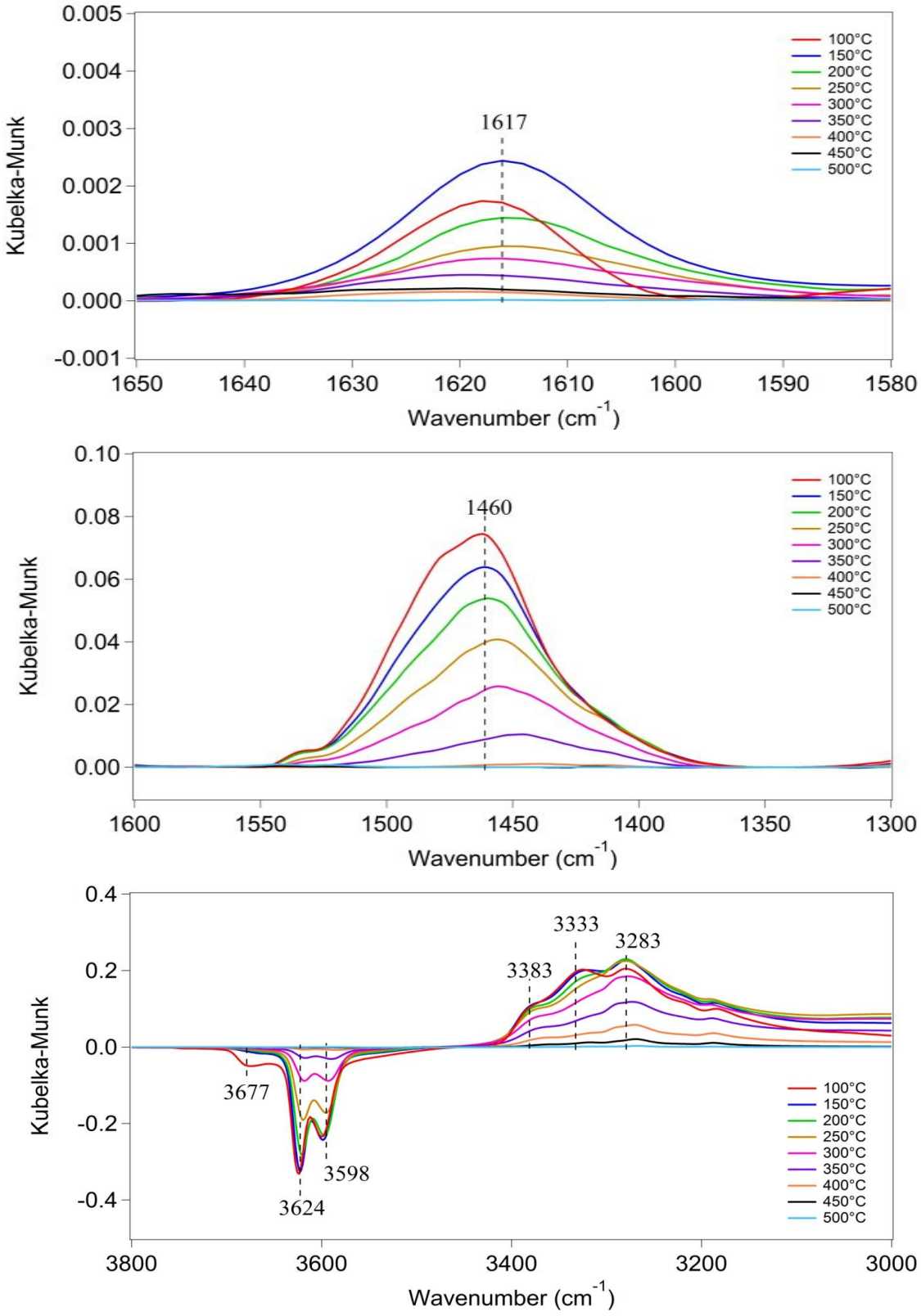

Figure 3.7 DRIFTS spectra obtained during a TPD (10°C/min) after the sample had been exposed to 500 ppm NH_3/He, followed by a He-only exposure for 30 min

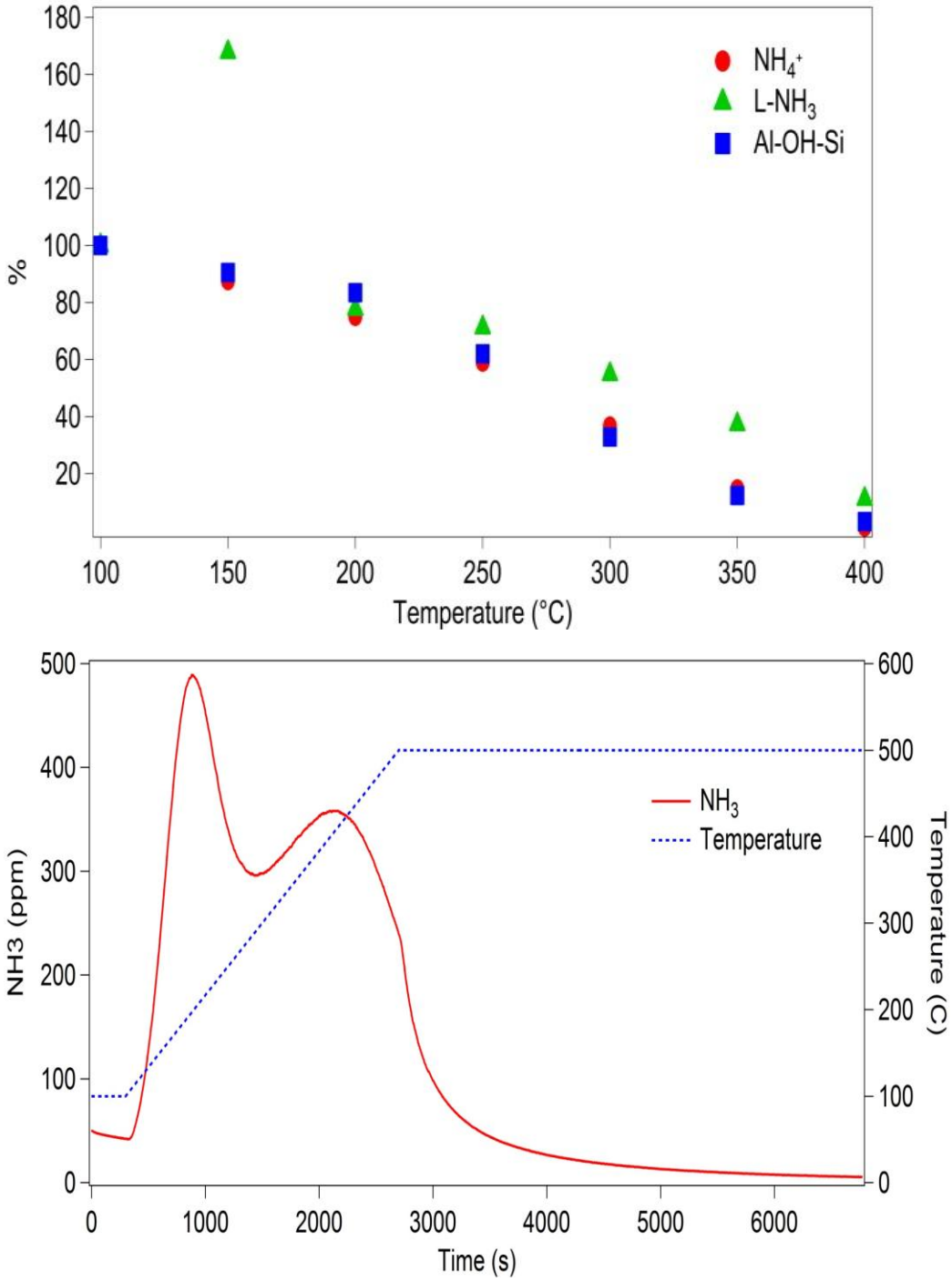

Figure 3.8 Normalized DRIFTS peak intensities during the TPD (Fig.3.7), and NH_3 evolved

In order to more clearly evaluate the evolution of NH_3, the normalized peak areas of each key band were calculated and are shown in Figure 3.8. As shown in Figure 3.8,

NH_4^+ and Al-OH-Si resulted in a monotonic decreasing trend with increasing temperature. This demonstrates that the OH bridging band is the major source of Brønsted acid sites on Cu-SAPO-34. Furthermore, both 3598 and 3624 cm^{-1} bands, corresponding to Brønsted acid sites, decreased in unison (Figure 3.7) indicating these two acid sites are energetically similar. Figure 3.8 clearly shows the significant increase in the size of the feature associated with the increase in the NH_3 concentration on Lewis acid sites at 150°C due to re-adsorption of NH_3 released from other acid sites as suggested above. At temperatures above 200°C, NH_3 desorbing from Brønsted acid sites and Lewis acid sites showed analogous profiles, indicating that both types of sites have similar acid strengths on Cu-SAPO-34. This is inconsistent with the findings from studies of other metal exchanged zeolites which showed distinctly different Lewis and Brønsted acid site strengths [98, 99, 101, 105]. This unique acidity might be a crucial feature contributing to the SCR activity of Cu-SAPO-34, as it facilitates NH_3 migration between the two acid site types, potentially enabling more NH_3 to be transferred to the transition metal NO_x reduction reaction site. The outlet NH_3 concentrations as a function of temperature are also shown in Figure 3.8. The NH_3 desorption profile has two main desorption features, a narrow low temperature peak at about 200°C and a broad high temperature peak at 400°C. Via comparison with the DRIFTS spectra during the NH_3 desorption process, the low temperature peak is attributed to the weak acid sites (P-OH and extra-framework Al) and physisorbed NH_3. The broader peak at high temperature is attributed to NH_3 desorbed from Cu^{2+} Lewis acid sites and OH bridging Brønsted acid sites. No distinct features in the NH_3 desorption profile above 200°C further supports the energetically indistinguishable two acid site types on Cu-SAPO-34 as evident from DRIFTS spectra.

3.3.4 Reactivity of NH_3 on Cu-SAPO-34

DRIFTS spectra obtained during the reaction between NO and pre-adsorbed NH_3 at 200°C are shown in Figure 3.9.

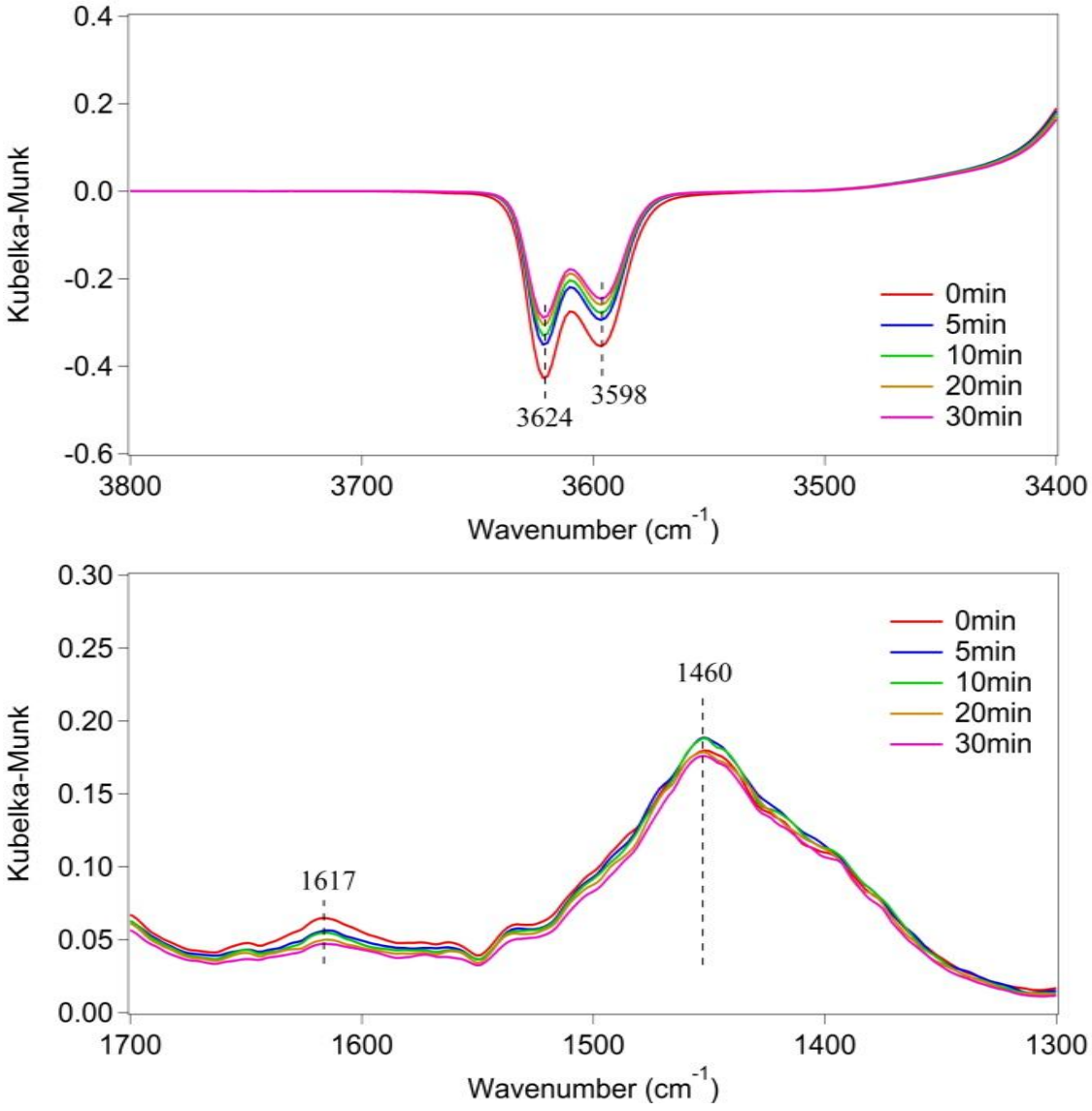

Figure 3.9 DRIFTS spectra obtained at 200°C while exposing the Cu-SAPO-34 sample to 500 ppm NO/He after being saturated with NH_3

Upon exposure to 500 ppm NO, slight decreases in the OH bridging band (3624 cm^{-1} and 3598 cm^{-1}) and the band (1617 cm^{-1}) assigned to NH_3 on Lewis acid sites were

detected. Simultaneously, only a small amount of N_2 was detected in the outlet, indicating that NO itself was not active in reacting with surface NH_3. In comparison, when 500 ppm NO and 5% O_2 were passed over the NH_3 pre-adsorbed catalyst sample at 200°C, the surface NH_3 was consumed at a significantly increased rate, as shown in Figure 3.10.

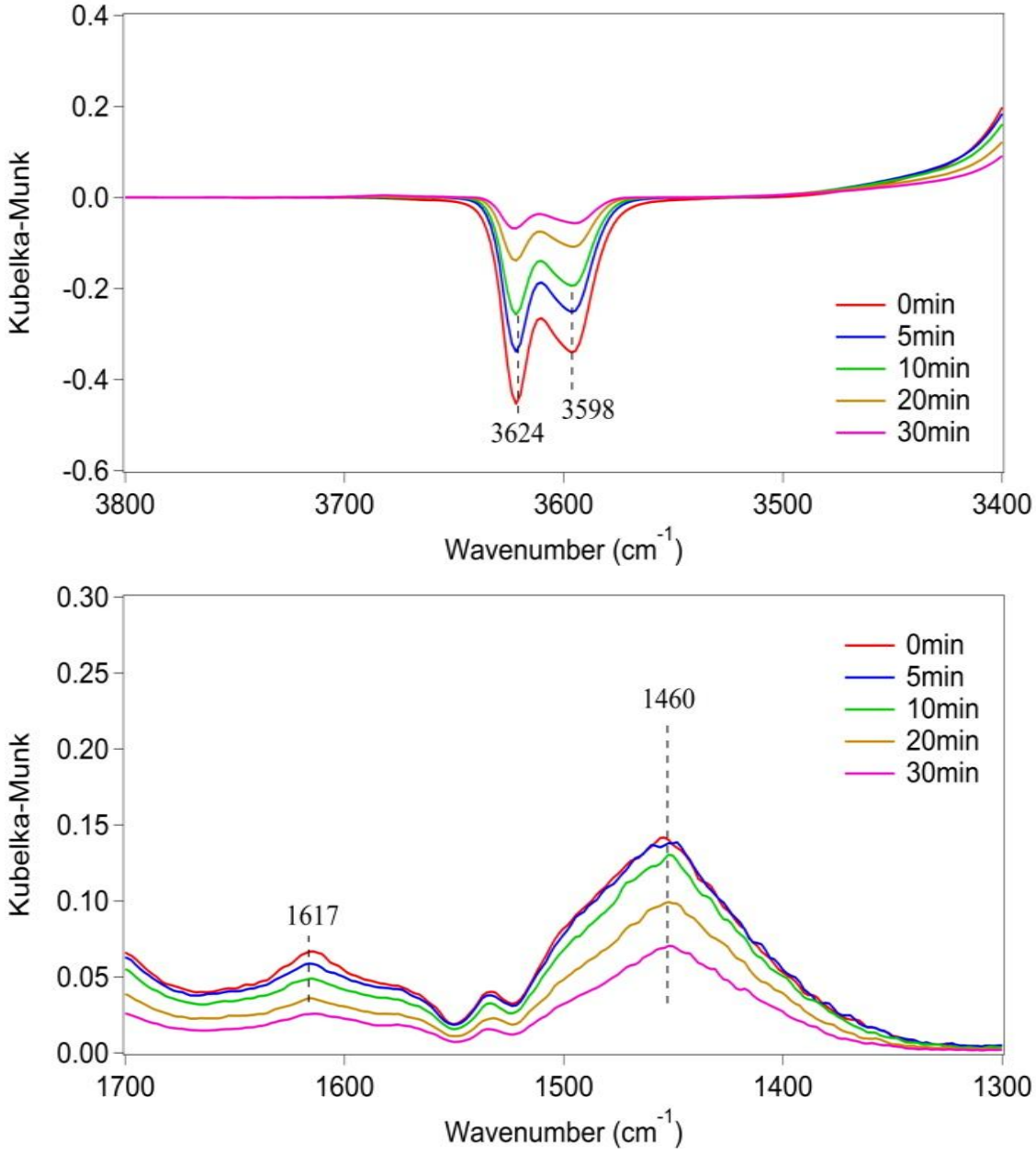

Figure 3.10 Evolution of (a) -OH bridging bond peaks; and (b) peaks of NH_3 on Lewis acid sites and Brønsted acid sites; upon exposure to 500 ppm NO + 5% O_2 at 200°C

After 30 min, all bands related to NH_3 were greatly reduced, which was also accompanied by a significantly larger amount of N_2 in the outlet gas, observed over the entire 30 minute exposure to NO + O_2. Obviously, the SCR reaction activity was enhanced by the addition of O_2 in the feed, i.e., the reaction between NH_3 and NO is promoted by NO oxidation, enhancing the storage of surface nitrates and nitrites on the catalyst surface. Indeed, similar results have been obtained on other SCR catalysts and it is widely accepted that NO has to be first oxidized to NO_2 (gas-phase or some oxidized surface species) for the standard SCR reaction over zeolite catalysts [43, 51, 53, 106]. Normalized peak areas were used to evaluate the reactivity of NO + O_2 with NH_3 adsorbed on different sites.

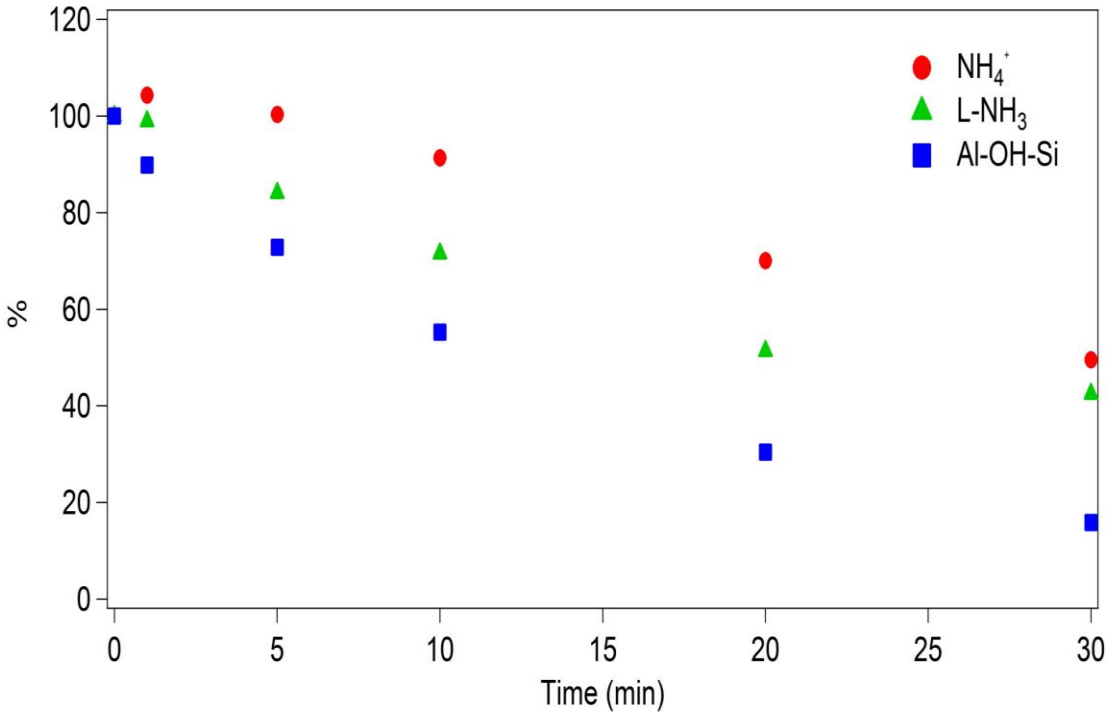

Figure 3.11 Normalized peak intensities associated with the DRIFTS results shown in Figure 3.8

As shown in Figure 3.11, both NH_3 adsorbed on Lewis acid sites and OH bridging bond sites show a relatively linear decreasing trend. However, the IR band intensity

corresponding to NH_4^+ did not change in step with Brønsted acid sites. This additional NH_4^+ must originate from another source of NH_3 on the catalyst surface. Since NH_3 exists as NH_4^+ or molecular NH_3 on the surface, as demonstrated in the NH_3 adsorption study, the only possibility is that some NH_3 bound to the Lewis acid sites is protonated and transformed into NH_4^+ species during the interaction with NO + O_2. Interestingly, no such NH_4^+ evolution was observed during exposure to NO.

In order to clarify the origin of this evolution, 500 ppm NO_2 was passed over the NH_3 pre-adsorbed catalyst sample at 100°C. Such lower temperature potentially allows the capture of the reaction intermediate on the surface that was produced during the reaction. As shown in Figure 3.12, the NH_3 adsorbed on P-OH (3677 cm^{-1}) and OH bridging sites (3624 and 3598 cm^{-1}) were gradually consumed during exposure to NO_2 for 30 minutes. On the other hand, the intensity of band at 1617 cm^{-1}, associated with the NH_3 adsorbed on Lewis acid sites, rapidly decreased and completely disappeared after 5 minutes. However, the NH_4^+ vibration mode significantly increased for the first 10 minutes and slightly decreased subsequently. Surface nitrates, with a band at 1575 cm^{-1}, appeared after 10 minutes and the intensity of the DRIFTS feature increased over the remaining 20 minute exposure.

In addition to the surface NH_3 and nitrates species (bands at 1617, 1575 and 1460cm^{-1}), a new band at 1596 cm^{-1} was detected after 10 minutes. The initial increase of NH_4^+ band was very likely due to the formation of NH_4NO_2 which caused the increase in the of NH_4^+ signal during the first 10 minutes. However, with further exposure to NO_2, some NH_4NO_3 were formed on the surface, which is explained by the appearance of band at 1575 cm^{-1} and 1596 cm^{-1} after 10 minutes in the DRIFTs spectra.

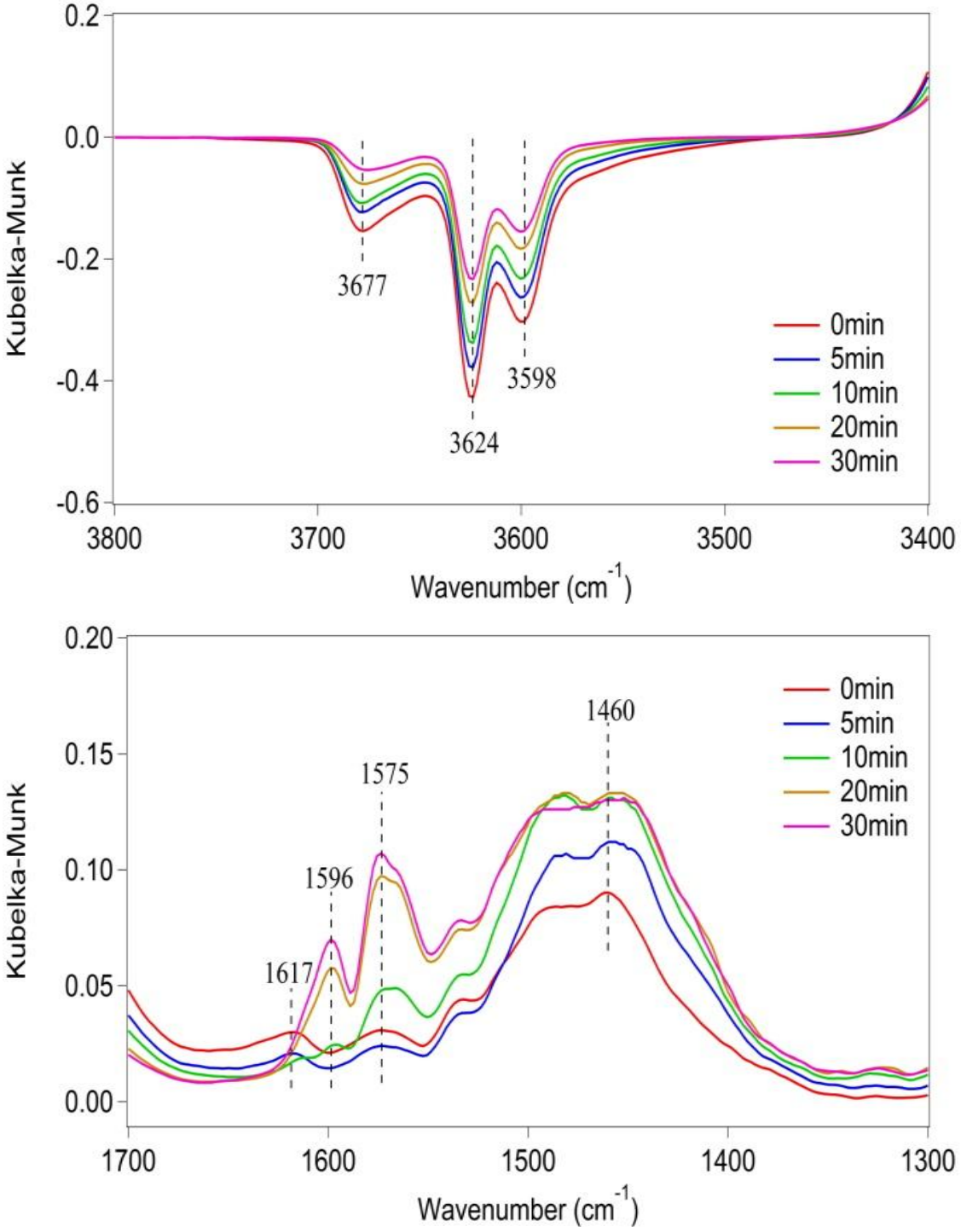

Figure 3.12 DRIFTS spectra obtained at 100°C during exposure to 500 ppm NO_2/He after pre-saturating with NH_3

As indicated by the normalized peak areas (Figure 3.13), the bands at 1596 cm^{-1} and 1575 cm^{-1} showed a very similar trend, suggesting that they might originate from the

same surface intermediate, likely NH_4^+-NO_3^- species. Indeed, similar surface species have been found on many other SCR catalysts upon exposure to NH_3 and NO_2. For example, Long and Yang detected a reaction intermediate with a band of 1602 cm^{-1} when NO_2 was introduced onto an NH_3-adsorbed Fe-ZSM-5 sample and they predicted this band to be an $NO_2(NH_4^+)_2$ like species [43]. Nova et al., found an intense band at 1380 cm^{-1} upon passing NH_3 and NO_2 over a V_2O_5–WO_3/TiO_2 catalyst at 140°C. They assigned this peak to an NH_4NO_3 deposit since the IR spectrum of pure NH_4NO_3 contains the same peak [107]. Malpartida et al., [108] reported that the activity of a commercial zeolite-based catalyst was decreased by the formation of NH_4NO_3 deposits when passing NO_2 over an NH_3 pre-adsorbed sample, which was evidenced by comparing the operando IR spectra of a NH_4NO_3 mixed sample with the spectra taken during test with NO_2 at 165 °C.

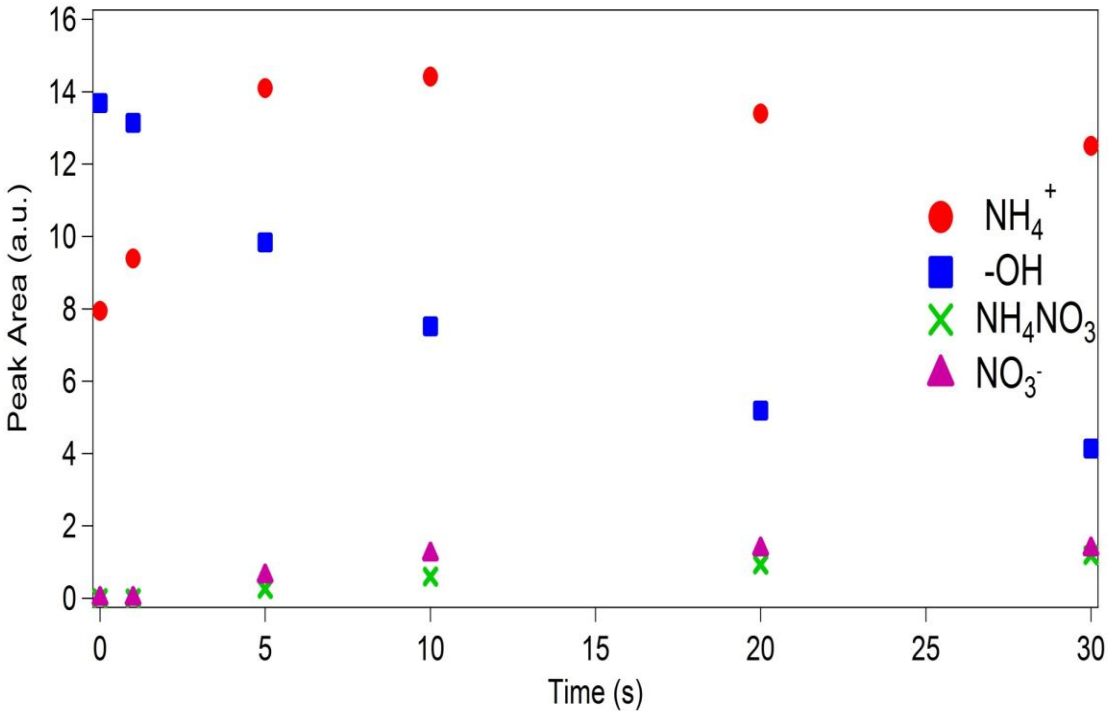

Figure 3.13 Normalized peak areas, associated with the DRIFTS results shown in Figure 3.12

On the other hand, it is obvious that the increase in NH_4^+ was more distinct compared with that during exposure to NO + O_2. This further suggests that the higher level of nitrate and nitrite species formed upon NO_2 adsorption facilitates the transformation of molecular NH_3 adsorbed on Lewis acid sites to the NH_4^+-NO_x species that enhances the NH_4^+ signal. Since molecular NH_3 only exists on the Lewis acid sites, it is reasonable to believe that the formation of this intermediate occurred on Lewis acid sites. Meanwhile, the NH_3 on Brønsted acid sites might migrate to Cu sites and supply NH_3 for reaction, which coincides with the hydroxyl IR bands approaching the baseline. Indeed, the change in the band corresponding to NH_4^+ was in fact not in step with OH group changes, further indicating that NH_4NO_3 was perhaps not interacting with Brønsted acid sites, at least not very strongly. It seems reasonable that this kind of migration could be facilitated by the small pores of the SAPO-34 material in which the distance between the Brønsted acid sites and Lewis acid sites is small. Interestingly, the band at 1596 cm^{-1} was not observed upon exposure to NO + O_2 on the sample with pre-adsorbed NH_3. This could be explained by the following: first, as shown in Figure 3.3 and Figure 3.4, a significantly larger amount of surface nitrates was formed by NO_2 compared to NO + O_2. In other words, this intermediate was promoted by the presence of surface NO_3^-. Second, this intermediate and surface nitrate could be quickly reduced by NO and therefore were not observed on the surface. Indeed, when we exposed the NH_3 pre-adsorbed samples to 500 ppm NO + 50 ppm NO_2 at the same temperature (50 ppm NO_2 could be generated at 200°C via NO oxidation as shown in Figure 3.5), no band at 1596 cm^{-1} (band assignments verified below) was detected in the DRIFTS spectra (Figure 3.14). This provides strong evidence that NO_2 was either first formed and stored on the surface

followed by formation of surface NH_4^+-NO_x, or nitrates were formed via oxidation of surface NO_x species and then NH_4^+-NO_x formed, which could be easily reduced by NO under standard SCR inlet conditions.

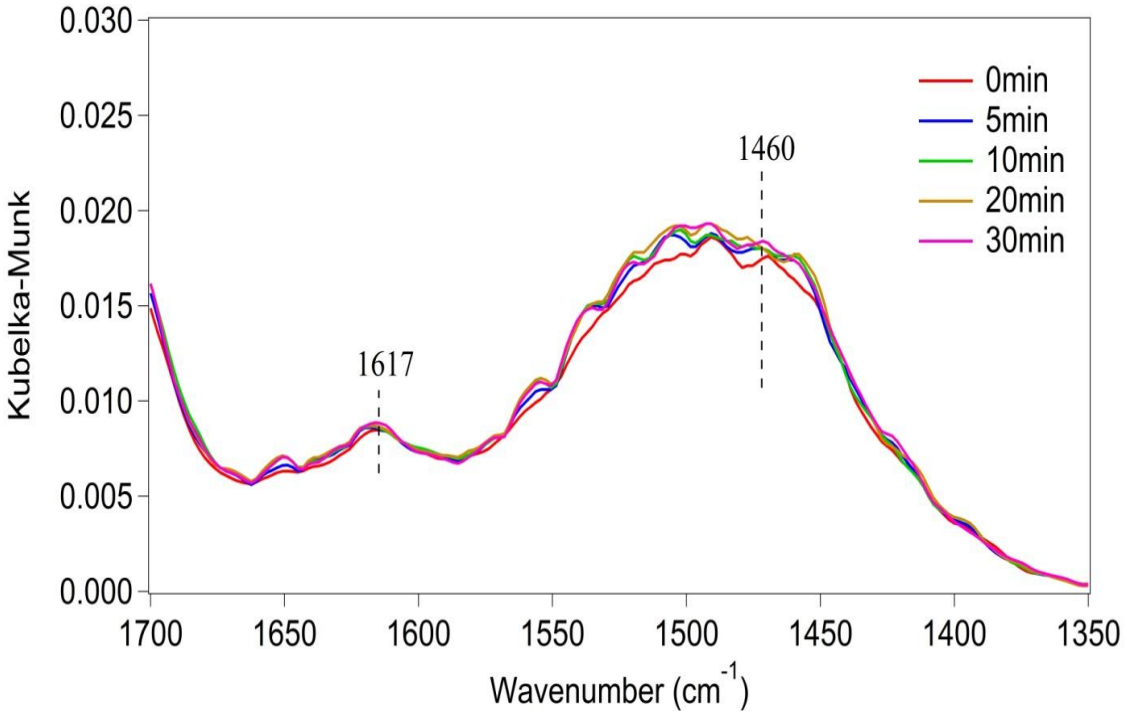

Figure 3.14 DRIFTS spectra taken at 200°C upon exposing the NH_3 pre-saturated Cu-SAPO-34 sample to 500 ppm NO, 50 ppm NO_2/He

3.3.5 Confirmation of the NH_4NO_3 intermediate

To identify the intermediate, a TPD experiment was conducted after it was formed. The DRIFTS spectra and outlet concentrations of different species are shown in Figure 3.15. During the temperature ramp, the band at 1596 cm^{-1}, which corresponded to the deposit formed by surface NH_3 and NO_3^-, decreased in intensity starting from 200°C and was completely removed from the surface by 500°C. Concurrently, a significant amount of N_2O was observed in the outlet gas starting at about 200°C.

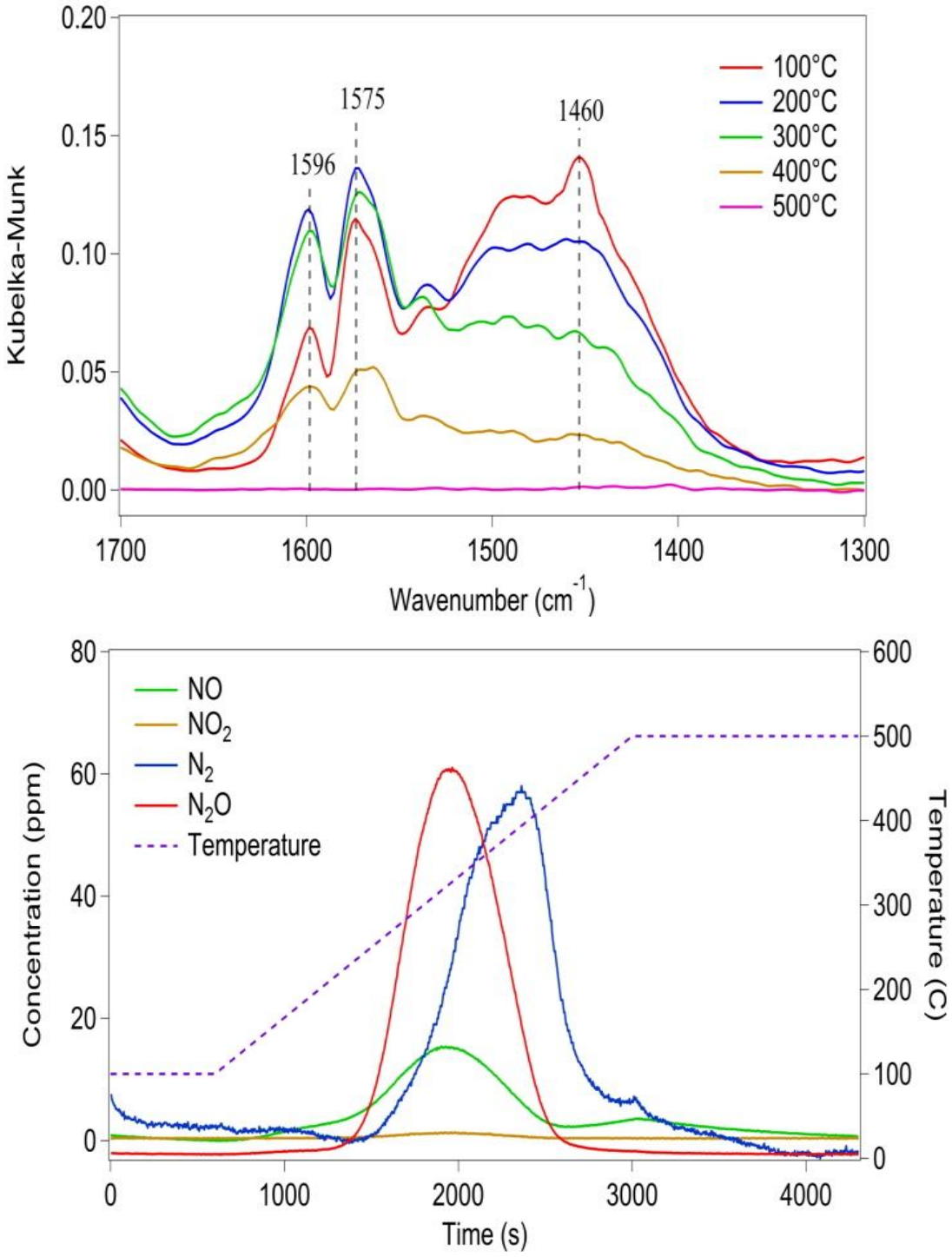

Figure 3.15 DRIFTS spectra obtained during a TPD (in He, 10°C/min) after exposing the NH_3-presaturated sample to 500 ppm NO_2/He

According to literature [51, 106, 109], N_2O originates from NH_4NO_3 at low temperature and NH_3 oxidation at higher temperature, and since 200°C is the onset

temperature of the NH_4NO_3 decomposition reaction these results suggest it is a major reaction intermediate present on the catalyst. During the temperature ramp, no NH_3 evolution was detected in the outlet gas, meaning that all the NH_3 was involved in combining with nitrates that stored on the surface and formed NH_4NO_3. This result is consistent with a similar study conducted on Fe-ZSM-5 which concluded that the NH_3 spills over to the nitrates that formed during NO_2 adsorption and only NH_4NO_3 species were present on the catalyst [109]. Interestingly, the band at 1596 cm^{-1} initially increased with increasing temperature, from 100 to 200°C. This might be attributed to enhanced mobility of NH_3 at higher temperature that enables more NH_3 to reach Lewis acid sites to form the NH_4NO_3 intermediate.

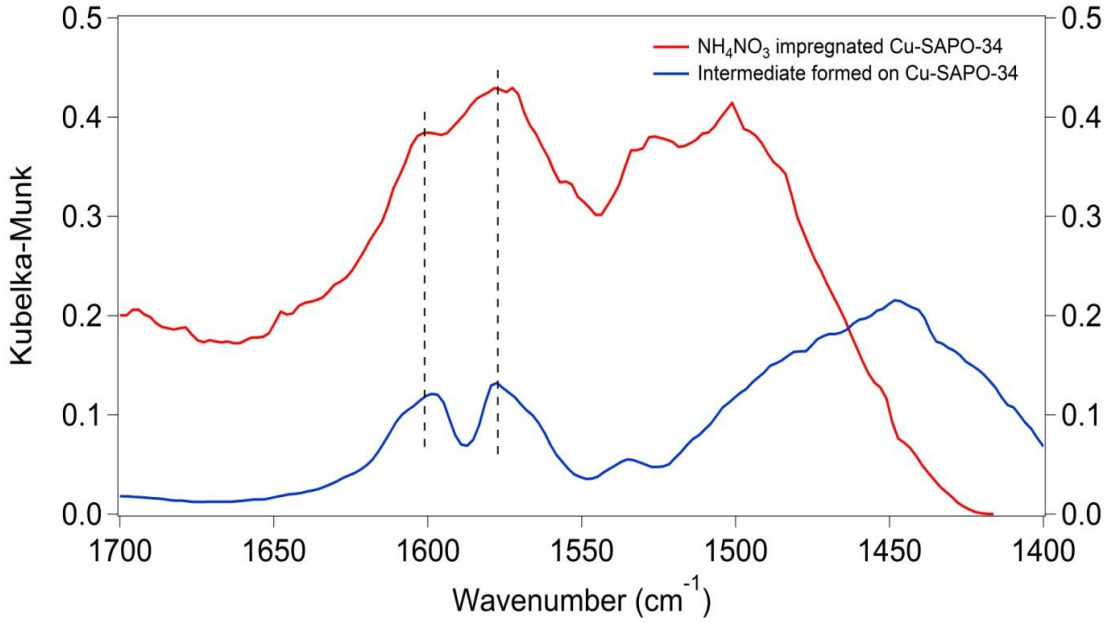

Figure 3.16 Comparison of DRIFTS spectra of a fresh Cu-SAPO-34 catalyst sample impregnated with NH_4NO_3 and the sample after exposure to NH_3 and NO_2 at 100°C

In order to further confirm the formation of NH_4NO_3 on the surface, a DRIFTS single beam spectrum was taken on a fresh Cu-SAPO-34 sample that was mechanically

mixed with 3 wt% NH_4NO_3 powder (Sigma Aldrich). By subtracting this spectrum of a pure Cu-SAPO-34 sample at the same temperature, the NH_4NO_3 species that stored on the surface of the catalyst might be distinguished. Figure 3.16 compares the spectrum of the impregnated sample with the one taken at 100°C after exposing the Cu-SAPO-34, with pre-adsorbed NH_3, to NO_2 for 30 min. It is evident that the bands at 1596 and 1575 cm^{-1} appeared in both spectra and their positions closely match, providing further evidence for the assignments of these bands to NH_4NO_3.

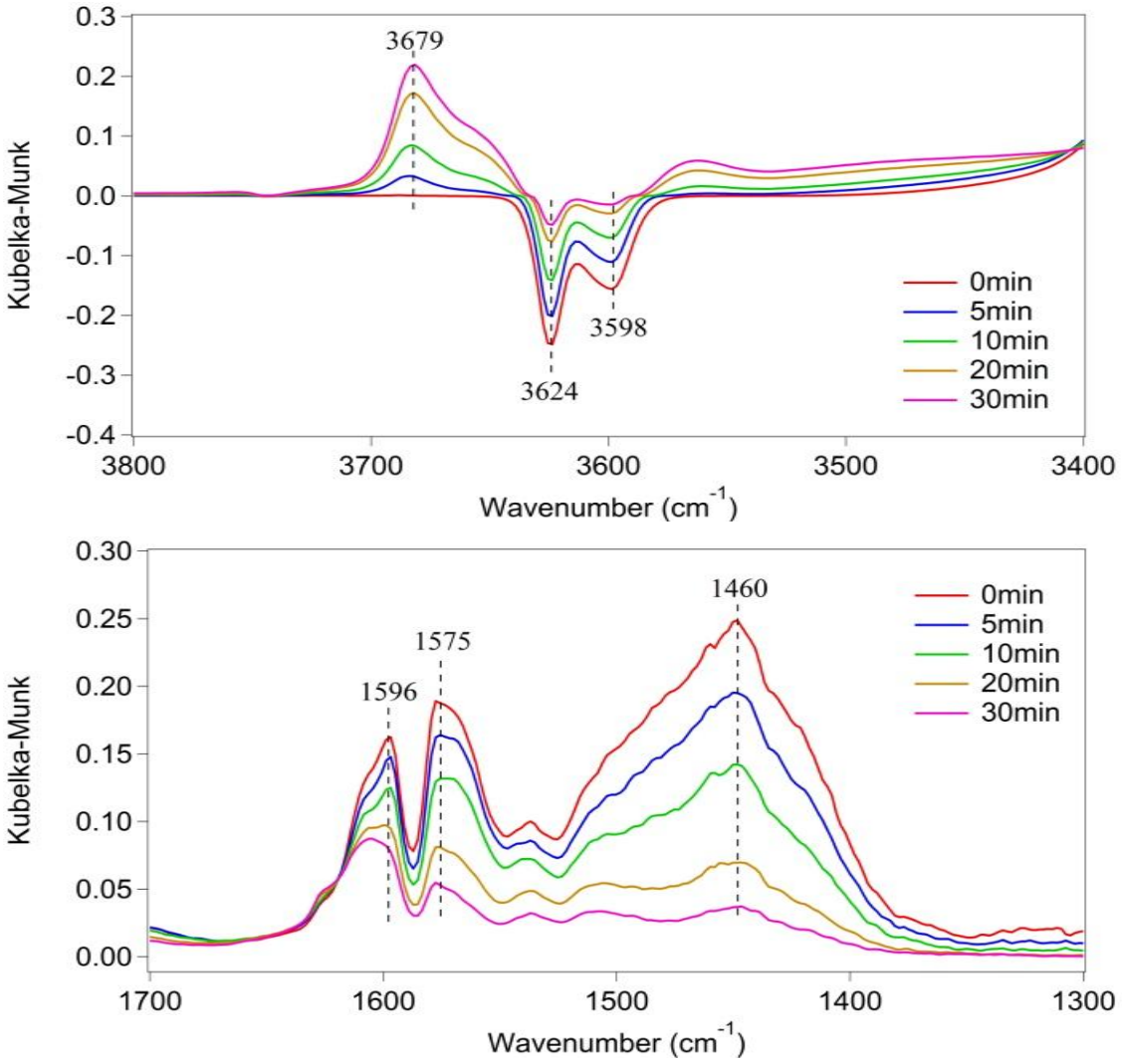

Figure 3.17 DRIFTS spectra obtained at 100°C during exposure to 500 ppm NO, after the NH_3 saturated sample had been exposed to 500 ppm NO_2/He

In order to investigate the role of NO in the SCR reaction, 500 ppm NO was passed over the sample containing NH_4NO_3 at 100°C. As shown in Figure 3.17, the bands at 1596, 1575 and 1460 cm^{-1}, being indicative of NH_4NO_3 and NH_4^+, were significantly decreased after 30 minutes. N_2 was detected in the outlet over the entire 30 minute period. This further proves that this surface intermediate is very active in reacting with gaseous NO, reacting to N_2 at as low a temperature as 100°C.

3.3.6 Reaction pathway

As discussed above, the SCR reaction starts with NO oxidation on the surface to form NO_2 (gas-phase or some oxidized surface species), in the form of surface nitrates and nitrites. These surface nitrate and nitrite species were produced through surface NO_2 dimerization and disproportionation:

$$2NO+O_2 \leftrightarrow 2NO_2, \quad (3.3)$$

$$2NO_2 \leftrightarrow N_2O_4, \text{ and} \quad (3.4)$$

$$N_2O_4 \leftrightarrow NO_3^- + NO^+. \quad (3.5)$$

Reactions (3.4) and (3.5) have been extensively reported for the formation of surface NO_3^- and NO_2^- species on other zeolite catalyst systems [94, 110, 111]. The observation of a broad peak at around 2144 cm^{-1} in our spectra confirmed the existence of NO^+ ions on Cu-SAPO-34. It has also been proposed by many authors [86, 112, 113] that NO^+ may incorporate with surface oxygen or coordinated oxygen to form NO_2^- species according to reaction

$$NO^+ + O^{2-} \leftrightarrow NO_2^-. \quad (3.6)$$

The existence of coordinated oxygen (lattice O^{2-} or OH^-) has been confirmed using DFT, EPR and synchrotron-based technologies and research has shown that isolated Cu^{2+} could associate with at most four oxygen atoms under SCR conditions [59, 114, 115]. However, surface NO_2^- or nitrite related species are difficult to detect in our spectra either due to its overlapping regions with zeolite asymmetric vibrations or their rapid reactivity with NH_3 on the surface. NO^+ produced from NO_2 dimerization and disproportionation was found to replace the proton on Brønsted acid sites and forms HNO_3 species according to reaction (3.7) [86]

$$NO_3^- + NO^+ + \text{Zeo-O-H} \leftrightarrow \text{Zeo-O-}NO^+ + HNO_3. \quad (3.7)$$

This replacement is evidenced by the evolution of negative bands associated with OH bridging bonds when NO, NO + O_2 or NO_2 was passed over the catalyst, as shown in Figure 3.2-3.4. The existence of HNO_3 has been reported by Rivallan et al., who observed a broad NO_2 adsorption band that covers the whole 1650-1450 cm^{-1} region on H-ZSM-5 and attributed this band to be neutral weakly adsorbed HNO_3 species [86]. Indeed, a similar broad band that spans the whole nitrate adsorption region was also detected in our DRIFTS spectra upon NO_2 exposure and adsorption (Figure 3.4). Therefore, HNO_3 is apparently present on Cu-SAPO-34 as well. Ahrens et al., have concluded HNO_3 is the main NO_2 adsorption species on Fe-ZSM-5 and Fe-BEA catalysts [116]. It is also worth pointing out that the HNO_3 may be formed via a H_2O-involved reaction as reported elsewhere [90, 116]

$$2NO_2 + H_2O \leftrightarrow HNO_3 + HNO_2. \quad (3.8)$$

However, as the DRIFTS experiment operating conditions used here do not include water, this reaction may not be relevant in our study. Moreover, in a separate experiment, significant gas-phase NO evolution was immediately observed when exposing Cu-SAPO-34 to NO_2 (monolith-supported sample, data shown in Figure 3.18). This could be explained by reaction (3.9) or (3.10)

$$NO_2 + NO_2^- \leftrightarrow NO + NO_3^- \text{ and} \quad (3.9)$$

$$NO_2 + HNO_2 \leftrightarrow NO + HNO_3, \quad (3.10)$$

in which the surface NO_2^- and HNO_2 species were further oxidized to NO_3^- (or HNO_3) by NO_2 [90, 91, 117].

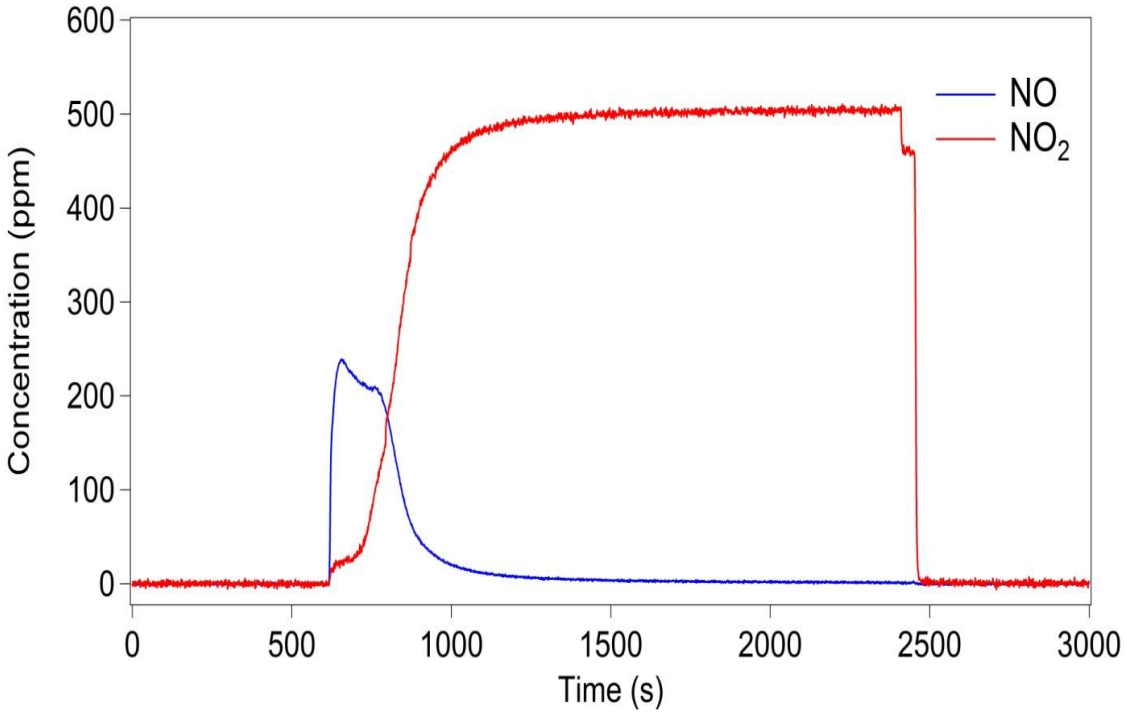

Figure 3.18 NO and NO_2 profiles during NO_2 adsorption (500 ppm in N_2) over Cu-SAPO-34 at 150°C

Conversely, NO_2 was observed when the sample, with NO_3^- (or HNO_3) present on the surface, was exposed to NO, via the reversibility of reactions (3.9) and (3.10). Thus,

both nitrate and nitrite species might exist on the catalyst surface and their proportions are primarily determined by the NO_2/NO_x ratio in the feed. The reduction of these surface nitrate species by NO has been considered the key step for SCR activity on other catalysts, since it transforms surface NO_3^- to NO_2^- (or HNO_2), which can readily react with NH_3 to form NH_4NO_2 [79, 81, 107, 118, 119]

$$NH_4^+ + NO_2^- \leftrightarrow NH_4NO_2 \text{ and} \quad (3.11)$$

$$NH_3 + HNO_2 \leftrightarrow NH_4NO_2. \quad (3.12)$$

The NH_4NO_2 is unstable and easily decomposes to N_2 and H_2O at temperatures above 80 °C (3.13) [117, 120] and the reaction is expressed as

$$NH_4NO_2 \leftrightarrow N_2 + 2H_2O. \quad (3.13)$$

In the presence of NO_2 in the feed, surface NH_4NO_2 could be further oxidized to NH_4NO_3 according to

$$NH_4NO_2 + NO_2 \leftrightarrow NH_4NO_3 + NO. \quad (3.14)$$

When surface nitrates were formed on the catalyst, they readily react with NH_3 pre-adsorbed on Cu Lewis acid sites to form NH_4NO_3 as well and the reaction is

$$NH_3 + HNO_3 \leftrightarrow NH_4NO_3. \quad (3.15)$$

NH_4NO_3 formation has been observed on many other SCR catalyst systems (ZSM-5, V-based catalysts and BaNa-Y catalysts) under NO_2-rich conditions [78, 121, 122] and is reportedly relatively stable at low temperature. It could therefore block the active sites of

the SCR reaction [78, 108]. At temperatures higher than 200°C, NH_4NO_3 decomposes to N_2O and H_2O according to [51, 106, 109]

$$NH_4NO_3 \leftrightarrow N_2O + H_2O. \quad (3.16)$$

N_2O is regarded as a potential greenhouse gas, and ideally none would form during the SCR reaction. N_2O was not observed in our experiments under standard SCR reaction conditions (data not shown) over all temperature ranges, providing strong evidence that NH_4NO_3 readily reacts with NO on Cu-SAPO-34 via the following reaction

$$NO + NH_4NO_3 \leftrightarrow N_2 + H_2O + NO_2. \quad (3.17)$$

Again, reaction (3.17) is believed to be crucial in SCR reaction chemistry since it removes surface NH_4NO_3 and continuously converts NO into N_2. The NO_2 that concurrently formed could again adsorb and react with NH_3. It has been reported that the reaction between NH_4NO_3 and NO is the rate determining step for the fast SCR reaction on Fe-ZSM-5 [79] and the onset temperature is 170-190°C [78, 117, 123]. However, on Cu-SAPO-34, this reaction proceeded at even lower temperature, i.e., at 100°C. The enhanced reactivity of NH_4NO_3 with NO also leads to selectivity improvement, since N_2O originates from NH_4NO_3 decomposition, but the NH_4NO_3 is consumed at low temperatures. This could also be the key factor that explains the excellent low temperature SCR reaction activity of Cu-SAPO-34. Indeed, Tronconi et al., discovered that the injection of NH_4NO_3 into the feed could significantly enhance NO_x reduction efficiency over both Fe-ZSM-5 and V_2O_5-WO_3/TiO_2 catalysts [124, 125]. The NH_4NO_3 intermediate was detected on the Cu-SAPO-34 catalyst only under fast SCR reaction conditions, not under standard SCR reaction conditions. Besides, only a negligible

amount of N_2O was detected under standard SCR reaction conditions, indicating that the NH_4NO_3 decomposition reaction was not significant. In other words, any NH_4NO_3 formed was quickly reduced by the larger concentration of NO under standard SCR conditions and therefore was not observed via DRIFTS on the surface. Grossale et al., proposed that NH_4NO_3 formation on the Fe-ZSM-5 was not influenced by the order of NH_3 and NO_2 adsorption [109]. Interestingly, for Cu-SAPO-34, the DRIFTS bands associated with the NH_4NO_3 intermediate were not detected when the sample was exposed to NH_3 after pre-adsorbing NO_2 at 100°C (Figure 3.19).

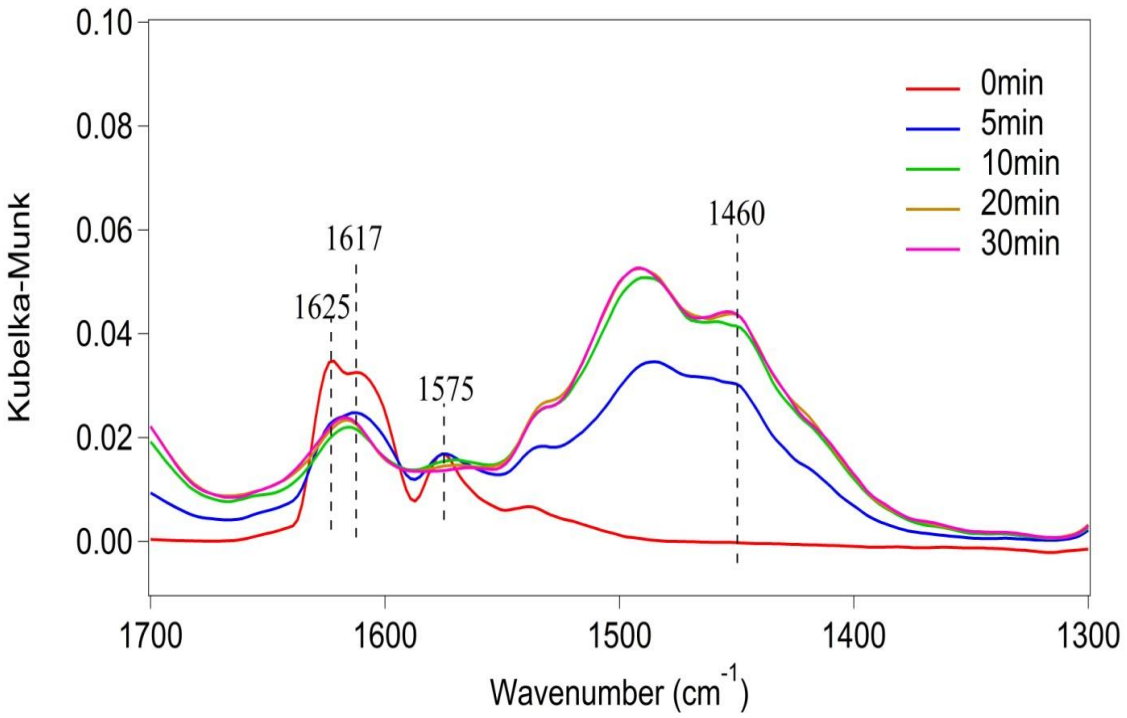

Figure 3.19 DRIFTS spectra taken at 100°C after pre-exposing the sample to NO_2 and then exposing the sample to 500 ppm NH_3/He for 0-30min

Concurrently, some N_2 was detected in the outlet immediately after NH_3 was introduced. To explain this, NH_4NO_3 might be generated first and quickly reduced by gaseous NH_3 according to reaction (3.18)

$$2NH_3 + 3NH_4NO_3 \leftrightarrow 4N_2 + 9H_2O. \quad (3.18)$$

This reaction is confirmed on Cu-SAPO-34 when NH_3 was introduced over NH_4NO_3 in-situ formed sample at 200°C and all the peaks corresponding to NH_4NO_3 were reduced and completely disappeared after 20 minutes, as shown in Figure 3.20. The other possibility is that gaseous NH_3 directly reacts with surface nitrates to N_2 according to the reaction (3.19)

$$5NH_3 + 3HNO_3 \leftrightarrow 4N_2 + 9H_2O. \quad (3.19)$$

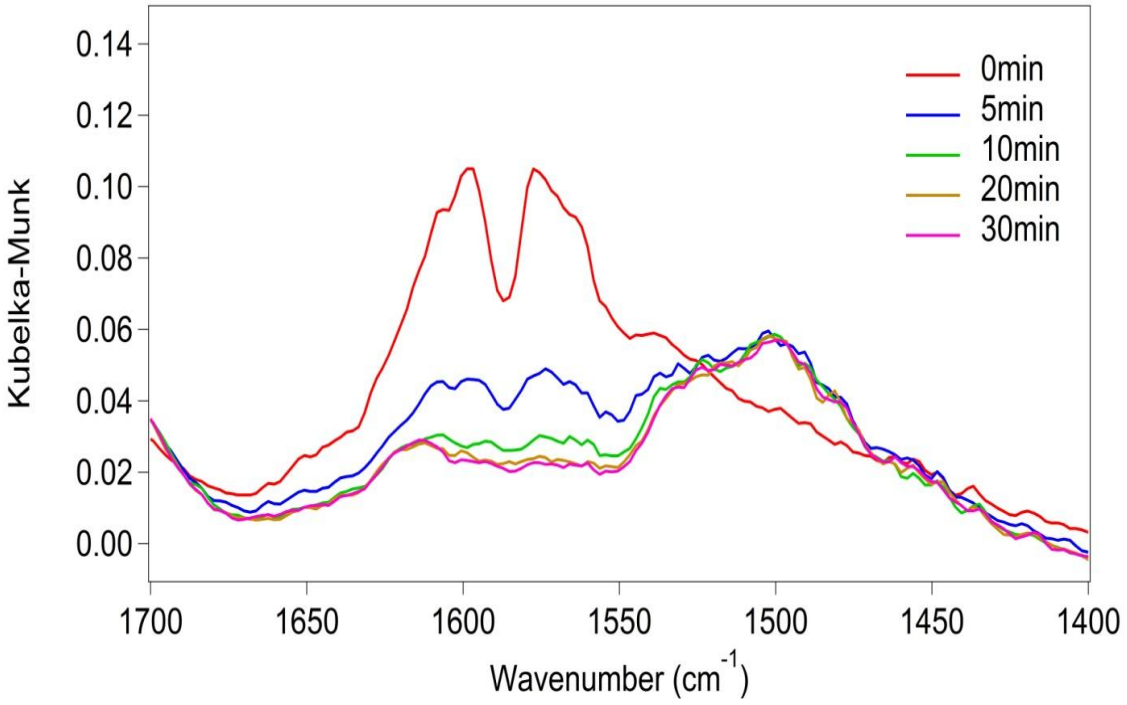

Figure 3.20 DRIFTS spectra taken at 200°C upon exposing the catalyst to 500 ppm NH_3/He after forming NH_4NO_3 on the sample

Both reactions (3.18) and (3.19) are regarded as NO_2 SCR reactions and reportedly start between 220 to 230°C on Fe-ZSM-5 [126]. However, on Cu-SAPO-34, it again seems that the reactivity of adsorbed nitrates with NH_3 is significantly enhanced.

To summarize, the reaction mechanism of SCR on Cu-SAPO-34 can be described by Figure 3.21. The reaction pathway involves NH_4NO_3 intermediate formation on Lewis acid sites followed by reaction with NO to produce N_2. This reaction on Cu sites matches the SCR reaction pathway that has been previously proposed over other zeolite-based SCR catalysts. The NH_3 on Brønsted acid sites might migrate to Lewis acid sites to provide more NH_3 for reaction instead of being directly involved in the SCR reaction. NH_3 migration on Cu-SAPO-34 at low temperature is attributed to its unique acid properties and has not been observed on other zeolite-based SCR catalysts. On the other hand, the participation of nitrite species in the SCR reaction pathway is still likely to occur, even if NH_4NO_2 species were not observed in our DRIFTS spectra. This is explained by its high reactivity, which is likely also the key in the low-temperature activity of SAPO-34 SCR catalysts.

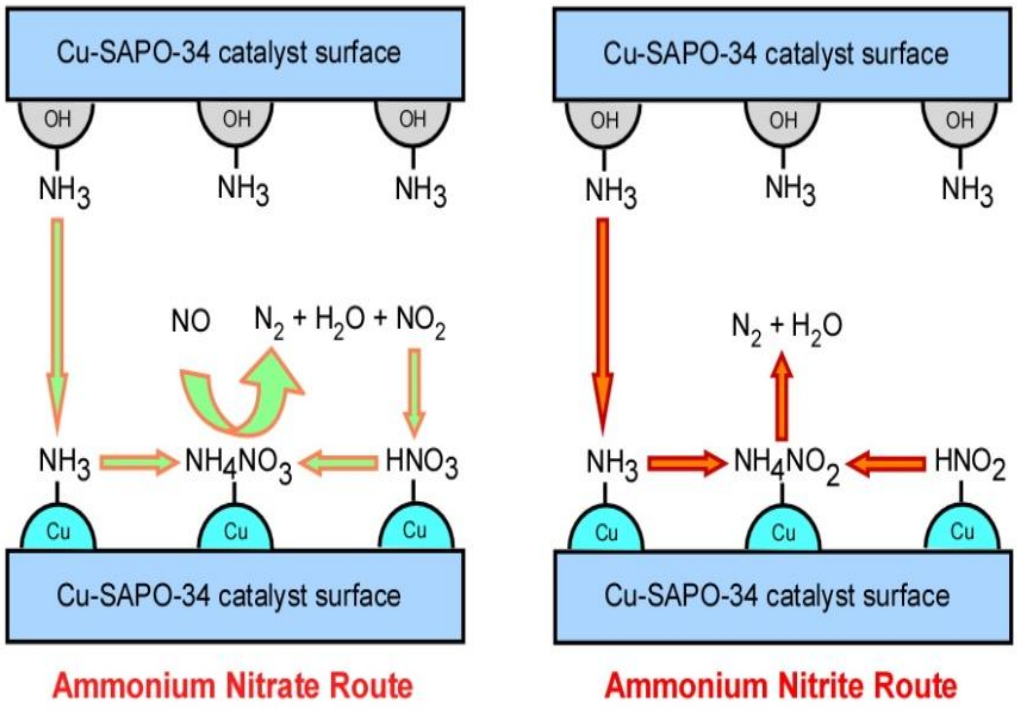

Figure 3.21 Proposed SCR reaction pathway on Cu-SAPO-34

3.4 Conclusions

In-situ DRIFTS results show that formation of surface nitrates and nitrites is the key step in NH_3-SCR over Cu-SAPO-34. The surface nitrate and nitrite species form on the catalyst surface by dimerization and disproportionation reactions. These surface complexes readily react with surface NH_3 to form NH_4NO_2 and NH_4NO_3 on the Lewis acid sites. When NO_2 was present in the feed, NH_4NO_2 could be further oxidized to NH_4NO_3. NH_4NO_3 was reduced to N_2 in the presence of NO at temperatures as low as 100°C, which accounts for the superior low temperature SCR reaction activity of this catalyst. The Brønsted acid sites act as an NH_3 reservoir instead of being directly involved in the SCR reaction. Actually the similar acidity strength of different acid sites on the SAPO-34 material, observed via ammonia release profiles and from IR band intensity changes during NH_3-TPD, may enable this migration. However, the possibility of NH_4NO_2 formation on Brønsted acid sites does exist as evidenced by the fast consumption of NH_4^+ species upon interaction with NO_2. Therefore, the participation of nitrite species in the SCR reaction pathway is still likely to occur, even if NH_4NO_2 species were not observed in the DRIFTS spectra, and is explained by its high reactivity.

Chapter 4 Zeolite acidity and Cu structure changes as a function of Cu loading in Cu-SAPO-34

Note: the material in this chapter has been published. The introduction and experimental methods material has been summarized to avoid redundancy with Chapters 1 and 2, however, the rest of the manuscript has been left "as is" with reference and figure numbers changed for thesis consistency.

4.1 Introduction

The conventional wetness ion exchange (WIE) method has been extensively applied to prepare Cu-SSZ-13 [45, 47, 58, 61]. WIE process involves adding the NH_4^+ or H^+ form zeolite material to the Cu^{2+} salt solution under constant stirring for several hours followed by several wash and dry processes [45, 51, 62, 66]. However, the preparation of Cu-SAPO-34 is not as straightforward. For example, Akolekar et al., found that both the surface area and pore volume of SAPO-34 significantly dropped after WIE, which is consistent with previous experimental results [127, 128]. More recently, Feng et al., reported that more severe irreversible hydrolysis could occur with SAPO-34, resulting in a significant drop in zeolite crystallinity as well as surface area [66]. They also discovered that SAPO-34 synthesized by different SDAs underwent different levels of structural damage during the WIE process. Alternatively, Deka et al., designed a direct synthesis methodology to prepare Cu-SAPO-34 by incorporating Cu in a combination of SDAs, such as Cu^{2+}-triethylenetetramine complex and tetraethylammonium cations [71]. Corma et al., used different SDAs, copper-tetrathylenepentamine (Cu-TEPA) and diethylamine (DEA), in a similar "one pot" synthesis method and the obtained catalysts showed good SCR activity and hydrothermal stability [70].

In this study, a family of Cu-SAPO-34 samples with different Cu loadings was prepared by a solid state ion exchange (SSIE) method. The acid properties were investigated by NH_3-TPD combined with in-situ DRIFTS. Cu structures were characterized by XRD, DRIFTs, H_2-TPR and UV-vis techniques and their various functionalities in NH_3-SCR were also studied.

4.2 Experimental

4.2.1 Catalyst preparation by the solid state ion exchange (SSIE) method

The H-form SAPO-34 zeolite support used in this study was purchased from ACS materials. The H-SAPO-34 powder was first calcined at 500°C in 10% O_2 before the ion exchange process. The solid state ion exchange was conducted in a tube furnace with 130 sccm of air flow. In each batch, one gram of the H-SAPO-34 powder sample was first physically mixed with a certain amount (10mg-50mg) of CuO nanosized particles (purchased from Sigma Aldrich) depending on the target Cu loading. The mixtures were then thoroughly homogenized and the color of the resulting samples was uniformly grey. The thermal treatment includes several steps and is described in Figure 4.1. The furnace temperature was first maintained at 120°C for 4h and then was ramped to 600°C at 2°C/min and held there for 5 hours. The temperature was then further increased to 800°C at 2°C/min and held for 12 hours before cooling to room temperature. The 12 hour thermal treatment enables the Cu ions to migrate inside the zeolite pores and exchange with protons. After the solid state ion exchange, the color of the samples was blue suggesting that the Cu ions were successfully exchanged into the zeolite.

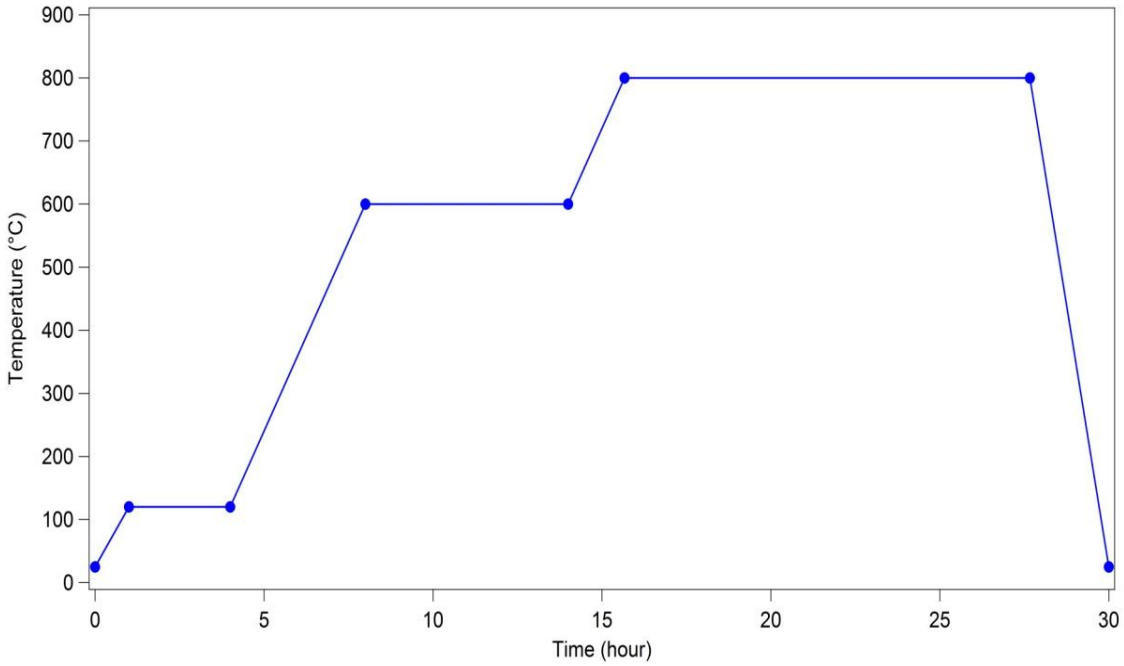

Figure 4.1 Procedure for the solid state ion exchange process (SSIE)

4.2.2 Characterization of as-prepared Cu-SAPO-34

The elemental compositions of the as-prepared samples were analyzed by ICP (Galbraith Laboratories). The as-prepared samples are named in the format of SSIE-x, where x stands for the Cu wt% in each sample. X-ray diffraction (XRD) experiments were conducted using a Siemens D5000 Diffractometer equipped with a Cu-Kα detector. UV-vis spectra were collected with a Hitachi UV-vis U-2001 Spectrophotometer. The NH_3 temperature programmed desorption (NH_3-TPD) experiments were carried out by loading 120 mg of powder catalyst in the quartz tube reactor. The NH_3 effluent concentration was measured by FTIR (MultiGas 2030). The as-prepared samples were first pretreated in 10% O_2 in N_2 at 500°C for 1 h. After pretreatment, a total flow of 300 sccm containing 500 ppm NH_3 in N_2 was metered into the reactor for 2 h at 35 °C to saturate the catalyst. Once the system reached steady state, NH_3 was switched off and

only N_2 was fed to the reactor for another 2 h to remove any gas phase or weakly adsorbed NH_3. The final stage involved a temperature ramp to 535°C with a heating rate of 10 °C/min.

The H_2-TPR experiments were performed by loading 100 mg of powder catalyst in a quartz tube reactor. The effluent H_2, H_2O and O_2 signal was detected by the mass spectrometer. The samples were first pretreated in 150 sccm with 5% O_2 in He at 550°C for 2 h followed by purging with pure He for 1 h at the same temperature. Subsequently, the reactor temperature was reduced to 50°C and 1% H_2 in a total flow of 33 sccm (He balance) was metered into the reactor for 5 h in order to saturate the catalyst and stabilize the H_2 signal. An O_2 trap was used to remove any trace amount of O_2 from the gas supply. After saturation, the temperature was ramped to 1000°C at 10°C/min with flowing 1% H_2 in He and the H_2 consumption was calculated afterwards.

In the in-situ DRIFTS experiments, powder samples were pressed into a 60 mg pellet placed in the sample cup with a porous screen at the bottom surface. Prior to each test, the catalyst sample was pretreated at 550°C in a flow of 10% O_2 in He for 1 h before cooling to room temperature. For the skeleton vibration spectra, the background spectra were recorded in flowing He on pure KBr powder and subtracted from the absorption sample spectrum. For NH_3 and NO adsorption experiments, the spectra were collected by subtracting the background spectra recorded during exposure to the sample to pure He. NH_3 adsorption was conducted in a 50 cm^3/min flow containing 500 ppm NH_3 in a balance of He and NO adsorption spectra were performed in a 50 cm^3/min flow containing 200 ppm NO in a balance of He.

4.2.3 NH_3-SCR and NH_3 oxidation reaction tests

The reaction data were collected using a micro-reactor system. In each experiment, 120 mg of sieved powder catalyst samples were mixed with 360 mg quartz beads and put into a quartz tube reactor. Before testing, the catalyst was degreened at 550°C for 2 h in flowing 10% O_2 in a balance of N_2.

The standard SCR performance tests were conducted with a simulated exhaust gas containing 500 ppm NO, 500 ppm NH_3, 10% O_2 and 10% H_2O with a balance of N_2 and a corresponding gas hourly space velocity (GHSV) of 240000 h^{-1}. The NH_3 oxidation reaction tests were carried out in a flow of 500 ppm NH_3, 10% O_2 and 10% H_2O with a balance of N_2. The total flow rate was 600 cm^3/min. The NO and NH_3 conversions were calculated using the following equations

$$X_{NO} = \frac{C_{NO_{x_{in}}} - C_{NO_{x_{out}}}}{C_{NO_{in}}} \times 100\% \text{ and} \quad (4.1)$$

$$X_{NH_3} = \frac{C_{NH_{3_{in}}} - C_{NH_{3_{out}}}}{C_{NH_{3_{in}}}} \times 100\%. \quad (4.2)$$

4.3 Results and Discussion

4.3.1 Characterization of Cu-SAPO-34 prepared by SSIE

According to the ICP results, the Si/(Al+P) ratio of the H-SAPO-34 support was approximately 0.16 and the final Cu loading of each sample was estimated to be 0.7 wt%, 1.0 wt%, 1.5%, 2.0 wt% and 3.0 wt%, respectively. These numbers are close to the target values based on initial amounts of Cu precursors, meaning that no significant loss of Cu species occurred during the preparation. The crystal structures of Cu-SAPO-34 samples

prepared by SSIE were verified by the XRD measurements. As shown in Figure 4.2, all the XRD peak features of Cu-SAPO-34 coincide with those of the H-SAPO-34, indicating that well-defined CHA framework structures were maintained after the high temperature treatment during the SSIE process. However, two extra peaks at 36.30° and 38.72° were observed for samples SSIE-2.0 and SSIE-3.0. These two peaks are related to CuO phases, with XRD data obtained from the physical mixture of CuO particles and H-SAPO-34 shown in the inset of Figure 4.2. Some of CuO nanoparticles that were used in the SSIE method were not completely exchanged into the support for the SSIE-2.0 and SSIE-3.0, leading to some remaining CuO phases in these samples.

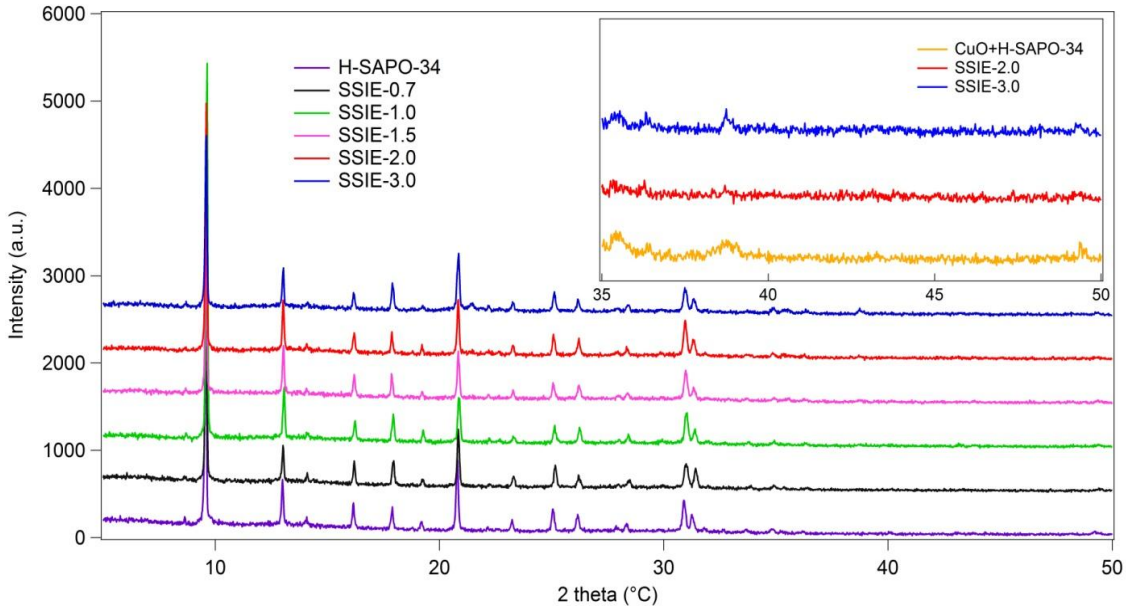

Figure 4.2 XRD patterns of the as-prepared samples

The zeolite skeleton vibrations were characterized by *ex situ* DRIFTS in order to study the influence of Cu on the zeolite framework (Figure 4.3). In the OH stretching vibration region, multiple positive bands corresponding to different hydroxyl groups were observed. The intense bands at 3625 and 3600 cm^{-1} are due to the stretching vibrations of bridging OH groups (Al-OH-Si) [61]. And the bands at 3730 and 3671 cm^{-1} are assigned

to the external surface Si-OH and P-OH groups, respectively [61]. All of these OH groups decreased as the Cu loading increased, which strongly suggests that more protons were replaced by the increasing amounts of Cu during the SSIE and as a result, hydroxyl vibrations diminished.

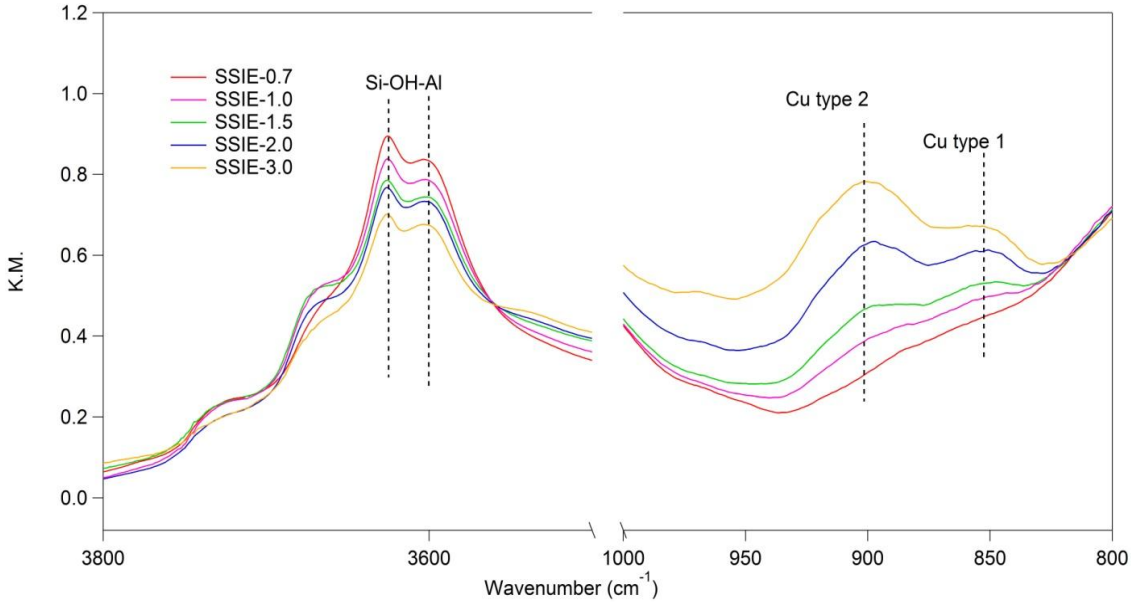

Figure 4.3 *Ex-situ* DRIFTS spectra obtained from the as-prepared Cu-SAPO-34 samples

On the other hand, two positive bands around 900 and 850 cm^{-1} were detected. The bands in this region originated from the perturbed zeolite skeleton vibrations. Specifically, these two bands are assigned to the tetrahedral-oxygen-tetrahedral (T-O-T) vibrations that interact with two types of exchanged Cu ions [129, 130]. In this work, we denominated the lower wavenumber band (850 cm^{-1}) to be type 1 Cu and higher wavenumber band (900 cm^{-1}) to be type 2 Cu. The appearance of these two bands strongly suggests that Cu was successfully exchanged with the protons in the pores. Indeed, the peak intensities of these two bands monotonically increased with increasing Cu loading, further demonstrating that more Cu exchanged with an increase in target Cu loading. Furthermore, UV-vis results (Figure 4.4) showed a single peak centered at 12500

cm^{-1} and a broad peak in the range of 35000-50000 cm^{-1} for the Cu-SAPO-34 samples. The former is due to the d-d transition of the hydrated isolated Cu^{2+} structure and the latter is the ligand to metal charge transfer (LMCT) that is caused by isolated Cu^{2+} [71]. The intensities of both peaks monotonically increased with increasing Cu loading, providing further evidence that isolated Cu^{2+} sites were created during the solid state ion exchange process.

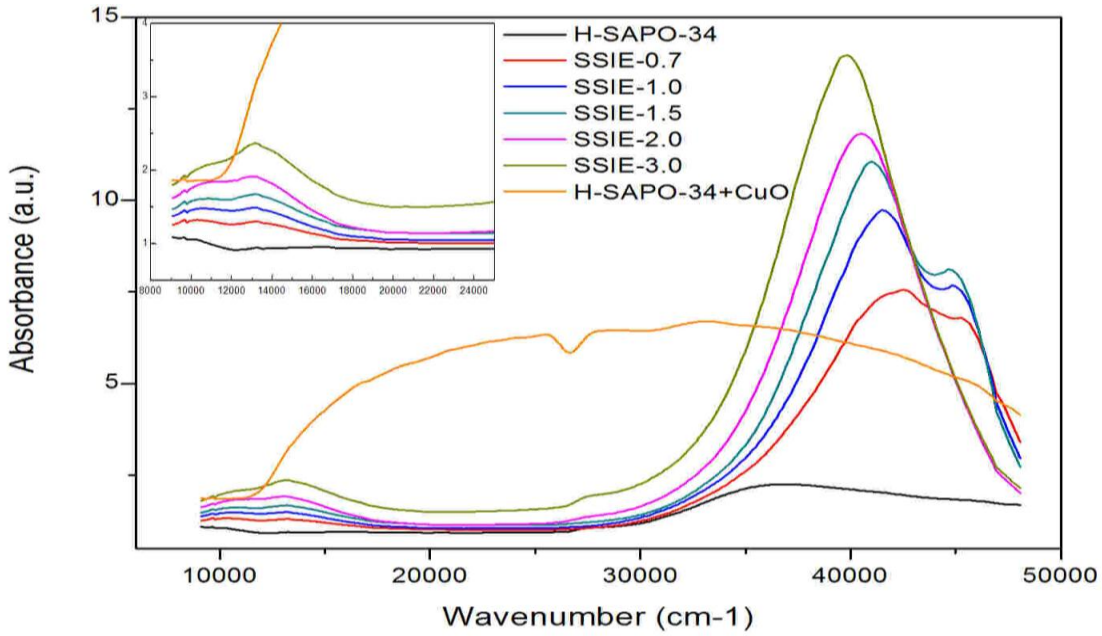

Figure 4.4 UV-vis spectra obtained from the as-prepared Cu-SAPO-34 samples

4.3.2 NH_3-SCR performance

Standard SCR performance tests were conducted on as-prepared samples and the NO and NH_3 conversions at different reaction temperatures are shown in Figures 4.5 and 4.6, respectively. The maximum NO conversion did not exceed 14% over the H-SAPO-34 sample. This is consistent with previous results on H-ZSM-5, H-Beta and H-SSZ-13, where the proton form zeolite is not very active for the standard SCR reaction [62, 131, 132]. In comparison, all the Cu-SAPO-34 samples prepared via SSIE showed significant

NO conversions, indicating that Cu species are essentially responsible for the NH_3-SCR performance.

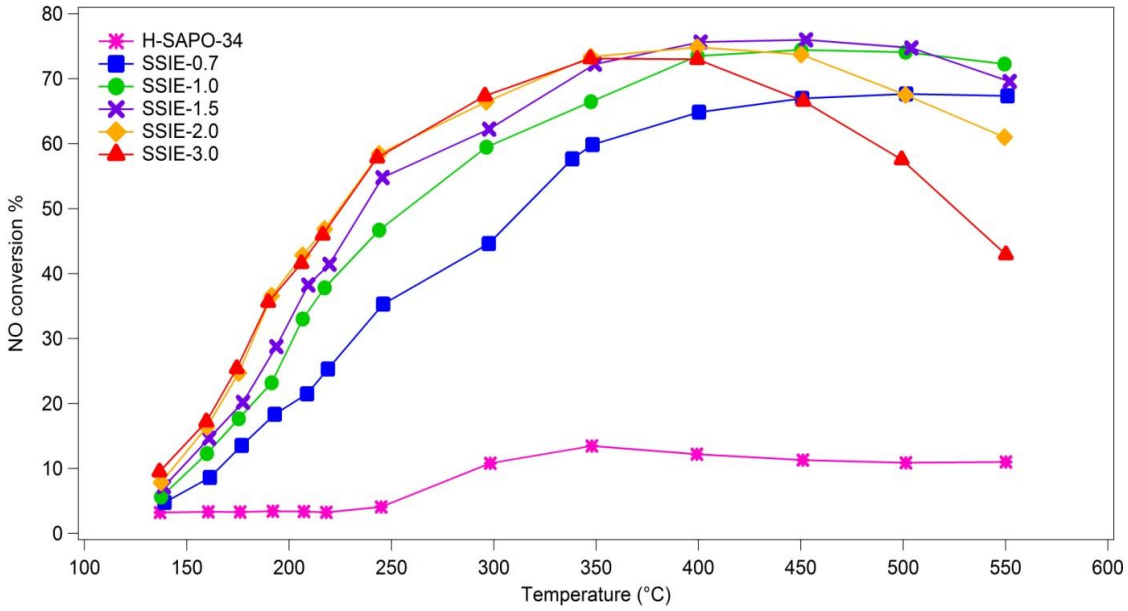

Figure 4.5 NO conversions during the standard SCR reaction over the as-prepared Cu-SAPO-34 samples

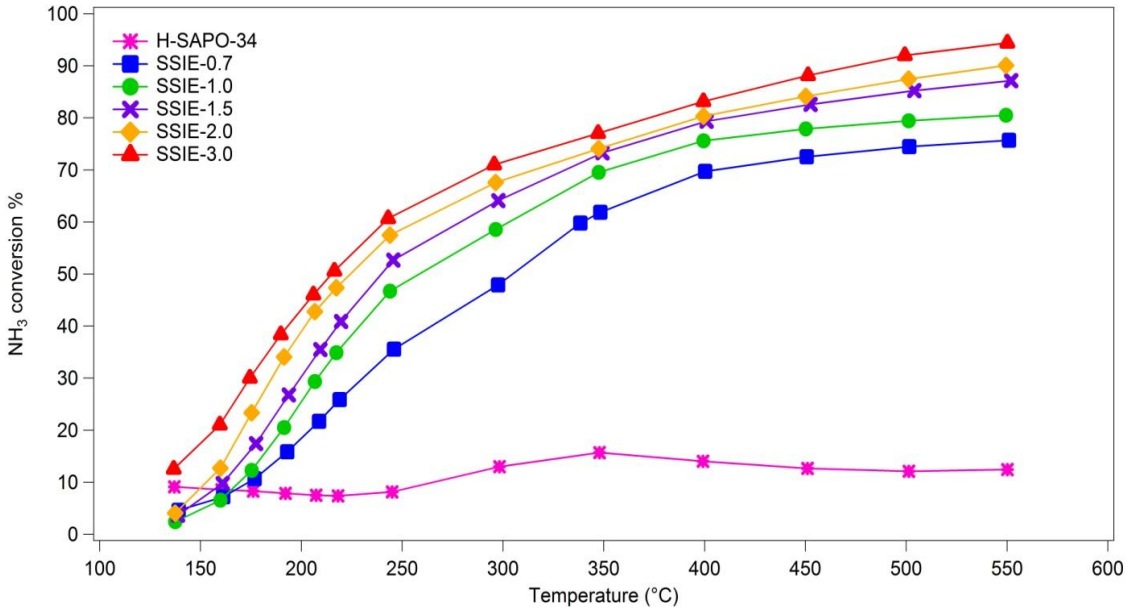

Figure 4.6 NH_3 conversions during the standard SCR reaction over the as-prepared Cu-SAPO-34 samples

Furthermore, it is obvious that the relationship between NO conversion and Cu loading shows distinct trends in two different temperature regions. In the low temperature region (130 - 350°C), both the NO and NH_3 conversions monotonically increased with increasing Cu loading. This strongly suggests that the low temperature SCR performance is mainly affected by the exchanged Cu species. On the other hand, the NO conversion dropped with increasing Cu loading from 1.5% to 3.0% in the high temperature region (350 - 550°C). In order to further investigate the Cu species' impacts on the NO conversion rate, the turnover frequency (TOF) values in a differential region were estimated based on the total amounts of Cu species calculated by ICP.

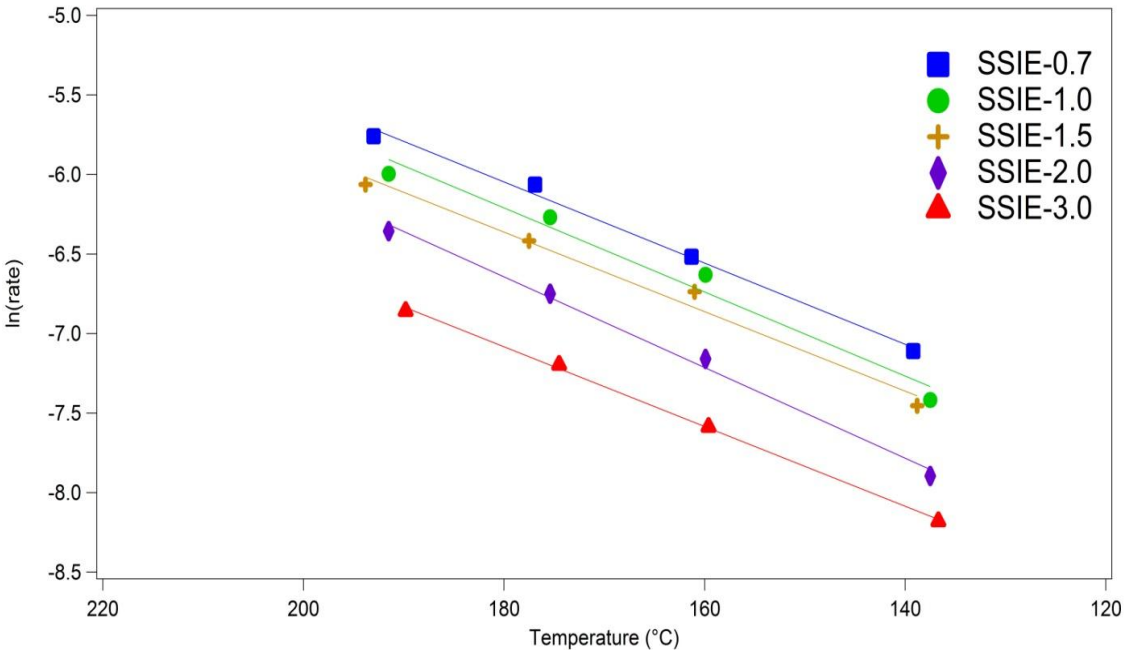

Figure 4.7 Calculated NO reaction rates at different temperatures

As shown in Figure 4.7, the NO reaction rate clearly increased with increasing total Cu amount. This further proves that Cu sites are the active sites for NH_3-SCR on these samples. Additionally, the Arrhenius plots result in parallel slopes, suggesting that the low temperature reaction mechanism did not change with increasing Cu loading and

the NO reaction rate seems to be only affected by the number of Cu sites. In other words, the presence of CuO species on SSIE-2.0 and SSIE-3.0 doesn't seem to change the SCR reaction pathway at low temperature. The apparent activation energies for the samples were estimated to be 41.5 ± 3.7 kJ/mol, which is close to the activation energy on CHA catalysts reported by other groups [66, 72].

4.3.3 Acidity

Zeolite acidity has been reported to influence the SCR activity [98, 99, 133]. In this study, the acid properties of as-prepared samples were studied via NH_3-TPD experiments. NH_3 has been accepted as an efficient probe molecule to characterize zeolite acidity [134-136]. Here, the NH_3-TPD experiments were conducted in both the micro-reactor and DRIFTS reactor to better understand the NH_3 adsorption and desorption features as a function of Cu loading. Figure 4.8 shows the effluent NH_3 profiles during the NH_3-TPD process on each sample.

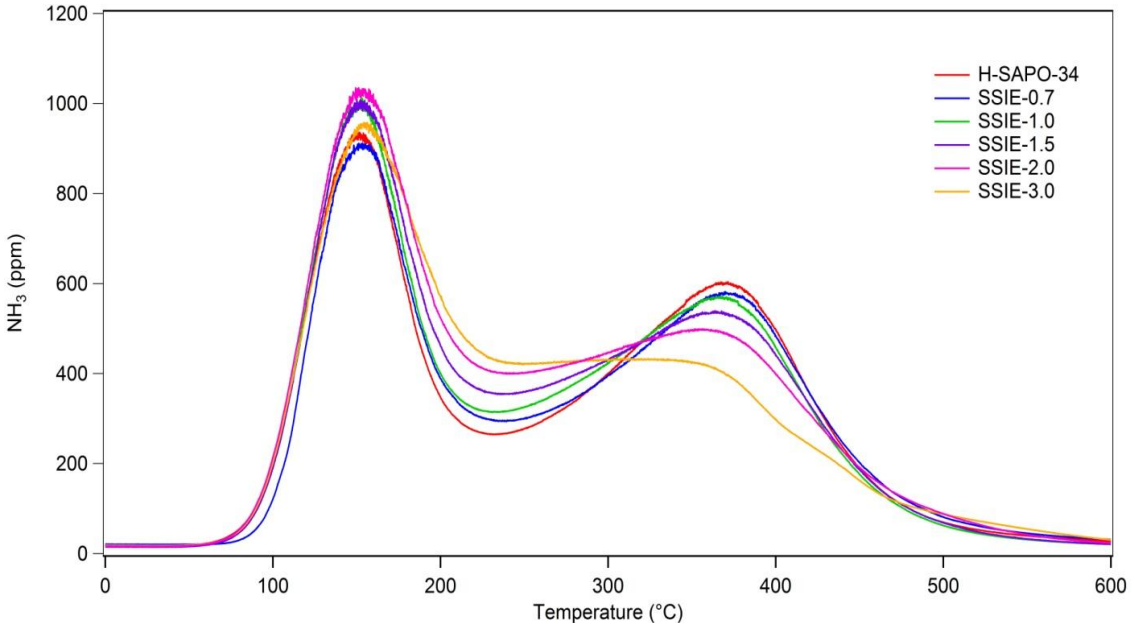

Figure 4.8 Effluent NH_3 profiles during the NH_3-TPD

Three NH_3 desorption peaks were evident in the NH_3-TPD results: a low temperature peak at 150°C, a high temperature peak at 385°C and one in the valley between the low and high temperature peaks, at ~250°C. These NH_3 desorption peaks originate from NH_3 that adsorbed on sites with different acid strengths. However, the assignments of these features are not straightforward. Therefore, the NH_3-TPD was further conducted in DRIFTS reactor in order to better distinguish the sites. The DRIFTS spectra obtained from each sample after 60 minutes of NH_3 exposure, to saturation, at 30°C are shown in Figure 4.9.

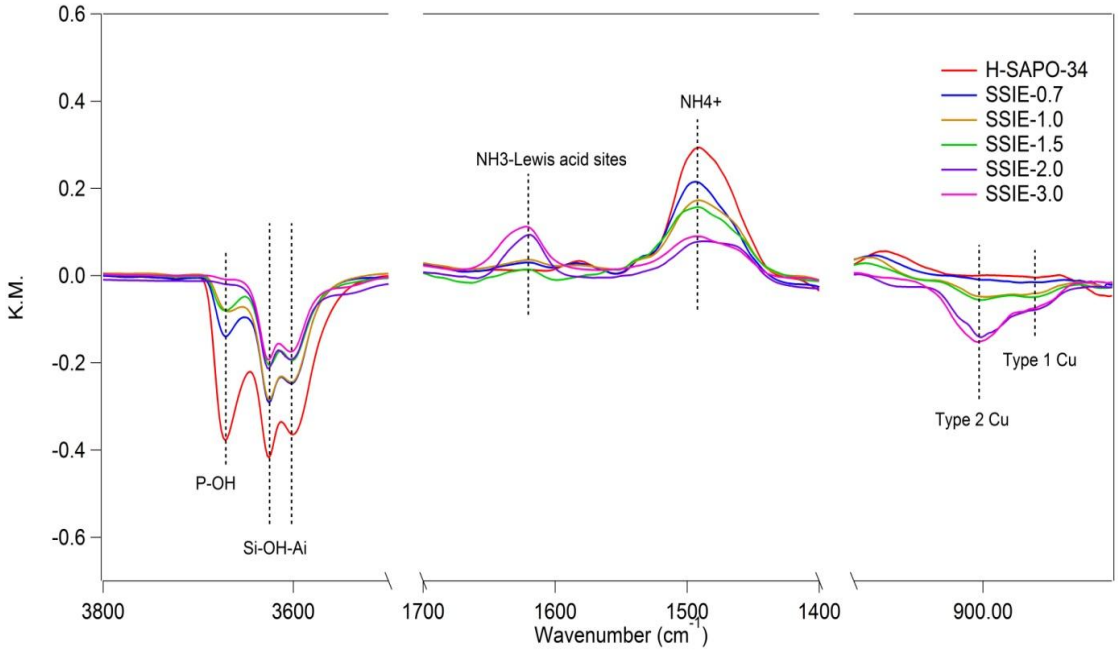

Figure 4.9 DRIFTS spectra after NH_3 adsorption for 60 minutes over H-SAPO-34 and as-prepared samples

Similar to the zeolite framework vibrations, the same hydroxyl group stretching vibration bands were evident upon NH_3 adsorption but with negative intensity. This is because the hydroxyl groups were consumed by NH_3 and therefore reduced the corresponding stretching vibration intensities. As the Cu loading increased, the absolute intensities of the bands corresponding to OH bridging sites generally reduced, indicating

that the number of Brønsted acid sites decreased with increasing Cu loading. On the other hand, two bands at 1617 cm^{-1} and 1460 cm^{-1} were observed. The former is assigned to the molecular NH_3 vibration on Lewis acid sites and the latter one to the asymmetrical vibrations of NH_4^+ ions formed on Brønsted acid sites [61, 97]. From the DRIFTS spectra it is clear that as the Cu loading increased, the number of Lewis acid sites monotonically increased while the number of Brønsted acid sites decreased. Again, the evolution of the two types of acid sites is consistent with the results observed for the zeolite skeleton vibrations, which also showed a reduction in the number of Brønsted acid sites with increasing Cu loading. Overall, more Lewis acid sites were created via Cu occupation of Brønsted acid sites in the pores.

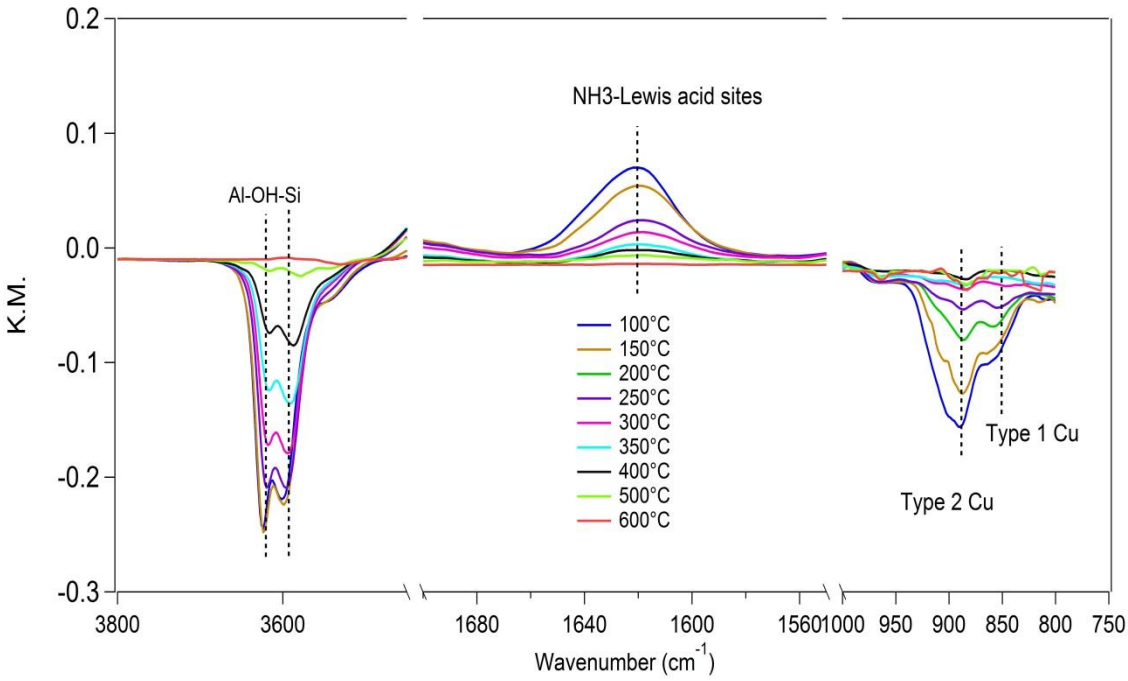

Figure 4.10 DRIFTS spectra taken during the NH_3-TPD with sample SSIE-2.0

DRIFTS spectra during the NH_3-TPD process were also collected (an example obtained with SSIE-2.0 is shown in Figure 4.10). By integrating the DRIFTS peak areas associated with the NH_4^+ and NH_3 bands at different desorption temperatures, the relative

amounts of NH_3 adsorbed on the two types of sites were calculated at the different temperatures. The results are described by Figure 4.11.

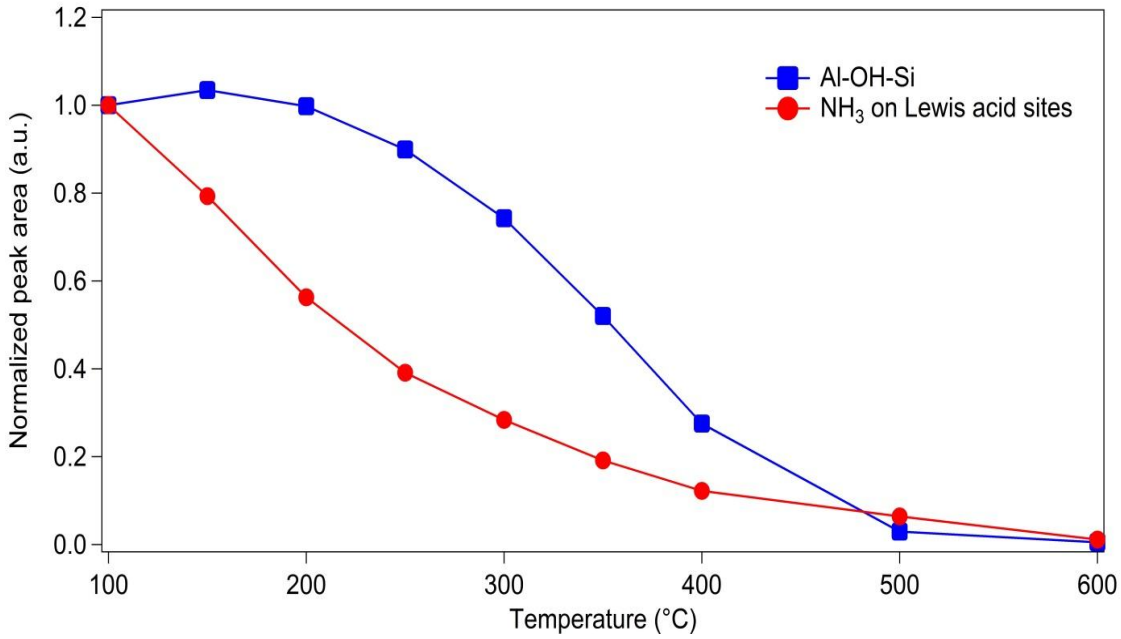

Figure 4.11 Integrated peak areas of Al-OH-Si and NH_3 on Lewis acid sites during the NH_3-TPD over sample SSIE-2.0

Adsorbed NH_3 started to desorb from both acid site types at the onset of the temperature ramp, from 30°C, however, the NH_3 associated with Lewis acid sites decreased more rapidly than the Brønsted acid sites with increasing temperature. For example, 30% of the Brønsted acid sites were still occupied by NH_3 at 400°C, while almost no detectable peak corresponding to NH_3 on Lewis acid sites was present. This indicates that Brønsted acid sites are generally stronger than Lewis acid sites on this catalyst. Based on these data, the low temperature peak at 150°C is due to the weakly adsorbed NH_3, the NH_3 desorption peak at 250°C is associated with the NH_3 adsorbed on Lewis acid sites and the desorption peak at 385°C originated from NH_3 adsorbed on Brønsted acid sites. Furthermore, the NH_3-TPD profile was deconvoluted and the area of each deconvoluted peak was calculated to reflect the amount of different acid sites.

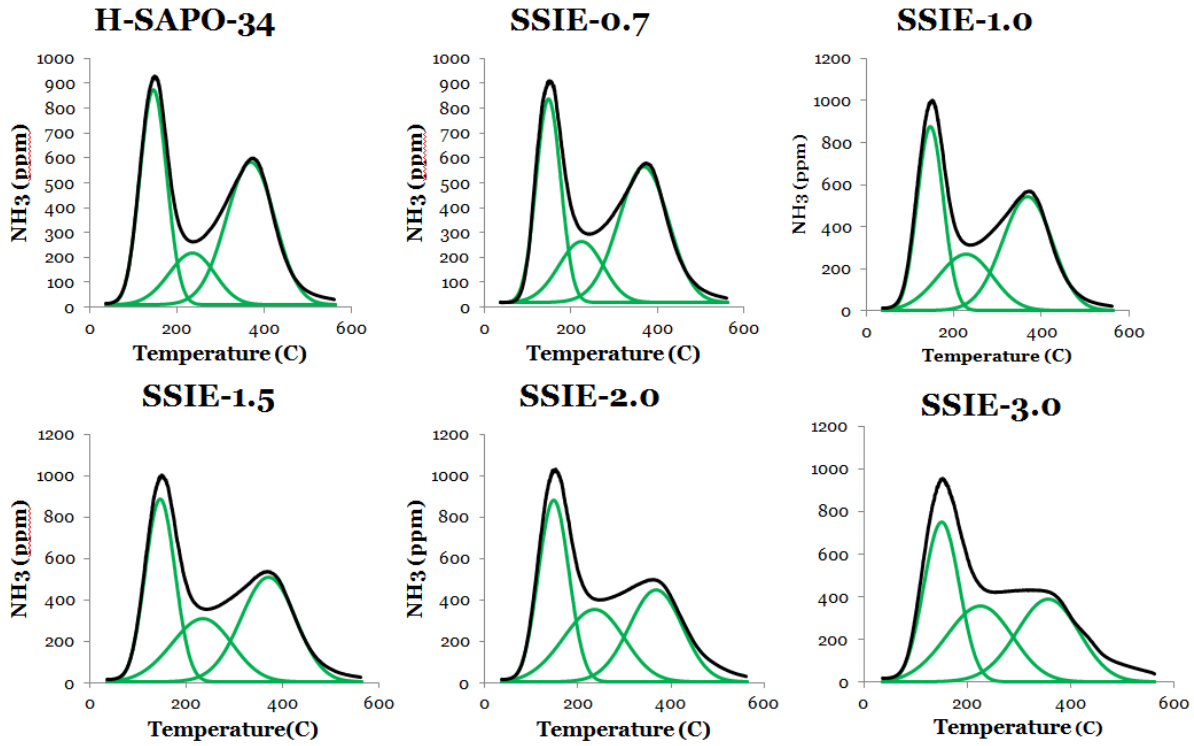

Figure 4.12 Deconvoluted NH_3-TPD

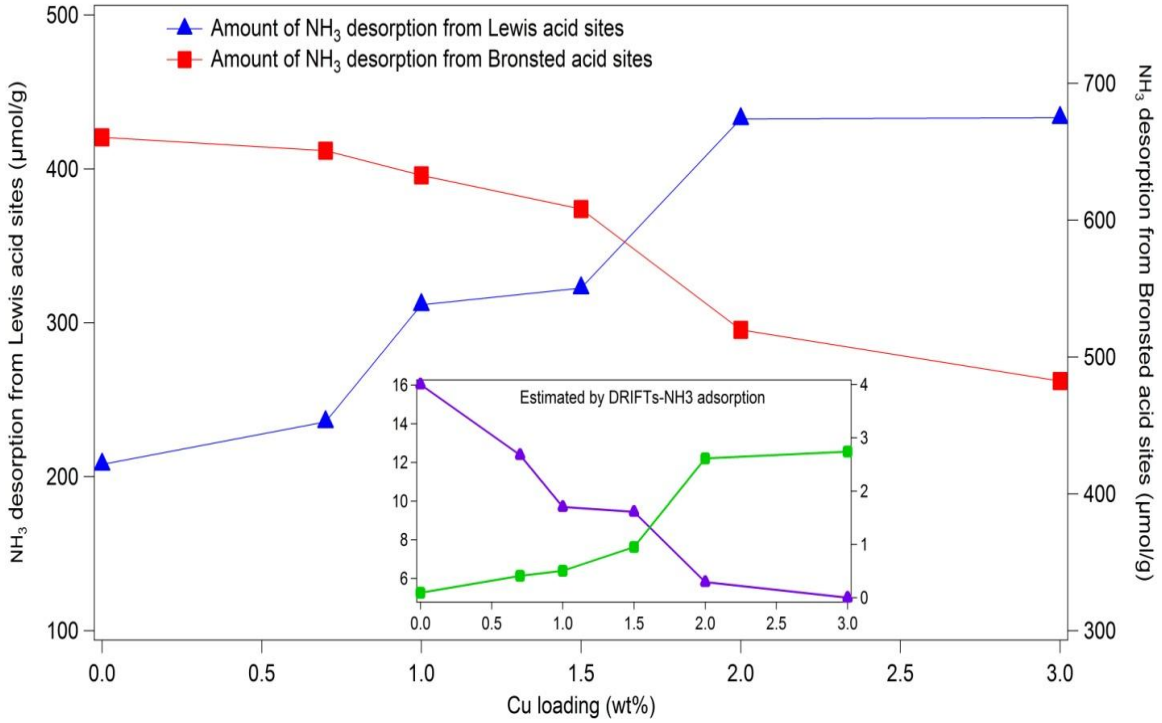

Figure 4.13 The calculated amount of Brønsted acid sites (peak at 385°C) and Lewis acid sites (peak at 250°C) as a function of Cu loading

The deconvoluted NH_3-TPD profiles are shown in Figure 4.12 and Figure 4.13 depicts the calculated amount of Brønsted acid sites (peak at 385°C) and Lewis acid sites (peak at 250°C) as a function of Cu loading. It is clearly shown that the amount of Brønsted acid sites decreased with increasing Cu loading, and at the same time additional Lewis acid sites were created. This is again consistent with the results discussed above (DRIFTS of NH_3 adsorption inset of Figure 4.13). The transformation of the Brønsted acid sites to Lewis acid sites proves the successful replacement of protons by Cu ions during the preparation process, or in other words, the solid state ion exchange process is applicable to preparing Cu-exchanged small pore zeolite. In addition, as we observed in the SCR performance results, the NO conversion at low temperature was elevated due to the inclusion of Cu, in the meanwhile the number of Lewis acid sites increased. This strongly suggests that the Lewis acid sites could play a key role in the SCR activity at low temperature. On the other hand, the Brønsted acid sites may not directly involve in the SCR reaction at low temperature. Interestingly, only a slight increase in the amount of Lewis acid sites was observed for SSIE-3.0 compared with that of sample SSIE-2.0. This could possibly be due to the presence of CuO particles that do not show acid properties. The total NH_3 storage capacities estimated by NH_3-TPD are shown in Figure 4.14. No straightforward relationship between NH_3 storage capacities and low temperature NH_3-SCR activity were found on as-prepared samples. For example, the NH_3 storage dropped from 1581 μmol/g to 1494 μmol/g with increasing Cu loading from 2 wt% to 3 wt%, however, the low temperature NO conversion monotonically increased with increasing the Cu loading.

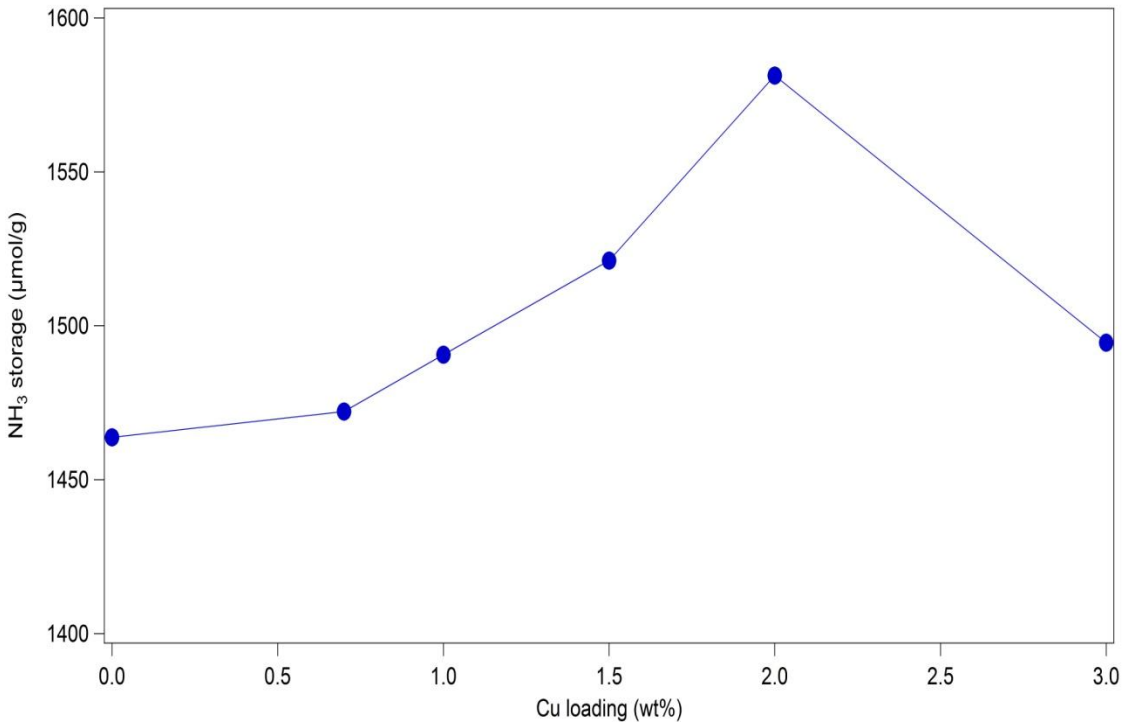

Figure 4.14 Total NH_3 storage capacities as a function of Cu loading over as-prepared Cu-SAPO-34

4.3.4 Cu structures in as-prepared Cu-SAPO-34

As discussed above, two bands were observed in the zeolite skeleton vibration DRIFTS spectra of the as-prepared Cu-SAPO-34 samples and the intensities of both bands monotonically increased with an increase in Cu loading. This indicates that two types of Cu exchanged sites were present in the samples and the amounts increased with increasing Cu loading. Interestingly, DRIFTS bands corresponding to T-O-T vibrations perturbed by two different types of Cu upon NH_3 adsorption (900 and 850 cm^{-1}) were also detected (Figure 4.9). These two bands are negative because the adsorbed NH_3 on exchanged Cu sites deformed the T-O-T vibrations, therefore reducing the band strength. Similar to the features appearing in the skeleton vibrations, the intensities of both

monotonically increased with increased Cu loading, proving that the amounts of two types of exchanged Cu sites increased with increasing Cu loading.

In order to further describe these two types of Cu exchanged sites, DRIFTS spectra were obtained before and after NO exposure. The spectra taken after the samples were saturated with NO at 35°C are shown in Figure 4.15.

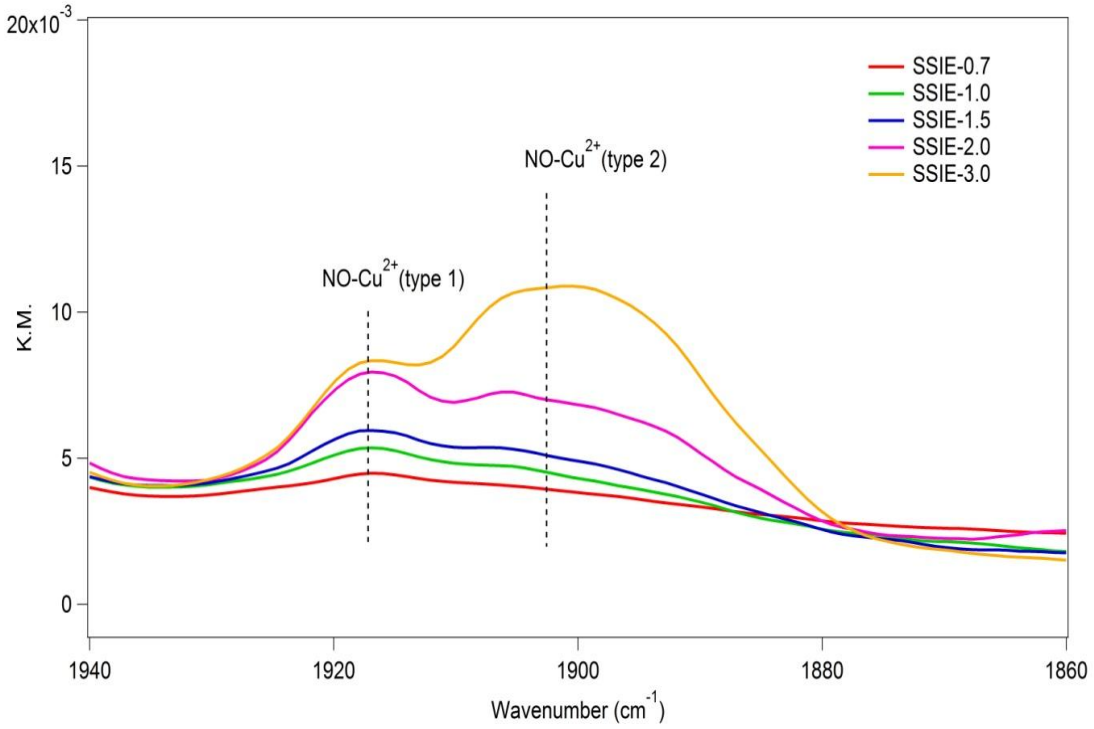

Figure 4.15 DRIFTS spectra upon NO adsorption at 35°C over as-prepared Cu-SAPO-34

Several features were observed, at 2154, 1944, 1916, 1906 and 1575 cm^{-1}. The broad band at 2154 cm^{-1} is assigned to the formation of NO^{+} and the band at 1575 cm^{-1} to the formation of surface nitrate species [83, 87, 91] (this region not shown for brevity). Additionally, the band at 1916 cm^{-1}, which was always accompanied with one at 1944 cm^{-1}, is attributed to the NO adsorbed on one type of Cu^{2+} site (type 1 Cu), while the band at 1906 cm^{-1} indicates another type of Cu^{2+} (type 2 Cu) [56, 111]. It is worthwhile noting that no features corresponding to NO adsorbed on Cu^{+} sites were observed in the

1800-1700 cm^{-1} range. This is seemingly inconsistent with recent findings proposing that both Cu^{2+} and Cu^{+} sites exist on Cu-SSZ-13 and Cu-SAPO-34 catalysts [60, 64]. However, we have to point out that the pretreatment for the NO adsorption experiment in this study was consistently conducted in an O_2 environment; therefore, Cu^{2+} would not be reduced to Cu^{+} under these oxidizing conditions, whereas in the presence of annealing or reducing conditions, a reductant, Cu^{+} sites could indeed form.

Again, both NO and NH_3 adsorption provides evidence that two types of exchanged Cu sites exist in the as-prepared samples and both are able to adsorb NH_3 and NO. In terms of identifications, it is reported that the band positions of T-O-T vibrations are closely related to the energy that stabilizes the exchanged cations by the zeolite framework and in particular, the lower wavenumber band corresponds to a stronger interaction between the exchanged Cu cations and zeolite framework [137, 138]. In addition, Lei et al., observed T-O-T framework vibration bands during flowing O_2, He, CO and NO on Cu-ZSM-5 and they identified these bands to associate with isolated Cu^{+} ions and oxygen bridged Cu dimers Cu-O-Cu [130]. Interestingly, Kwak et al., also suggested that two different Cu ions existed in/on Cu-SSZ-13 via H_2-TPR and DRIFTS measurements, and they proposed that Cu ions primarily exchanged with protons in the six-membered rings at low Cu loading, while at high Cu loading, Cu is also located in the large cages [64]. Both of the bands seem to co-exist on these samples prepared by SSIE, even on the sample with the lowest Cu loading. It is worthwhile mentioning that the referenced SSZ-13 samples were prepared by a liquid ion exchange method, which could explain the differences. The relative amounts of these two Cu sites were calculated by integrating the DRIFTS peak areas associated with the skeleton vibrations and NO

adsorption. As shown in Figure 4.16 (a) and (b), these two Cu sites show distinct evolution trends with the change in Cu loading, as indicated by both skeleton vibration and NO adsorption spectra. Obviously, the Cu structure features in both spectra show very consistent results: type 2 (higher wavenumber) Cu increased almost linearly with increasing Cu loading while the type 1 Cu (lower wavenumber) feature intensity initially also increased relatively linearly, except at the high loadings where only a slight increase was observed between the 2.0 to 3.0 Cu loadings. Also, only a slight increase in the standard SCR performance was observed when the Cu loading was increased from 2.0 wt% to 3.0 wt%. If type 2 Cu is the active site for the NH_3-SCR reaction at low temperature, a more significant improvement in the NO conversion would be expected for SSIE-3.0, however, this was not the case. In addition, it has been widely reported that isolated Cu is the active site for NH_3-SCR on Cu-CHA catalysts [57, 59-61, 72]. Therefore, it is very likely that the type 1 Cu site corresponds to isolated Cu sites and type 2 Cu is associated with larger Cu_xO_y clusters (dimeric or oligomeric Cu species) that seem to have inevitably formed during the solid state ion exchange process. Indeed, a significant fraction of metal oxide complex (dimers and oligomers) could be present in high load Fe and Cu-exchanged zeolite and these sites are active for NO decomposition reaction but do not necessarily contribute to NH_3-SCR [59, 130, 139-141].

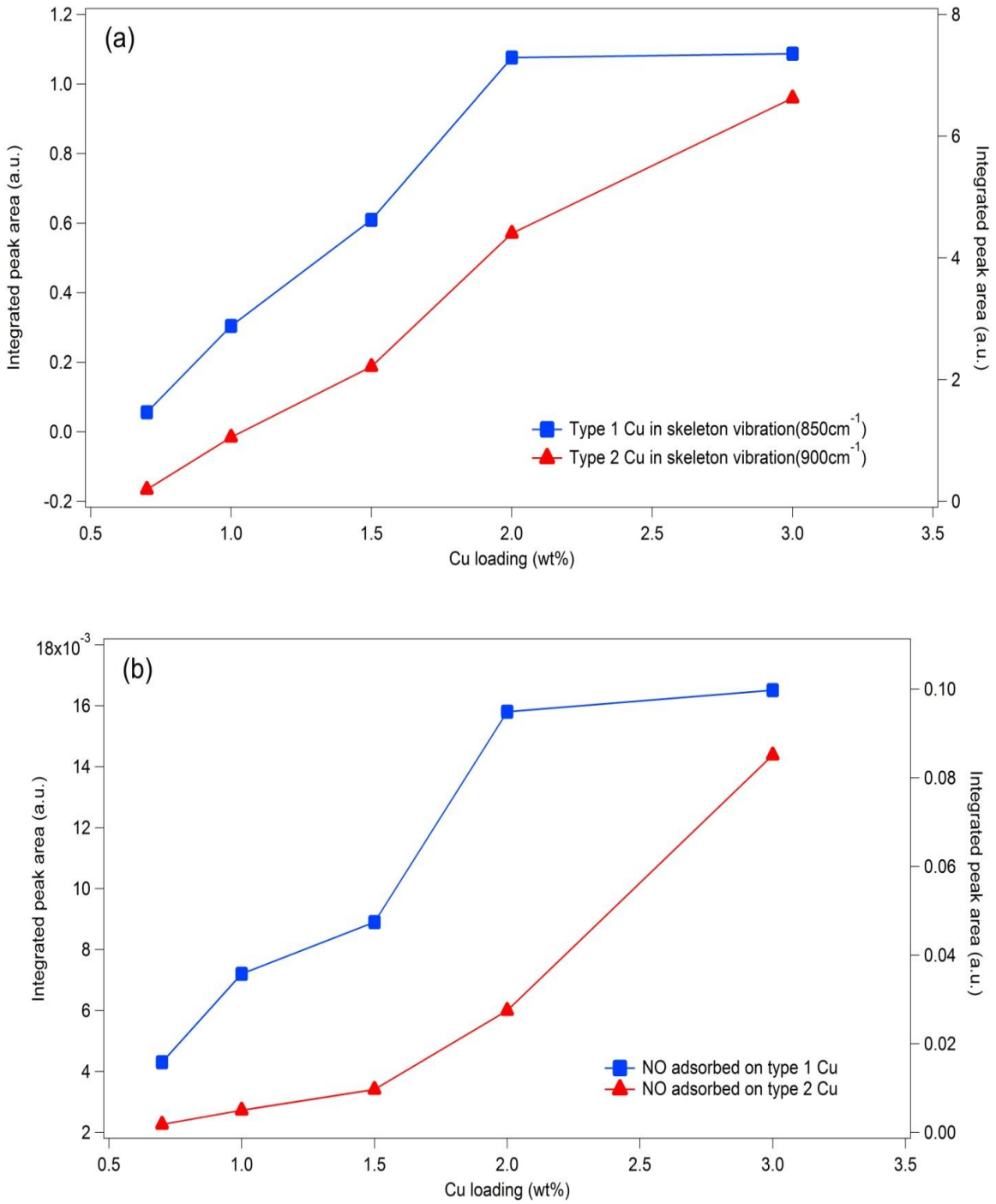

Figure 4.16 Evolution of two types of exchanged Cu sites calculated by integrating the peak areas in: (a) framework vibration DRIFTS spectra; (b) NO adsorption DRIFTS spectra

H_2-TPR was used to quantitatively distinguish the amounts of these two Cu sites for each sample. As shown in Figure 4.17, three main H_2 consumption peaks, at 260, 340

and 375°C, were observed during reduction to 500°C. However, there is no real consensus on the identification of these peaks. For example, Xue et al., [60] observed similar H_2 consumption peaks on Cu-SAPO-34, prepared by a liquid ion exchange method, and they assigned these peaks to be isolated Cu^{2+}, nanosized CuO and reduction of Cu^{+} to Cu^{0}, respectively. However, a H_2-TPR experiment performed on pure nanosized CuO showed that the reduction of CuO took place at much lower temperature, around 250°C. Therefore, it seems reasonable to assign the H_2 consumption peak at around 260°C to CuO particles.

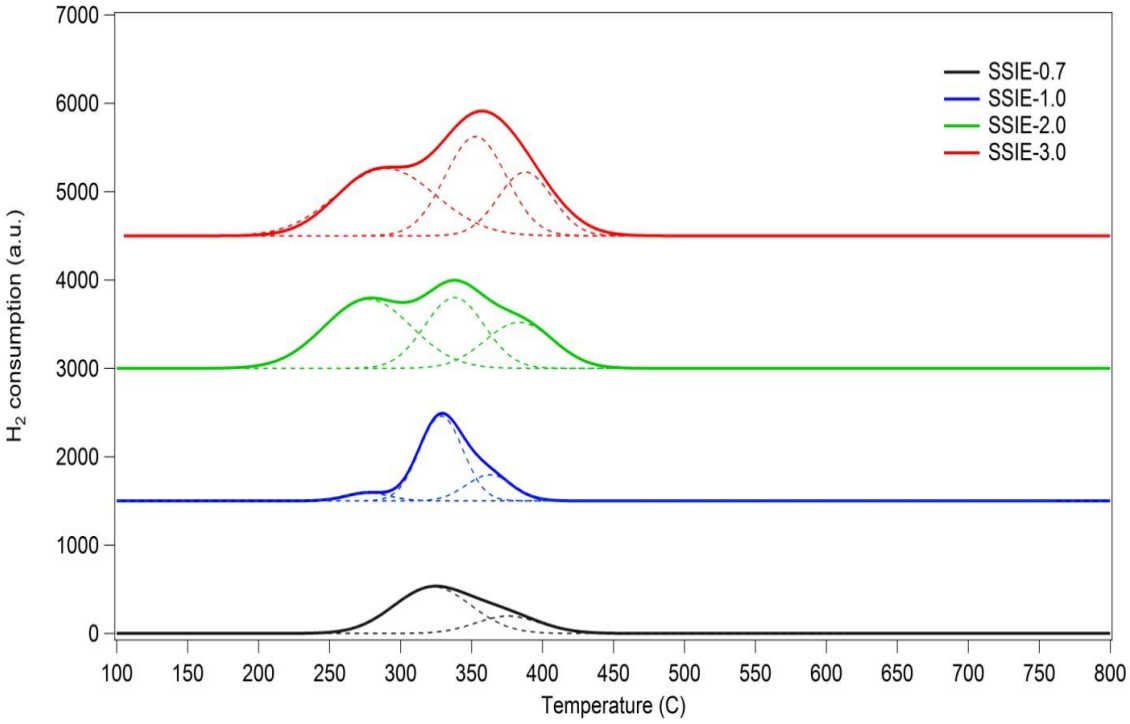

Figure 4.17 H_2 consumption profiles during H_2-TPR

Furthermore, Feng et al., [62] observed a H_2 consumption peak at ~613°C on Cu-SSZ-13 and attributed it to the reduction of Cu^{+} to Cu^{0}. However, no such peak was observed in this study, indicating that the reduction profile for Cu-SAPO-34 may differ from Cu-SSZ-13. It is also worthwhile noticing that the areas of the second peak is larger

than the third peak, which suggests that these peaks may not be caused by the two-step reduction of Cu^{2+} to Cu^{+} and Cu^{+} to Cu^{0}. Kwak et.al., [64] found that Cu-SSZ-13 with a relatively low Cu loading resulted in only a single H_2 consumption peak, while the higher Cu loading sampled showed an additional peak at lower temperature. The authors proposed that the Cu^{2+} species in the six-membered rings are the most stable sites, requiring higher reduction temperature. Based on this hypothesis, the H_2 consumption peak at 375°C is assigned to isolated Cu^{2+} and the peak at 340°C attributed to the Cu_xO_y clusters. Based on these tentative assignments, the amounts of different Cu sites were calculated by quantifying the H_2 consumption and the results are shown in Figure 4.18.

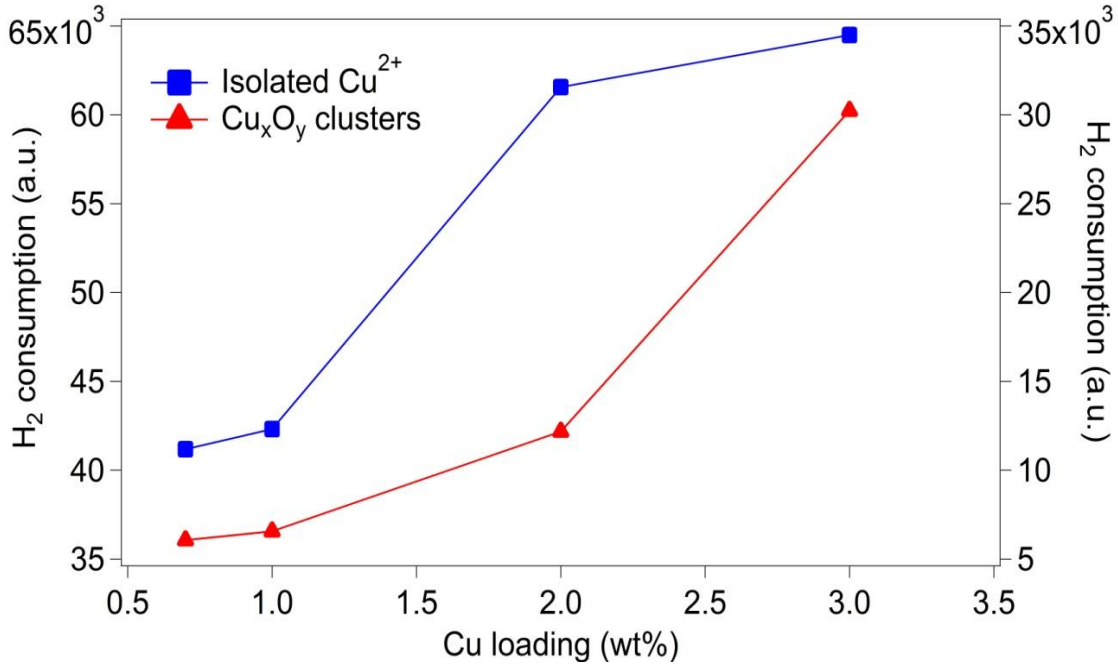

Figure 4.18 Amounts of isolated Cu^{2+} and Cu_xO_y clusters estimated by H_2-TPR

The general evolution of the isolated Cu^{2+} and CuO cluster species are very similar to the trends observed via DRIFTS. For example, the amount of isolated Cu^{2+} only slightly increased with increasing the Cu loading from 2.0% to 3.0% while the Cu cluster sites still significantly increased for SSIE-3.0. In addition, a H_2 consumption peak

at around 900°C was also observed. A similar high temperature peak has previously been assigned to the reduction of Cu^{+} to Cu^{0} on the exchanged sites [62]. However, the same peak was also observed on the H-SAPO-34 sample, i.e., without any Cu species. Furthermore, the sample color remained blue if the H_2-TPR experiment was terminated at 800°C. This suggests that the Cu sites might not have completely reduced to Cu^{0} below 800°C, otherwise the sample should change to dark brown. Therefore, this high temperature H_2 consumption peak could be due to the reduction of Cu^{+} to Cu^{0} and/or the reaction with framework oxygen.

4.3.5 NH_3 oxidation

NH_3 conversion during NH_3 oxidation results are shown in Figure 4.19. NH_3 oxidation is quite active on the as-prepared samples, especially above 400°C. For example, the NH_3 conversion reached as high as 96% on sample SSIE-3.0. NH_3 oxidation activity monotonically increased with the increase in Cu loading.

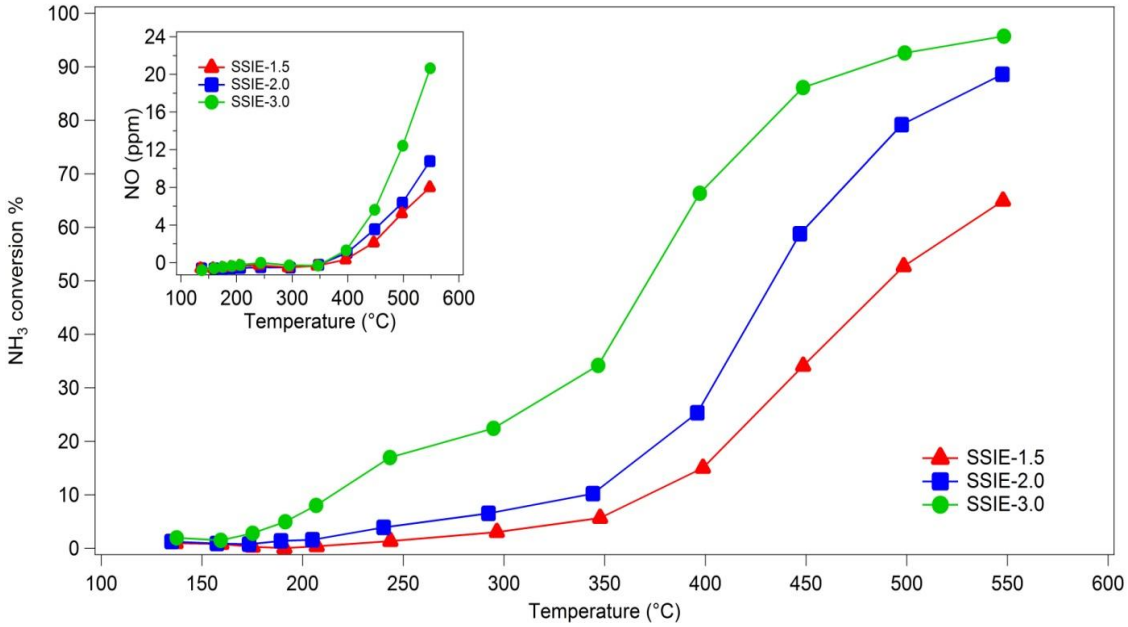

Figure 4.19 NH_3 conversions and NO formation during NH_3 oxidation

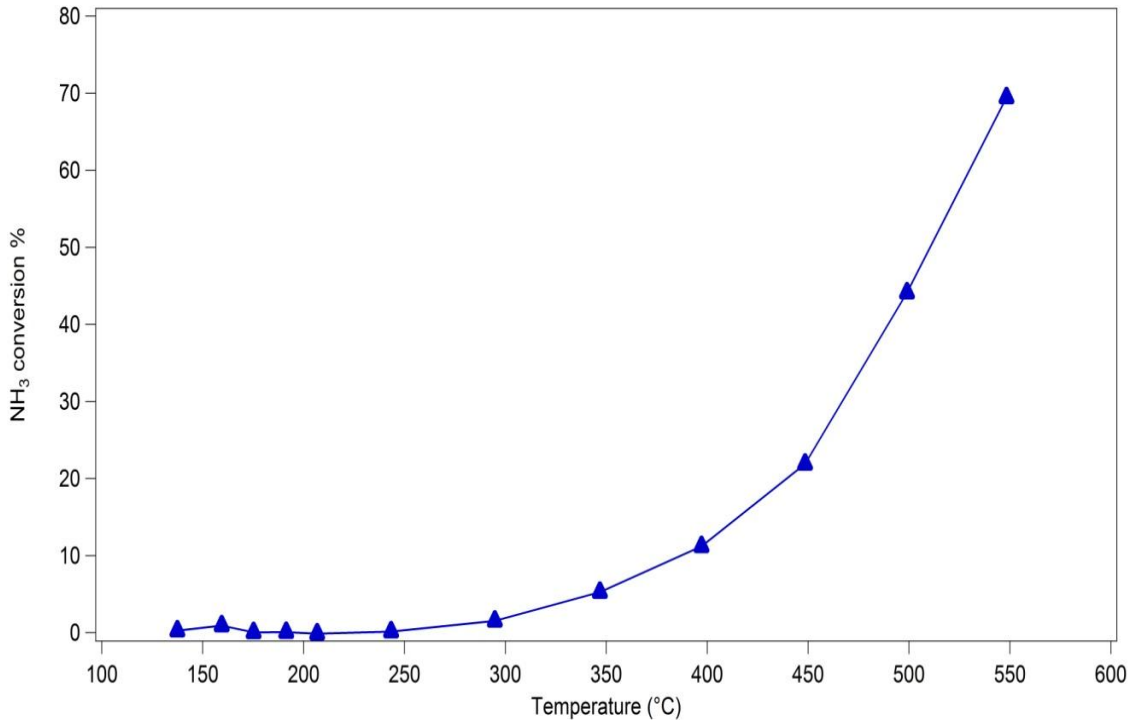

Figure 4.20 NH_3 conversions during NH_3 oxidation over a physical mixture of CuO+H-SAPO-34

As a result, a monotonic increase in the selectivity to NO with increasing Cu loading was also observed at temperatures above 400°C, while below 400°C, all the NH_3 was selectively converted to N_2. In addition, Kwak et al., [142] found that For Cu/γ-Al_2O_3 samples, the CuO particle dispersion plays an important role in NH_3 oxidation activity. They observed decent NH_3 oxidation activity over aggregated CuO/γ-Al_2O_3 while well dispersed CuO showed negligible oxidation performance. Therefore, it is likely that NH_3 oxidation over Cu-SAPO-34 is related to the presence of the Cu_xO_y clusters. Furthermore, a physical mixture of CuO and H-SAPO-34 essentially showed good NH_3 oxidation ability (Figure 4.20). In addition, NH_3 oxidation activity extensively increased with increasing Cu loading from 2 to 3%, which correlates to the evolution in the amount of Cu_xO_y that significantly increased when the Cu loading was increased to 3%. Therefore, it appears that NH_3 oxidation is definitely influenced by the Cu_xO_y

clusters. Furthermore, NO conversion dropped with increasing Cu loading from 1.5% to 3.0% in the high temperature region (350-550°C). Simultaneously, the NH_3 conversion continued to increase with increasing Cu loading. Again, the high temperature standard SCR performance could be significantly inhibited by the competitive NH_3 oxidation which consumes NH_3 and produces undesired NO.

4.4 Conclusions

A series of Cu-SAPO-34 catalyst with various Cu loadings (ranging from 0.7 to 3 wt%) were prepared by a solid state ion exchange method. Different types of Cu structures were observed in the as-prepared samples: isolated Cu^{2+} and Cu_xO_y clusters (dimeric or oligomeric Cu species) and CuO particles. The presence of Cu^{+} sites was primarily determined by the oxidizing/reducing environments. For example, under oxidizing conditions, only Cu^{2+} sites were observed. The amounts of isolated Cu^{2+} and Cu_xO_y clusters increased as the Cu loading increased. However, they showed different trends as a function of Cu loading. The amount of isolated Cu^{2+} continued to increase with increasing Cu loading up to 2.0 wt% and only slightly increased with higher Cu loadings. However, the amount of Cu_xO_y clusters continuously increased with increasing Cu loading. Isolated Cu^{2+} sites were responsible for the NH_3-SCR reaction at low temperature while the Cu_xO_y could catalyze NH_3 oxidation at high temperature.

Chapter 5 Excellent performance in NH_3-SCR over Cu-SSZ-13 catalyst prepared by a solid state ion exchange method

5.1 Introduction

The solid state ion exchange (SSIE) method has been previously applied to obtain Fe-exchanged ZSM-5 for NO_x reduction [143-146]. Different iron sources (e.g., $FeCl_2$, $FeCl_3$ and $FeSO_4$) were also used [143, 147, 148]. However, it was reported that Fe-ZSM-5 prepared by the SSIE method were more active for N_2O decomposition reactions, while less active for NH_3-SCR in comparison to that obtained by WIE [144, 149-151]. In contrast, SSIE has been much less mentioned for the preparation of Cu-exchange zeolite SCR catalysts.

This chapter described a follow-on study to the one detailed in Chapter 4, where a solid state ion exchange method (SSIE) for the synthesis of Cu-SAPO-34 catalysts was developed. In this chapter, the solid state ion-exchange method was further improved and extended to synthesize Cu-SSZ-13 catalysts. By tuning the optimal preparation protocol of the solid state procedure, Cu-SAPO-34 and Cu-SSZ-13 catalysts with highly active SCR performance and excellent hydrothermal stability were prepared. Compared with the conventional wetness ion exchange process, which requires several time-consuming processes such as concentration/pH control, calcination steps, and wash and dry processes, the solid state method is relatively simple and therefore is an alternative to obtain Cu-exchanged small pore zeolite SCR catalysts. In the second part the chapter, the acid properties and Cu structures of Cu-SSZ-13 with different Cu loadings were characterized and compared with those of Cu-SAPO-34 samples.

5.2 Experimental

The method followed to synthesize the Na^+ form of SSZ-13 (Na-SSZ-13) zeolite is described in Ref [45]. The synthesized Na-SSZ-13 material has a Si/Al ratio of 6. The Na-SSZ-13 is transformed into the NH_4^+ form by adding the powder zeolite sample into a 0.1 M NH_4NO_3 solution at 80°C for 8 hours [62]. The solid state ion exchange was conducted in a tube furnace equipped with a continuous flow of air. One gram of the NH_4-SSZ-13 powder sample was first thoroughly mixed with 50 mg of CuO nanosized particles (Sigma Aldrich, <50nm) until the color of the resulting physical mixture became uniformly grey. The physical mixture was loaded in to a quartz boat and placed in a tube furnace followed by heating to either 700 or 800°C in the presence of 350 cm^3/min dry air. The temperature profile followed several ramp and hold procedures. The tube furnace was first heated to 120°C, maintained at that temperature for 4h in order to remove any moisture from the sample and then was ramped to 600°C at 2°C/min and held there for 5 hours to remove the NH_3 from the Brønsted acid sites as well as the residual structural directing agents (SDAs). Subsequently, the temperature was increased to either 700°C or 800°C, at 2°C/min and maintained at that temperature for 16 hours before cooling to room temperature. The resulting samples, with the final thermal treatment at 700 and 800°C, are named as SS-CuSSZ-13(700C) and SS-CuSSZ-13(800C), respectively.

The standard SCR performance tests were performed with a flow containing 500 ppm NO, 500 ppm NH_3, 10% O_2 and 10% H_2O with a balance of N_2 and a corresponding gas hourly space velocity (GHSV) of 240000 h^{-1}. The NH_3 oxidation reaction tests were conducted in a flow containing 500 ppm NH_3, 10% O_2 and 10% H_2O with a balance of

N_2. The total flow rate was 600 cm^3/min. The NO and NH_3 conversions were calculated using the following equations

$$X_{NO} = \frac{C_{NO_{x\,in}} - C_{NO_{x\,out}}}{C_{NO_{in}}} \times 100\% \text{ and} \quad (5.1)$$

$$X_{NH_3} = \frac{C_{NH_{3\,in}} - C_{NH_{3\,out}}}{C_{NH_{3\,in}}} \times 100\%. \quad (5.2)$$

X-ray diffraction (XRD) measurements were performance on a Siemens D5000 Diffractometer equipped with a Cu-Kα detector. The BET surface area and pore volume measurements were carried out in a Micromeritics® ASAP 2020 machine. 200 mg powder form sample was used for each test. The NH_3 temperature programmed desorption (NH_3-TPD) experiments were performed by loading 120 mg of powder catalyst in the quartz tube reactor. The as-prepared samples were first calcined in 10% O_2 in N_2 at 500°C for 1 h followed by decreasing the temperature to 35°C. The NH_3 adsorption process was conducted by introducing 500 ppm NH_3 in 300 cm^3/min total flow onto the catalyst for 2 h. Once the catalyst was saturated, NH_3 was turned off and the catalyst was purged with N_2 only for 2 h. Subsequently, the temperature was increased to 550°C with a 10°C/min. The in-situ DRIFTS experiments were conducted by loading 60 mg powder catalysts into the sample cup of the high temperature reaction chamber. Prior to each test, the catalyst sample was pretreated at 550°C in 10% O_2/He for 1h before cooling to 30°C. NH_3 and NO adsorption experiments were performed by introducing 500 ppm NH_3 or 200 ppm NO onto the samples for 1 h and the spectra were collected by subtracting the background spectra recorded during exposure to pure Helium at 30°C.

5.3 Results and Discussion

5.3.1 Excellent SCR performance of Cu-SSZ-13 prepared by solid state method

The crystallinity of the as-prepared samples was analyzed using X-ray diffraction (XRD), and the data are shown in Figure 5.1. The zeolite frameworks were well maintained after the solid state ion exchange process, as all the diffraction peaks match those in the XRD pattern taken from the H-SSZ-13 reference. In addition, CuO phases were observed at 35.54° and 38.76° in both Cu-containing samples, and these features were also observed in the XRD pattern of the physical mixture of H-SSZ-13 and CuO.

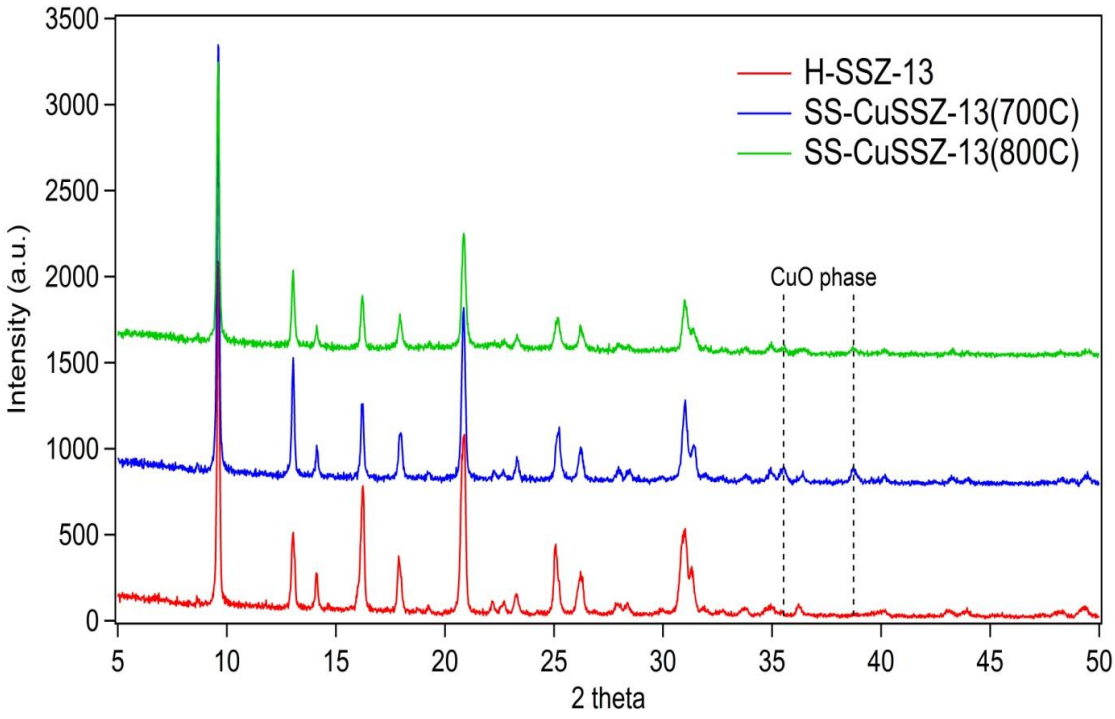

Figure 5.1 XRD patterns of as-prepared Cu-SSZ-13 samples and H-SSZ-13

As listed in Table 5.1, the BET surface area and micro pore volume of the 700°C prepared Cu-exchanged sample are slightly lower than those of H-SSZ-13. However, SS-CuSSZ-13(800C), prepared at 800°C in the solid state ion exchange process, showed

significant drops in both surface area and micro pore volume. This is possibly due to some structural damage of the zeolite framework at this temperature.

Table 5.1 BET surface area and pore volume on as-prepared samples and H-SSZ-13

Samples	Si/Al	Cu loading (wt%)	BET surface area (m^2/g)	Micro pore volume (cm^3/g)
H-SSZ-13	6	0	646.63	0.43
SS-CuSSZ-13(700C)	6	4.10%	529.39	0.45
SS-CuSSZ-13(800C)	6	4.01%	360.79	0.29

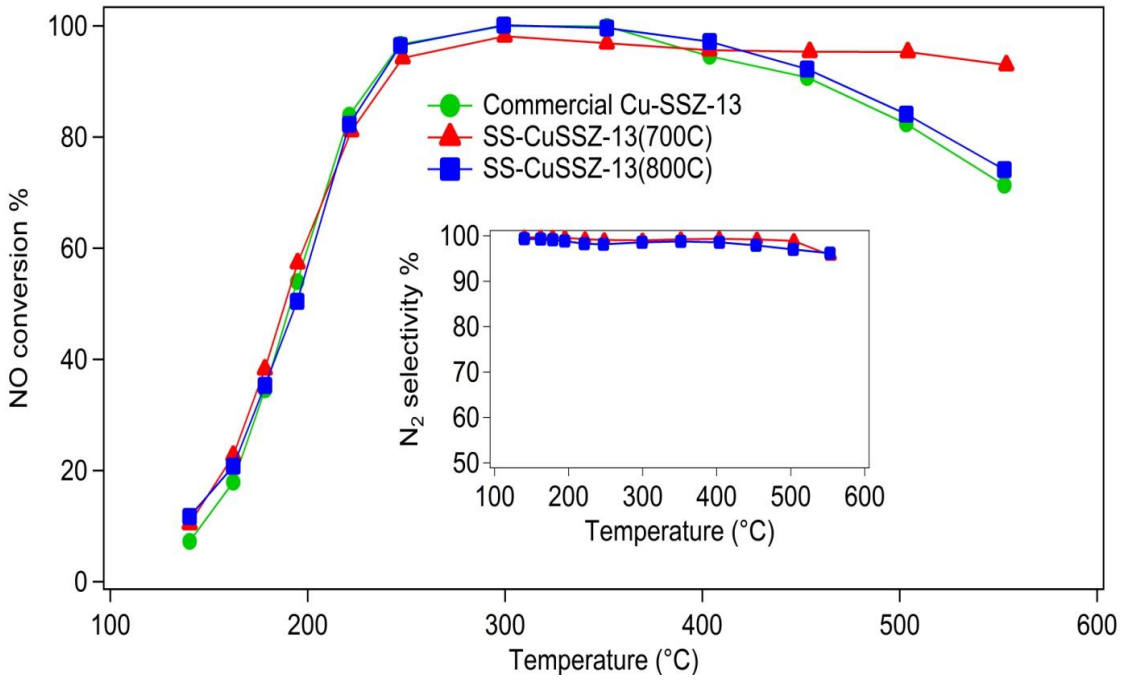

Figure 5.2 Comparison of SCR activities over samples prepared by the solid state exchange method and a commercial catalyst (Reaction conditions: 500 ppm NH_3, 500 ppm NO, 10% H_2O, 10% O_2, balance N_2, GHSV = 240,000 hr^{-1})

Figure 5.2 compares NO_x conversion of the as-prepared solid state ion exchanged Cu-SSZ-13 catalysts with a commercial Cu-SSZ-13 whose details are described in ref [152]. The gas hourly space velocity (GHSV) of these performance tests was 240,000 h^{-1}.

The Cu-SSZ-13 samples prepared via the solid state approach showed very similar SCR activity as compared to the commercial sample. For example, both SS-CuSSZ-13(700C) and SS-CuSSZ-13(800C) achieved above 95% NO conversion between 250 - 450°C. The NO conversions with SS-CuSSZ-13(700C) are even higher than the commercial sample at temperatures above 450°C. In addition, both of the as-prepared samples obtained very high N_2 selectivity (nearly 100%) over the test temperature window. The solid state method proved to produce highly active and selective SCR catalysts.

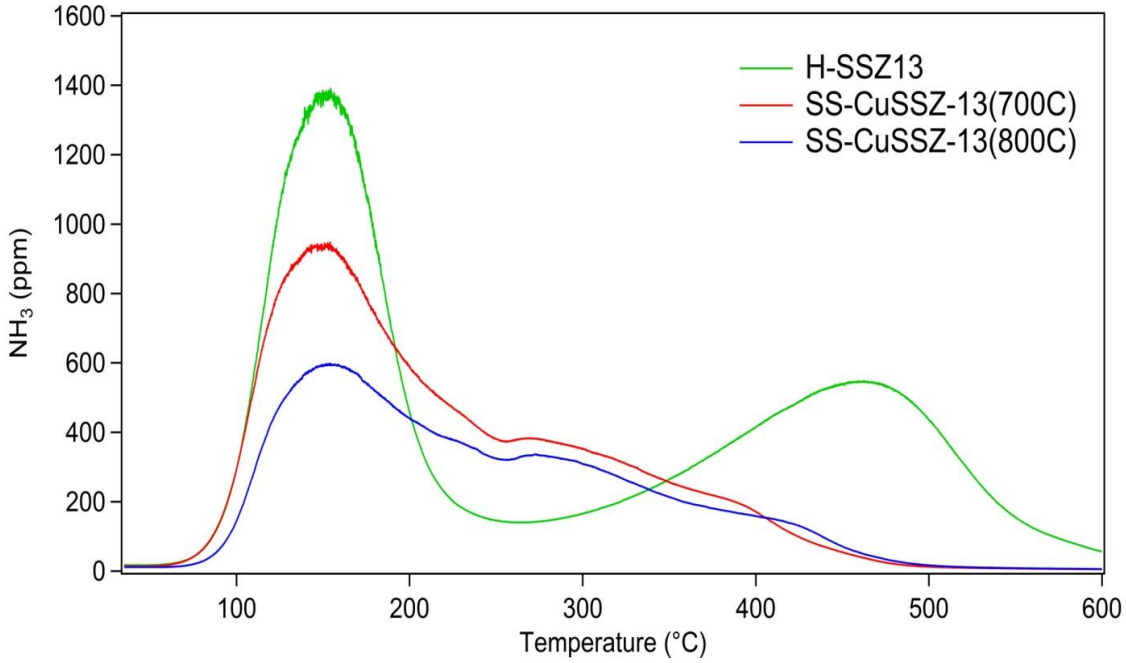

Figure 5.3 NH_3-TPD over as-prepared samples and H-SSZ-13 (experimental conditions: 500 ppm NH_3 adsorption at 35 ^oC for 2h followed by purging by N_2 for 2h, subsequently the temperature was ramped to 550 ^oC with 10^oC/min)

NH_3 temperature programmed desorption (NH_3-TPD) experiments were performed on the as-prepared samples as well as H-SSZ-13 (Figure 5.3). During the TPD, three peaks were observed: a low temperature peak at 150°C, a high temperature peak above 400°C and a smaller feature between these low and high temperature peaks at around 280°C. The low temperature peak at 150°C is assigned to weakly adsorbed NH_3

such as physisorbed NH_3 and NH_3 adsorbed on weak Lewis acid sites. The desorption at 280°C and the high temperature peak above 400°C are associated with NH_3 adsorbed on Lewis acid sites and Brønsted acid sites, respectively. Compared with the H-SSZ-13 sample, the total number of Lewis acid sites was greater, due to the inclusion of Cu ions, while the amount of Brønsted acid sites was significantly reduced. This provides strong evidence that the Brønsted acid sites were indeed replaced by Cu during the solid state ion exchange process.

In order to further confirm Cu ion exchange, NH_3 adsorption experiments were conducted in a DRIFTS reactor. As shown in Figure 5.4, negative bands at 3733, 3660, 3612 and 3585 cm^{-1} were observed. The bands at 3733 and 3660 cm^{-1} are assigned to NH_3 adsorbed on the external Si-OH and Al-OH groups, respectively [153]. The bands at 3612 and 3585 cm^{-1} correspond to the stretching vibrations of the Al-OH-Si groups, which are the signatures of the Brønsted acid sites on zeolite materials [153-155]. The intensities of these two bands were weaker on the Cu-containing samples in comparison to H-SSZ-13, indicating that the amounts of Brønsted acid sites were decreased after Cu exchange. In other words, the solid state ion exchange did lead to Cu ions replacing the protons on the Brønsted acid sites, and therefore weakened the OH stretching vibration intensities. On the other hand, a negative band was detected around 900 cm^{-1}, which was accompanied by a weak shoulder at 940 cm^{-1}. The peaks in this region are assigned to the tetrahedral cation-oxygen-tetrahedral cation (T-O-T) framework vibrations that were perturbed by ion exchanged copper species [64]. These bands are negative due to the restored T-O-T vibrations due to NH_3 adsorption on the Cu sites, again confirming the reaction of CuO with Brønsted acid protons to form exchanged Cu sites according to

$$2ZO\text{-}H + CuO \rightarrow ZO\text{-}Cu\text{-}OZ + H_2O, \quad (5.3)$$

where ZO^- and ZO-H represent the zeolite lattice and Brønsted acid protons, respectively. It is worth mentioning here that the peak at 900 cm^{-1} was significantly more intense than that at 940 cm^{-1}. It has been reported that the IR band at 900 cm^{-1} corresponds to isolated Cu^{2+} sites located in the six-membered ring in the Chabazite framework and the 940cm^{-1} band results from a different type and/or location of Cu site [64]. Therefore, it is apparent that isolated Cu^{2+} sites were selectively formed in the as-prepared samples, which could explain the excellent NO conversion on the samples prepared.

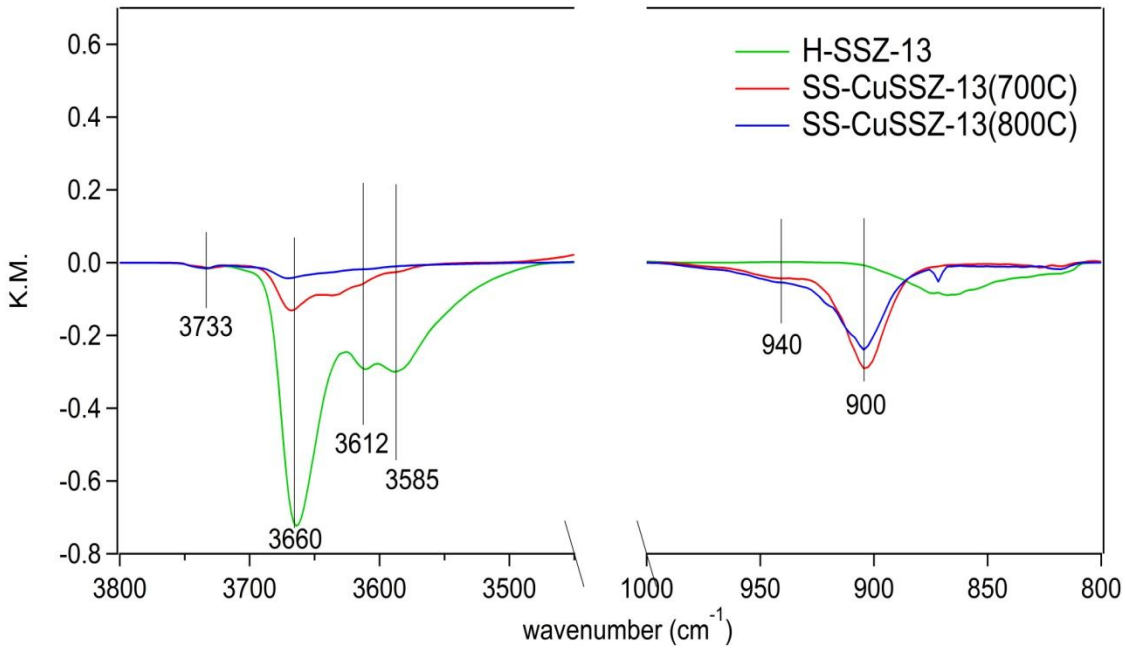

Figure 5.4 DRIFTS spectra taken over NH_3 saturated as-prepared samples and H-SSZ-13 (experimental conditions: sample exposed to 500 ppm NH_3 in He at 30°C for 60 minutes, total flow was 50 cm^3/min)

At high temperatures NH_3 oxidation with oxygen leads to lower NO_x conversion [156]. Therefore, the drop in NO conversion at high temperature on sample SS-CuSSZ-13(800C) is very likely caused by an increase in the competitive NH_3 oxidation reaction.

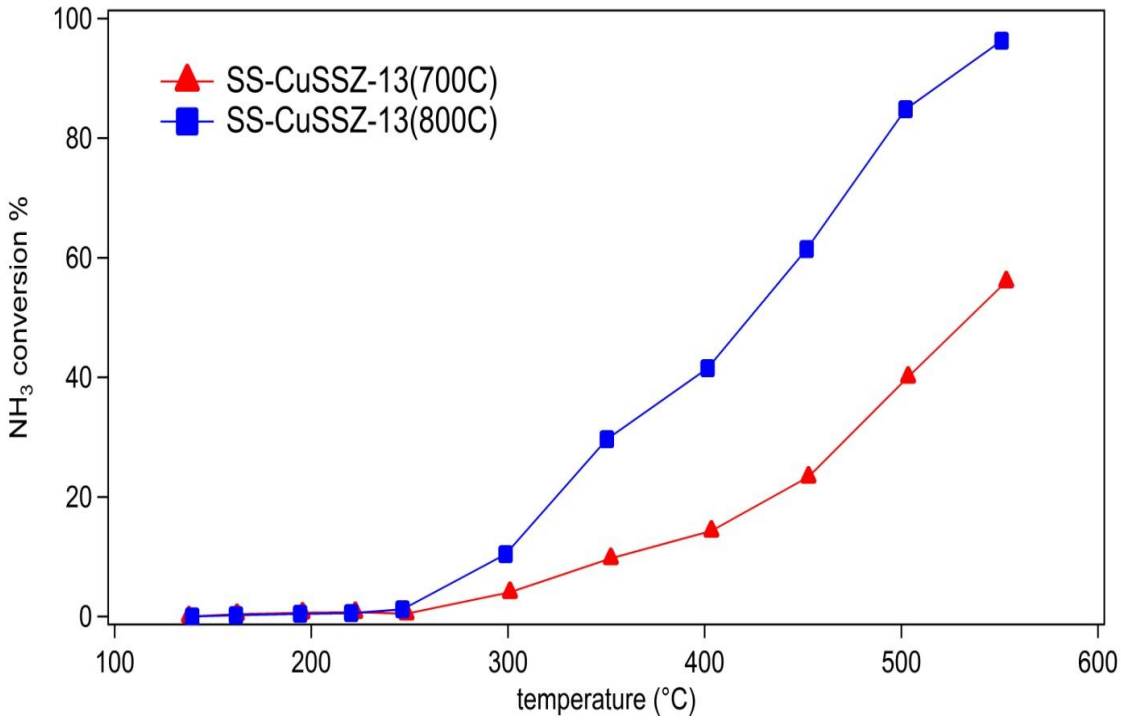

Figure 5.5 NH_3 conversions in NH_3 oxidation reaction on as-prepared samples (reaction conditions: 500 ppm NH_3, 10% H_2O, 10% O_2, balance N_2, GHSV = 240,000 hr^{-1})

To verify, NH_3 oxidation experiments were performed on the as-prepared samples and, as shown in Figure 5.5, the NH_3 conversion was much higher on SS-CuSSZ-13(800C), as compared to sample SS-CuSSZ-13(700C). For example, the NH_3 conversion reached 96% at 550°C over SS-CuSSZ-13(800C) while it only reached 56% over SS-CuSSZ-13(700C) at the same reaction temperature. This implies that some of the Cu may have aggregated during the 800°C thermal treatment of the synthesis, relative to the amount at 700°C. The NO production rates were also calculated in order to clearly compare the selectivity of NH_3 oxidation on the two samples. In particular, the NO production rates at temperature below 450°C were nil for both samples, indicating that a high N_2 selectivity was achieved in NH_3 oxidation. In addition, the NO production rates of SS-CuSSZ-13(700C) at 450°C, 500°C and 550°C are 4.38×10^{-6}, 2.51×10^{-5} and

$5.34x10^{-5}$ (mol NO*mol Cu^{-1}*s^{-1}), respectively. In comparison, the NO production rates on SS-CuSSZ-13(800C) 450°C, 500°C and 550°C are $8.84x10^{-6}$, $4.18x10^{-6}$ and $1.44x10^{-4}$ (mol NO*mol Cu^{-1}*s^{-1}), respectively. Therefore, the selectivity to NO indeed increased with the higher temperature condition. This is consistent with other findings, where aggregation of CuO species was observed on Cu-SAPO-34 and Cu-SSZ-13 catalysts after a high temperature treatment [46, 63]. It seems that more CuO aggregates were generated on SS-CuSSZ-13(800C), which enhanced the unselective NH_3 oxidation reaction [142].

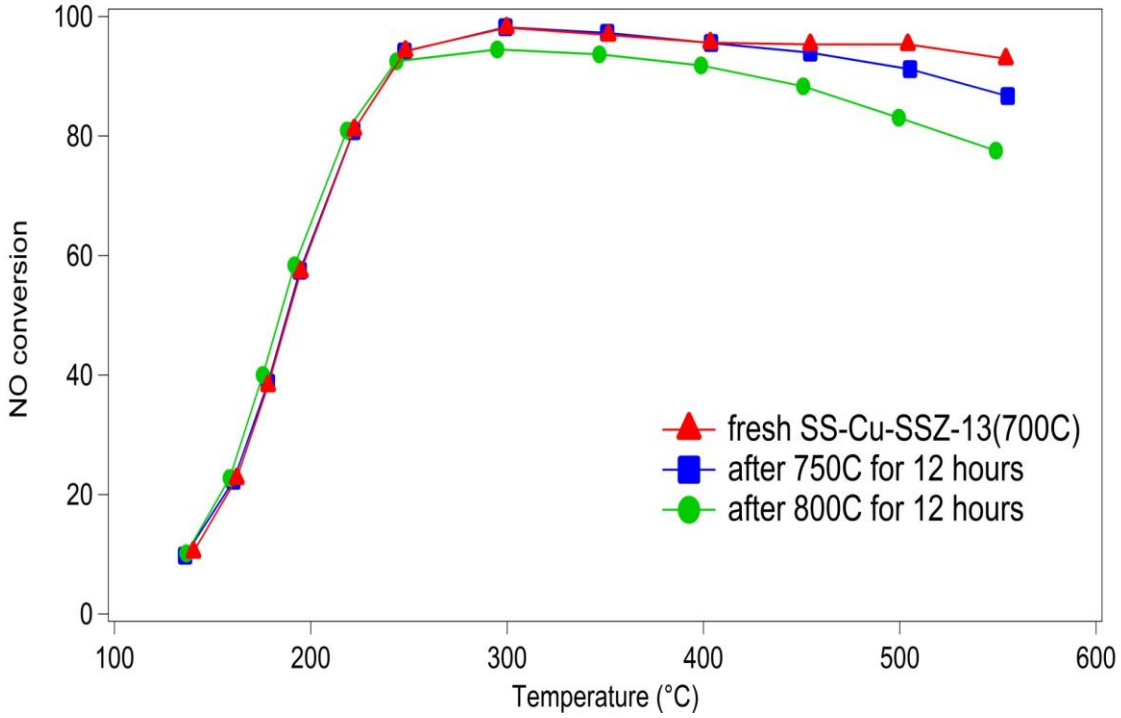

Figure 5.6 NO conversions in standard SCR reaction on as-prepared samples under different thermal treatment (Thermal treatment conditions: 20% O_2, and balance N_2 in 300 cm^3/min total flow)

In order to further confirm the evolution of CuO during the high temperature treatment of the solid state process, a fresh SS-Cu-SSZ-13(700C) sample was thermally treated in 20% O_2 without H_2O at 750°C and 800°C for 12 h, and was then characterized. NO conversions under standard SCR reaction conditions at different temperatures are

shown in Figure 5.6. After a high temperature treatment at 750°C, the NO conversions at temperatures lower than 400°C were maintained while the NO conversions dropped slightly at temperatures above 400°C. When the sample was further treated at 800°C for 12h, the NO conversions at temperatures higher than 250°C continued to decrease, however, the low temperature SCR activity was retained. It appears that the high temperature treatment, in dry conditions, did not change the nature or number of isolated Cu^{2+} sites, which are responsible for the low temperature activity.

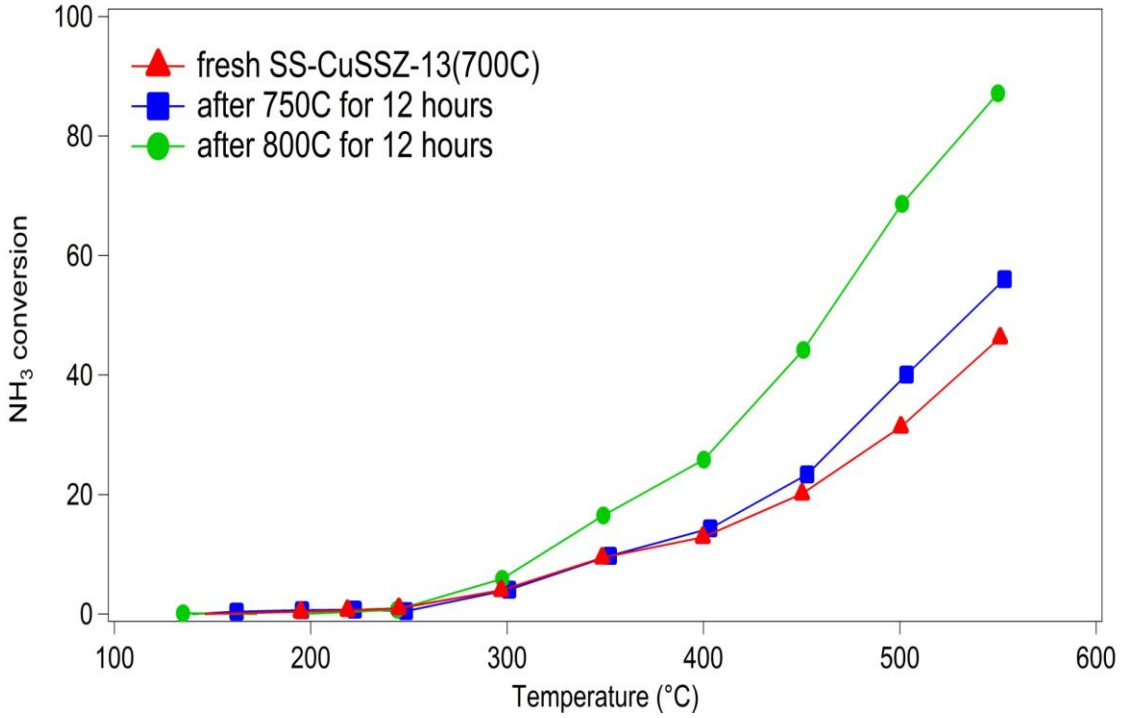

Figure 5.7 NH_3 conversions in NH_3 oxidation on as-prepared samples under different thermal treatment (Thermal treatment conditions: 20% O_2, and balance N_2 in 300 cm^3/min total flow)

The decrease in high temperature activity is believed to be due to the non-selective NH_3 oxidation reaction. Indeed, the NH_3 oxidation activity showed an increasing tread with increasing thermal aging temperature from 750°C to 800°C, as described in Figure 5.7. This evolution coincides with the observation that CuO particles

aggregated during the high temperature thermal treatment. As a result, the NH_3 oxidation activity was promoted and the high temperature SCR activity dropped.

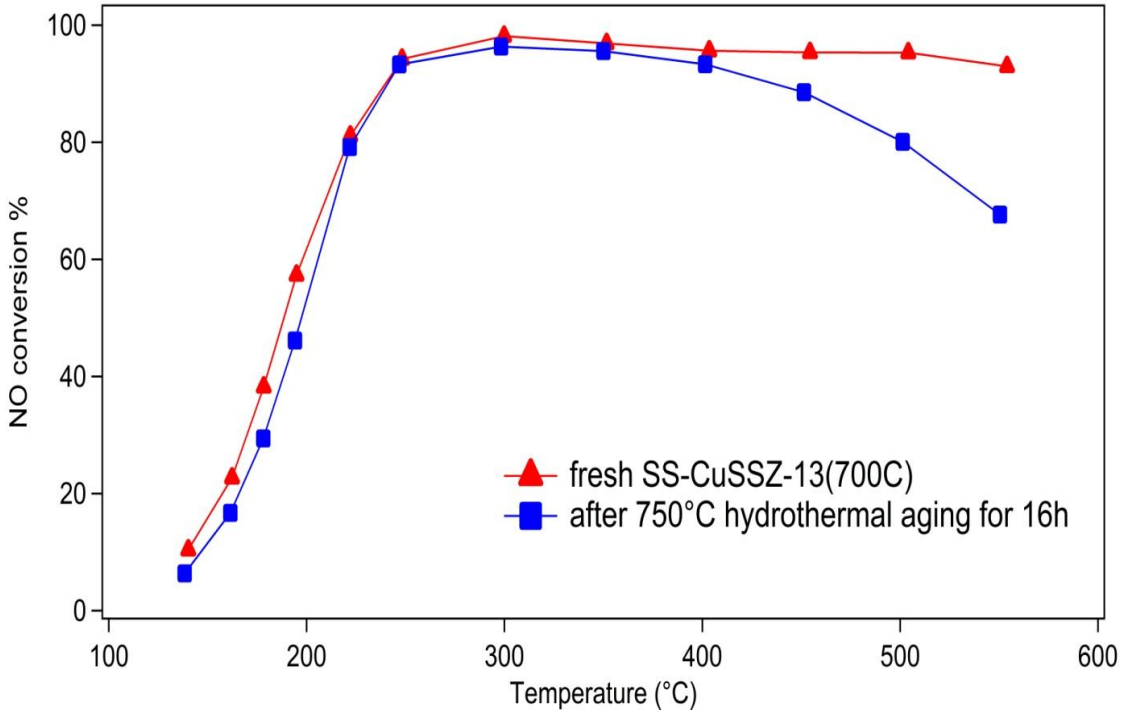

Figure 5.8 SCR performances performed over sample SS-CuSSZ-13(700C) before and after 750°C hydrothermal aging for 16h (aging conditions: 10% H_2O, 10% O_2, balance N_2, GHSV = 240,000 hr^{-1})

The hydrothermal stability of the as-prepared samples are estimated by treating the catalyst at 750°C for 16 hours in flowing 10% H_2O + 10% O_2 in a balance of N_2. As shown in Figure 5.8, after the 750°C hydrothermal aging, the low temperature SCR activity was maintained. Simultaneously, the NO conversions at temperatures above 400°C were decreased. Again, the drop of the NO conversions at high temperature is likely due to the formation of aggregated CuO that leads to higher competitive NH_3 oxidation reaction rates. Therefore, the overall hydrothermal stability of the Cu-SSZ-13 sample prepared by the solid state is promising.

5.3.2 Characterizations of Cu structure in Cu-SSZ-13

In order to study Cu structure changes as a function of Cu loading, a series of Cu-SSZ-13 samples with different Cu loadings were prepared, using the same solid state procedure at 700°C that was described at the beginning of this chapter. The estimated Cu loadings are 1.7 wt%, 2.2 wt% and 4.1 wt%, respectively, according to ICP analysis. These samples are named SS-SSZ-1.0, SS-SSZ-1.7, SS-SSZ-2.2 and SS-SSZ-4.1 in this section. The surface areas and pore volumes of the as-prepared samples are listed in Table 5.2. For example, the measured surface area and pore volume of sample SS-SSZ-1.0 were 602 m^2/g and 0.41 cm^3/g, respectively. This turned out to be slightly lower than those of the H-SSZ-13 sample. As the Cu loading increased, the BET surface area of the samples generally decreased, however, most of the surface areas and pore volumes were maintained after the high temperature treatment associated with the solid state procedure.

Standard SCR performance tests were conducted and the NO conversions at different temperatures are shown in Figure 5.9. At temperatures lower than 400°C, NO conversions monotonically increased with increasing Cu loading. This result is consistent with SCR performance tests conducted with the Cu-SAPO-34 samples that were discussed in Chapter 4. Again, the low temperature SCR activity is mainly affected by the exchanged Cu species. On the other hand, the NO conversions at temperatures above 400°C were all quite high, almost 95% for all the samples. This differs from what was observed with Cu-SAPO-34, where the NO conversion dropped in the same temperature range with increasing Cu loading from 1.5 wt% to 3.0 wt%.

Table 5.2 BET surface area and pore volume measurement on as-prepared samples with different Cu loading

Sample	Si/Al	Cu loading (wt%)	BET surface area (m^2/g)	Micropore volume (cm^3/g)
SS-SSZ-1.0	6	1.0%	602	0.41
SS-SSZ-1.7	6	1.7%	547	0.38
SS-SSZ-2.2	6	2.2%	591	0.40
SS-SSZ-4.1	6	4.1%	529	0.45

Standard SCR performance tests were conducted and the NO conversions at different temperatures are shown in Figure 5.9. At temperatures lower than 400°C, NO conversions monotonically increased with increasing Cu loading. This result is consistent with SCR performance tests conducted with the Cu-SAPO-34 samples that was discussed in Chapter 4. Again, the low temperature SCR activity is mainly affected by the exchanged Cu species. On the other hand, the NO conversions at temperatures above 400°C were all quite high, almost 95% for all the samples. This differs from what was observed with Cu-SAPO-34, where the NO conversion dropped in the same temperature range with increasing Cu loading from 1.5 wt% to 3.0 wt%.

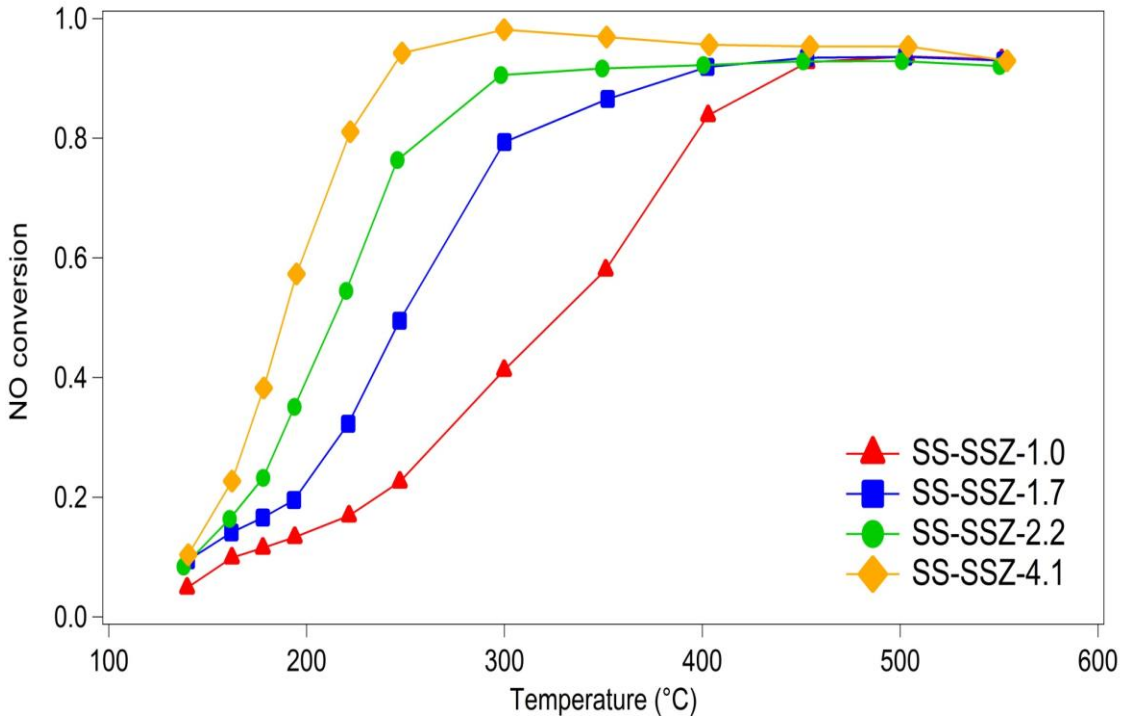

Figure 5.9 Comparison of SCR activities over as-prepared samples with different Cu loading (Reaction conditions: 500 ppm NH_3, 500 ppm NO, 10% H_2O, 10% O_2, balance N_2, GHSV = 240,000 hr^{-1})

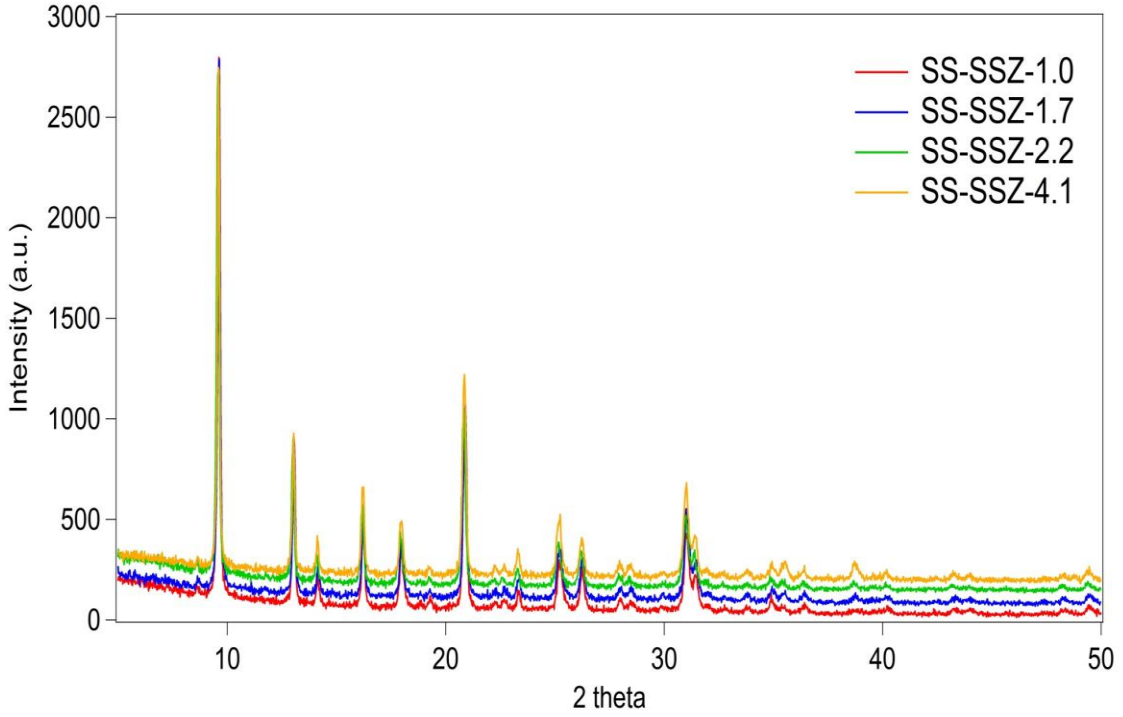

Figure 5.10 XRD patterns of as-prepared Cu-SSZ-13 samples with different Cu loading

The crystallinity of the as-prepared samples was verified using XRD. As shown in Figure 5.10, all the diffraction peaks of the CHA crystal phases were well maintained as observed in the XRD patterns. Therefore, the crystallinity of the as-prepared samples was intact after the solid state process. In addition, CuO phases, with diffraction peaks at 35.54° and 38.76°, were also detected in all the Cu-SSZ-13 samples. Indeed, like Cu-SAPO-34, some of CuO particles may not have completely exchanged into the pores, resulting in some remaining CuO phases on the samples.

The zeolite acid properties of the as-prepared Cu-SSZ-13 were studied using NH_3-TPD. As described in Figure 5.11, three desorption peaks were present in NH_3 profiles during the temperature ramp process. As previously mentioned, the low temperature peak at 150°C is assigned to physisorbed NH_3 and NH_3 adsorbed on weak acid sites, such as extraframework Al-OH sites. The desorption peak at 280°C and the high temperature peak above 400°C are assigned to the NH_3 adsorbed on strong Lewis acid sites and Brønsted acid sites, respectively. Similar to the NH_3-TPD profiles collected from the SAPO-34 samples, the amount of Lewis acid sites increased with increasing Cu loading, proving that more Cu ions were incorporated with the zeolite framework when additional CuO precursors were used in the solid state process. Additionally, if we compare the total NH_3 uptake of the Cu-SAPO-34 and Cu-SSZ-13, it is obvious that the Cu-SAPO-34 has a much larger NH_3 storage capacity than that of Cu-SSZ-13, which could be due to different Si/Al and (Al+P)/Si ratios in the H-SSZ-13 and H-SAPO-34 samples as well as different resistances towards the high temperature treatment.

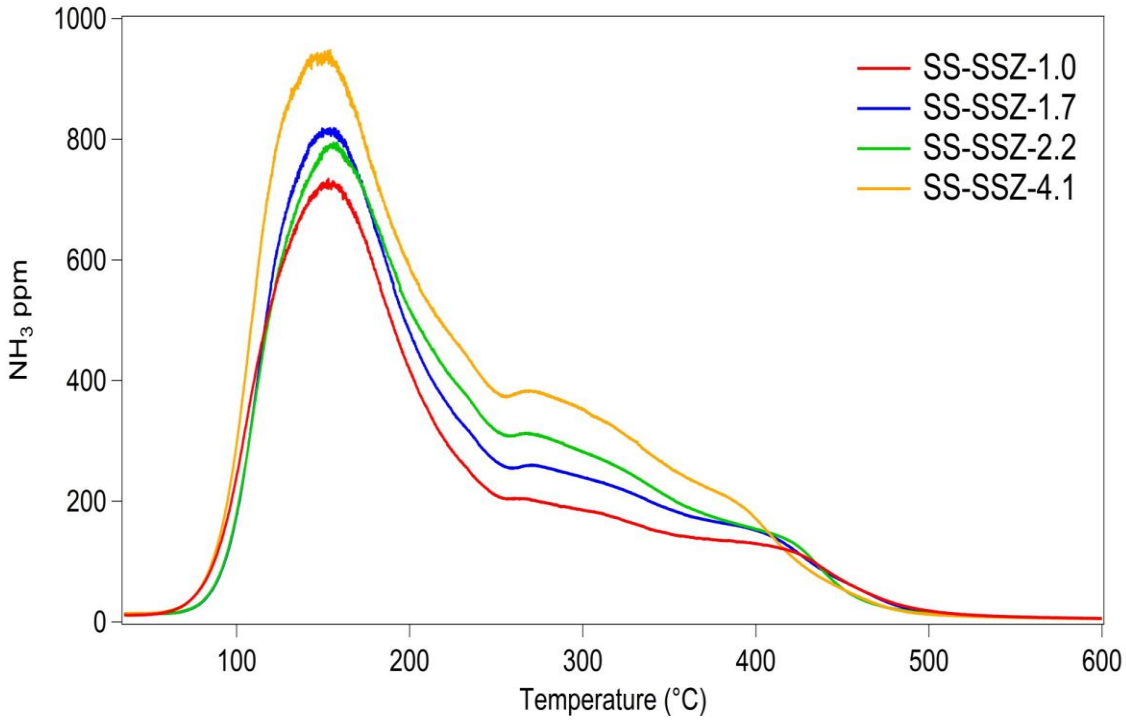

Figure 5.11 NH_3-TPD results over as-prepared samples with different Cu loading

DRIFTS was also used to probe the Cu structures, using NH_3 adsorption. As shown in Figure 5.12, exchanged Cu features, which were observed on Cu-SAPO-34 samples, were also detected at 940 cm^{-1} and 900 cm^{-1} over the Cu-SSZ-13 samples during the NH_3 adsorption process. However, the characteristics of the bands are different for Cu-SAPO-34 and Cu-SSZ-13. In Cu-SSZ-13, the bands at 900 cm^{-1} were very sharp while the bands at 940 cm^{-1} only appeared to be shoulders. This trend differs from that observed on the Cu-SAPO-34. For Cu-SAPO-34, the bands at the higher wavenumber (type 2 Cu) were much broader and larger than the bands at the lower wavenumber (type 1 Cu). Type 1 Cu was attributed to the isolated Cu sites while type 2 Cu was associated with the Cu_xO_y clusters. Based on these assignments, it appears that decent amounts of Cu_xO_y clusters were formed on Cu-SAPO-34 relative to Cu-SSZ-13, and most of the Cu ions were incorporated as isolated Cu^{2+} sites on the SSZ-13 samples. Both of the

exchanged Cu sites on Cu-SSZ-13 increased with increase Cu loading, again proving that more Cu could exchange with the protons in the pores of the SSZ-13 material, as was observed in Cu-SAPO-34 samples as well.

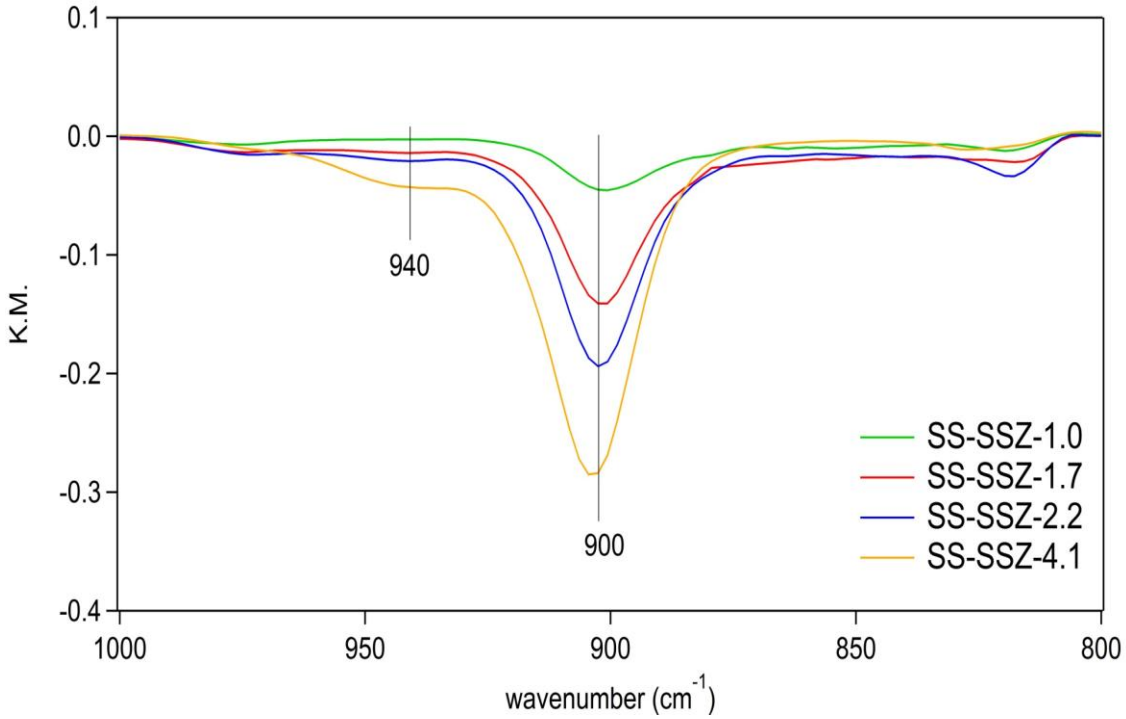

Figure 5.12 DRIFTS spectra taken over NH_3 saturated as-prepared samples with different Cu loadings (experimental conditions: the sample was exposed to 500 ppm NH_3 in He at 30°C for 60 minutes, total flow was 50 cm^3/min)

To further probe the evolution of the exchanged Cu sites, DRIFTS spectra were also obtained during NO adsorption at 30°C. Major bands were detected between 1800-2000 cm^{-1} in the DRIFTS spectra, as depicted in Figure 5.13. As a reminder, the bands in this wavenumber range are caused by NO adsorbed on different types/locations of Cu^{2+} sites. In particular, the band at 1909 cm^{-1}, which is accompanied by one at 1947 cm^{-1}, corresponds to NO adsorbed on isolated Cu^{2+} sites and the band at 1893 cm^{-1} is assigned to NO adsorbed on another type of Cu^{2+} site, possibly Cu_xO_y clusters. All the band intensities increased monotonically with increasing Cu loading, which is consistent with

the DRIFTS spectra upon NH_3 adsorption showing that the number of all types of Cu^{2+} sites increased as the Cu loading increased. Interestingly, the bands corresponding to isolated Cu^{2+} were much more intense than the bands associated with Cu_xO_y clusters. This further supports isolated Cu^{2+} sites being formed preferentially on Cu-SSZ-13. It is worth mentioning that a larger Cu_xO_y feature was detected on the Cu-SAPO-34 samples. Therefore, it seems that Cu structure distributions, which originate during the solid state ion exchange, are indeed different in as-prepared Cu-SSZ-13 and Cu-SAPO-34.

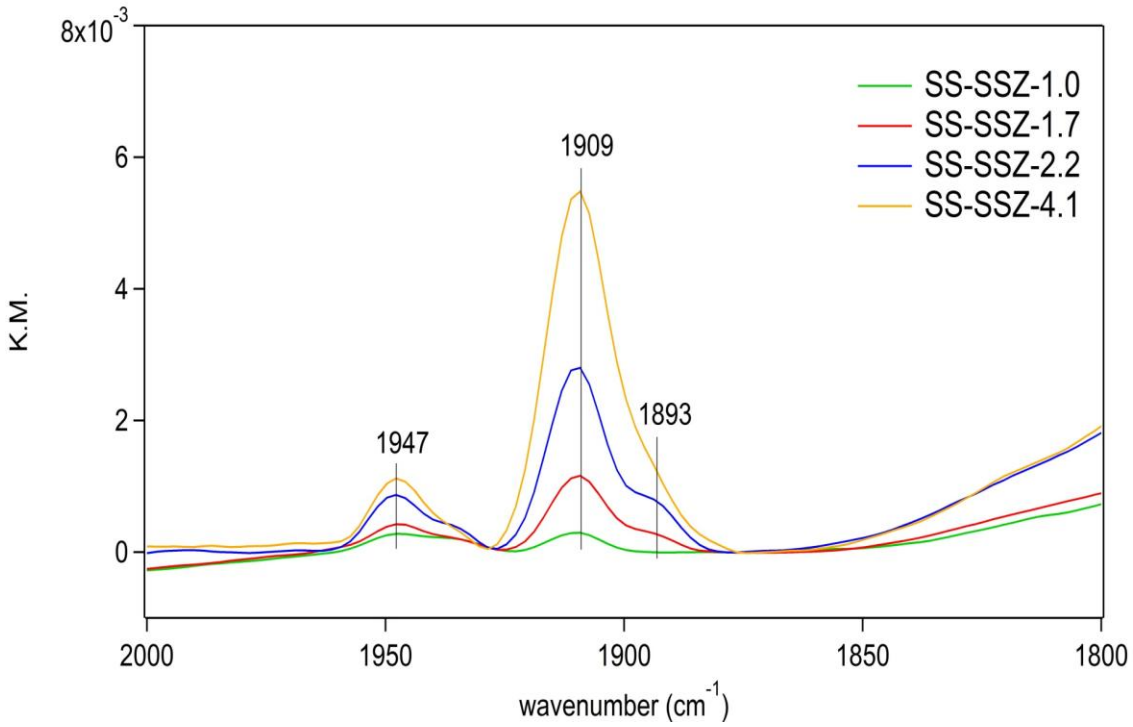

Figure 5.13 DRIFTS spectra taken over NO saturated as-prepared samples with different Cu loadings (experimental conditions: the sample was exposed to 200 ppm NO in He at 30°C for 60 minutes, total flow was 50 cm^3/min)

NH_3 oxidation was evaluated and the conversions are shown in Figure 5.14. NH_3 conversion monotonically increased with increasing Cu loading, which is in step with the results obtained with Cu-SAPO-34, Chapter 4. However, NH_3 oxidation is much less active on the Cu-SSZ-13 samples than that on Cu-SAPO-34. This difference can be

explained by the larger amount of Cu_xO_y clusters/particles present on Cu-SAPO-34 relative to Cu-SSZ-13, as discussed in the DRIFTS characterization results above.

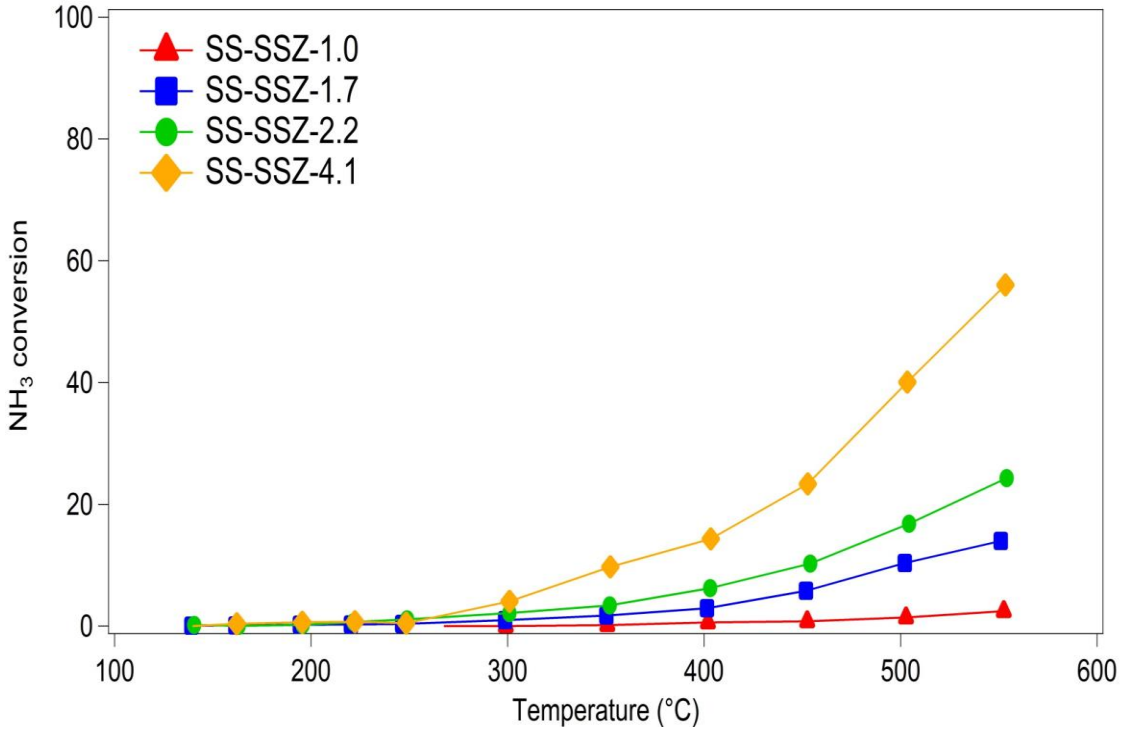

Figure 5.14 NH_3 conversions during an NH_3 oxidation reaction experiment (reaction conditions: 500 ppm NH_3, 10% H_2O, 10% O_2, balance N_2, GHSV = 240,000 hr^{-1})

5.4 Conclusions

A solid state ion exchange method was used to prepare Cu-exchanged SSZ-13 catalysts, which were then evaluated for the NH_3-SCR reaction. The prepared catalysts showed excellent SCR activity as well as sustainable hydrothermal stability. The data suggest that isolated Cu^{2+} sites were more selectively formed on Cu-SSZ-13 which accounted for the excellent NO conversion observed. Compared with the conventional wetness ion exchange process, the solid state method is relatively efficient and simple and therefore, it is an alternative to obtain the highly active and stable Cu-CHA catalysts.

Chapter 6 Comparison between Cu-SSZ-13 and Cu-SAPO-34 upon hydrothermal aging

6.1 Introduction

In a typical diesel engine after-treatment system, a diesel oxidation catalyst (DOC) and diesel particulate filter (DPF) are used to remove the unburned hydrocarbons, CO and particulate matter upstream of the SCR catalyst. The DPF needs to be periodically regenerated and a great deal of heat can then be transferred to the SCR catalyst. The high temperature exposure (>650°C) with the presence of moisture in the feed could damage the zeolite framework structure via a dealumination process. One of the significant advantages of the small pore Cu-CHA zeolite catalysts is its excellent hydrothermal stability. Both Cu-SSZ-13 and Cu-SAPO-34 are reported to maintain their SCR activity after hydrothermal aging at 800°C [45, 46, 66]. SSZ-13 and SAPO-34 zeolites have the largest pore opening of 3.8Å. The dealumination product $Al(OH)_3$, which has a calculated kinetic diameter of 5.03 Å, is likely to be restrained in the small pores and as a result, the dealumination process is hindered during the hydrothermal aging process [45]. In this chapter, the hydrothermal aging effects on Cu-SSZ-13 and Cu-SAPO-34 catalysts are investigated and compared. XRD, DRIFTS and NH_3-TPD were used to characterize the structure, acidity and Cu site changes during the hydrothermal treatment. Different resistances to hydrothermal aging were discussed.

6.2 Experimental

6.2.1 Catalyst preparation

The H-form SAPO-34 zeolite support was purchased from ACS materials. The Na-form SSZ-13 zeolite was synthesized in house using the hydrothermal method that was reported in Ref [45]. The obtained Na-SSZ-13 zeolite has a Si/Al ratio of 6. Subsequently, the Na-SSZ-13 was added into a 0.1 M NH_4NO_3 solution with continuous stirring at 80°C for 8 hours. The resulting NH_4-SSZ-13 powder was separated from the solution by filtration followed by several washing steps. Finally, the material was dried in an oven at 120 °C overnight. The solid state ion exchange was performed in a tube furnace equipped with a continuous flow of air. The detailed procedure is described in Chapter 4 and Chapter 5. Both SAPO-34 and SSZ-13 were heated at 700°C in the presence of 350 cm^3/min dry air for 16h. The as-prepared samples are named as SS-CuSSZ-13(700C) and SS-CuSAPO-34(700C), respectively.

6.2.2 Catalyst characterization

The elemental compositions of the samples were analyzed by ICP (Galbraith Laboratories). X-ray diffraction (XRD) measurements were performed in a Siemens D5000 Diffractometer equipped with a Cu-Kα detector. The NH_3 temperature programmed desorption (NH_3-TPD) experiments were conducted in the micro-scale reactor system described in Chapter 2. In each test, 120 mg of powder catalyst sample, mixed with 360 mg quartz beads, was pretreated in 10% O_2 in N_2 at 550°C for 1 h. After pretreatment, a total flow of 300 cm^3/min containing 500 ppm NH_3 in N_2 was introduced into the reactor for 2 h at 35 °C. After the catalyst was saturated, NH_3 was switched off

and only N_2 was fed to the reactor for another 2 h to remove any gas phase or weakly adsorbed NH_3. The final stage involved a temperature ramp to 550°C with a heating rate of 10 °C/min. In-situ DRIFTS experiments were performed by loading 60 mg powder catalysts into the sample cup of the high temperature reaction chamber. The pretreatment was conducted at 550°C in 10% O_2/He for 1h before cooling to 30°C. For NH_3 and NO adsorption experiments, the spectra were taken by subtracting the background spectra recorded during exposure to the sample to 50 cm^3/min pure He. NH_3 adsorption was conducted in a 50 cm^3/min flow containing 500 ppm NH_3 in a balance of He and NO adsorption spectra were performed in a 50 cm^3/min flow containing 200 ppm NO in a balance of He.

6.2.3 NH_3-SCR and NH_3 oxidation reaction tests

The standard SCR reaction and NH_3 oxidation reaction tests were performed by loading 120 mg powder catalyst mixed with 360 mg quartz beads in the micro-scale reactor. Prior to each test, the catalyst was pretreated 550°C for 2 h in flowing 10% O_2 in a balance of N_2. The simulated exhaust gas contained 500 ppm NO, 500 ppm NH_3, 10% O_2 and 10% H_2O with a balance of N_2. The NH_3 oxidation reaction tests were carried out in a flow of 500 ppm NH_3, 10% O_2 and 10% H_2O with a balance of N_2. The total flow rate was 600 cm^3/min and the corresponding gas hourly space velocity (GHSV) was 240000 h^{-1}. The NO and NH_3 conversions were calculated using the following equations

$$X_{NO} = \frac{C_{NO_{x_{in}}} - C_{NO_{x_{out}}}}{C_{NO_{in}}} \times 100\% \text{ and} \quad (6.1)$$

$$X_{NH_3} = \frac{C_{NH_{3_{in}}} - C_{NH_{3_{out}}}}{C_{NH_{3_{in}}}} \times 100\%. \quad (6.2)$$

6.3 Results and Discussion

6.3.1 SCR performance

The SCR performance results of SS-CuSSZ-13(700C) and SS-CuSAPO-34(700C) are shown in Figure 6.1 and Figure 6.2, respectively. Both Cu-SSZ-13 and Cu-SAPO-34 samples show good SCR activity over the range of temperatures used. In particular, over 90% NO conversions between 300-450°C were achieved on both samples. The Cu-SSZ-13 sample maintained the high activity at temperatures above 450°C. However, the Cu-SAPO-34 showed slightly lower NO_x conversions at temperatures above 450°C. Both samples resulted in high N_2 selectivity (near 100%). After 750 °C hydrothermal aging for 16h, the low temperature SCR activity was maintained on Cu-SSZ-13 while the NO conversions at temperatures higher than 400°C were decreased. On the other hand, the NO conversion at low temperature was obviously enhanced with the Cu-SAPO-34 sample. This result is consistent with the findings from the literature, which show that the Cu-SAPO-34 became even more active after a hydrothermal aging treatment [66, 72, 133]. One group of authors attributed it to the formation of additional isolated Cu^{2+} ions during the aging process [133]. Feng et al., reported a 50% loss of the surface area and pore volume of the Cu-SAPO-34 catalysts after 800°C hydrothermal aging for 16h. However, more isolated Cu^{2+} ions were indeed formed during this high temperature treatment and correspondingly, a higher NO_x conversion at low temperature was obtained with the aged sample [66]. Recently, Wang et al., prepared a Cu/SAPO-34 sample using precipitation and wetness ion exchange (WIE) methods and they found that the after hydrothermal treatment at 700°C for 48 h, the Cu-SAPO-34 prepared by WIE showed no loss in SCR activity as well as no structural changes. However, the Cu-SAPO-34

prepared by precipitation obtained significantly enhanced SCR activity after aging. The XAS analysis conducted by the authors indicated that Cu migration occurred during the high temperature treatment, which initially involved the formation of metallic Cu followed by re-oxidation of copper ions [72]. All of these findings are consistent with our results regarding hydrothermal treatment effects on Cu-SAPO-34.

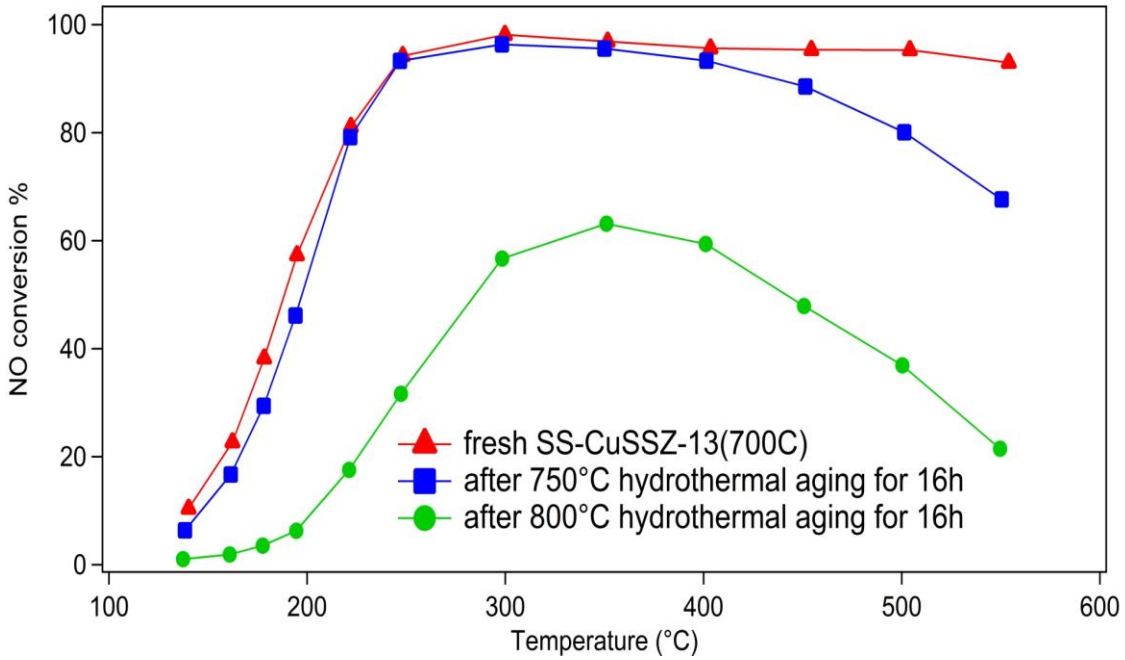

Figure 6.1 SCR performance for SS-CuSSZ-13(700C) before and after 750°C or 800°C hydrothermal aging for 16h (aging conditions: 10% H_2O, 10% O_2, balance N_2, GHSV= 240,000 hr^{-1})

The NO conversion significantly dropped for Cu-SSZ-13 after hydrothermal aging at 800°C for 16 hours. For example, the maximum NO conversion was observed to be 63% at 350 °C, corresponding to a 30% reduction of that of the fresh sample. In comparison, most of the SCR activity could be maintained over Cu-SAPO-34 after the same aging process, where, only a slight drop in the NO conversions was observed over the test temperature range. Therefore, it seems that the Cu-SAPO-34 sample is more

resistant to hydrothermal aging than Cu-SSZ-13, at least under the applied aging conditions.

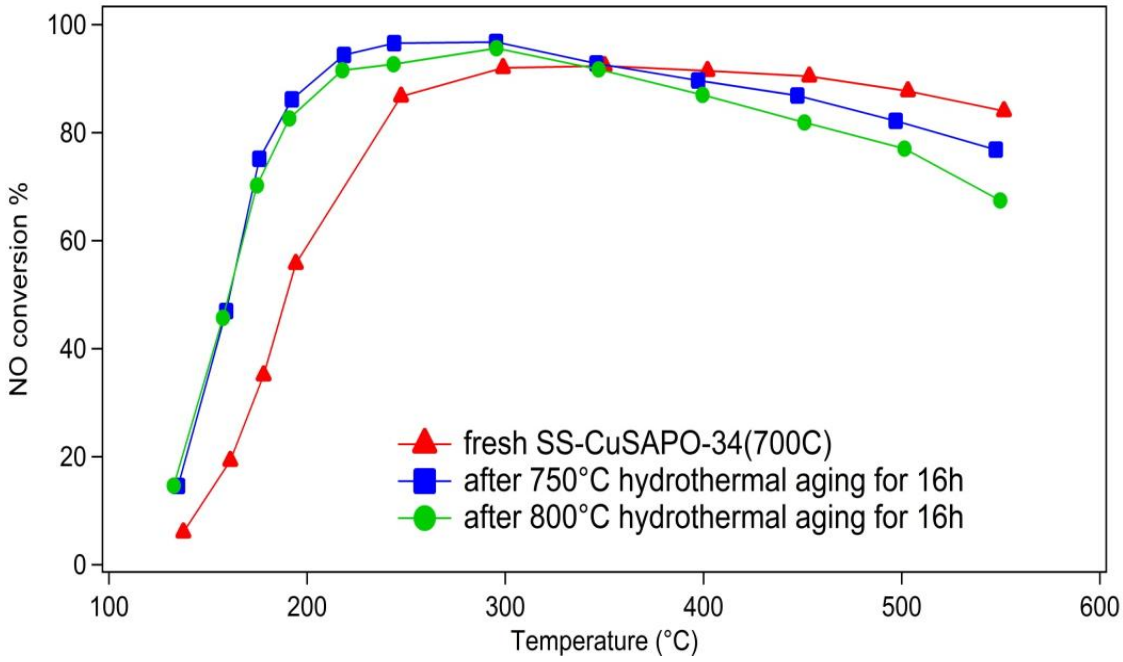

Figure 6.2 SCR performance for SS-CuSAPO-34(700C) before and after 750°C or 800°C hydrothermal aging for 16h (aging conditions: 10% H_2O, 10% O_2, balance N_2, GHSV = 240,000 hr^{-1})

6.3.2 NH_3 oxidation

The NH_3 oxidation activity was tested over the Cu-SSZ-13 and Cu-SAPO-34 samples before and after the hydrothermal aging. As shown in Figure 6.3, NH_3 oxidation lit off at 300°C and increased with increasing temperature on the fresh SS-CuSSZ-13(700C) sample. After 750°C hydrothermal aging, the NH_3 conversion increased, with 100% NH_3 conversion at 550°C. This is probably due to the aggregated CuO species that formed during the high temperature treatment as discussed in previous chapters. Indeed, it was reported that Cu could migrate from isolated Cu^{2+} species of the Cu-CHA catalysts and form CuO particles during the hydrothermal aging process [63]. The agglomeration

of isolated Cu^{2+} sites after the hydrothermal aging was also observed using TEM [63, 157]. CuO particles are known to have poor SCR activity and selectivity and higher NH_3 oxidation activity [142]. The increasing trend of NH_3 conversion in non-selective NH_3 oxidation could explain the drop in NO conversion in standard SCR tests after 750°C hydrothermal aging. However, with further hydrothermal treatment at 800°C, the NH_3 oxidation activity dropped, which could be explained by the fact that the surface area and pore structure were severely damaged at this aging condition and therefore the catalytic activity was significantly hindered. On the other hand, after 750 and 800°C hydrothermal aging, no significant change in the NH_3 conversion was observed with Cu-SAPO-34, which differs from that observed with Cu-SSZ-13. It is also worth noting that the NH_3 conversion on fresh SS-CuSAPO-34(700C) was much higher than that on fresh SS-CuSSZ-13(700C) (Figure 6.4).

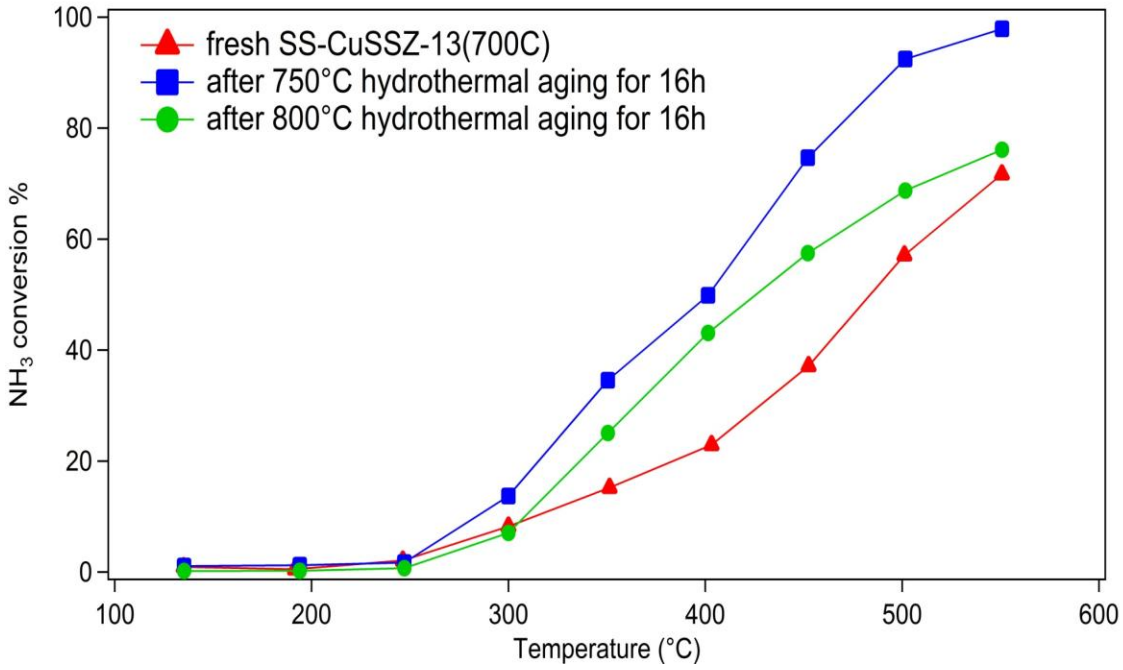

Figure 6.3 NH_3 conversions during NH_3 oxidation reaction on SS-CuSSZ-13 (reaction conditions: 500 ppm NH_3, 10% H_2O, 10% O_2, balance N_2, GHSV = 240,000 hr^{-1})

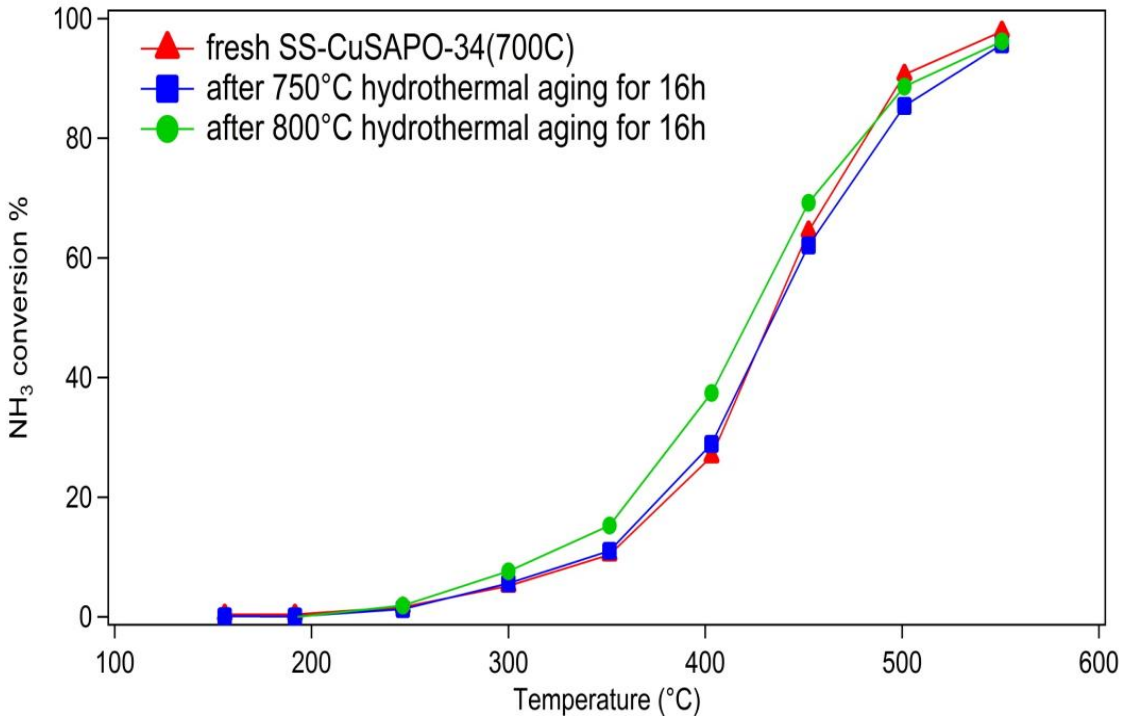

Figure 6.4 NH_3 conversions during NH_3 oxidation reaction on SS-CuSAPO-34 (reaction conditions: 500 ppm NH_3, 10% H_2O, 10% O_2, balance N_2, GHSV = 240,000 hr^{-1})

6.3.3 NH_3-TPD

NH_3 temperature programmed desorption (NH_3-TPD) experiments were conducted in order to investigate the acidity evolution during the hydrothermal aging process. Figure 6.5 shows the NH_3 profile collected during the temperature ramp over SS-CuSSZ-13(700C). Three peaks were observed on the fresh sample: a low temperature peak at 150°C, a high temperature peak above 400°C and a smaller feature between these low and high temperature peaks at around 280°C. Based on the analysis in previous chapters, the low temperature peak at 150°C is assigned to weakly adsorbed NH_3 such as physisorbed NH_3 and NH_3 adsorbed on weak Lewis acid sites. The desorption peak at 280°C and the high temperature peak above 400°C are associated with NH_3 adsorbed on

Lewis acid sites and Brønsted acid sites, respectively. After 750°C hydrothermal aging, all the NH_3 desorption peaks were reduced, indicating that both the Brønsted and Lewis acid sites were lost due to the hydrothermal aging. Furthermore, the 800°C hydrothermal treatment resulted in a more significant reduction of the number of acid sites.

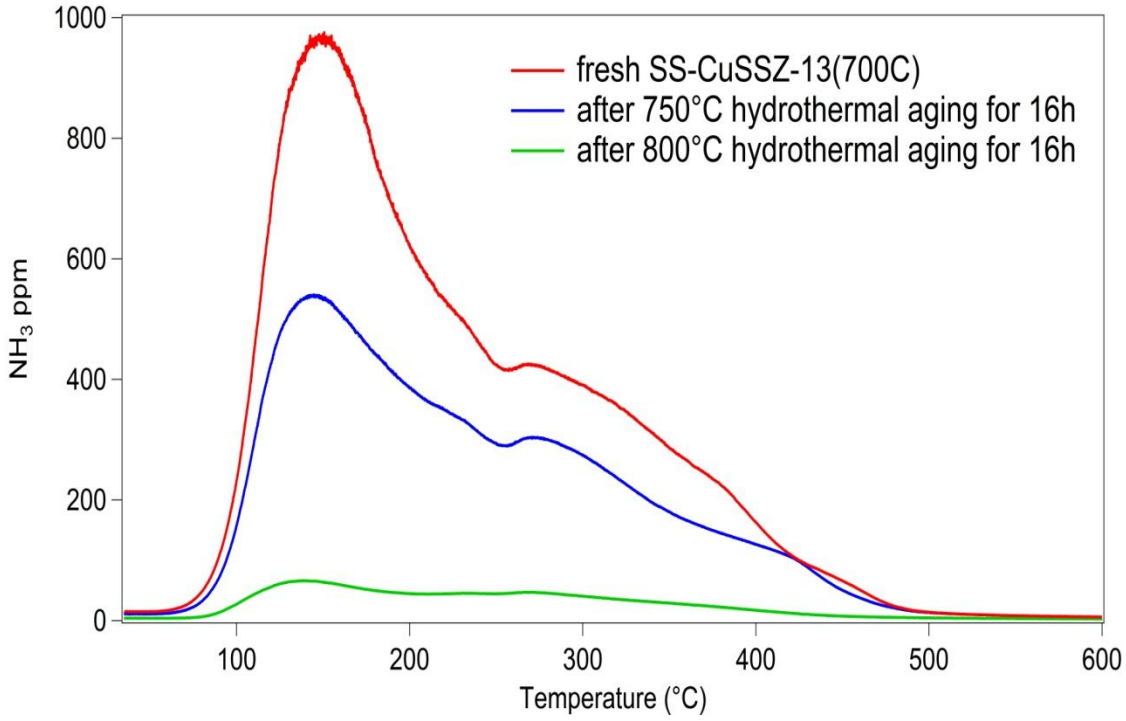

Figure 6.5 NH_3-TPD results over SS-CuSSZ-13(700C) sample (500 ppm NH_3 adsorption at 35 ^oC for 2h followed by purging by N_2 for 2h, subsequently the temperature was ramped to 550 ^oC with a heating rate of 10^oC/min in N_2)

In comparison, the NH_3 profile during the TPD taken over SS-CuSAPO-34(700C) also showed three similar desorption peaks (Figure 6.6). Interestingly, the high temperature desorption peak corresponding to the NH_3 desorbed from Brønsted acid sites was more intense on Cu-SAPO-34 than that on Cu-SSZ-13. This could be explained by the fact that the Cu-SAPO-34 is more robust to dealumination, which took place during the high temperature treatment of the solid state process, therefore resulting in much less loss of the Brønsted acid sites on Cu-SAPO-34. Surprisingly, the intensities of NH_3

desorption peaks, which corresponds to NH_3 adsorbed on the Lewis acid sites, increased after hydrothermal aging at 750°C and 800°C. This strongly indicates that Cu ions could continue to migrate and exchange with protons during the hydrothermal treatment on Cu-SAPO-34. As a result, the number of Lewis acid sites that were created by exchanged Cu sites increased. Indeed, the increasing number of exchanged Cu sites after the hydrothermal aging could be responsible for the enhanced low temperature SCR activity that was observed with the Cu-SAPO-34 sample. However, this result was not observed on the NH_3-TPD profiles taken over Cu-SSZ-13.

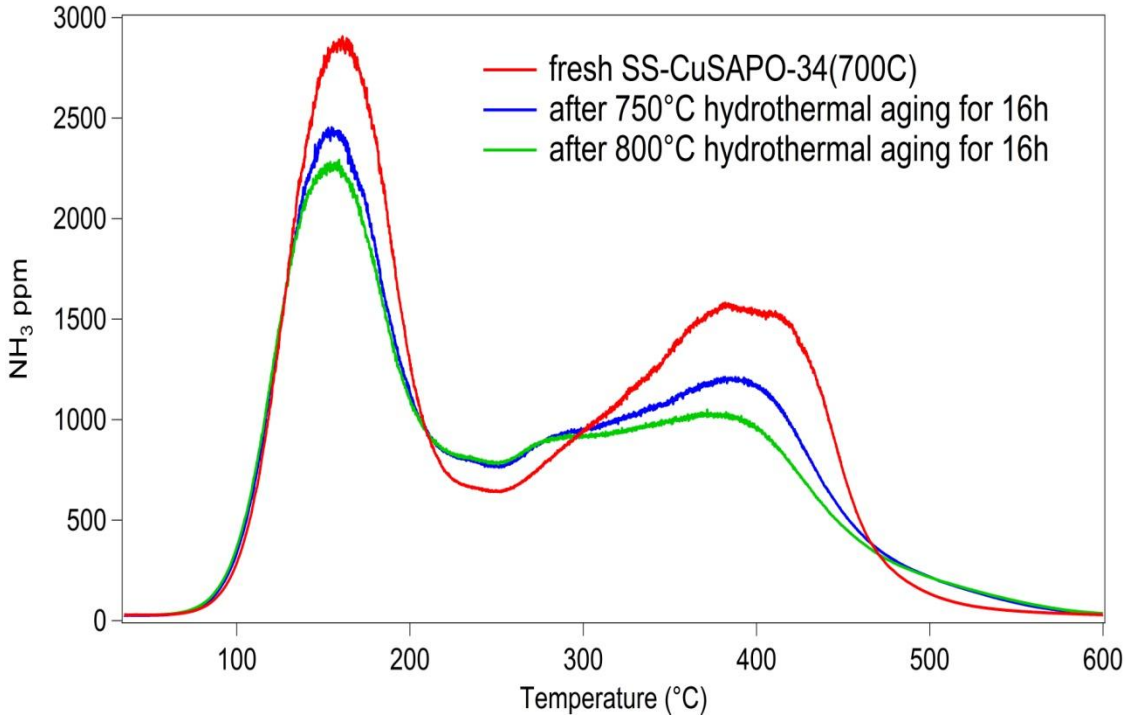

Figure 6.6 NH_3-TPD results over SS-CuSAPO-34(700C) (500 ppm NH_3 adsorption at 35 ^oC for 2h followed by purging by N_2 for 2h, subsequently the temperature was ramped to 550 ^oC with a heating rate of 10^oC/min in N_2)

6.3.4 XRD

In order to further probe the structural changes during the hydrothermal aging process over Cu-SAPO-34 and Cu-SSZ-13 samples, XRD measurements were taken on samples before and after the hydrothermal treatment. As shown in Figure 6.7, the crystallinity of fresh SS-CuSSZ-13(700C) was well maintained after the solid state ion exchange process as all the diffraction peaks related to CHA phases were observed in the XRD pattern. After 750 ^{o}C hydrothermal aging, some of the crystallinity of Cu-SSZ-13 disappeared in the XRD pattern, which could be explained by some structural damage caused by the hydrothermal aging. In addition, a broad peak was observed in the 2 theta range of 10 to 20°. This further confirms the formation of some amorphous phases that formed during the hydrothermal aging process. 800 ^{o}C hydrothermal aging resulted in an even more dramatic collapse of the crystal structure of Cu-SSZ-13. This is evidenced by the loss of some CHA phases in the XRD pattern. In summary, more significant structural damage of the zeolite framework was detected as the hydrothermal aging temperature increased from 750^{o}C to 800^{o}C, which corresponds to the dramatic drop in NO conversion during SCR tests with Cu-SSZ-13 sample after 800^{o}C hydrothermal aging.

The XRD patterns of SS-CuSAPO-34(700C) before and after hydrothermal aging are shown in Figure 6.8. Sharp diffraction peaks, which correspond to the CHA phases, were obtained on the fresh Cu-SAPO-34 sample. These crystal phases were very well maintained after hydrothermal aging at 750°C as evidenced by the fact that almost no disappearance of diffraction peaks was observed. In addition, a broad peak, which may originate from some amorphous phases, was detected on Cu-SAPO-34 as well. When the aging temperature was increased to 800°C, there was still no significant loss of the

crystallinity detected on Cu-SAPO-34 material. This again proves that Cu-SAPO-34 structure is indeed more robust than Cu-SSZ-13.

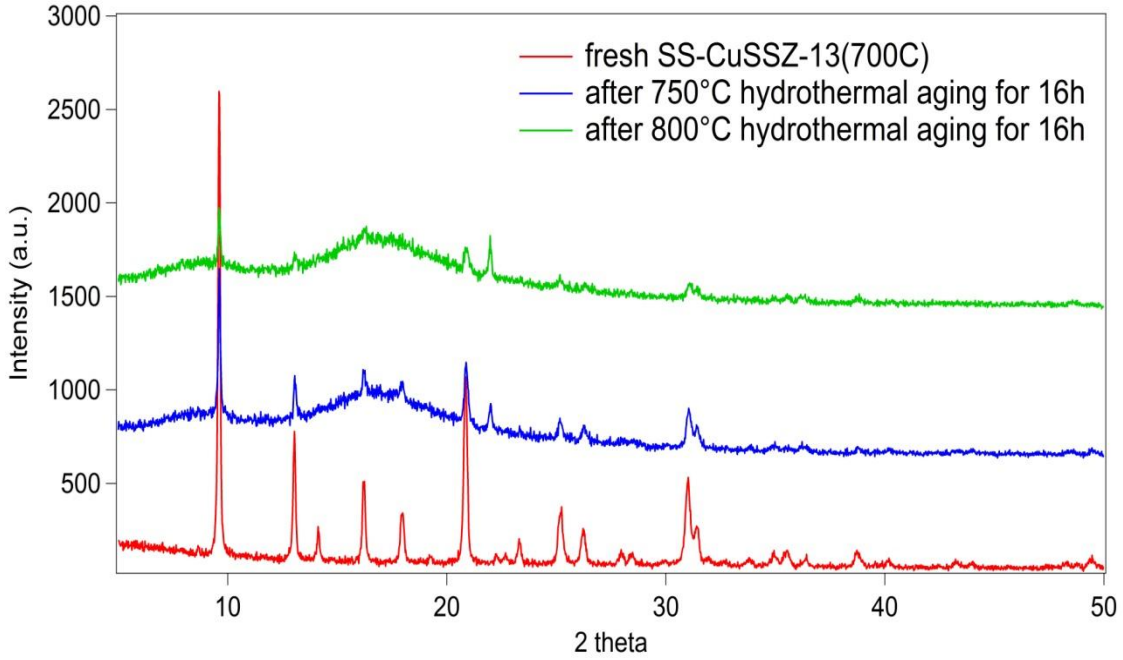

Figure 6.7 XRD patterns of as-prepared SS-CuSSZ-13(700C) samples before and after hydrothermal aging at 750 or 800°C

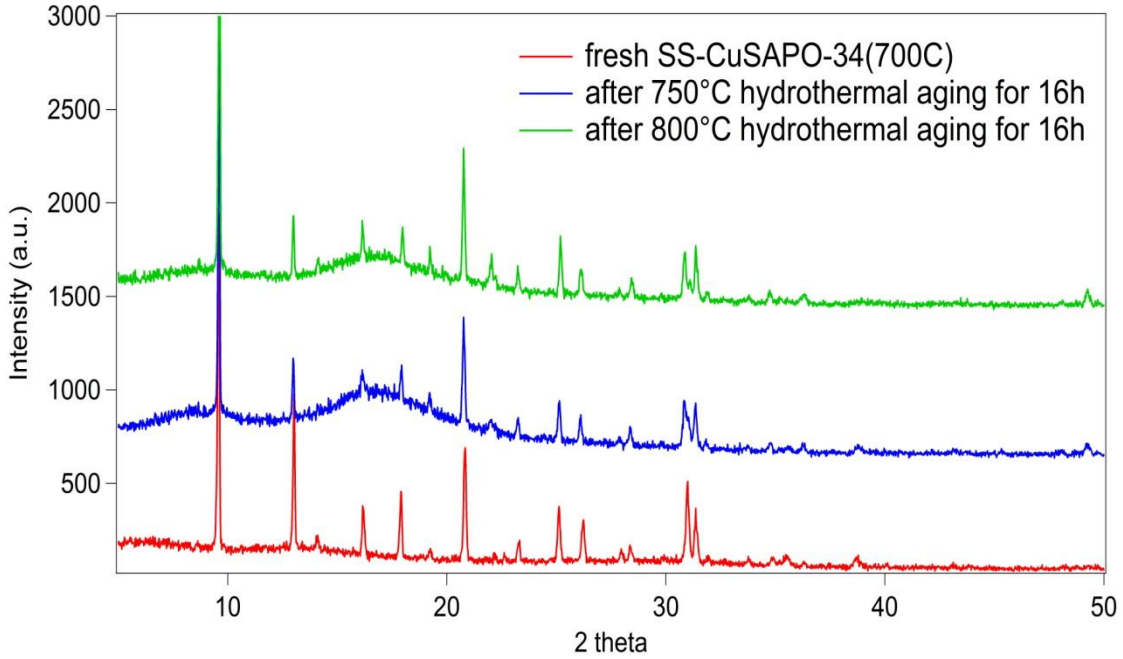

Figure 6.8 XRD patterns of as-prepared SS-Cu-SAPO-34(700C) samples before and after hydrothermal aging at 750 or 800°C

6.3.5 DRIFTS-NH_3 adsorption

In order to further investigate the different hydrothermal aging effects, in-situ DRIFTS experiments were used to characterize the different Cu sites. First, NH_3 was used as a probe molecule since NH_3 can adsorb on both Brønsted acid sites and Lewis acid sites of the zeolite material. Therefore, the intensities of the DRIFTS spectra features after NH_3 saturation are indicative of the total amounts of different acid sites. The DRIFTS spectra taken after NH_3 saturation of the SS-CuSSZ-13(700C) sample are shown in Figure 6.9. Several negative bands at 3733, 3660, 3612 and 3585 cm^{-1} were observed in the spectra. The bands in this area are typically assigned to OH stretching vibrations on the zeolite surface. These bands were negative due to weakened vibrations caused by NH_3 adsorption on the OH groups. For example, the bands at 3733 and 3660 cm^{-1} are assigned to NH_3 adsorbed on the external Si-OH and Al-OH groups, respectively [153]. The bands at 3612 and 3585 cm^{-1} correspond to the stretching vibrations of the Al-OH-Si groups, which are signatures of Brønsted acid sites on CHA materials [153-155]. After hydrothermal aging at 750°C, all of these bands were decreased, which is again due to the structural collapse caused by the hydrothermal aging. This reduction is more significant after the sample was hydrothermally aged at 800°C. As shown in Figure 6.9, almost no OH stretching vibrations could be identified in the DRIFTS spectra taken after NH_3 adsorption, further confirming the loss in surface OH groups after hydrothermal aging. On the other hand, an intense negative band was detected at 900 cm^{-1} and was accompanied by a weak shoulder at 940 cm^{-1}. The peaks in this region are assigned to the tetrahedral cation-oxygen-tetrahedral cation (T-O-T) framework vibrations that were perturbed by ion exchanged copper species [64]. These bands are negative due to the

restored T-O-T vibrations due to NH_3 adsorption on the Cu sites, confirming the existence of two different exchanged copper species. After 750°C hydrothermal aging, the amounts of these two exchanged copper species were evidently reduced, as compared to the fresh sample. With increasing the hydrothermal aging temperature from 750°C to 800°C, these two negative peaks almost disappeared from the spectra, indicating a severe loss in the amount of exchanged Cu sites during this process. This is also consistent with the NH_3-TPD results from on the same catalyst showing that both Brønsted acid sites and Lewis acid sites were decreased after hydrothermal aging.

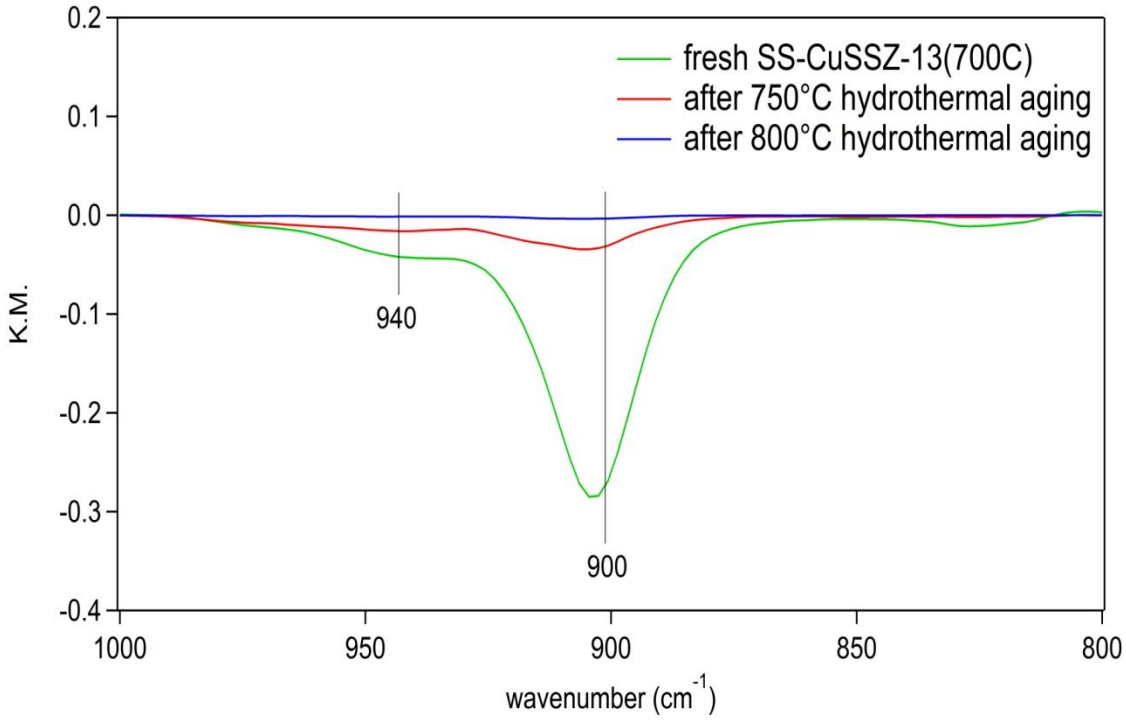

Figure 6.9 DRIFTS spectra taken over NH_3 saturated as-prepared SS-CuSSZ-13 (700C) sample (experimental conditions: sample exposed to 500 ppm NH_3 in He at 30°C for 60 minutes, total flow was 50 cm^3/min

A completely different evolution in the surface structural changes was observed in the DRIFTS spectra taken after saturating the SS-CuSAPO-34(700C) sample with NH_3, as shown in Figure 6.10. In the OH stretching region, the weak negative band at 3671 cm^-

^{1} is assigned to the external surface P-OH groups [61]. Two intense negative bands at 3625 and 3600 cm^{-1} originated from the stretching vibrations of bridging OH groups (Al-OH-Si) [61]. 750°C hydrothermal aging for 16h resulted in slight decreases in the intensities of the Al-OH-Si groups, hinting at a mild decrease in the amount of Brønsted acid sites on this sample. It is also worth noting that the degree of this reduction is much less evident than that observed on the 750°C hydrothermally aged Cu-SSZ-13 sample. Furthermore, the band intensities of Al-OH-Si groups maintained their intensities after 800°C hydrothermal aging, which was not observed on Cu-SSZ-13 aged at the same condition. The distinction between the Cu-SSZ-13 and Cu-SAPO-34 was further verified by the comparing the exchanged Cu DRIFTS features upon NH_3 adsorption. As shown in Figure 6.10, two intense bands with negative intensities were observed at 900 and 850 cm^{-1}. Similar to those detected on the Cu-SSZ-13 sample, these two bands are assigned to the tetrahedral cation-oxygen-tetrahedral cation (T-O-T) framework vibrations that were perturbed by ion exchanged copper species. Noticeably, the shapes of these Cu features are distinct from those observed with Cu-SAPO-34. For example, the exchanged Cu feature at 900 cm^{-1} (type 2 Cu) is very intense for Cu-SAPO-34 while it was only a shoulder for Cu-SSZ-13. This could be explained by the fact that a different type and/or location of Cu site was predominantly formed on the Cu-SAPO-34 sample [64]. This band was previously assigned to be associated with the Cu_xO_y clusters that formed on the sample. After the 750°C hydrothermal treatment, both of the exchanged Cu features significantly increased in intensities. This is not surprising since the NH_3-TPD results showed more Lewis acid sites, which were generated by the post solid state ion exchange of Cu during the hydrothermal aging process. This Cu movement was not observed on

the as-prepared Cu-SSZ-13 sample. As the hydrothermal aging temperature increased from 750°C to 800°C, Cu migration is more evident as more intense exchanged Cu features were detected on the 800°C hydrothermally aged sample. Accordingly, the SCR performance was further enhanced on the Cu-SAPO-34.

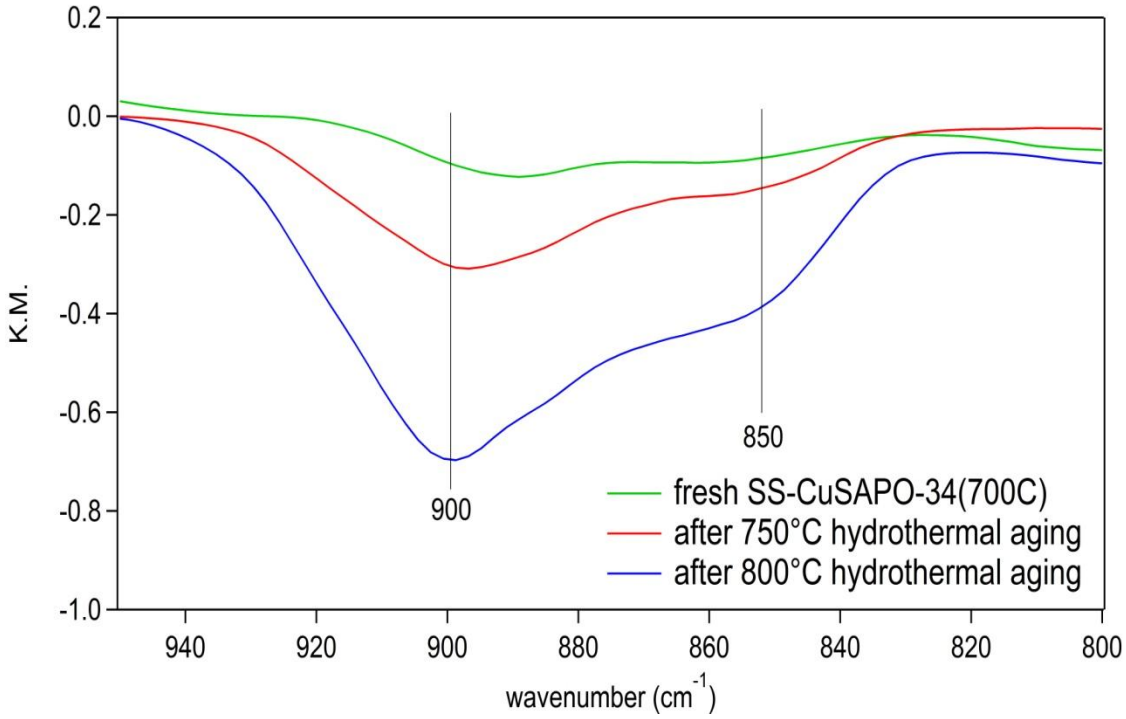

Figure 6.10 DRIFTS spectra taken over NH_3 saturated as-prepared SS-CuSAPO-34(700C) sample (experimental conditions: sample exposed to 500 ppm NH_3 in He at 30°C for 60 minutes, total flow was 50 cm^3/min)

6.3.6 DRIFTS-NO adsorption

The Cu migration during the aging of Cu-SAPO-34 was further confirmed by NO adsorption experiments performed and characterized using DRIFTS. Figure 6.11 shows the DRIFTS spectra taken upon exposing the SS-CuSSZ-13(700C) sample to NO. Here, the catalysts were treated with 10% O_2 before NO was introduced, therefore all the surface exchanged Cu sites are presumed to be in the Cu^{2+} state. During the NO

adsorption process, major bands in the range of 1800-2000 cm^{-1} were immediately observed. The band at 1909 cm^{-1}, which was accompanied by the band at 1947 cm^{-1}, was assigned to NO adsorbed on the isolated Cu^{2+} sites, as discussed in previous chapters. Additionally, the band at 1897 cm^{-1} corresponds to NO adsorbed on another type of Cu^{2+} site, possibly Cu_xO_y clusters [56, 111]. Thus, these bands could be the signatures of surface Cu^{2+} sites. After 750°C hydrothermal aging, all of these bands decreased for Cu-SSZ-13, proving that the number of Cu^{2+} sites dropped after aging. Moreover, these bands were almost absent in the spectra taken over the sample after 800°C hydrothermal aging. All of these results coincide with the fact that the exchanged Cu^{2+} sites were lost by the hydrothermal aging.

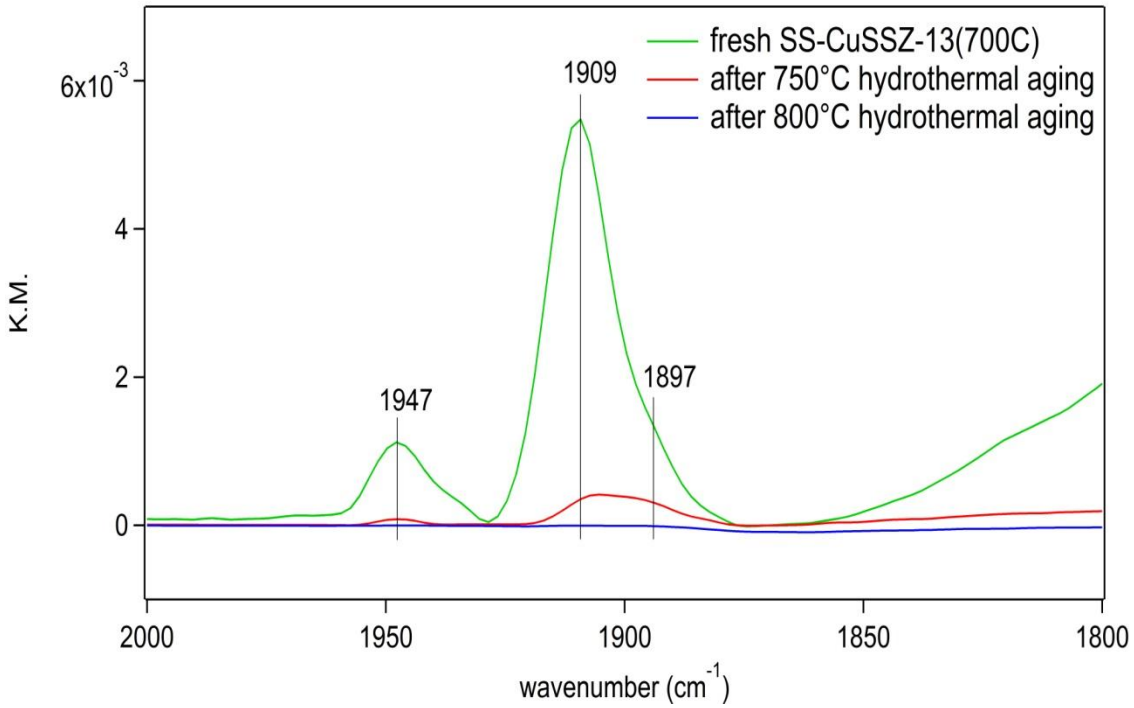

Figure 6.11 DRIFTS spectra taken over NO saturated as-prepared SS-CuSSZ-13 (700C) sample (experimental conditions: sample exposed to 200 ppm NO in He at 30°C for 60 minutes, total flow was 50 cm^3/min)

The DRIFTS spectra taken after exposing the Cu-SAPO-34(700C) sample to NO are shown in Figure 6.12. Several bands were observed, at 1944, 1916, 1906, and 1893 cm^{-1}, upon NO adsorption. Similar to Cu-SSZ-13, these bands corresponded to NO that adsorbed on different Cu^{2+} sites. After 750°C hydrothermal aging, the band intensities were higher than those observed on the fresh Cu-SAPO-34, indicating that the total amount of Cu^{2+} increased after hydrothermal aging. With 800°C hydrothermal aging, the band intensities again increased, further confirming that more Cu ions were incorporated into the zeolite framework and generated exchanged Cu^{2+} sites.

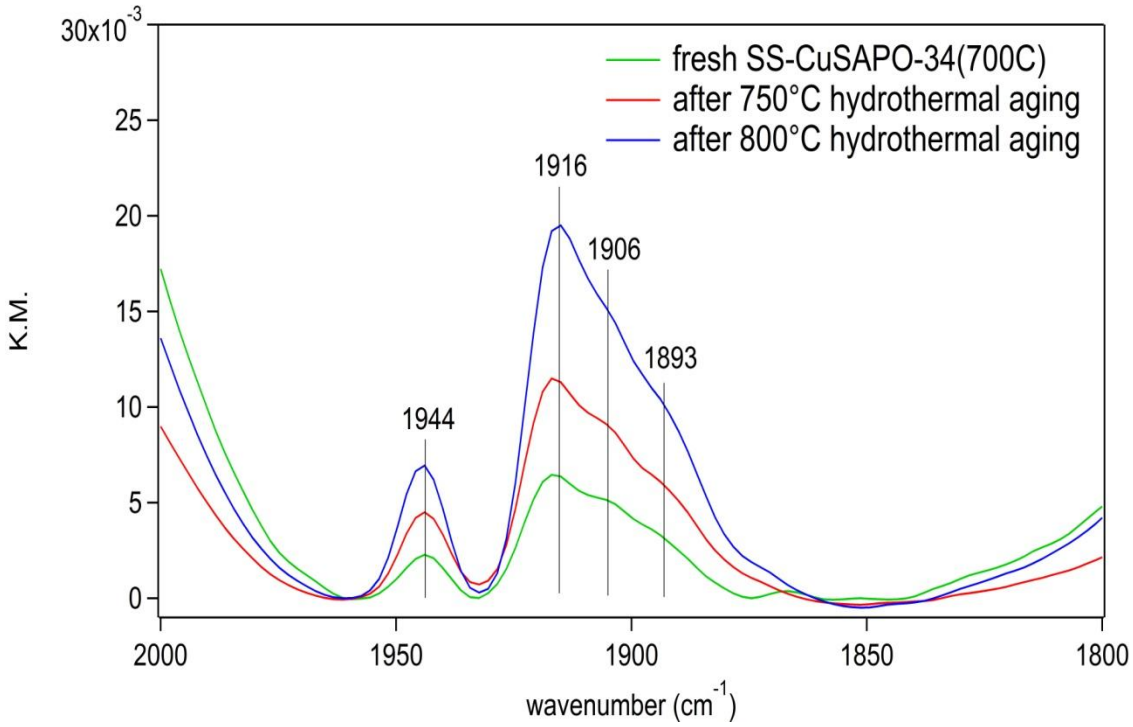

Figure 6.12 DRIFTS spectra taken over NO saturated as-prepared SS-CuSAPO-34 (700C) sample (experimental conditions: sample exposed to 200 ppm NO in He at 30°C for 60 minutes, total flow was 50 cm^3/min)

All of these observations coincide with in the observations from the NH_3-TPD and NH_3-exposure DRIFTS results. Cu-SAPO-34 is more resistant to the hydrothermal aging than the Cu-SSZ-13. And Cu could still migrate into the pores of Cu-SAPO-34

materials and further the solid state ion exchange process. As a result, more isolated Cu^{2+} sites, which are active for the NH_3-SCR reaction, formed on Cu-SAPO-34. For the Cu-SSZ-13 catalyst, hydrothermal aging led to a significant drop in the SCR activity due to severe structural damage. In addition, the initial increase in NH_3 oxidation activity indicates Cu site changes. Indeed, it is likely that some exchanged Cu^{2+} sites detached from the framework and formed large CuO particles that consumed additional NH_3 and produced NO_x through the NH_3 oxidation reaction. However, this does not seem to be the case for Cu-SAPO-34, where the NH_3 oxidation activity was maintained after the hydrothermal aging process.

6.4 Conclusions

The hydrothermal stabilities of Cu-SSZ-13 and Cu-SAPO-34 catalysts were characterized and compared. The results show that both Cu-SSZ-13 and Cu-SAPO-34 could maintain their performance with 750°C hydrothermal aging for 16 h. However, 800°C hydrothermal aging for 16 h result in a significant reduction of the SCR performance of the Cu-SSZ-13 catalyst, which was accompanied by a drastic loss in crystallinity and active Cu sites. On the other hand, Cu-SAPO-34 did not lose activity with the same aging conditions, but actually the low temperature NO conversion was increased after the hydrothermal aging. This was explained by Cu migrating into the pores of SAPO-34 during the high temperature treatment and forming additional isolated Cu^{2+} sites via the post solid state ion exchange process.

Chapter 7 SO_2 Poisoning impact on the NH_3-SCR reaction over commercial Cu-SAPO-34

7.1 Introduction

Cu-zeolite SCR catalysts are sensitive to sulfur poisoning [73-75]. And even with ultra-low sulfur fuels, sulfur species can accumulate over time, leading to decreased performance. Diesel oxidation catalysts (DOCs) are typically used in diesel exhaust applications and are located upstream of the SCR catalyst. Therefore, depending on temperature primarily, SO_2 and SO_3 may co-exist in the exhaust feed. Previous work has suggested that sulfur poisoning by SO_2 differs from that of SO_3. For example, Ramachandran et al., have found that V–ZSM-5 is relatively stable for the SCR reaction in the presence of H_2O and SO_2, but in the presence of SO_3 rapid deactivation was observed. In terms of the mechanism, the authors concluded that ammonium bisulfate formed when both NH_3 and SO_3 were present [74]. Cheng et al., compared deactivation of a Cu-BEA catalyst by SO_2 and SO_3 and found that SO_3 was more significant than SO_2, and the authors proposed that $CuSO_4$ formed upon SO_3 exposure, resulting in deactivation [75]. Their analysis also showed that even after the sulfate formed, the Cu remained in a highly dispersed state, at its initial ion-exchange locations. Jiang et al., [158] studied the poisoning effects of SO_2 over a Fe-Mn/TiO_2 catalyst, and concluded that SO_2 inhibition was due to surface sulfate formed, which in turn affected NO adsorption. Xu et al., [159] investigated a Ce/TiO_2 SCR catalyst and proposed that the SO_2 could react with

the catalyst to form thermally stable $Ce(SO_4)_2$ and $Ce_2(SO_4)_3$, which in turn affected redox cycling between Ce(IV) and Ce(III) and inhibited nitrate formation.

Overall, based on the literature different sulfur poisoning mechanisms of NH_3-SCR catalysts have been proposed. And thus far, the SO_2 deactivation mechanism of Cu-SAPO-34 has not been clearly explained. In the present study, the impact of SO_2 exposure on the SCR performance of a Cu-SAPO-34 was characterized.

7.2 Experimental

The Cu-SAPO-34 catalyst was supplied by Cummins Inc. The Cu-SAPO-34 catalyst sample had a Si/(Al+P) ratio of 0.2. The Cu loading was 0.95 wt%, as detailed previously, and also contained ~2 wt% Ce. For SCR activity tests, a monolithic-supported sample with 1.4″ long and 0.8″ inner diameter (ID) was placed in a quartz tube reactor inside the furnace of the bench-scale reactor system. Before testing, the catalyst was pretreated at 550°C for 4 h in 10% O_2/N_2. For SCR activity tests, the simulated exhaust gas contained 500 ppm NO, 500 ppm NH_3, and 10% O_2, with a balance of N_2. The total flow rate was 5 L/min, and the corresponding gas hourly space velocity (GHSV) was 28,000 h^{-1}. For SO_2 oxidation, the reaction gas mixture consisted of 200 ppm SO_2, 10% O_2 and a N_2 balance.

To evaluate the performance of the sample with some or all sulfur removed ($DeSO_x$), the S-exposed samples were exposed to 10% O_2/N_2 and temperature programmed experiments were carried with a heating rate of 5ºC/min at a flow rate of 5 L/min. The samples were heated to 600, 700 or 735ºC and held at that temperature overnight.

Temperature-programmed desorption (TPD) experiments were carried out after the catalyst was exposed to SO_2, NH_3, $SO_2 + NH_3$, NO_x, or $SO_2 + NO_x$, using the same reactor described above. Typically, the sample was pretreated in 5 L/min of 10% O_2/N_2, while heating from room temperature to 600^oC with a heating rate of 25^oC/min, and was held at 600^oC for 0.5 h and then cooled back to room temperature in 10% O_2/N_2. For the SO_2-TPD experiment, the adsorption phase consisted of 200 ppm SO_2, 10% O_2, in a balance of N_2, with exposure at 150^oC and the total flow rate was 5 L/min. This was followed by a purge phase in N_2 for 1h, and then the temperature was increased from 150 to 735^oC at a rate of 10^oC/min. For NH_3 and $SO_2 + NH_3$-TPD, the adsorption phase consisted of 500 ppm NH_3 and 200 ppm SO_2 (if added), 10% O_2 in a N_2 balance, with exposure at 150^oC and the same 5 L/min flow rate. This was followed by purging in N_2 for 1h, and then TPD from 150 to 735^oC at 10^oC/min. For NO_x-TPD and $NO_x + SO_2$-TPD experiments, the adsorption phase consisted of 500 ppm NO, 200 ppm SO_2 (if added) and 10% O_2 in a N_2 balance, with exposure at 150^oC and the 5 L/min flow rate. This was again followed by purging in N_2 for 1h, and then TPD from 150 to 735^oC at 10^oC/min.

Surface species formed during catalyst exposure to SO_2, NO_x and NH_3 were characterized with in-situ DRIFTS. The powder sample was scraped from the monolith sample and was pressed into a 60 mg pellet of 6.5 mm diameter and placed in the sample cup. A feed gas mixture was supplied at a flow rate of 50 mL/min. The samples were first treated in a flow of 10% O_2/He at 500^oC for 0.5 h and then cooled to room temperature. At the temperatures used for analysis, a background spectrum was recorded in flowing He, and it was subtracted from the sample spectrum obtained at the same temperature.

7.3 Results and Discussion

7.3.1 SO_2 exposure impact on NH_3-SCR

The standard SCR reaction activity was evaluated over the monolith-supported Cu-SAPO-34 catalyst from 130 to 580°C, and the NO conversion results in the absence and presence of SO_2 as a function of temperature are shown in Figure 7.1. Under the conditions tested, appreciable NH_3-SCR activity was observed in the absence of SO_2 between 130-580°C. About 90% NO conversion was achieved at 200°C. With increasing temperature, the conversion decreased because of competitive NH_3 oxidation at high temperatures, as evidenced by 100% NH_3 conversion at these temperatures. In addition, very little N_2O (< 5 ppm) was detected during these tests, indicating a high selectivity of NO to N_2 was achieved.

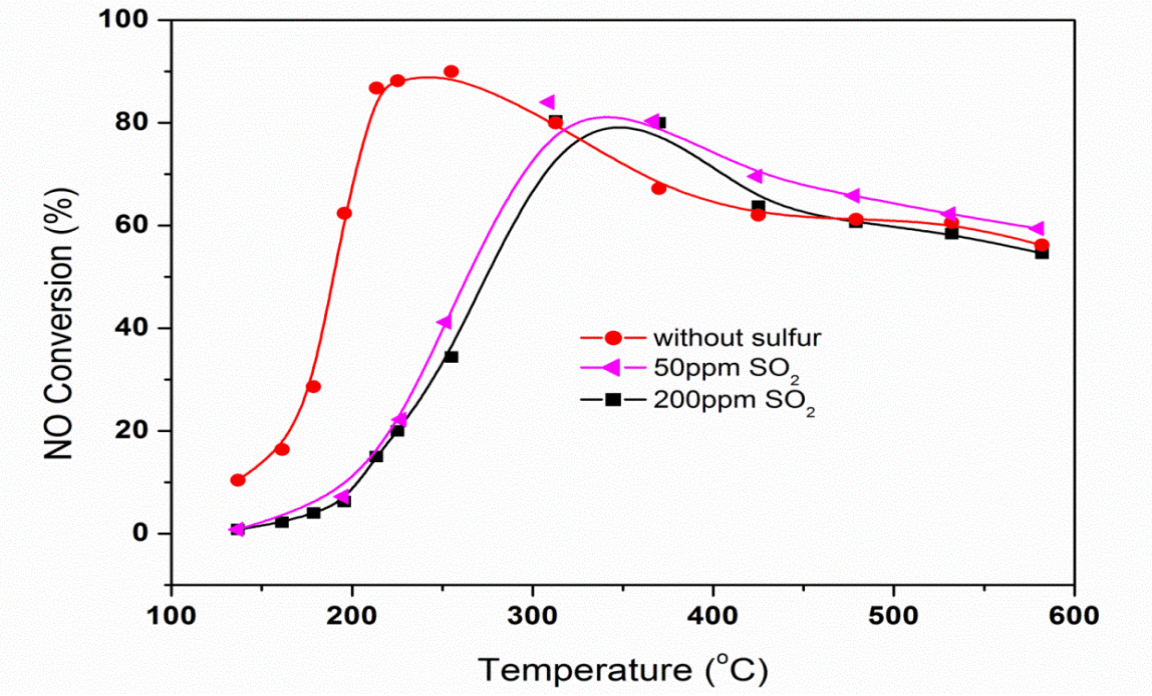

Figure 7.1 SCR reaction activity in the absence and presence of SO_2 (Reaction conditions: 500 ppm NH_3, 500 ppm NO, 50/200 ppm SO_2, 10% O_2, balance N_2, GHSV = 28,000 hr^{-1})

The effect of SO_2 on the SCR activity is also illustrated in Figure 7.1. Low temperature catalytic activity (130-300°C) significantly decreased with the addition of 50 ppm SO_2. For example, the NO conversion dropped from 90% to 15% at 200°C. On the other hand, at temperatures above 300ºC, there is a slight improvement or no impact observed. When 200 ppm SO_2 was added to the system instead of 50 ppm, the poisoning effects on NO conversion were similar, indicating that different concentrations do not lead to different poisoning mechanisms.

7.3.2 SO_2 oxidation

SO_2 exposure only affected the SCR performance over Cu/SAPO-34 at low temperature. It has been reported that both SO_2 and SO_3 could poison Cu-zeolite catalyst and the impact of SO_3 on the SCR reaction [73] differs from that of SO_2, and is indeed more severe. In order to determine whether SO_2 oxidation to SO_3 could occur over the Cu-SAPO-34 sample, and thus lead to a convoluted interpretation of the individual S species effects, SO_2 oxidation activity was evaluated.

In order to determine whether SO_3 could be produced over the Cu-SAPO-34 sample, SO_2 oxidation activity on this catalyst was evaluated. SO_2 oxidation conversion as a function of temperature is shown in Figure 7.2. Interestingly, no SO_3 was detected at temperature below 300°C, which is within the temperature range that the SO_2 poisoning effect was observed. SO_2 conversion light off was observed around 400^{o}C, and increased with increasing temperature, reaching a maximum of only 15% when at 580^{o}C under the conditions of this test. Therefore, the low temperature deactivation observed was not caused by the formation of SO_3.

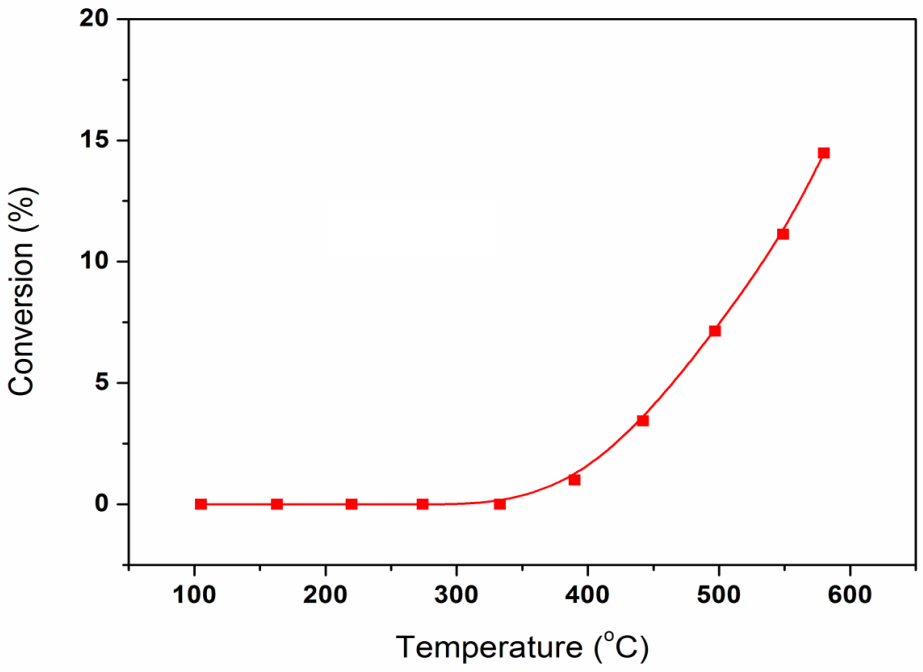

Figure 7.2 SO_2 oxidation conversion as a function of temperature (Reaction conditions: 200 ppm SO_2, 10% O_2, 10% H_2O, balance N_2, total flow rate 5L/min)

7.3.3 DRIFTS characterization of SO_2 + O_2 adsorption

As discussed above, SO_2 exposure primarily affected SCR reaction activity at low temperatures. The interactions between SO_2 and the surface of the Cu-SAPO-34 catalyst were studied using in-situ DRIFTS in order to better understand this impact. DRIFTS spectra obtained during adsorption of SO_2, in the presence of gas phase O_2 are shown in Figure 7.3. During this process, several bands in the range of 1200 to 1800 cm^{-1} were immediately detected. The large feature at 1612 cm^{-1} was assigned to H-O-H vibrations caused by SO_2 interacting with OH groups [159]. Several smaller features at 1434, 1324, 1304, 1287 and 1226 cm^{-1} were observed and these peaks were attributed to the formation of surface SO_2 groups and sulfate species associated with different adsorption sites (e.g., Cu or Ce sites) [159-161]. Here, we need to emphasize that CeO_2 is a part of the catalyst formulation so SO_2 adsorption on CeO_2 is also possible. It is also worth

noting that the intensities of these bands are relatively weak, suggesting that no significant amount of adsorbed SO_2 species were present on the surface. On the other hand, features at 3675, 3650, 3558, 3500 cm^{-1} were also detected during SO_2 exposure. The three positive peaks at 3675, 3650 (shoulder) and 3558 cm^{-1} are assigned to perturbed P–OH, and perturbed OH groups associated with the extra-framework Al and Cu, respectively [72, 74, 93]. The appearance of a broad band at 3500 cm^{-1} might be due to hydrogen-bonded OH [162].

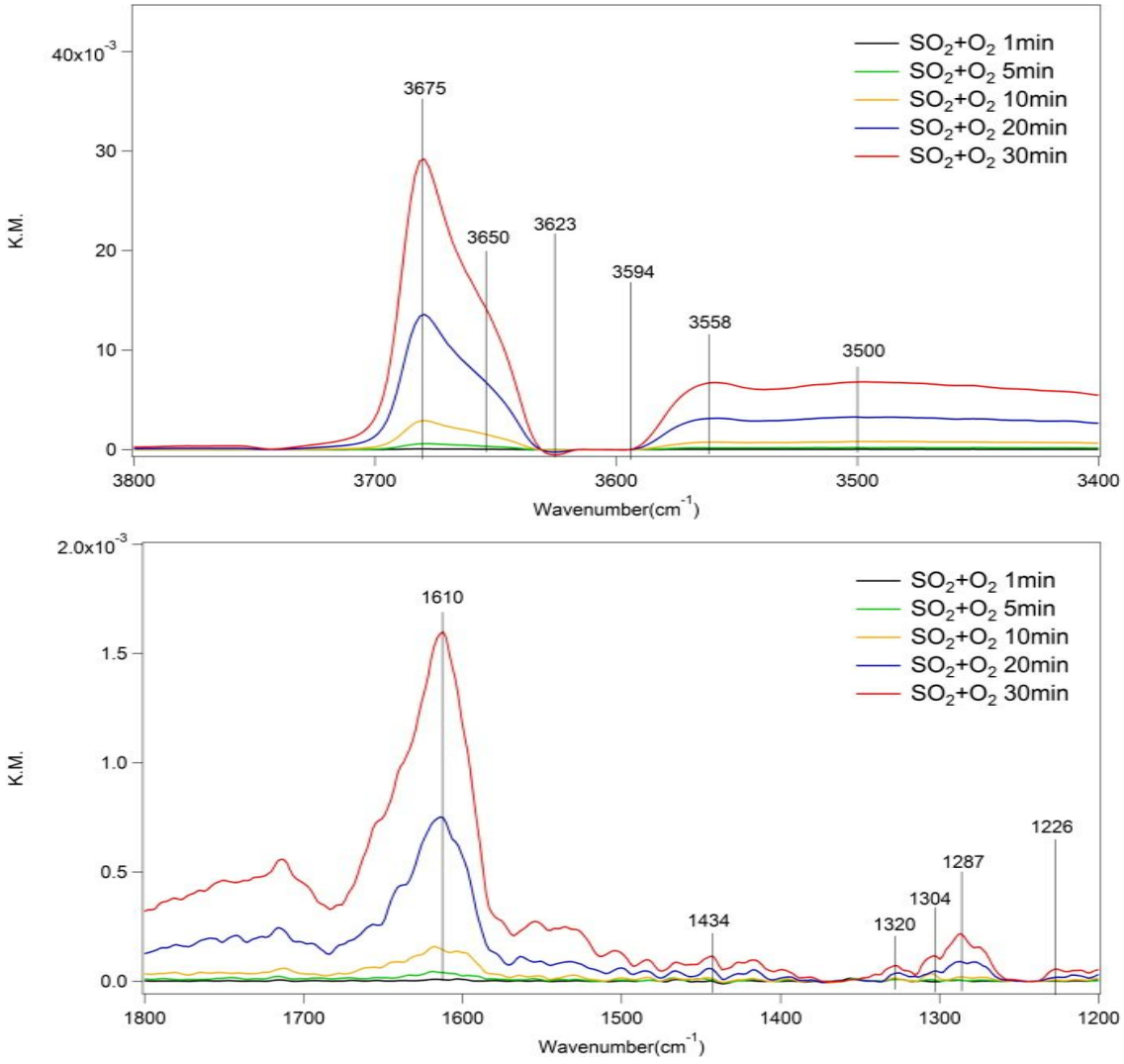

Figure 7.3 DRIFTS spectra of adsorbed SO_2 + O_2 at 100°C (Experiment conditions: 100°C exposure to 200 ppm SO_2, 10% O_2, total flow rate 50 ml/min)

In addition, two negative peaks appeared at 3623 and 3594 cm^{-1} and were caused by the consumption by SO_2 of Si (OH) Al groups [74, 163] that are associated with the Brønsted acid sites. Indeed, it has been reported that –OH groups could be responsible for the adsorption of SO_2 [164, 165]. Marcu et al., proposed that SO_2 molecules could adsorb via hydrogen bonding to one or two conveniently positioned surface hydroxyl groups on the zeolite to form hydrogen sulfite OH-OSO (HSO_3) or OH-OSO-HO [162]. Based on the DRIFTS results, it appears that SO_2 could coordinate with the Cu and/or CeO_2 sites as well as the surface hydroxyl groups (e.g., Si-OH-Al).

7.3.4 TPD of adsorbed $SO_2 + O_2$

Temperature programmed desorption (TPD) experiments were performed after the catalyst was exposed to SO_2 and O_2 to characterize SO_2 adsorption/desorption features while at the same time outlet SO_2 and SO_3 concentrations were measured. As shown in Figure 7.4, some amount of SO_2 desorbed from the surface during the TPD and interestingly, no SO_3 was detected. On the other hand, the overall SO_2 uptake is relatively small and most of the SO_2 desorbed from the Cu-SAPO-34 catalyst between 450-700^oC. Such data demonstrate that adsorbed SO_2 species could remain on the surface at temperatures below 450^oC. Two desorption peaks were observed at around 500^oC and 700^oC and are believed to originate from different adsorption sites. The lower temperature peak is assigned to SO_2 chemisorbed on the catalyst surface as sulfate species as observed in the DRIFTS spectra (shown in Figure 7.3). And the higher temperature peak is likely due to decomposition of $CuSO_4$ or $Ce_x(SO_4)_y$ species that formed, as these typically decompose to SO_2 at a relatively high temperature [166, 167]. This observation

is consistent with other studies, which noted the formation of metal sufate during sulfur poisoning [75, 159, 161].

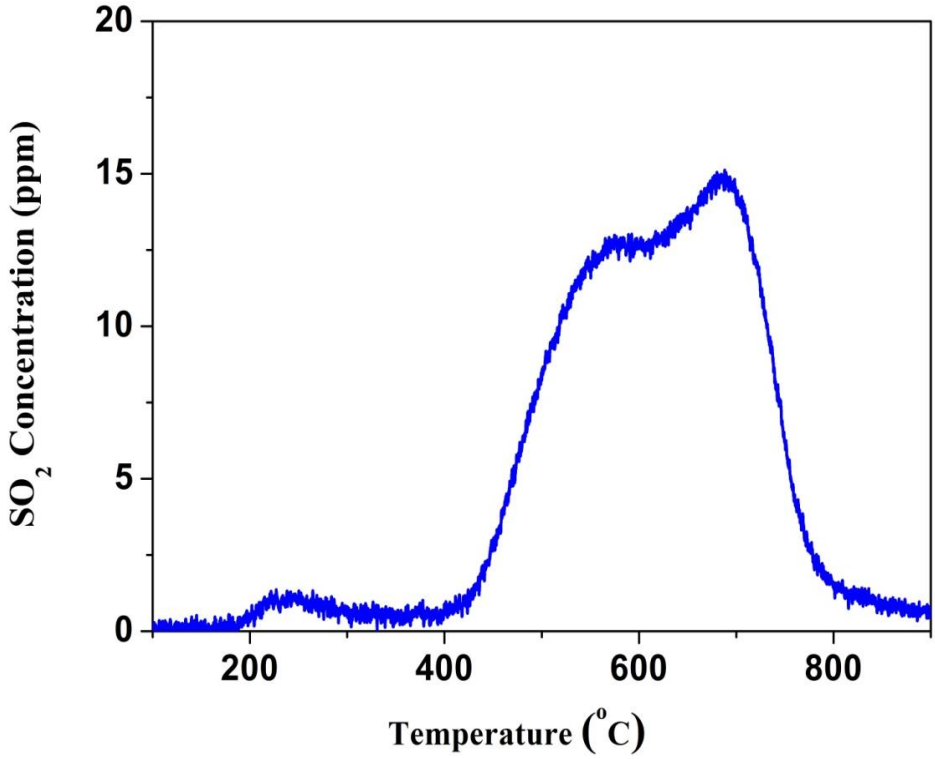

Figure 7.4 SO_2 concentration during SO_2-TPD (Experimental condition: 200 ppm SO_2, 10 % O_2 at 150 ^oC, purged by N_2, then TPD with a heating rate of 10^oC/min in N_2)

7.3.5 Characterization of the interaction between SO_2 and NH_3

NH_3 adsorption is a key step in the SCR reaction [163], so in order to determine how SO_2 might impact this function, DRIFTS was used to characterize the surface during NH_3 and NH_3 + SO_2 co-adsorption. In the DRIFTS spectra taken during NH_3 adsorption, the catalyst was saturated with NH_3, so the band intensities provide an indication of the amount of NH_3 adsorbed on different acid sites. As shown in Figure 7.5, NH_3 adsorption results in a significant feature at 1460 cm^{-1} and a weaker one at 1617 cm^{-1}. The former is assigned to the NH_4^+ vibrations, via NH_3 adsorbed on Brønsted acid sites, and the latter

to NH_3 bound to Lewis acid sites [74]. In comparison, the same catalyst was subsequently exposed to both NH_3 and SO_2. After a 60 minute exposure, the band intensities during the interaction of NH_3 and SO_2 were compared with that during the NH_3 adsorption itself. Very interestingly, the band corresponding to NH_3 on the Lewis acid sites (1617 cm^{-1}) slightly decreased and the band intensity for the NH_4^+ vibration increased.

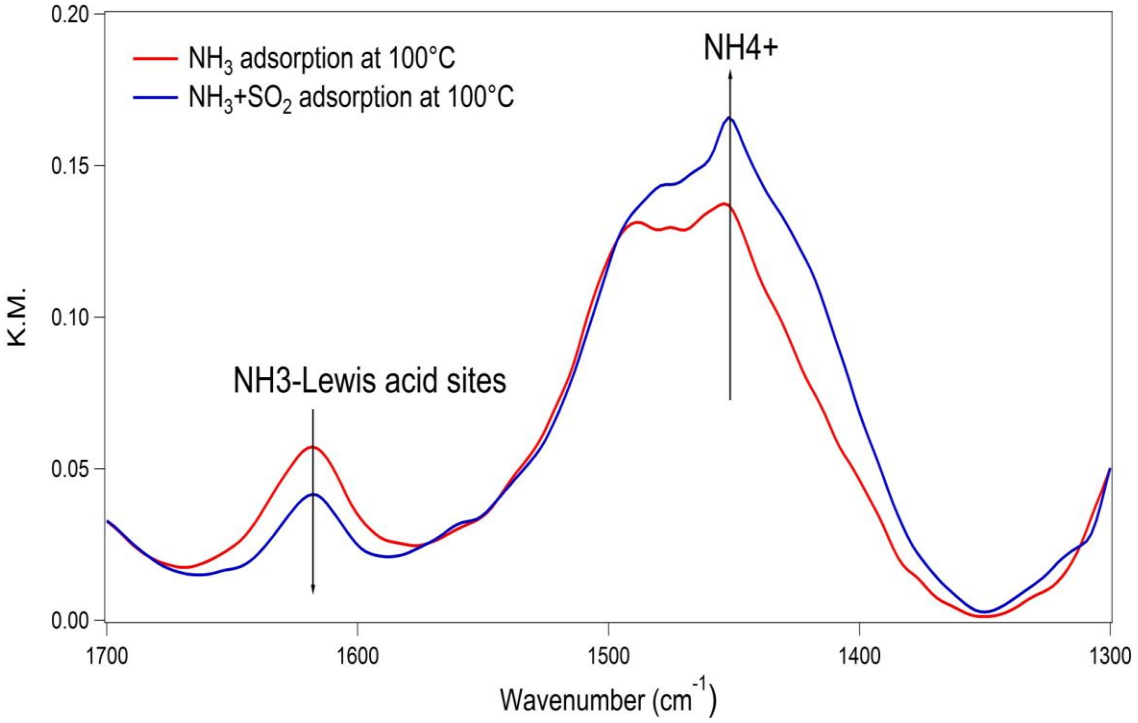

Figure 7.5 DRIFTS spectra obtained after a 60 minute exposure to NH_3 and NH_3 + SO_2 at 100°C (Experiment conditions: 500 ppm NH_3, 10% O_2, 200 ppm SO_2 (if added) in a He balance)

7.3.6 NH_3-TPD and NH_3+SO_2-TPD

TPD experiments were run after the catalyst was exposed to both NH_3 and SO_2. As shown in Figure 7.6, during the TPD, with the catalyst just exposed to SO_2, desorption peaks were observed at temperatures higher than 450°C. However, with exposure to both NH_3 and SO_2, another peak was observed at about 400°C, with the onset of the desorption

noted at ~300°C. This extra SO_2 feature is associated with the enhancement in the NH_4^+ band observed in the DRIFTS spectrum detailed previously. These data taken together suggest that some surface ammonium-sulfate or ammonium-bisulfate species were formed and decomposed releasing SO_2 at lower temperature.

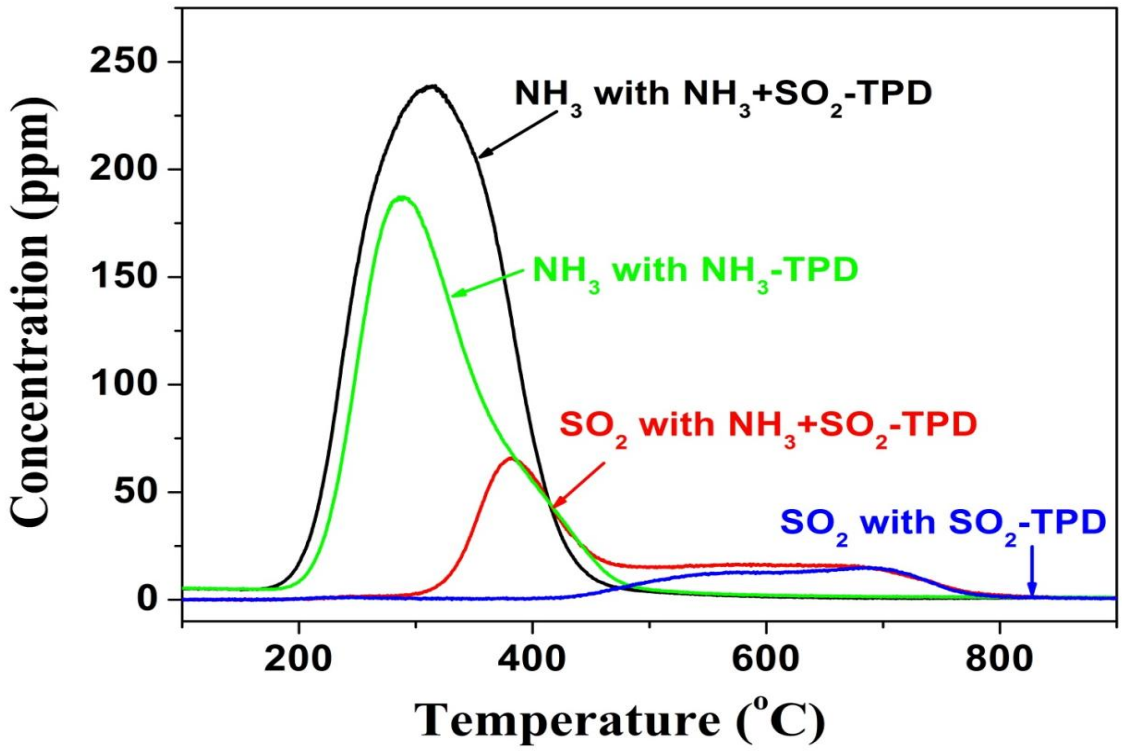

Figure 7.6 TPD results after exposure to SO_2 + NH_3, NH_3 or SO_2 (Experimental condition: 500 ppm NH_3 (if added), 200 ppm SO_2 (if added), 10 % O_2 at 150 °C, purged by N_2, then TPD with a heating rate of 10°C/min in N_2)

At the same time, NH_3 profiles during the TPD in the absence or presence of SO_2 clearly show that a significantly larger amount of NH_3 was released when the catalyst was also exposed to SO_2 during the adsorption process. Indeed, the ratio of this increased amount of NH_3 to the amount of the additional SO_2 that was released at 400°C is 2:1. This coincides with the typical decomposition reaction of $(NH_4)_2SO_4$ according to

$$(NH_4)_2SO_{4(S)} \leftrightarrow NH_4HSO_{4(S)} + NH_{3(g)} \text{ and} \qquad (7.1)$$

$$NH_4HSO_{4(s)} \leftrightarrow NH_{3(g)} + SO_{2(g)} + {}^{1}/_{2}\ O_{2(g)} + H_2O_{(g)}, \quad (7.2)$$

in which involves the initial decomposition to NH_3 and NH_4HSO_4 at around 300°C and the surface NH_4HSO_4 species continue to decompose to NH_3 and SO_2 at higher temperature. Therefore the overall released NH_3 and SO_2 is in a 2:1 ratio.

7.3.7 Interaction between SO_2 and pre-adsorbed NO_x

The interaction between SO_2 and NO_x was investigated by comparing the DRIFTS spectra taken during catalyst exposure to NO + O_2 and then exposing the sample to SO_2 after a NO + O_2 exposure.

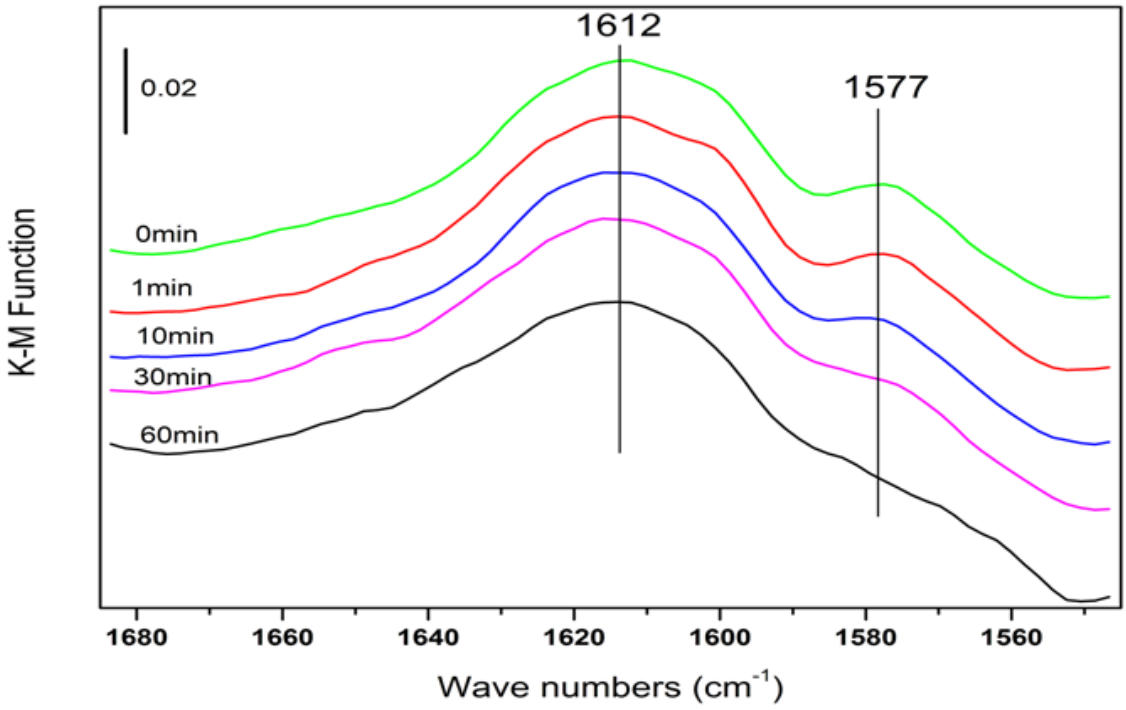

Figure 7.7 DRIFTS spectra taken during exposure to SO_2 after exposure to NO + O_2 at 150°C (Experimental conditions: 500 ppm NO, 10%O_2, then followed by 200 ppm SO_2)

As shown in Figure 7.7, bands at 1612 and 1577 cm^{-1} were immediately observed during exposure to NO + O_2. Based on literature studies, these two peaks are tentatively

assigned to adsorbed bidentate (1577 cm^{-1}) and bridging (1608 cm^{-1}) nitrate species [168-170]. It is also worth noting that the band at 1577 cm^{-1} was not observed during NO + O_2 adsorption on H-SAPO-34, therefore is considered to be a unique feature for bidentate nitrate formed on Cu sites. When the sample was exposed to SO_2 after it was exposed to NO + O_2, the feature at 1577 cm^{-1}, which is assigned to the nitrates formed on Cu sites, quickly disappeared with time. Thus, SO_2 affected NO_x adsorption, specifically the nitrate species formed on the Cu sites.

7.3.8 Interaction between NO_x and pre-adsorbed SO_2

The interaction between NO_x and pre-adsorbed SO_2 was then investigated by exposing the sample to SO_2 and O_2 first, followed by a He purge, and then exposure to NO + O_2. The DRIFTS results during the NO_x exposure are shown in Figure 7.8.

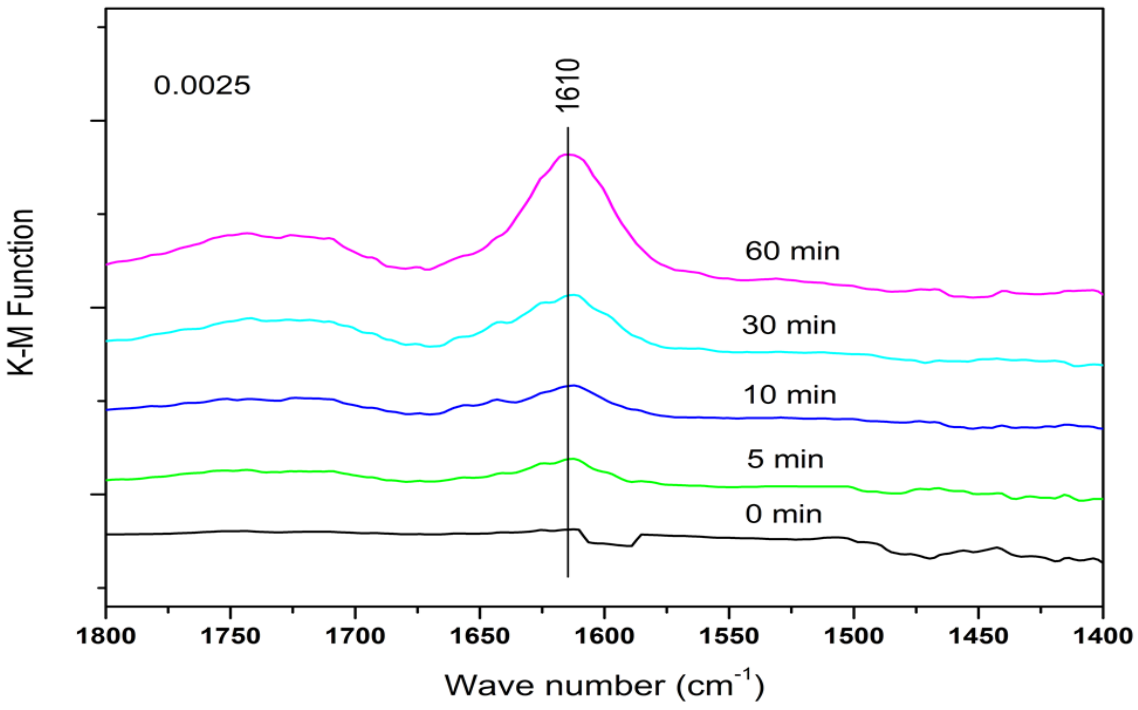

Figure 7.8 DRIFTS spectra taken during exposure to NO + O_2 after exposure to SO_2 at 150°C (Experimental condition: 200 ppm SO_2 over Cu-SAPO-34 at 150 °C, and then followed 500 ppm NO, 10% O_2 in He, total flow rate 50 ml/min)

With NO_x exposure, a weak peak appeared at 1610 cm^{-1}, assigned to the bridging nitrate species. No bidentate nitrate ad-species (1577 cm^{-1}) appeared. In addition, the intensity of the NO_x adsorption peak in Figure 7.8 is less than that in Figure 7.7, demonstrating that less NO_x adsorbed when the sample was first exposed to $SO_2 + O_2$, especially the NO_x associated with the Cu sites. These data again proves that SO_2 competes with NO_x for surface adsorption sites.

7.3.9 TPD of adsorbed NO_x and adsorbed $NO_x + SO_2$

In order to further confirm the competitive adsorption of NO_x and SO_2, two temperature programmed desorption experiments were conducted for comparison. Figure 7.9(a) shows the concentrations during a TPD after the catalyst was exposed to $NO + O_2$. A significant amount of NO (12.7 µmol/g) and NO_2 (31.1 µmol/g) desorbed from the catalyst surface. NO_2 was the primary species desorbed at temperatures below 375°C, and at higher temperature, NO – with equilibrium limitations between NO and NO_2 playing a role. With SO_2 added during $NO + O_2$ adsorption, much less NO and NO_2 were released from the surface during the TPD experiment as compared to that in the absence of SO_2 during adsorption as shown in Figure 7.9 (b). In addition, some SO_3 (41.6 µmol/g) desorption was observed at temperatures above 400°C and a large amount of SO_2 (126 µmol/g) desorbed at higher temperatures. This further proves SO_2 decreases NO_x adsorption extent. It is also worth mentioning that no SO_3 was detected during the TPD taken after SO_2 adsorption over the Cu-SAPO-34 catalyst (Figure 7.4), while some SO_3 was formed on the catalyst during the co-adsorption process of both NO_x and SO_2. It has been reported that SO_2 could be oxidized by NO_2 to form SO_3 [169]. Therefore, it is

likely that SO_2 was oxidized by NO_2 into SO_3, which was released at a relatively high temperature.

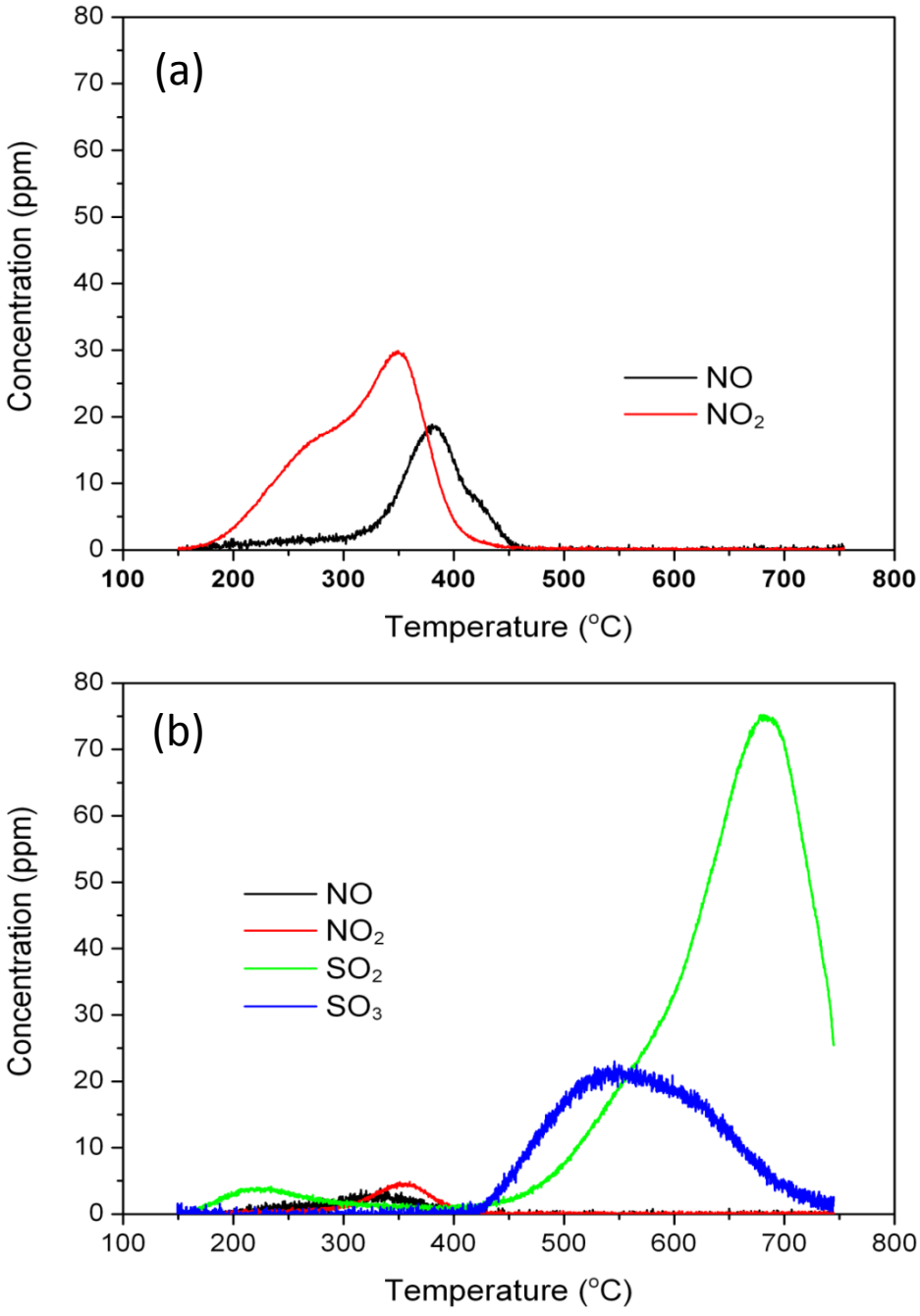

Figure 7.9 TPD after exposure to (a) NO + O_2 and (b) SO_2 + NO + O_2 (Experimental conditions: 500 ppm NO, 10% O_2, 200 ppm SO_2 (if added) at 150°C, purged by N_2, followed by the TPD with a heating rate of 10°C/min in N_2)

Based on the TPD and DRIFTS characterization data, exposure to SO_2 results in sulfate formation, which in turn leads to two possible degradation modes. First, there is clear evidence of $(NH_4)_2SO_4$ formation. Such species can foul surface sites, block pores and in general limit reactant/catalyst interactions. Second, exposure to SO_2 preferentially blocked key NO_x adsorption sites on the surface. Specifically, formation of bidentate nitrate species, previously identified as the signature of NO_x stored on Cu sites, was considerably inhibited in the presence of SO_2. Of particular note, catalyst performance was only inhibited below 300°C. Based on the TPD results, it is in this temperature range that the $(NH_4)_2SO_4$ decomposes. This therefore suggests that the formation of the $(NH_4)_2SO_4$ is the low temperature SO_2 poisoning degradation mode.

7.3.10 Regeneration of the SO_2 poisoned catalyst by O_2/N_2

After SO_2 exposure, the Cu/SAPO-34 sample was heated to different temperatures (300 to 700^{o}C) in order to investigate the potential SCR reaction activity recovery. Figure 7.10 shows the NO conversion at 260^{o}C on the catalysts treated at different temperatures after 50 ppm SO_2 poisoning. NO conversion in the presence of 50 ppm SO_2 reached only 61% of the original activity obtained in the absence of SO_2. However, if the catalyst was heated at 300^{o}C for 12 hours after the SO_2 exposure, the catalyst activity attained 68% of the original SCR performance. Furthermore, when the regeneration temperature was increased to 500^{o}C, at which the $(NH_4)_2SO_4$ surface species were completely removed, 90% of the SCR performance was recovered, which strongly suggests that the SO_2 poisoning effect was mainly due to the formation of $(NH_4)_2SO_4$. Interestingly, there is still 10% NO conversion loss even if the $(NH_4)_2SO_4$ was removed from the catalyst surface. This is due to the formation of small amounts of $CuSO_4$ or

$Ce_x(SO_4)_y$ on the catalyst. As previously discussed, these species typically decompose at a relatively high temperature.

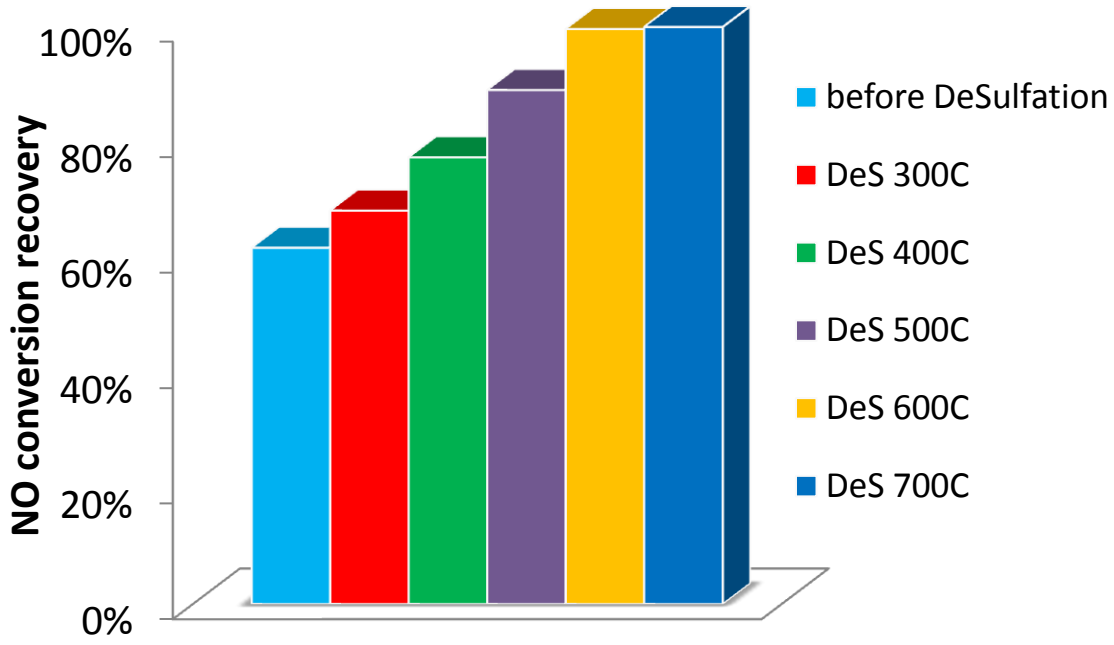

Figure 7.10 NH_3-SCR activity after stepwise desulfation at different temperatures (Experimental condition: 100 ppm SO_2, 500 ppm O_2 was introduced at 130 ^oC for 3h, NH_3-SCR activity is collected at 250 ^oC)

As shown in Figure 7.11, indeed, with increasing the temperature above 500^{o}C, the NO conversion was further recovered. Almost 100% regeneration was achieved. Surprisingly, with the highest temperature exposure, higher low temperature activity was obtained relative to the fresh sample, which has been previously observed [72] and is likely due to further ion-exchange during the high temperature exposure.

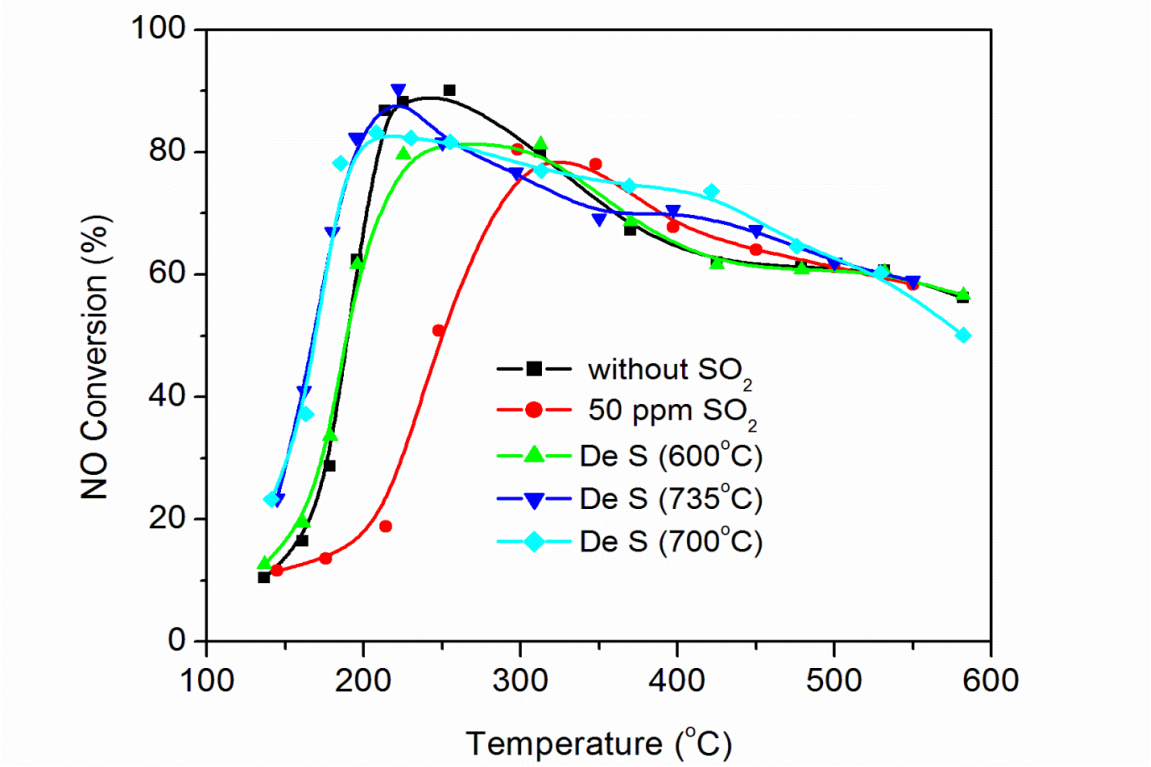

Figure 7.11 NH_3-SCR SCR activity with and without SO_2 and after a high temperature desulfation exposure (Reaction conditions: 500ppm NH_3, 500ppm NO, 50ppm SO_2, 10% O_2, calcination at 600, 700, or 735°C in 10% O_2)

7.4 Conclusions

In this study, the effect of SO_2 poisoning on the SCR reaction activity of a Cu-SAPO-34 catalyst was characterized. SO_2 did inhibit the reaction, specifically in the low temperature region (< 300°C). The SO_2 poisoning mechanism involves the formation of $(NH_4)_2SO_4$ species that may poison the active sites and block the zeolite pores. SO_2 adsorption also competes with NO_x adsorption on the Cu sites, also potentially contributing to the inhibition observed. In addition, the formation of $CuSO_4$ or $Ce_x(SO_4)_y$ may also result in some activity loss. SO_2 poisoning was reversible with NO conversions recovered after high temperature treatment in an O_2/N_2 mixture.

Chapter 8 Conclusions and Recommendations

The focus of this dissertation is the characterization of the selective catalytic reduction of NO_x by NH_3 (NH_3-SCR) reaction over small pore Cu-CHA catalysts (Cu-SAPO-34 and Cu-SSZ-13). This work is an effort towards understanding the catalytic performance, surface chemistry, acid properties, Cu structures, Cu loading effects and deactivation mechanism (hydrothermal aging and sulfur poisoning) through the application of bench-scale and micro-scale catalytic reactor systems combined with material characterization techniques. The present findings suggest that all of the listed factors are important for the NH_3-SCR reaction.

8.1 Conclusions

8.1.1 Reaction mechanism of NH_3-SCR over Cu-SAPO-34

An in-situ DRIFTS study was carried out with a Cu-SAPO-34 catalyst to study the elementary steps occurring in the NH_3-SCR reaction and to identify the key pathways to produce N_2 and H_2O. The results demonstrate that the formation of surface nitrates and nitrites are the key steps in NH_3-SCR over Cu-SAPO-34. The results reveal that the NO, $NO+O_2$ and NO_2 adsorption process all resulted in the formation of surface nitrates and nitrites species on the catalyst surface. This was evidenced by the detection of DRIFTS features associated with NO^+ species and surface nitrates with different structures. NO^+ could easily combine with surface oxygen or coordinated oxygen to form NO_2^-. In order to study the reactivity of NO, $NO+O_2$ and NO_2 with surface NH_3, these combinations of reactants were individually introduced over NH_3 pre-adsorbed sample at 200°C. The

DRIFTS spectra indicate that the reaction between NO itself and surface NH_3 was inactive. However, with the presence of O_2, the pre-adsorbed NH_3 was rapidly consumed by NO, indicating that the inclusion of O_2 essentially activated the NH_3-SCR reaction. Indeed, it was found that NO+O_2 formed a larger amount of surface NO^+ and NO_3^- than NO itself. In other words, NO+O_2 significantly promoted the surface NO_x storage capacity therefore accelerated its reaction with surface NH_3. In addition, the interaction between NO_2 and surface NH_3 led to the formation of NH_4NO_3 surface species. NH_4NO_3 is typically considered to be detrimental to the SCR reaction since it may block the active sites at low temperature. However, it was found to be rapidly consumed by NO at temperatures as low as 100°C on the Cu-SAPO-34 catalyst. Furthermore, the participation of nitrite species in the SCR reaction is very likely to occur. The interaction between surface nitrites and NH_3 forms NH_4NO_2, which is very unstable and readily decomposes to N_2 and H_2O at temperatures higher than 80°C. Therefore, it could be the key in the low-temperature activity of Cu-SAPO-34 due to its high reactivity. However, the evolution of surface nitrites species was not detected in the DRIFTS spectra since it overlapped with the zeolite framework vibration modes in the same region. Furthermore, the role of Brønsted acid sites and Lewis acid sites in the NH_3-SCR was investigated. Lewis acid sites act as the active centers for the NH_3-SCR reactions and the Brønsted acid sites provided more sites for NH_3 adsorption instead of being directly involved in the SCR reaction.

8.1.2 Zeolite acidity and Cu structure characterizations in Cu-SAPO-34

With the knowledge gained about the mechanism, the acidity changes as a function of Cu loading on Cu-SAPO-34 were probed. Furthermore, the structure-

activity relationship was studied by preparing a series of SAPO-34 catalysts with Cu loadings ranging from 0.7 to 3.0 wt%. The Cu-SAPO-34 samples were prepared using a solid state ion exchange (SSIE) method in which a physical mixture of nano-sized CuO and and H-SAPO-34 material was thermally treated at 800°C in air. The acid properties of the catalysts were characterized by NH_3-TPD and in-situ DRIFTS. More Cu exchanged at the Brønsted acid sites with increasing amounts of Cu precursor during the SSIE, resulting in a monotonic reduction in the total number of Brønsted acid sites. Interestingly, the Lewis acid sites created by Cu ions linearly increased with increasing Cu loading up to 2.0 wt% and then only slightly increased with a further increase to 3.0 wt%. XRD, H_2-TPR, UV-vis and DRIFTS were used to probe Cu structures. From the DRIFTS, two different perturbed T-O-T vibrations were observed for both the zeolite skeleton and NH_3 adsorption spectra, indicating the existence of two different types of exchanged Cu species. This is also consistent with the results of NO adsorption DRIFTS spectra, in which two different Cu^{2+} sites were observed to adsorb NO molecules. One of the sites was assigned as isolated Cu^{2+} species and the other could be another type of exchanged Cu site, possibly Cu_xO_y clusters (dimeric or oligomeric Cu species). The isolated Cu^{2+} on each sample was further identified by UV-vis and quantified by H_2-TPR experiments. Based on these results, isolated Cu^{2+} species were found to be the active sites of NH_3-SCR at low temperature. Furthermore, CuO phases were detected on the samples with high Cu loadings via XRD. The presence of Cu_xO_y may promote NH_3 oxidation by O_2, leading to the observed decrease in standard SCR performance at high temperature.

8.1.3 Excellent NH_3-SCR performance over a Cu-SSZ-13 catalyst prepared by SSIE

The solid state ion exchange method was further developed to synthesize Cu-SSZ-13 catalysts with excellent NH_3-SCR performance and durable hydrothermal stability. After the solid state ion exchange (SSIE) process, the SSZ framework structure and surface area was maintained as evidenced by BET surface area and XRD measurements. The obtained Cu-SSZ-13 catalysts showed very high activity and N_2 selectivity. The incorporation of Cu with the zeolite Brønsted acid sites were probed by NH_3 temperature programmed desorption (NH_3-TPD) combined with in-situ DRIFTS. NH_3-TPD results reveal that the total number of Lewis acid sites on the as-prepared Cu-SSZ-13 was larger than that of H-SSZ-13, demonstrating that Cu successfully exchanged with Brønsted acid sites creating additional Lewis acid sites. DRIFTS spectra obtained during NH_3 adsorption further confirmed this. The tetrahedral cation-oxygen-tetrahedral cation (T-O-T) framework vibrations perturbed by ion exchanged copper species were observed in the DRIFTS spectra. These bands are considered signatures of exchanged Cu^{2+} sites on the zeolite materials and therefore again confirms the formation of active Cu^{2+} sites. In addition, the T-O-T band corresponding to the isolated Cu^{2+} was more intense than the band related to the Cu_xO_y clusters. Therefore, isolated Cu^{2+} sites, which are responsible for the low temperature SCR activity, were believed to be selectively formed by SSIE. Furthermore, the hydrothermal stability of the as-prepared Cu-SSZ-13 was estimated by treating the samples at 750°C for 16 hours in 10% H_2O and 10% O_2. After the hydrothermal aging process, the NO conversions were maintained in the full temperature window, which is indicative of the excellent hydrothermal stability of the as-prepared Cu-SSZ-13.

8.1.4 Comparison between Cu-SSZ-13 and Cu-SAPO-34 upon hydrothermal aging

The impact of hydrothermal aging on both Cu-SSZ-13 and Cu-SAPO-34 were the compared. After 750°C hydrothermal aging for 16h, the NO conversions on both materials were maintained. However, a significant difference appeared after hydrothermal aging at 800°C. The Cu-SSZ-13 sample resulted in remarkably lower NO conversions at all temperatures tested while the Cu-SAPO-34 still maintained its high SCR activity. In fact, the NO conversions over Cu-SAPO-34 were even enhanced at temperatures below 350°C, due to a post solid state ion exchange process occurring during the high temperature treatment. Indeed, the NH_3-TPD results suggest an increase in strong Lewis acid sites in/on the Cu-SAPO-34 sample after hydrothermal aging at 750°C and 800°C. However, all types of acid sites were decreased by hydrothermal aging the Cu-SSZ-13 sample, verified by in-situ DRIFTS of NH_3 and NO adsorption experiments. Furthermore, hydrothermal aging at 800°C resulted in a significant reduction in the amount of exchanged Cu^{2+} sites and accordingly, the SCR activity on Cu-SSZ-13 was dramatically decreased by hydrothermal aging. As for the framework structure, XRD showed that some CHA phases disappeared after 800°C hydrothermal aging on Cu-SSZ-13; however, all the diffraction peaks still existed on Cu-SAPO-34 after the same aging treatment. The NH_3 oxidation activity over Cu-SSZ-13 increased after 750°C hydrothermal aging, caused by the aggregation of isolated Cu^{2+} sites into CuO particles. Further increasing the aging temperature to 800°C led to a decrease in NH_3 oxidation activity, possibly due to the severe damage of the framework structure as indicated by the loss of crystallinity in XRD. On the other hand, no significant change of NH_3 oxidation activity was observed on Cu-SAPO-34 after hydrothermal aging at 750°C

and 800°C, proving that Cu-SAPO-34 structure is more robust to hydrothermal aging than Cu-SSZ-13.

8.1.5 SO_2 poisoning impact on the NH_3-SCR reaction over Cu-SAPO-34

Sulfur poisoning is a durability issue for Cu-SAPO-34 in NH_3-SCR reactions, thus the impact of SO_2 on the SCR performance and the deactivation mechanism were investigated. The data showed that SO_2 mainly inhibited SCR activity at low temperature (<300°C), while no evident effect was observed at higher temperatures. Temperature programmed desorption of SO_2 indicated that SO_2 desorbed starting from 300°C, thus the lack of impact noted at high temperature. SO_3 was only formed by SO_2 oxidation at temperatures above 350°C therefore the drop of low temperature performance with the presence of SO_2 was not be caused by SO_3 formed via SO_2 oxidation DRIFTS spectra indicated the formation of surface SO_2 and sulfate species during SO_2 adsorption. When SO_2 was introduced over the NH_3 pre-adsorbed sample at low temperature, some $(NH_4)_2SO_4$ like species were formed on the surface. The formation of $(NH_4)_2SO_4$ is further confirmed by the temperature programmed desorption (TPD) experiments. When NH_3 and SO_2 were simultaneously introduced on the catalyst, more NH_3 was adsorbed on the surface as compared to the NH_3 uptake during NH_3-SCR, and was also accompanied by a new desorption peak of SO_2 at around 400°C in comparison to the SO_2-TPD result. The ratio of this increased amount of NH_3 to the amount of additional SO_2 that adsorbed with the presence of both NH_3 and SO_2 turned out to be 2:1, providing evidence that $(NH_4)_2SO_4$ was formed at low temperature. The competitive adsorption of SO_2 with NO_x was also studied by DRIFTS spectra combined with TPD experiments. The results showed that the NO_x adsorption capacity decreased in the presence of SO_2 in the feed.

Overall, the low temperature deactivation mode is attributed to both the formation of ammonium sulfate species and the competitive adsorption of SO_2 with NO_x adsorption. Fortunately, the SO_2 poisoning effect was reversible. When the catalyst was thermally treated at 700°C, the surface sulfur species decomposed and the original SCR activity was retained.

8.2 Recommendations for future work

i. The NH_3-SCR reaction mechanism was studied using in-situ DRIFTS. However, all the DRIFTS experiments were performed in the absence of water. Similar studies should be performed in the presence of water. In addition, the SCR reaction pathway proposed in this study could be further combined with the kinetic modeling.

ii. It was concluded that isolated Cu^{2+} sites were responsible for NH_3-SCR activity at low temperature. However, the high temperature active sites still need further investigation. High temperature NO conversions were limited by the non-selective NH_3 oxidation, which was enhanced by the Cu_xO_y species. However, the correlation of the overall NO_x reduction rate and the amount of active sites at high temperature still needs to be carefully probed. Additionally, the structures of the Cu_xO_y clusters need to be accurately characterized.

iii. CuO particles were detected in both Cu-SAPO-34 and Cu-SSZ-13 catalysts prepared by the solid state ion exchange method. CuO is known to be inactive for NH_3-SCR and converts NH_3 to NO_x at high temperature, therefore decreasing the SCR performance. Therefore, the solid state method could be further improved by somehow eliminating the formation of CuO from the catalysts.

iv. The data showed that the Cu-SAPO-34 was more resistant to hydrothermal aging than Cu-SSZ-13. Detailed material characterization could be conducted to explain the intrinsic aging mechanisms for Cu-SSZ-13 and Cu-SAPO-34.

v. The impact of SO_2 poisoning of Cu-SAPO-34 was studied. However, the upstream oxidation catalyst oxidizes some SO_2 to SO_3. SO_2 and SO_3 may have different deactivation effects towards the SCR catalysts and with the presence of H_2O, some H_2SO_4 is also likely to form. Therefore, a similar study can be extended with the systems including SO_3 and/or H_2O.

References

[1] National nitrogen oxides emissions by source sector (NEI 2011 v1 GPR), *http://www.epa.gov/air/emissions/nox.htm*, in.

[2] Air Quality Reference Guide for the Houston-Galvestion-Brazoria Area, *http: //www.h-gac.com/taq/airquality/raqpc*, in.

[3] G.M. Parsons, Clean diesel and after-treatment systems, *http://savebiodiesel.com/ chevron_dpf.pdf*, in.

[4] Emission standards of heavy-duty truck and bus engines, *http://www.dieselnet.com /standards/eu/hd.php*, in.

[5] Cummins aftertreatment system, *http://cumminsengines.com/cummins-aftertreatment-system*, in.

[6] M. Shrivastava, A. Nguyen, Z. Zheng, H.W. Wu, H.S. Jung, Kinetics of soot oxidation by NO_2, *Environmental Science & Technology*, 44 (2010) 4796-4801.

[7] A. Russell, W.S. Epling, Diesel Oxidation Catalysts, *Catalysis Reviews*, 53 (2011) 337-423.

[8] A. Setiabudi, M. Makkee, J.A. Moulijn, The role of NO_2 and O_2 in the accelerated combustion of soot in diesel exhaust gases, *Applied Catalysis B: Environmental*, 50 (2004) 185-194.

[9] Q. Ye, L. Wang, R.T. Yang, Activity, propene poisoning resistance and hydrothermal stability of copper exchanged chabazite-like zeolite catalysts for SCR of NO with ammonia in comparison to Cu/ZSM-5, *Applied Catalysis A: General*, 427–428 (2012) 24-34.

[10] J.Y. Luo, H. Oh, C. Henry, W. Epling, Effect of C_3H_6 on selective catalytic reduction of NO_x by NH_3 over a Cu/zeolite catalyst: A mechanistic study, *Applied Catalysis B: Environmental*, 123–124 (2012) 296-305.

[11] N.S. Hom, L.S. Steven, B.M. Ashish, Interactions of sulfur oxides with diesel oxidation catalysts (DOCs), in: Novel Materials for Catalysis and Fuels Processing, *American Chemical Society*, 2013, pp. 117-155.

[12] M. Kaneeda, H. Iizuka, T. Hiratsuka, N. Shinotsuka, M. Arai, Improvement of thermal stability of NO oxidation Pt/Al_2O_3 catalyst by addition of Pd, *Applied Catalysis B: Environmental*, 90 (2009) 564-569.

[13] M. Chen, L.D. Schmidt, Morphology and composition of Pt-Pd alloy crystallites on SiO_2 in reactive atmospheres, *Journal of Catalysis*, 56 (1979) 198-218.

[14] M. Skoglundh, L.O. Lowendahl, J.E. Ottersted, Combinations of Platinum and Palladium on alumina supports as oxidation catalysts, *Applied Catalysis*, 77 (1991) 9-20.

[15] T. Watanabe, Kawashima, K., Tagawa, Y., Tashiro, K., Anoda, H., Ichioka, K., Sumiya, S. and Zhang, G., New DOC for light duty diesel DPF system, in, *SAE Technical Paper Series*, 2007-01-1920.

[16] P.L. Hansen, A.M. Molenbroek, A.V. Ruban, Alloy formation and surface segregation in zeolite-supported Pt-Pd bimetallic catalysts, *Journal of Physical Chemistry B*, 101 (1997) 1861-1868.

[17] F. Haass, H. Fuess, Structural characterization of automotive catalysts, *Advanced Engineering Materials*, 7 (2005) 899-913.

[18] A. Morlang, U. Neuhausen, K.V. Klementiev, F.W. Schutze, G. Miehe, H. Fuess, E.S. Lox, Bimetallic Pt/Pd diesel oxidation catalysts - Structural characterisation and catalytic behaviour, *Applied Catalysis B-Environmental*, 60 (2005) 191-199.

[19] O.I. Smith, Fundamentals of soot formation in flames with application to diesel engine particulate emissions, *Progress in Energy and Combustion Science*, 7 (1981) 275-291.

[20] B. van Setten, M. Makkee, J.A. Moulijn, Science and technology of catalytic diesel particulate filters, *Catalysis Reviews-Science and Engineering*, 43 (2001) 489-564.

[21] M. Matti Maricq, Chemical characterization of particulate emissions from diesel engines: A review, *Journal of Aerosol Science*, 38 (2007) 1079-1118.

[22] O. Salvat, P. Marez, G. Belot, Passenger car serial application of a particulate filter system on a common rail direct injection diesel engine in, *SAE Paper*, Proc Soc Auto Eng 2000. World Congress. Detroit, Michigan, U.S.A.

[23] M. Khair, J. Lemaire, S. Fishcher, Achieving heavy-duty diesel NOx/PM levels below the EPA 2002 Standards - an integrated solution. , in, *SAE Paper*, Proc Soc Auto Eng 2000. World Congress. Detroit, Michigan, U.S.A. .

[24] Diesel retrofit, *http://www.meca.org/diesel-retrofit/what-is-retrofit*, in.

[25] K. Chen, Temperature excursions during regeneration of diesel particulate filters in, 2010.

[26] G. Liu, P. X. Gao, A review of NO_x storage/reduction catalysts: mechanism, materials and degradation studies, in, *Catalysis Science & Technology*, 2011, pp. 552-568.

[27] I. Nova, L. Lietti, L. Castoldi, E. Tronconi, P. Forzatti, New insights in the NO_x reduction mechanism with H_2 over Pt-Ba/gamma-Al_2O_3 lean NO_x trap catalysts under near-isothermal conditions, *Journal of Catalysis*, 239 (2006) 244-254.

[28] L. Lietti, I. Nova, P. Forzatti, Role of ammonia in the reduction by hydrogen of NO_x stored over Pt-Ba/Al_2O_3 lean NOx trap catalysts, *Journal of Catalysis*, 257 (2008) 270-282.

[29] W.P. Partridge, J. S. Choi, NH_3 formation and utilization in regeneration of Pt/Ba/Al_2O_3 NO_x storage-reduction catalyst with H_2, *Applied Catalysis B-Environmental*, 91 (2009) 144-151.

[30] I.S. Pieta, W.S. Epling, M. Garcia-Dieguez, J.Y. Luo, M.A. Larrubia, M.C. Herrera, L.J. Alemany, Nanofibrous Pt-Ba Lean NO_x trap catalyst with improved sulfur resistance and thermal durability, *Catalysis Today*, 175 (2011) 55-64.

[31] A. Kumar, M.P. Harold, V. Balakotaiah, Isotopic studies of NO_x storage and reduction on Pt/BaO/Al_2O_3 catalyst using temporal analysis of products, *Journal of Catalysis*, 270 (2010) 214-223.

[32] A. Kumar, M.P. Harold, V. Balakotaiah, Estimation of effective diffusivity of stored NO_x in the Barium phase of Pt/BaO/Al_2O_3 catalysts using TAP, *Industrial & Engineering Chemistry Research*, 49 (2010) 10334-10340.

[33] R.J. Gorte, Ceria in Catalysis: From Automotive Applications to the Water Gas Shift Reaction, *Aiche Journal*, 56 (2010) 1126-1135.

[34] S. Damyanova, J.M.C. Bueno, Effect of CeO_2 loading on the surface and catalytic behaviors of CeO_2-Al_2O_3-supported Pt catalysts, *Applied Catalysis A-General*, 253 (2003) 135-150.

[35] H.C. Yao, Y.F.Y. Yao, Ceria in automotive exhaust catalysts: I. Oxygen storage, *Journal of Catalysis*, 86 (1984) 254-265.

[36] M. Hatanaka, N. Takahashi, T. Tanabe, Y. Nagai, K. Dohmae, Y. Aoki, T. Yoshida, H. Shinjoh, Ideal Pt loading for a Pt/CeO_2-based catalyst stabilized by a Pt–O–Ce bond, *Applied Catalysis B: Environmental*, 99 (2010) 336-342.

[37] Y. Ji, J.S. Choi, T.J. Toops, M. Crocker, M. Naseri, Influence of ceria on the NO_x storage/reduction behavior of lean NO_x trap catalysts, *Catalysis Today*, 136 (2008) 146-155.

[38] G. Jacobs, L. Williams, U. Graham, G.A. Thomas, D.E. Sparks, B.H. Davis, Low temperature water–gas shift: in situ DRIFTS-reaction study of ceria surface area on the evolution of formates on Pt/CeO_2 fuel processing catalysts for fuel cell applications, *Applied Catalysis A: General*, 252 (2003) 107-118.

[39] B. H, J. F, Catalytic reduction of nitrogen oxides, in, *Catalysis Today*, 1988.

[40] R.Q. Long, R.T. Yang, Catalytic performance of Fe-ZSM-5 catalysts for selective catalytic reduction of nitric oxide by ammonia, *Journal of Catalysis*, 188 (1999) 332-339.

[41] M. Iwamoto, H. Furukawa, Y. Mine, F. Uemura, S.I. Mikuriya, S. Kagawa, Copper(II) ion-exchanged ZSM-5 zeolites as highly-active catalysts for direct and continuous decomposition of nitrogen monoxide, *Journal of the Chemical Society-Chemical Communications*, (1986).

[42] M. Schwidder, S. Heikens, A. De Toni, S. Geisler, M. Berndt, A. Brueckner, W. Gruenert, The role of NO_2 in the selective catalytic reduction of nitrogen oxides over Fe-ZSM-5 catalysts: Active sites for the conversion of NO and of NO/NO_2 mixtures, *Journal of Catalysis*, 259 (2008).

[43] R.Q. Long, R.T. Yang, Reaction mechanism of selective catalytic reduction of NO with NH_3 over Fe-ZSM-5 catalyst, *Journal of Catalysis*, 207 (2002) 224-231.

[44] P.S. Metkar, N. Salazar, R. Muncrief, V. Balakotaiah, M.P. Harold, Selective catalytic reduction of NO with NH(3) on iron zeolite monolithic catalysts: Steady-state and transient kinetics, *Applied Catalysis B-Environmental*, 104 (2011) 110-126.

[45] D.W. Fickel, E. D'Addio, J.A. Lauterbach, R.F. Lobo, The ammonia selective catalytic reduction activity of copper-exchanged small-pore zeolites, *Applied Catalysis B-Environmental*, 102 (2011).

[46] J.H. Kwak, D. Tran, S.D. Burton, J. Szanyi, J.H. Lee, C.H.F. Peden, Effects of hydrothermal aging on NH_3-SCR reaction over Cu/zeolites, *Journal of Catalysis*, 287 (2012) 203-209.

[47] J.H. Kwak, R.G. Tonkyn, D.H. Kim, J. Szanyi, C.H.F. Peden, Excellent activity and selectivity of Cu-SSZ-13 in the selective catalytic reduction of NO_x with NH_3, *Journal of Catalysis*, 275 (2010).

[48] J.H.K. Feng Gao, Janos Szanyi, Charles H. F. Peden, Current understanding of Cu-exchanged Chabazite molecular sieves for use as commercial diesel engine $DeNO_x$ catalysts, in, *Topics in Catalysis*, 2013.

[49] D.W. Fickel, J.M. Fedeyko, R.F. Lobo, Copper coordination in Cu-SSZ-13 and Cu-SSZ-16 investigated by variable-temperature XRD, *Journal of Physical Chemistry C*, 114 (2010).

[50] B. RW, Zeolite types and structures. In: KulprathipanjaS (ed) Zeolites in Industrial Separation and Catalysis., Wiley-CVH, Weinheim, 2010.

[51] S. Brandenberger, O. Kroecher, A. Tissler, R. Althoff, The state of the art in selective catalytic reduction of NO_x by ammonia using metal-exchanged zeolite catalysts, *Catalysis Reviews-Science and Engineering*, 50 (2008) 492-531.

[52] M. Koebel, M. Elsener, M. Kleemann, Urea-SCR: a promising technique to reduce NOx emissions from automotive diesel engines, *Catalysis Today*, 59 (2000) 335-345.

[53] M. Devadas, O. Krocher, M. Elsener, A. Wokaun, N. Soger, M. Pfeifer, Y. Demel, L. Mussmann, Influence of NO_2 on the selective catalytic reduction of NO with ammonia over Fe-ZSM5, *Applied Catalysis B-Environmental*, 67 (2006) 187-196.

[54] K. Rahkamaa-Tolonen, T. Maunula, M. Lomma, M. Huuhtanen, R.L. Keiski, The effect of NO_2 on the activity of fresh and aged zeolite catalysts in the NH_3-SCR reaction, *Catalysis Today*, 100 (2005) 217-222.

[55] J.H.K. Feng Gao, Janos Szanyi, Charles H. F. Peden, Current Understanding of Cu-Exchanged chabazite molecular sieves for use as commercial diesel engine $DeNO_x$Catalysts, in, *Topics in Catalysis*, 2013, pp. 1441-1459.

[56] J. Szanyi, J.H. Kwak, H. Zhu, C.H.F. Peden, Characterization of Cu-SSZ-13 NH_3 SCR catalysts: an in situ FTIR study, *Physical Chemistry Chemical Physics*, 15 (2013) 2368-2380.

[57] U. Deka, A. Juhin, E.A. Eilertsen, H. Emerich, M.A. Green, S.T. Korhonen, B.M. Weckhuysen, A.M. Beale, Confirmation of isolated Cu^{2+} ions in SSZ-13 Zeolite as active sites in NH_3-selective catalytic reduction, *Journal of Physical Chemistry C*, 116 (2012).

[58] J.H. Kwak, D. Tran, J. Szanyi, C.H.F. Peden, J.H. Lee, The Effect of copper loading on the selective catalytic reduction of nitric oxide by Ammonia Over Cu-SSZ-13, *Catalysis Letters*, 142 (2012).

[59] U. Deka, I. Lezcano-Gonzalez, B.M. Weckhuysen, A.M. Beale, Local environment and nature of Cu active sites in zeolite-based catalysts for the selective catalytic reduction of NO_x, *ACS Catalysis*, 3 (2013) 413-427.

[60] J. Xue, X. Wang, G. Qi, J. Wang, M. Shen, W. Li, Characterization of copper species over Cu/SAPO-34 in selective catalytic reduction of NO_x with ammonia: Relationships between active Cu sites and de-NO_x performance at low temperature, *Journal of Catalysis*, 297 (2013) 56-64.

[61] L. Wang, W. Li, G.S. Qi, D. Weng, Location and nature of Cu species in Cu/SAPO-34 for selective catalytic reduction of NO with NH_3, *Journal of Catalysis*, 289 (2012) 21-29.

[62] F. Gao, E.D. Walter, E.M. Karp, J. Luo, R.G. Tonkyn, J.H. Kwak, J. Szanyi, C.H.F. Peden, Structure-activity relationships in NH_3-SCR over Cu-SSZ-13 as probed by reaction kinetics and EPR studies, *Journal of Catalysis*, 300 (2013) 20-29.

[63] L. Ma, Y. Cheng, G. Cavataio, R.W. McCabe, L. Fu, J. Li, Characterization of commercial Cu-SSZ-13 and Cu-SAPO-34 catalysts with hydrothermal treatment for NH_3-SCR of NOx in diesel exhaust, *Chemical Engineering Journal*, 225 (2013) 323-330.

[64] J.H. Kwak, H. Zhu, J.H. Lee, C.H.F. Peden, J. Szanyi, Two different cationic positions in Cu-SSZ-13?, *Chemical Communications*, 48 (2012) 4758-4760.

[65] Z. SI, Zeolite SSZ-13 and its method of preparation, in, 1985.

[66] F. Gao, E.D. Walter, N.M. Washton, J. Szanyi, C.H.F. Peden, Synthesis and evaluation of Cu-SAPO-34 catalysts for ammonia selective catalytic reduction. 1. Aqueous solution ion exchange, *ACS Catalysis*, (2013) 2083-2093.

[67] Q. Ye, L. Wang, R.T. Yang, Activity, propene poisoning resistance and hydrothermal stability of copper exchanged chabazite-like zeolite catalysts for SCR of NO with ammonia in comparison to Cu/ZSM-5, *Applied Catalysis A-General*, 427 (2012).

[68] S. Fan, J. Xue, T. Yu, D. Fan, T. Hao, M. Shen, W. Li, The effect of synthesis methods on Cu species and active sites over Cu/SAPO-34 for NH_3-SCR reaction, *Catalysis Science & Technology*, 3 (2013) 2357-2364.

[69] L. Ren, L. Zhu, C. Yang, Y. Chen, Q. Sun, H. Zhang, C. Li, F. Nawaz, X. Meng, F.-S. Xiao, Designed copper-amine complex as an efficient template for one-pot synthesis of Cu-SSZ-13 zeolite with excellent activity for selective catalytic reduction of NO_x by NH_3, *Chemical Communications*, 47 (2011) 9789-9791.

[70] R. Martinez-Franco, M. Moliner, C. Franch, A. Kustov, A. Corma, Rational direct synthesis methodology of very active and hydrothermally stable Cu-SAPO-34 molecular sieves for the SCR of NO_x, *Applied Catalysis B-Environmental*, 127 (2012) 273-280.

[71] U. Deka, I. Lezcano-Gonzalez, S.J. Warrender, A.L. Picone, P.A. Wright, B.M. Weckhuysen, A.M. Beale, Changing active sites in Cu-CHA catalysts: deNO(x) selectivity as a function of the preparation method, *Microporous and Mesoporous Materials*, 166 (2013) 144-152.

[72] L. Wang, J.R. Gaudet, W. Li, D. Weng, Migration of Cu species in Cu/SAPO-34 during hydrothermal aging, *Journal of Catalysis*, 306 (2013) 68-77.

[73] Y. Cheng, C. Montreuil, G. Cavataio, C. Lambert, The Effects of SO_2 and SO_3 Poisoning on Cu/Zeolite SCR Catalysts, *SAE International*, 01 (2009) 0898.

[74] B. Ramachandran, R.G. Herman, S. Choi, H.G. Stenger, C.E. Lyman, J.W. Sale, Testing zeolite SCR catalysts under protocol conditions for NO_x abatement from stationary emission sources, *Catalysis Today*, 55 (2000) 281-290.

[75] Y. Cheng, C. Lambert, D.H. Kim, J.H. Kwak, S.J. Cho, C.H.F. Peden, The different impacts of SO_2 and SO_3 on Cu/zeolite SCR catalysts, *Catalysis Today*, 151 (2010) 266-270.

[76] The Praying Mantis^{TM} User's Manuel, in.

[77] ThermoNicolet IR spectroscopy User's Manual, in.

[78] A. Grossale, I. Nova, E. Tronconi, D. Chatterjee, M. Weibel, The chemistry of the NO/NO_2-NH_3 "fast" SCR reaction over Fe-ZSM5 investigated by transient reaction analysis, *Journal of Catalysis*, 256 (2008).

[79] M. Iwasaki, H. Shinjoh, A comparative study of "standard", "fast" and "NO_2" SCR reactions over Fe/zeolite catalyst, *Applied Catalysis A-General*, 390 (2010).

[80] A. Grossale, I. Nova, E. Tronconi, Study of a Fe-zeolite-based system as NH_3-SCR catalyst for diesel exhaust aftertreatment, *Catalysis Today*, 136 (2008) 18-27.

[81] M.P. Ruggeri, A. Grossale, I. Nova, E. Tronconi, H. Jirglova, Z. Sobalik, FTIR in situ mechanistic study of the NH_3-NO/NO_2 "Fast SCR" reaction over a commercial Fe-ZSM-5 catalyst, *Catalysis Today*, 184 (2012) 107-114.

[82] J. Eng, C.H. Bartholomew, Kinetic and mechanistic study of NO_x reduction by NH_3 over H-form zeolites .2. Semi-steady-state and in situ FTIR studies, *Journal of Catalysis*, 171 (1997) 27-44.

[83] K. Hadjiivanov, J. Saussey, J.L. Freysz, J.C. Lavalley, FT-IR study of NO+O_2 co-adsorption on H-ZSM-5: re-assignment of the 2133 cm(-1) band to NO^+ species, *Catalysis Letters*, 52 (1998) 103-108.

[84] K.I. Hadjiivanov, Identification of neutral and charged N_xO_y surface species by IR spectroscopy, *Catalysis Reviews-Science and Engineering*, 42 (2000) 71-144.

[85] H. Sjovall, E. Fridell, R.J. Blint, L. Olsson, Identification of adsorbed species on Cu-ZSM-5 under NH_3SCR conditions, *Topics in Catalysis*, 42-43 (2007) 113-117.

[86] M. Rivallan, G. Ricchiardi, S. Bordiga, A. Zecchina, Adsorption and reactivity of nitrogen oxides (NO_2, NO, N_2O) on Fe-zeolites, *Journal of Catalysis*, 264 (2009) 104-116.

[87] B.J. Adelman, T. Beutel, G.D. Lei, W.M.H. Sachtler, Mechanistic cause of hydrocarbon specificity over Cu/ZSM-5 and Co/ZSM-5 catalysts in the selective catalytic reduction of NO_x, *Journal of Catalysis*, 158 (1996) 327-335.

[88] L. Olsson, H. Sjovall, R.J. Blint, Detailed kinetic modeling of NO_x adsorption and NO oxidation over Cu-ZSM-5, *Applied Catalysis B-Environmental*, 87 (2009) 200-210.

[89] P.S. Metkar, V. Balakotaiah, M.P. Harold, Experimental and kinetic modeling study of NO oxidation: Comparison of Fe and Cu-zeolite catalysts, *Catalysis Today*, 184 (2012) 115-128.

[90] M. Colombo, I. Nova, E. Tronconi, NO_2 adsorption on Fe- and Cu-zeolite catalysts: The effect of the catalyst red-ox state, *Applied Catalysis B-Environmental*, 111 (2012).

[91] M. Iwasaki, H. Shinjoh, NO evolution reaction with NO_2 adsorption over Fe/ZSM-5: In situ FT-IR observation and relationships with Fe sites, *Journal of Catalysis*, 273 (2010) 29-38.

[92] J. Szanyi, M.T. Paffett, The adsorption of NO and reaction of NO with O_2 on H-, NaH-, CuH-, and Cu-ZSM-5: An in situ FTIR investigation, *Journal of Catalysis*, 164 (1996).

[93] G.H. Li, S.C. Larsen, V.H. Grassian, Catalytic reduction of NO_2 in nanocrystalline NaY zeolite, *Journal of Molecular Catalysis A-Chemical*, 227 (2005) 25-35.

[94] C. Sedlmair, B. Gil, K. Seshan, A. Jentys, J.A. Lercher, An in situ IR study of the NO_x adsorption/reduction mechanism on modified Y zeolites, P*hysical Chemistry Chemical Physics*, 5 (2003).

[95] F. Poignant, J.L. Freysz, M. Daturi, J. Saussey, Mechanism of the selective catalytic reduction of NO in oxygen excess by propane on H-Cu-ZSM-5 - Formation of isocyanide species via acrylonitrile intermediate, *Catalysis Today*, 70 (2001) 197-211.

[96] M. Iwasaki, H. Shinjoh, Analysis of the adsorption state and desorption kinetics of NO_2 over Fe-zeolite catalyst by FT-IR and temperature-programmed desorption, *Physical Chemistry Chemical Physics*, 12 (2010) 2365-2372.

[97] G.V.A. Martins, G. Berlier, C. Bisio, S. Coluccia, H.O. Pastore, L. Marchese, Quantification of brønsted acid sites in microporous catalysts by a combined FTIR and NH_3-TPD study, *Journal of Physical Chemistry C*, 112 (2008) 7193-7200.

[98] S. Brandenberger, O. Krocher, A. Wokaun, A. Tissler, R. Althoff, The role of Bronsted acidity in the selective catalytic reduction of NO with ammonia over Fe-ZSM-5, *Journal of Catalysis*, 268 (2009) 297-306.

[99] M. Schwidder, M.S. Kumar, U. Bentrup, J. Perez-Ramirez, A. Brueckner, W. Gruenert, The role of Bronsted acidity in the SCR of NO over Fe-MFI catalysts, *Microporous and Mesoporous Materials*, 111 (2008) 124-133.

[100] M. Bevilacqua, T. Montanari, E. Finocchio, G. Busca, Are the active sites of protonic zeolites generated by the cavities?, *Catalysis Today*, 116 (2006).

[101] D. Klukowski, P. Balle, B. Geiger, S. Wagloehner, S. Kureti, B. Kimmerle, A. Baiker, J.D. Grunwaldt, On the mechanism of the SCR reaction on Fe/HBEA zeolite, *Applied Catalysis B-Environmental*, 93 (2009) 185-193.

[102] J. Dedecek, L. Capek, P. Sazama, Z. Sobalik, B. Wichterlova, Control of metal ion species in zeolites by distribution of aluminium in the framework: From structural analysis to performance under real conditions of SCR-NO_x and NO, N_2O decomposition, *Applied Catalysis A-General*, 391 (2011).

[103] K. Suzuki, T. Noda, N. Katada, M. Niwa, IRMS-TPD of ammonia: Direct and individual measurement of Bronsted acidity in zeolites and its relationship with the catalytic cracking activity, *Journal of Catalysis*, 250 (2007) 151-160.

[104] B. Onida, Z. Gabelica, J. Lourenco, E. Garrone, Spectroscopic characterization of hydroxyl groups in SAPO-40 .1. Study of the template-free samples and their interaction with ammonia, *Journal of Physical Chemistry*, 100 (1996).

[105] A.C. Akah, G. Nkeng, A.A. Garforth, The role of Al and strong acidity in the selective catalytic oxidation of NH_3 over Fe-ZSM-5, *Applied Catalysis B-Environmental*, 74 (2007) 34-39.

[106] G. Delahay, D. Valade, A. Guzman-Vargas, B. Coq, Selective catalytic reduction of nitric oxide with ammonia on Fe-ZSM-5 catalysts prepared by different methods, *Applied Catalysis B-Environmental*, 55 (2005) 149-155.

[107] I. Nova, C. Ciardelli, E. Tronconi, D. Chatterjee, B. Bandl-Konrad, NH_3-NO/NO_2 chemistry over V-based catalysts and its role in the mechanism of the Fast SCR reaction, *Catalysis Today*, 114 (2006).

[108] I. Malpartida, O. Marie, P. Bazin, M. Daturi, X. Jeandel, The NO/NO_x ratio effect on the NH_3-SCR efficiency of a commercial automotive Fe-zeolite catalyst studied by operando IR-MS, *Applied Catalysis B-Environmental*, 113 (2012).

[109] A. Grossale, I. Nova, E. Tronconi, Ammonia blocking of the "Fast SCR" reactivity over a commercial Fe-zeolite catalyst for Diesel exhaust aftertreatment, *Journal of Catalysis*, 265 (2009).

[110] Q. Sun, Z.X. Gao, H.Y. Chen, W.M.H. Sachtler, Reduction of NOx with ammonia over Fe/MFI: Reaction mechanism based on isotopic labeling, *Journal of Catalysis*, 201 (2001).

[111] J. Szanyi, J.H. Kwak, R.A. Moline, C.H.F. Peden, The adsorption of NO_2 and the NO+O_2 reaction on Na-Y,FAU: an in situ FTIR investigation, *Physical Chemistry Chemical Physics*, 5 (2003).

[112] M. Iwasaki, H. Shinjoh, Analysis of the adsorption state and desorption kinetics of NO_2 over Fe-zeolite catalyst by FT-IR and temperature-programmed desorption, *Physical Chemistry Chemical Physics*, 12 (2010).

[113] A. Desikusumastuti, T. Staudt, M. Happel, M. Laurin, J. Libuda, Adsorption and reaction of NO_2 on ordered alumina films and mixed baria-alumina nanoparticles: Cooperative versus non-cooperative reaction mechanisms, *Journal of Catalysis*, 260 (2008).

[114] U. Deka, A. Juhin, E.A. Eilertsen, H. Emerich, M.A. Green, S.T. Korhonen, B.M. Weckhuysen, A.M. Beale, Confirmation of Isolated Cu^{2+} Ions in SSZ-13 Zeolite as Active Sites in NH_3-Selective Catalytic Reduction, *Journal of Physical Chemistry C*, 116 (2012) 4809-4818.

[115] J.S. McEwen, T. Anggara, W.F. Schneider, V.F. Kispersky, J.T. Miller, W.N. Delgass, F.H. Ribeiro, Integrated operando X-ray absorption and DFT characterization of Cu-SSZ-13 exchange sites during the selective catalytic reduction of NOx with NH_3, *Catalysis Today*, 184 (2012).

[116] M. Ahrens, O. Marie, P. Bazin, M. Daturi, Fe-H-BEA and Fe-H-ZSM-5 for NO_2 removal from ambient air - A detailed in situ and operando FTIR study revealing an unexpected positive water-effect, *Journal of Catalysis*, 271 (2010).

[117] C. Ciardelli, I. Nova, E. Tronconi, D. Chatterjee, B. Bandl-Konrad, M. Weibel, B. Krutzsch, Reactivity of NO/NO(2)-NH(3) SCR system for diesel exhaust aftertreatment: Identification of the reaction network as a function of temperature and NO(2) feed content, *Applied Catalysis B-Environmental*, 70 (2007) 80-90.

[118] Y.H. Yeom, J. Henao, M.J. Li, W.M.H. Sachtler, E. Weitz, The role of NO in the mechanism of NO_x reduction with ammonia over a BaNa-Y catalyst, *Journal of Catalysis*, 231 (2005).

[119] C. Ciardelli, I. Nova, E. Tronconi, D. Chatterjee, B. Bandl-Konrad, A "Nitrate Route" for the low temperature "Fast SCR" reaction over a V_2O_5-WO_3/TiO_2 commercial catalyst, *Chemical Communications*, (2004).

[120] M.J. Li, J. Henao, Y. Yeom, E. Weitz, W.M.H. Sachtler, Low activation energy pathway for the catalyzed reduction of nitrogen oxides to N_2 by ammonia, *Catalysis Letters*, 98 (2004).

[121] I. Nova, C. Ciardelli, E. Tronconi, D. Chatterjee, B. Bandl-Konrad, NH_3-NO/NO_2 chemistry over V-based catalysts and its role in the mechanism of the Fast SCR reaction, *Catalysis Today*, 114 (2006) 3-12.

[122] H.Y. Chen, Q. Sun, B. Wen, Y.H. Yeom, E. Weitz, W.M.H. Sachtler, Reduction over zeolite-based catalysts of nitrogen oxides in emissions containing excess oxygen - Unraveling the reaction mechanism, *Catalysis Today*, 96 (2004) 1-10.

[123] A. Savara, M.-J. Li, W.M.H. Sachtler, E. Weitz, Catalytic reduction of NH_4NO_3 by NO: Effects of solid acids and implications for low temperature DeNO(x) processes, *Applied Catalysis B-Environmental*, 81 (2008) 251-257.

[124] P. Forzatti, I. Nova, E. Tronconi, Enhanced NH_3 selective catalytic reduction for NOx abatement, *Angewandte Chemie-International Edition*, 48 (2009) 8366-8368.

[125] P. Forzatti, I. Nova, E. Tronconi, New "Enhanced NH_3-SCR" Reaction for NO_x emission control, *Industrial & Engineering Chemistry Research*, 49 (2010) 10386-10391.

[126] A. Grossale, I. Nova, E. Tronconi, Role of nitrate species in the "NO_2-SCR" mechanism over a commercial Fe-zeolite catalyst for SCR mobile applications, *Catalysis Letters*, 130 (2009) 525-531.

[127] D.B. Akolekar, S.K. Bhargava, NO and CO adsorption studies on transition metal-exchanged silico-aluminophosphate of type 34 catalysts, *Applied Catalysis A-General*, 207 (2001) 355-365.

[128] D.B. Akolekar, S.K. Bhargava, K. Foger, FTIR investigations of the adsorption and disproportionation of NO on Cu-exchanged silicoaluminophosphate of type 34, *Journal of the Chemical Society-Faraday Transactions*, 94 (1998) 155-160.

[129] P.E. Fanning, M.A. Vannice, A DRIFTS study of Cu-ZSM-5 prior to and during its use for N_2O decomposition, *Journal of Catalysis*, 207 (2002) 166-182.

[130] G.D. Lei, B.J. Adelman, J. Sarkany, W.M.H. Sachtler, Identification of copper(II) and copper(I) and their interconversion in Cu/ZSM-5 $DeNO_x$ Catalysts, *Applied Catalysis B-Environmental*, 5 (1995) 245-256.

[131] S. Brandenberger, O. Kroecher, A. Tissler, R. Althoff, Effect of structural and preparation parameters on the activity and hydrothermal stability of metal-exchanged ZSM-5 in the selective catalytic reduction of NO by NH_3, *Industrial & Engineering Chemistry Research*, 50 (2011).

[132] A. Shishkin, P.-A. Carlsson, H. Harelind, M. Skoglundh, Effect of preparation procedure on the catalytic properties of Fe-ZSM-5 as SCR catalyst, *Topics in Catalysis*, 56 (2013) 567-575.

[133] J. Wang, T. Yu, X. Wang, G. Qi, J. Xue, M. Shen, W. Li, The influence of silicon on the catalytic properties of Cu/SAPO-34 for NO_x reduction by ammonia-SCR, *Applied Catalysis B-Environmental*, 127 (2012) 137-147.

[134] S.G. Hegde, R. Kumar, R.N. Bhat, P. Ratnasamy, Characterization of the acidity of zeolite-beta by FTIR spectroscopy and TPD of NH_3, *Zeolites*, 9 (1989) 231-237.

[135] N. Katada, H. Igi, J.H. Kim, M. Niwa, Determination of the acidic properties of zeolite by theoretical analysis of temperature-programmed desorption of ammonia based on adsorption equilibrium, *Journal of Physical Chemistry B*, 101 (1997) 5969-5977.

[136] R.Q. Long, R.T. Yang, Temperature-programmed desorption/surface reaction (TPD/TPSR) study of Fe-exchanged ZSM-5 for selective catalytic reduction of nitric oxide by ammonia, *Journal of Catalysis*, 198 (2001) 20-28.

[137] Z. Sobalik, J. Dedecek, I. Ikonnikov, B. Wichterlova, State and coordination of metal ions in high silica zeolites Incorporation, development and rearrangement during preparation and catalysis, *Microporous and Mesoporous Materials*, 21 (1998) 525-532.

[138] E. Broclawik, J. Datka, B. Gil, P. Kozyra, T-O-T skeletal vibration in CuZSM-5 zeolite: IR study and quantum chemical modeling, *Physical Chemistry Chemical Physics*, 2 (2000) 401-405.

[139] Y. Kuroda, H. Maeda, H. Moriwaki, N. Bamba, T. Morimoto, Local crystal-structure of exchanged ions in zeolite, *Physica B*, 158 (1989) 185-187.

[140] S. Brandenberger, O. Krocher, A. Tissler, R. Althoff, The determination of the activities of different iron species in Fe-ZSM-5 for SCR of NO by NH(3), *Applied Catalysis B-Environmental*, 95 (2010) 348-357.

[141] S. Brandenberger, O. Kroecher, A. Tissler, R. Althoff, Estimation of the fractions of different nuclear iron species in uniformly metal-exchanged Fe-ZSM-5 samples based on a Poisson distribution, *Applied Catalysis A-General*, 373 (2010) 168-175.

[142] J.H. Kwak, R. Tonkyn, D. Tran, D. Mei, S.J. Cho, L. Kovarik, J.H. Lee, C.H.F. Peden, J. Szanyi, Size-Dependent Catalytic Performance of CuO on gamma-Al_2O_3: NO Reduction versus NH_3 Oxidation, *ACS Catalysis*, 2 (2012) 1432-1440.

[143] M. Kogel, V.H. Sandoval, W. Schwieger, A. Tissler, T. Turek, Simultaneous catalytic reduction of NO and N_2O using Fe-MFI prepared by solid-state ion exchange, *Catalysis Letters*, 51 (1998) 23-25.

[144] R.Q. Long, R.T. Yang, Fe-ZSM-5 for selective catalytic reduction of NO with NH_3: a comparative study of different preparation techniques, *Catalysis Letters*, 74 (2001) 201-205.

[145] M. Iwasaki, K. Yamazaki, K. Banno, H. Shinjoh, Characterization of Fe/ZSM-5 DeNO(x) catalysts prepared by different methods: Relationships between active Fe sites and NH_3-SCR performance, *Journal of Catalysis*, 260 (2008).

[146] G.S. Qi, R.T. Yang, Ultra-active Fe/ZSM-5 catalyst for selective catalytic reduction of nitric oxide with ammonia, *Applied Catalysis B-Environmental*, 60 (2005) 13-22.

[147] L.J. Lobree, I.C. Hwang, J.A. Reimer, A.T. Bell, Investigations of the state of Fe in H-ZSM-5, *Journal of Catalysis*, 186 (1999) 242-253.

[148] M. Rauscher, K. Kesore, R. Monnig, W. Schwieger, A. Tissler, T. Turek, Preparation of a highly active Fe-ZSM-5 catalyst through solid-state ion exchange for the catalytic decomposition of N_2O, *Applied Catalysis A-General*, 184 (1999) 249-256.

[149] B.M. Abu-Zied, W. Schwieger, A. Unger, Nitrous oxide decomposition over transition metal exchanged ZSM-5 zeolites prepared by the solid-state ion-exchange method, *Applied Catalysis B-Environmental*, 84 (2008) 277-288.

[150] J. Perez-Ramirez, F. Kapteijn, G. Mul, J.A. Moulijn, Highly active SO_2-resistant ex-framework FeMFI catalysts for direct N_2O decomposition, *Applied Catalysis B-Environmental*, 35 (2002) 227-234.

[151] A. Guzmán-Vargas, G. Delahay, B. Coq, Catalytic decomposition of N_2O and catalytic reduction of N_2O and N_2O + NO by NH_3 in the presence of O_2 over Fe-zeolite, *Applied Catalysis B: Environmental*, 42 (2003) 369-379.

[152] Y. Zheng, Y. Liu, M.P. Harold, D. Luss, LNT–SCR dual-layer catalysts optimized for lean NO_x reduction by H_2 and CO, *Applied Catalysis B: Environmental*, 148–149 (2014) 311-321.

[153] L. Sommer, D. Mores, S. Svelle, M. Stocker, B.M. Weckhuysen, U. Olsbye, Mesopore formation in zeolite H-SSZ-13 by desilication with NaOH, *Microporous and Mesoporous Materials*, 132 (2010) 384-394.

[154] S. Bordiga, L. Regli, D. Cocina, C. Lamberti, M. Bjorgen, K.P. Lillerud, Assessing the acidity of high silica chabazite H-SSZ-13 by FTIR using CO as molecular probe: Comparison with H-SAPO-34, *Journal of Physical Chemistry B*, 109 (2005) 2779-2784.

[155] H. Zhu, J.H. Kwak, C.H.F. Peden, J. Szanyi, In situ DRIFTS-MS studies on the oxidation of adsorbed NH_3 by NO_x over a Cu-SSZ-13 zeolite, *Catalysis Today*, 205 (2013) 16-23.

[156] J.H. Park, H.J. Park, J.H. Baik, I.S. Nam, C.H. Shin, J.H. Lee, B.K. Cho, S.H. Oh, Hydrothermal stability of CuZSM5 catalyst in reducing NO by NH_3 for the urea selective catalytic reduction process, *Journal of Catalysis*, 240 (2006) 47-57.

[157] S.J. Schmieg, S.H. Oh, C.H. Kim, D.B. Brown, J.H. Lee, C.H.F. Peden, D.H. Kim, Thermal durability of Cu-CHA NH_3-SCR catalysts for diesel NO_x reduction, *Catalysis Today*, 184 (2012).

[158] B.Q. Jiang, Z.B. Wu, Y. Liu, S.C. Lee, W.K. Ho, DRIFT study of the SO_2 effect on low-temperature SCR reaction over Fe−Mn/TiO_2, *The Journal of Physical Chemistry C*, 114 (2010) 4961-4965.

[159] W. Xu, H. He, Y. Yu, Deactivation of a Ce/TiO_2 Catalyst by SO_2 in the selective catalytic reduction of NO by NH_3, *The Journal of Physical Chemistry C*, 113 (2009) 4426-4432.

[160] S. Yang, Y. Guo, H. Chang, L. Ma, Y. Peng, Z. Qu, N. Yan, C. Wang, J. Li, Novel effect of SO_2 on the SCR reaction over CeO_2: Mechanism and significance, *Applied Catalysis B-Environmental*, 136 (2013) 19-28.

[161] M. Ziolek, I. Sobczak, I. Nowak, M. Daturi, J.C. Lavalley, Effect of sulfur dioxide on nitric oxide adsorption and decomposition on Cu-containing micro- and mesoporous molecular sieves, *Topics in Catalysis*, 11 (2000) 343-350.

[162] I.C. Marcu, I. Sandulescu, Study of sulfur dioxide adsorption on Y zeolite, *Journal of the Serbian Chemical Society*, 69 (2004) 563-569.

[163] A. Sultana, T. Nanba, M. Sasaki, M. Haneda, K. Suzuki, H. Hamada, Selective catalytic reduction of NO_x with NH_3 over different copper exchanged zeolites in the presence of decane, *Catalysis Today*, 164 (2011) 495-499.

[164] H. Abdulhamid, E. Fridell, J. Dawody, M. Skoglundh, In situ FTIR study Of SO_2 interaction with Pt/$BaCO_3$/Al_2O_3 NO_x storage catalysts under lean and rich conditions, *Journal of Catalysis*, 241 (2006) 200-210.

[165] C.C. Chang, Infrared studies of SO_2 on γ-alumina, *Journal of Catalysis*, 53 (1978) 374-385.

[166] H. Chang, J. Li, J. Yuan, L. Chen, Y. Dai, H. Arandiyan, J. Xu, J. Hao, Ge, Mn-doped CeO_2–WO_3 catalysts for NH_3–SCR of NO_x: Effects of SO_2 and H_2 regeneration, *Catalysis Today*, 201 (2013) 139-144.

[167] G.Y. Xie, Z.Y. Liu, Z.P. Zhu, Q.Y. Liu, J. Ge, Z.G. Huang, Simultaneous removal of SO_2 and NO_x from flue gas using a CuO/Al_2O_3 catalyst sorbent I. Deactivation of SCR activity by SO_2 at low temperatures, *Journal of Catalysis*, 224 (2004) 36-41.

[168] F. Yin, A.L. Blumenfeld, V. Gruver, J.J. Fripiat, NH_3 as a probe molecule for NMR and IR Study of zeolite catalyst acidity, *The Journal of Physical Chemistry B*, 101 (1997) 1824-1830.

[169] G. Chen, J. Gao, J. Gao, Q. Du, X. Fu, Y. Yin, Y. Qin, Simultaneous removal of SO_2 and NO_x by calcium hydroxide at low temperature: effect of SO_2 absorption on NO_2 removal, *Industrial & Engineering Chemistry Research*, 49 (2010) 12140-12147.

[170] L. Zhang, J. Pierce, V.L. Leung, D. Wang, W.S. Epling, Characterization of Ceria's interaction with NO_x and NH_3, *The Journal of Physical Chemistry C*, 117 (2013) 8282-8289.